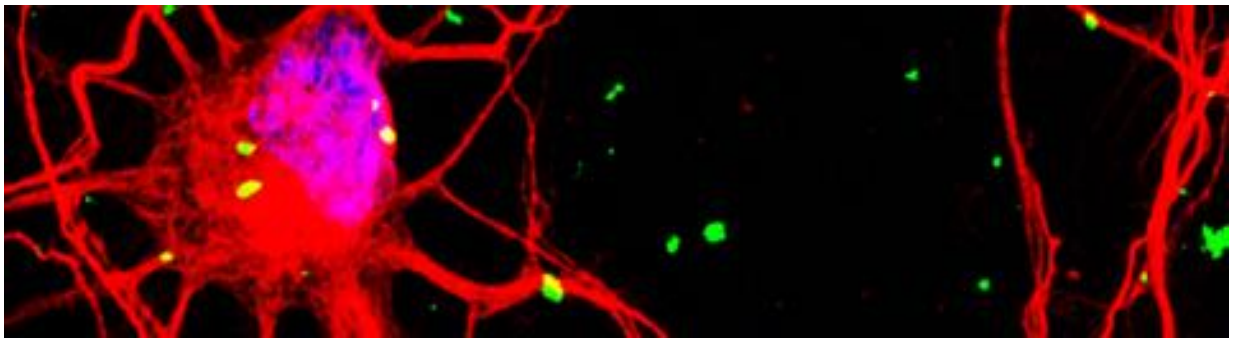

Corso di Dottorato in Neuroscienze
Curriculum Neuroscienze e Neurotecnologie
Ciclo XXXI

In vitro neuronal cultures on MEA: an engineering approach to study physiological and pathological brain networks

Ilaria Colombi

Supervisor: Dr. Michela Chiappalone

ISTITUTO ITALIANO DI TECNOLOGIA

UNIVERSITÀ DEGLI STUDI DI GENOVA

Contents

Introduction

Uncovering the mechanisms that underlie the brain's functioning would have a profound social impact. In fact, among the many diseases affecting health, brain disorders are major causes of impaired quality of life; problems related to such diseases involve cognitive, psychological and social consequences. According to estimates by the World Health Organization, more than one billion people suffer from disorders of the central nervous system (WHO 2012).

In this context, the neurosciences have begun in recent decades to address the complexity of the brain and the nervous system using a multilevel approach involving not only many different branches of biology (molecular and cellular biology, genetics, biochemistry, etc.) but also physics, mathematics, engineering and related fields.

Managing the brain's complexity and advancing our understanding of its function involves innovations in both the experimental methods used to observe and perturb brain activity and the computational tools used to analyze recorded data.

Among the different electrophysiological techniques, Microelectrodes Array technology (MEA) represents a powerful tool that permits long-term recording of local field potentials (LFPs) and extracellular action potentials (EAPs) from populations of neurons. Multisite extracellular recording by means of MEA has the potential to reveal a wide range of neural phenomena ranging from individual cell behavior to network dynamics.

Moreover, over the last few years, researchers have begun to use neuronal networks *in vitro* as a tool for investigating markers of sleep similar to those that can be observed by *in vivo* recording (Sengupta et al., 2011; Hinard et al., 2012). Sleep is usually considered a whole-brain phenomenon in which neuronal regulatory circuits impose sleep on the brain. Nevertheless, recent evidence suggests that sleep, or at least correlates of sleep, can be a regional phenomenon of the brain. Considerable effort in current sleep science aims at understanding to what extent an *in vitro* system can recapitulate the essential features of a sleeping brain. However, key question such as *What is the minimum amount of brain tissue required for sleep-features to manifest?* remain inadequately answered.

In this context, the main goal of this thesis is to answer to two specific questions: *i) Can we encompass some essential features of sleep in a simplified model of the brain through the use of MEAs? ii) Can our model recapitulate the essential features of sleep in a pathology characterized by sleep disturbances?*

Moreover, such systems are useful in investigating the effects of long-term exposure to pharmacological compounds with a view to developing novel neuropharmacological/ neurotoxicological assays for drug screening. MEAs couple neuronal cultures represent a simple, low-risk and accessible model that can be used to evaluate, in terms of electrophysiological activity, the effectiveness of new therapies in the preclinical phase. Findings from these studies could have significant implications for the treatment of human diseases such as congenital malformations, epilepsy, stroke and Alzheimer's disease (Hofmann et al., 2006, Görtz et al., 2009, Gullo et al., 2014). In this context, we performed neuropharmacological experiments on Down syndrome hippocampal cultures and acute slices couple to MEAs with the aim of testing the effect of a promising drug

The first part is entirely dedicated to the scientific and technical background on which our study relies, including basic notions concerning the *in vitro* electrophysiology of neuronal networks (Chapter 1) and a technical description of the experimental setup and the data analysis used for microelectrode array recordings (Chapter 2)

The second part deals with the results regarding sleep-related electrophysiological activity under both physiological and pathological conditions in neuronal cultures. In particular, Chapter 3 contains a brief introduction to the regulation and the measurement of sleep from human to mice and *in vitro* cultures. Chapter 4 presents the results regarding the modulation of sleep-like activity in a physiological condition. In Chapter 5 we show the results regarding the complexity of the evoked response from cultures in which sleep-like activity is modulated under physiological conditions. Chapter 6 presents the results regarding the modulation of sleep-like activity in a pathology in which sleep is affected (i.e., Prader-Willi pathology).

The third part of this thesis describes neuropharmacological experiments that are related to two neurological disorders (epilepsy and Down syndrome) and were performed in neuronal cultures and brain slices. Chapter 7 includes a description of our custom methodology for brain slice experiments, including the custom fitting of the experimental setup and the data analysis tools. Chapter 8 describes experiments using both neuronal cultures and brain slices from Down syndrome mice aiming to evaluate the efficacy of specific therapeutic drug.

Part I

Scientific and technical background

Chapter 1

In vitro neuronal networks

The human brain is the most complex structure in the known universe. The mathematician Ian Parker once said: "*If our brains were simple enough for us to understand them, we'd be so simple that we couldn't*". No other brain in the animal kingdom is capable of generating the level of higher consciousness associated with our ability to make plans or write poetry. Moreover, the nervous system perceives the enormous complexity and variability of the world surrounding us through a sophisticated array of sensors, i.e., the incoming sensory information is organized and elaborated in appropriate behavioral responses. Despite this complexity, individual nerve cells are relatively simple in their morphology; they all share the same basic architecture, although the human brain contains more than a thousand different types of neurons. Thus, sophisticated and complex human behavior depends largely on the way in which these cells form precise anatomical circuits. Hence, the capability of the nervous system to produce different actions in response to complex sensory stimuli derives from the way in which neurons are connected to each other in networks and to sensory receptors and muscles rather than from single-cell specialization (Kandel et al., 2000) For these reasons, the study of neuronal networks either *in vitro* or *in vivo* is fundamental to the understanding of brain function and brain pathologies.

1.1 Cell cultures preparation

The spectacular advances in biology that occurred in the second half of the 19th century resulted largely from the availability of a rapidly growing array of new experimental methods. Among the most important techniques in many areas of biology, especially neurobiology, methods have been developed for maintaining, culturing and growing cells and tissues *in vitro* (Carrel and T Burrows, 1910). The history of tissue culture began at the end of the 19th century when Ross Granville Harrison showed that cells and neurons could be maintained alive outside of a living animal (Harrison et al., 1907;Granville Harrison, 1910;Harrison, 1912;1924). According to Harrison (Harrison, 1912): "*Tissue from the chick were incubated at about 39 °C. The unusual hot weather which lasted during almost the experiments with chick tissues were under way rendered unnecessary any precaution to keep tissue warm during their preparation and examination*". Harrison demonstrated unequivocally that tissue could survive and grown outside the body (**Figure 1.1**).

Harrison's observations of neuronal development in cultures attracted many followers. The goal of

much of the work in the early decades was simply to demonstrate that complex aspect of neuronal maturation, such as synaptogenesis and myelination, could occur in culture (Peterson and Murray, 1955). Other works provided the first, detailed views of the dynamic activities of living nerve cells (Nakai, 1956;1960;Pomerat et al., 1967). In 1969, clonal lines of neuroblastoma cells were maintained in culture and continued to proliferate and to acquire properties characteristic of differentiated neurons (Augusti-Tocco and Sato, 1969).

In the ensuing years, many novel methods have been developed, increasing the possibility of preparing *in vitro* neuronal networks from different brain regions. Therefore, *in vitro* culturing began to gain a more prominent and important position in neurobiology. Today, tissue culture is an essential part of modern neurobiology: nearly one third of the papers that currently appear in the scientific journal *Neuron* use nerve cell cultures as an important method.

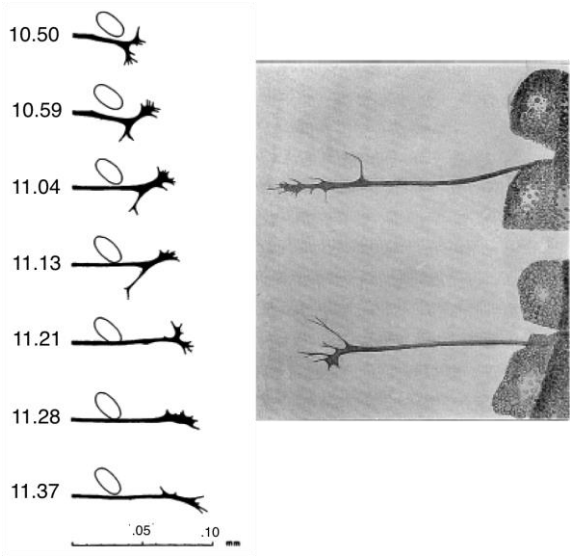

Figure 1.1 Harrison drawing illustrating cultured nerve fibers. Source (ref)

Neuronal cultures lack of the extrinsic physiological inputs and have reduced cellular and biochemical complexity but they offer the possibility of conducting biochemical studies of homogenous populations of neuronal cells. Moreover they provide a valuable complement to *in vivo* experiments by allowing more controlled manipulation of cellular functions and processes. Two types of *in vitro* cultures are mainly used, namely primary cultures and cell lines. The former are called primary cultures because they are prepared from cells taken directly from the animal; when plated on an appropriate substrate, neurons began to extend processes within several hours, forming dense networks. Under favorable conditions, it is possible to maintain such cultures for months, during which time the cells acquire most of the properties of mature neurons. They develop distinct axons and dendrites, form synapses with one another, and express receptors and ion channels that are characteristic of the corresponding cell types in situ. The morphological and physiological properties

of the cell population present in culture correspond closely to the characteristics of the cell population present in the tissue of origin (Kriegstein and Dichter, 1983;Banker and Waxman, 1988). The currently accepted protocol for culturing primary cultures of neurons is well defined and usually involves the dissection of brains from young rats, either embryonic or neonatal. Cultures are typically prepared from neurons located in specific regions of the brain such as the hippocampus or cortex. The main limitation of the use of primary cultures is that primary cultured cells have a finite lifespan and limited expansion capacity; consequently, for each preparation an animal must be sacrificed to obtain new tissue and prepare new cultures.

Alternatively, it is possible to use continuous cell lines, most of which are derived from tumor cells (e.g., mouse neuroblastoma C-1300) (Augusti-Tocco and Sato 1969). These cells can be subcultured repeatedly and express a reasonably stable phenotype. For decades, cell lines have played a critical role in scientific advancement because they are generally highly proliferative and easier to culture and transfect. However, one of the drawbacks of using cell lines rather than primary cultures is that they often do not express key aspects of neuronal differentiation (e.g., development of axons and dendrites, formation of synapses, etc.), although they may share many of the individual characteristics of differentiated neurons (e.g., neurotransmitters, ion channels, receptors and other neuron-specific proteins) (Banker et al., 1998).

Recently, neurons derived from human induced pluripotent stem cells (hiPSCs) have emerged as a promising tool for studying neurological disorders. Although many protocols for differentiating hiPSCs into neurons have been developed, many of these protocols show high variability, low reproducibility, and low efficiency. In 2017 Frega and coworkers published a rapid and reliable protocol for generating human neurons from hiPSCs coupled to MEAs (Frega et al., 2017). In contrast to cultures obtained from animal models, the use of hiPSC lines permits direct comparison between neurons derived from different (i.e., patient-specific) hiPSC lines with a same genetic background and provides robust consistency for pharmacological studies

In vitro development of primary cell cultures

Cultured neuronal networks represent an excellent *in vitro* model that has been used in many areas of neuroscience, including synaptogenesis, axon guidance, nerve regeneration and neuronal plasticity (Dotti et al., 1988;Bi and Poo, 1998;1999;Taylor et al., 2005;Valor et al., 2007). The structural and functional features of cultured neuronal networks depend upon several factors such as the animal model involved, the tissue of origin, the cell density and the physical and biochemical environment (Biffi et al., 2013). These characteristics of the cultured cells evolve over time due to the differentiation and maturation processes of neurons (Morin et al., 2005).

Changes in the morphological and electrophysiological features of neuronal networks can be studied by means of microscopy, calcium imaging and single-cell or multisite electrophysiological techniques (e.g., patch clamp or microelectrode arrays). Recent work has reported the existence of a relationship between the age of a culture and its properties, including the connections within the network and neuronal spiking activity (Ichikawa et al., 1993;Ben-Ari, 2001;Chiappalone et al., 2006)

At the early developmental stage, neuronal cultures usually display low synaptic density and low neuronal connectivity compared to the mature stage (i.e., Days in Vitro, DIV, greater than 14). Indeed, the electrical activity at 7 DIV is characterized by single spikes, whereas at 14 DIV networks exhibit an increase in firing rate, a rich and stable burst pattern (i.e., episodes of high- frequency spiking) and highly synchronized periods of high-frequency activity that simultaneously encompass different network sites.

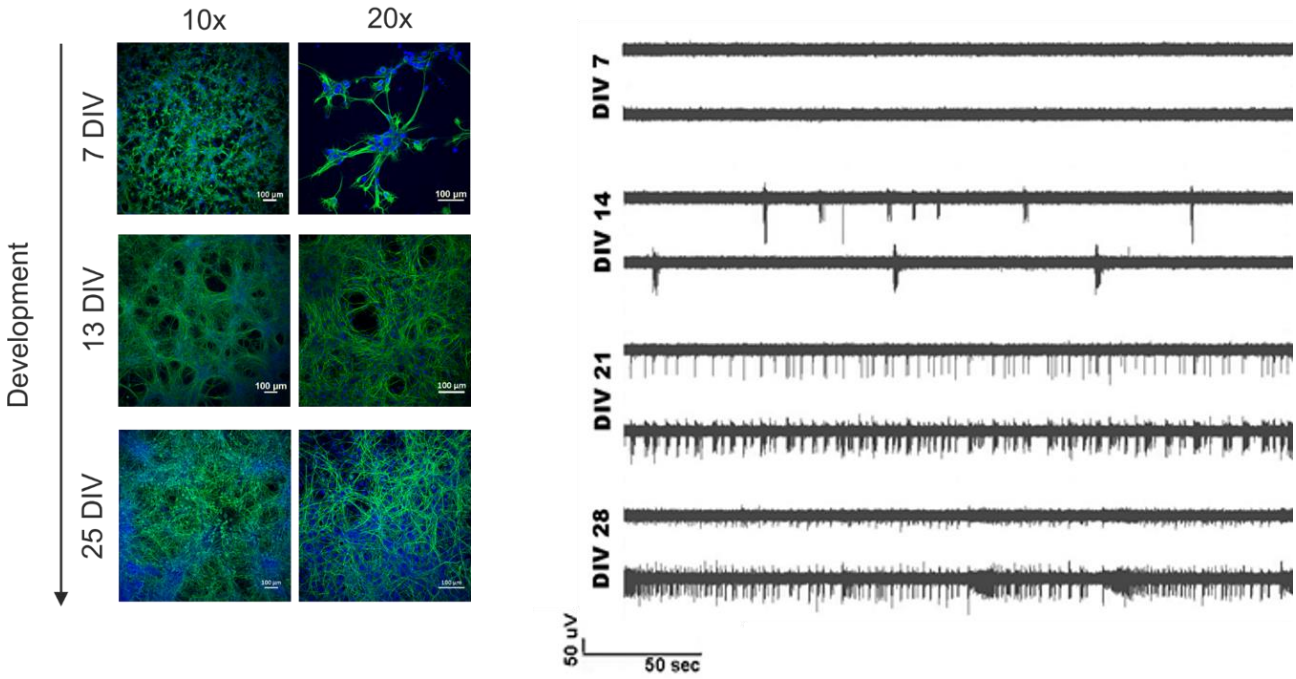

*Figure 1.2 Morphological changes in activity of in vitro cultures during development. On the left are immunofluorescence micrographs showing MAP2 immunostaining of a representative culture at three different developmental phases (7 DIV, 13 DIV and 25 DIV) at 2 different magnifications (*i.e.*, 10x and 20x; scale bars 100 µm and 50 µum, respectively) from Ito et al 2018). On the right, two representative traces of two channels from MEA at four developmental phases (7 DIV, 14 DIV, 21 DIV and 28 DIV) (from Chiappalone* et al. *2006)*

Moreover, the functional properties of developing neuronal networks are strongly affected by cell density due to variations in dendrite morphology and synaptic density (Akum et al., 2004) (Previtera et al., 2010). Neuronal cultures with different cell densities undergo network maturation in different ways by modulating the number of synapses per neuron and thus single-neuron synaptic transmission (Akum et al., 2004). Cell density also influences the regulation of the dendrite arborization in hippocampal cultures; as the initial plating density was increased, neurons showed decreased numbers of primary and secondary dendrites and decreased numbers of terminal points (Previtera et al., 2010).

Electrophysiological recordings obtained using cell-patch and calcium imaging techniques showed that plating at different densities (i.e., low, medium, and sparse) affects the connectivity among neurons; sparse networks (i.e., plating concentration of approximately 600-900 cells/mm^2) exhibited stronger synaptic connections between pairs of recorded neurons compared to dense cultures (plating concentration higher than 2500 cells/mm^2). Sparse networks showed higher synchronized activity than dense cultures, with enhanced bursting activity but with reduced frequency. Moreover, sparse neurons had simpler dendritic trees and fewer dendritic spines, demonstrating that neuronal density also affects the morphology of the dendrites and spines (Cohen et al., 2008;Ivenshitz and Segal, 2010). Biffi and colleagues (Biffi, Regalia et al. 2013) characterized the electrophysiological activity of neuronal cultures seeded at three different cell densities low (900 cells/mm2) medium (1800 cell/mm2) and high (3600 cell/mm2), recording their spontaneous electrical activity during maturation by means of MEAs. They showed that electrophysiological parameters were characterized by a functional peak during maturation maturation that was followed by a stable phase after 14 DIV for sparse- and medium-density cultures and by a decreased phase for high-density neuronal cultures (**Figure 1.3**).

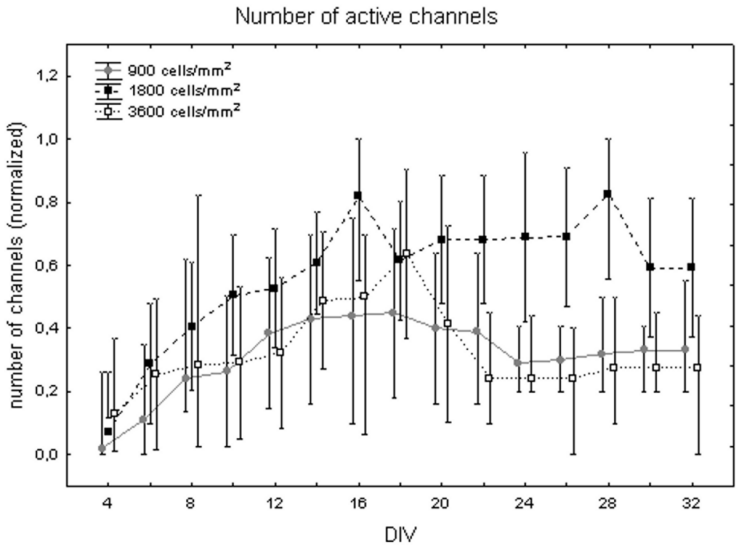

Figure 1.3 Variation in the number of active channels during cell culture maturation at different cell densities. Cell culture density equal to 900 cells/mm^2 (gray dots), 1800 cells/mm^2 (black squares) and 3600 cells/mm^2 (white squares). Values are normalized to the total number of channels (From Biffi E. et al 2013)

Medium-density cultures showed higher numbers of active channels, higher firing rates and higher busting activity than cells plated at other densities (**Figure 1.4**).

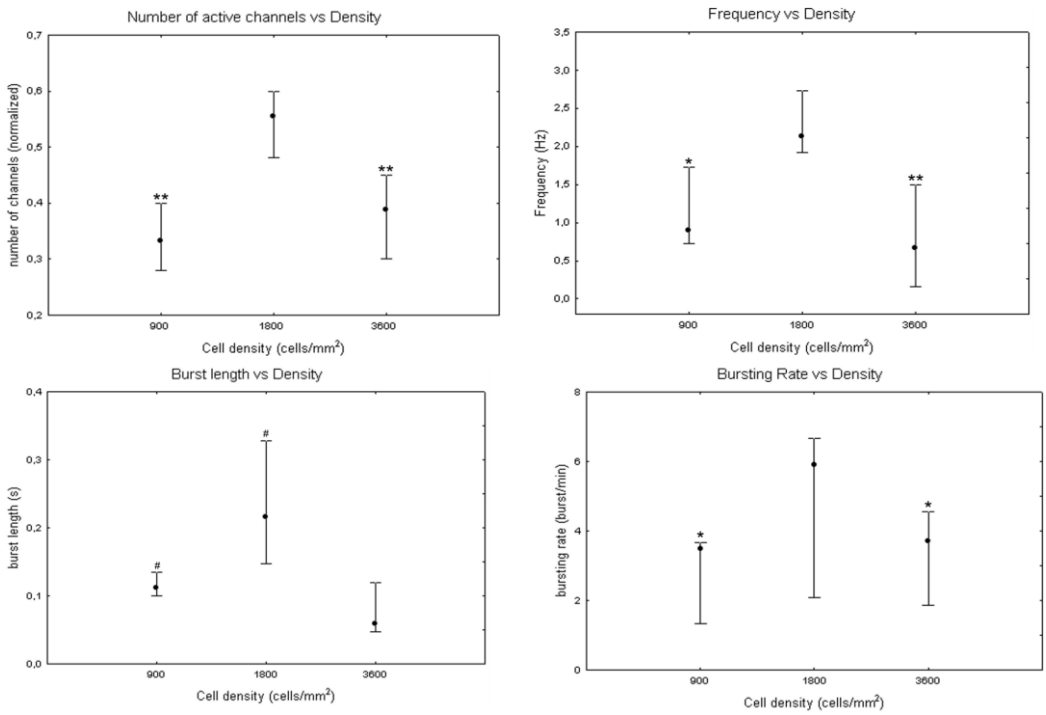

Figure 1.4 Electrophysiological parameters at different cell density. (from Biffi et al 2013)

Therefore, in many cases, the cultures used in MEA recordings were grown under medium-density conditions (over 1000 cells/mm^2) with overgrowth of glial cells to help maintain the health of long-term cultures. Moreover, growth of cells at that concentration can guarantee that the electrodes are covered by the neurons, avoiding low numbers of active channels. Recently, various strategies for improving MEA performance in terms of signal-to-noise ratio (SNR) have been proposed, including chemical functionalization of the electrodes (Mescola et al., 2016) and their topographical modification by increasing roughness or creating 3D features that improve the cell-to-electrode sealing. Examples of these approaches are the fabrication of electrodes with increased roughness (Dowell-Mesfin et al., 2004), of porous electrodes (Brüggemann et al., 2011), or of electrodes with 3D features (Ostrovsky et al., 2016) to name only a few. Alternatively, the use of new materials, especially carbon-based materials, such as graphene, has gained popularity (Yli‐Rantala et al., 2011;Ostrovsky et al., 2016).

Graphene, a single layer of carbon atoms arranged in a hexagonal lattice, has attracted attention from scientists in various fields since its discovery in 2004 (Novoselov et al., 2004). It is a very promising material that is recognized for its high conductance, high mechanical strength, optical transparency and biocompatibility (Geim and Novoselov, 2010). Recently, “graphene MEAs” consisting of graphene electrodes have been fabricated and successfully used to record the activity of primary rat cortical neurons (Du et al., 2015). Moreover, in other studies (Li et al., 2011;Convertino et al., 2018), it has been demonstrated that the viability of neuronal cells and average neurite length were

significantly enhanced when the cells were cultured on a graphene substrate instead of on the conventional tissue culture substrate, indicating that graphene may be a material that is favorable to neuronal growth. However, no study has presented a detailed, long-term analysis of neuronal network development on MEA functionalized with graphene. In a recent investigation in which I was directly involved (El Merhie et al., 2018), we functionalized the surface of commercial 60-electrode MEAs by transferring large-grain single-layer graphene (LG-SLG) via wet etching. The activity of neuronal networks cultured on this surface was recorded during the maturation of the network and compared to the activity of cultures maintained on standard non-functionalized devices as shown in **Figure 1.5**.

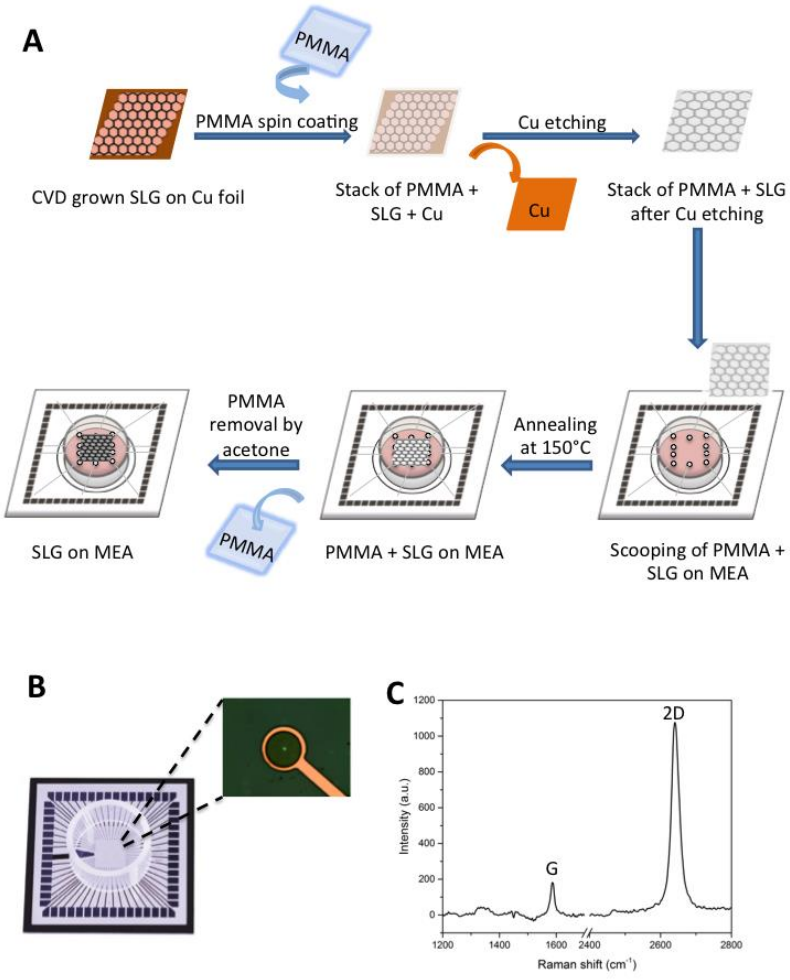

Figure 1.5 A) Schematic diagram illustrating the wet etching transfer of SLG onto a commercial MEA device. CVD-grown large crystal SLG on copper (Cu) foil, of 25 µm thickness, was transferred by wet etching technique on Cu as follows. A layer of poly (methyl methacrylate) (PMMA) (MicroChem, 950,000 MW, 9-6 wt. % in anisole) was spin-coated (Sawatec SM-180-BT spinner) on one side of the SLG/Cu foils at 3000 rpm for 45 s and heated for 5 min at 180oC; then, the SLG grown on the opposite side of the Cu foil was removed by 100 W oxygen plasma, followed by drying at room temperature for 12 h. The Cu was etched using 0.2 M Ammonium persulphate (APS) solution in a Petri dish and the PMMA/SLG stack was floated on the surface of the solution. The stack of PMMA/SLG was carefully rinsed in Milli-Q (Millipore, 18 MΩ) to remove the traces of the Cu etchant, and then it was transferred on the 60 channel Micro Electrode Array. The transferred SLG-MEA was annealed at 160°C for 3 hours in a vacuum oven for firm adhesion and washed with acetone for the removal of PMMA. For immunolabelling experiments, LG-SLG was transferred onto normal glass coverslips, following the same wet-etching protocol. B) Optical image of the functionalized MEA; the coated electrode source of the

spectrum is shown in the zoomed image on the left, where the laser spot for Raman analysis is visible in the middle of the electrode. C) Raman characterization of the transferred SLG showing the characteristic G and 2D bands. (from El Merhie et al., 2018)

Our work included investigation of the morphological properties of neuronal networks formed on conventional and functionalized MEAs and of the development and functionality of these networks. Immunolabeling revealed no significant changes in the morphology of neuronal networks cultured on LG-SLG coverslips compared to those cultured on control (glass) coverslips (**Figure 1.6**). Both cultures demonstrated morphology of healthy cells, indicating that the presence of LG-SLG does not trigger any adverse reaction in the neuronal networks. Quantification of the cell density showed that the density increased as development progressed, and there was no significant difference between the LG-SLG and control cultures, indicating an identical survival rate compared to standard conditions (**Figure 1.6 B**). Regarding neuronal density, immunostaining for the neuron-specific marker MAP2 showed that the number of neurons in LG-SLG cultures was generally higher than in control cultures (statistical significance was only found at DIV 13), indicating a higher survival rate or a higher propensity of cells to adhere to graphene, as we had previously reported (Keshavan et al., 2018) (**Figure 1.6 C**). With respect to neuronal growth, we showed that neurons cultured on LG-SLG-MEAs display twice the likelihood of long-term survival compared to neurons in control cultures. This result is very promising for the future development of graphene-based electronics since it demonstrates the robustness and biocompatibility of such interfaces.

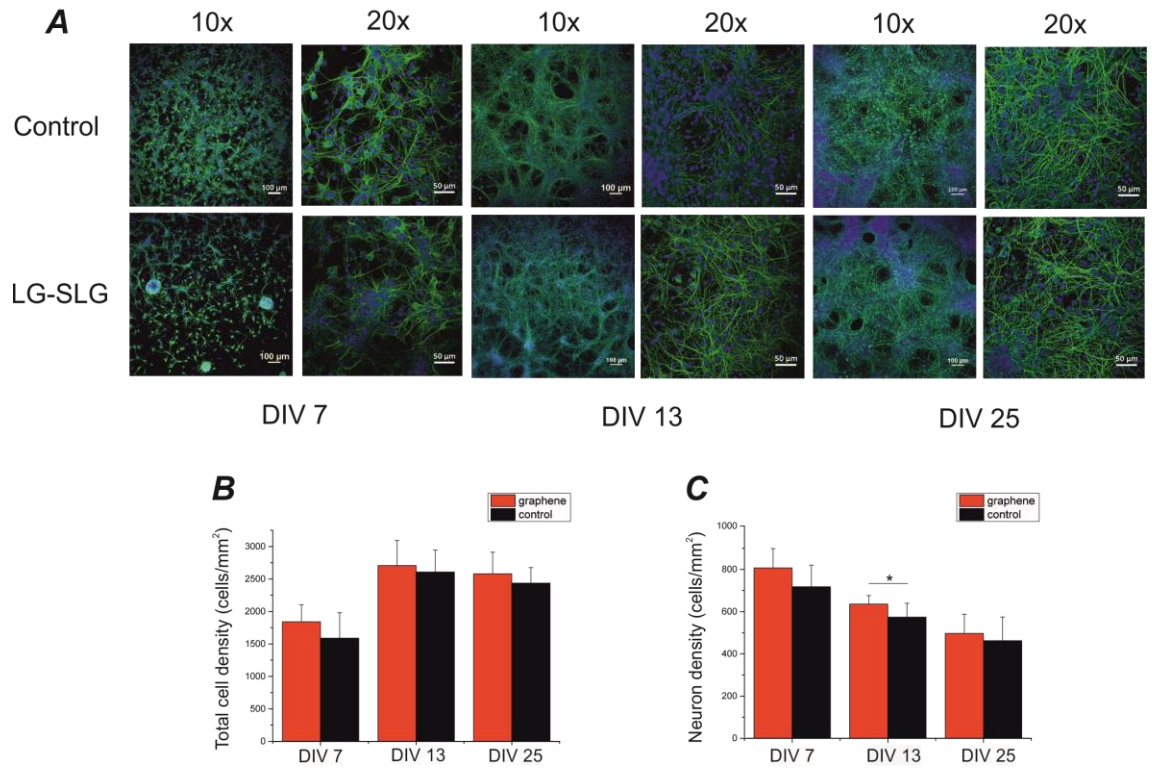

*Figure1.6 Morphological changes in hippocampal networks cultured on a graphene-transferred substrate during development. A) Micrographs showing MAP2 immunofluorescence in representative cultures grown on normal coverslips (top) and on LG-SLG-coated coverslips (bottom) at three different developmental stages (7 DIV, 13 DIV and 25 DIV, respectively, from left to right) at 2 different magnification factors (10x and 20x; scale bars 100 μm and 50 μm, respectively). B) Bar graph of the total cell density in the two groups. No significant difference was found. C) Bar graph of the neuronal density at different DIVs of hippocampal cultures grown on LG-SLG MEAs (red) and on the control (black). A significant difference was found only at 13 DIV. Since the hypothesis of normality was rejected in one of the experimental groups, we used the nonparametric Mann-Whitney test for statistical comparison. *p<0.05. (from El Merhie et al., 2018)*

The electrophysiological activity of the LG-SLG-MEA cultures showed a developmental profile consistent with that of neuronal networks cultured over conventional MEAs but, in general, with higher absolute values of the computed electrophysiological parameters. Specifically, the graphene-treated networks exhibited higher firing and bursting rates at the earliest stage of their development (i.e., at 7 DIV) (**Figure 1.7 A**).

Bursting activity was clearly visible beginning at 13 DIV, and from 19 DIV the LG-SLG-MEA displayed short bursts with a very high bursting rate (**Figure 1.7 B-C**). The IBR reached a minimum of 18% and remained stable during the developmental window under investigation (**Figure 1.7 D**).

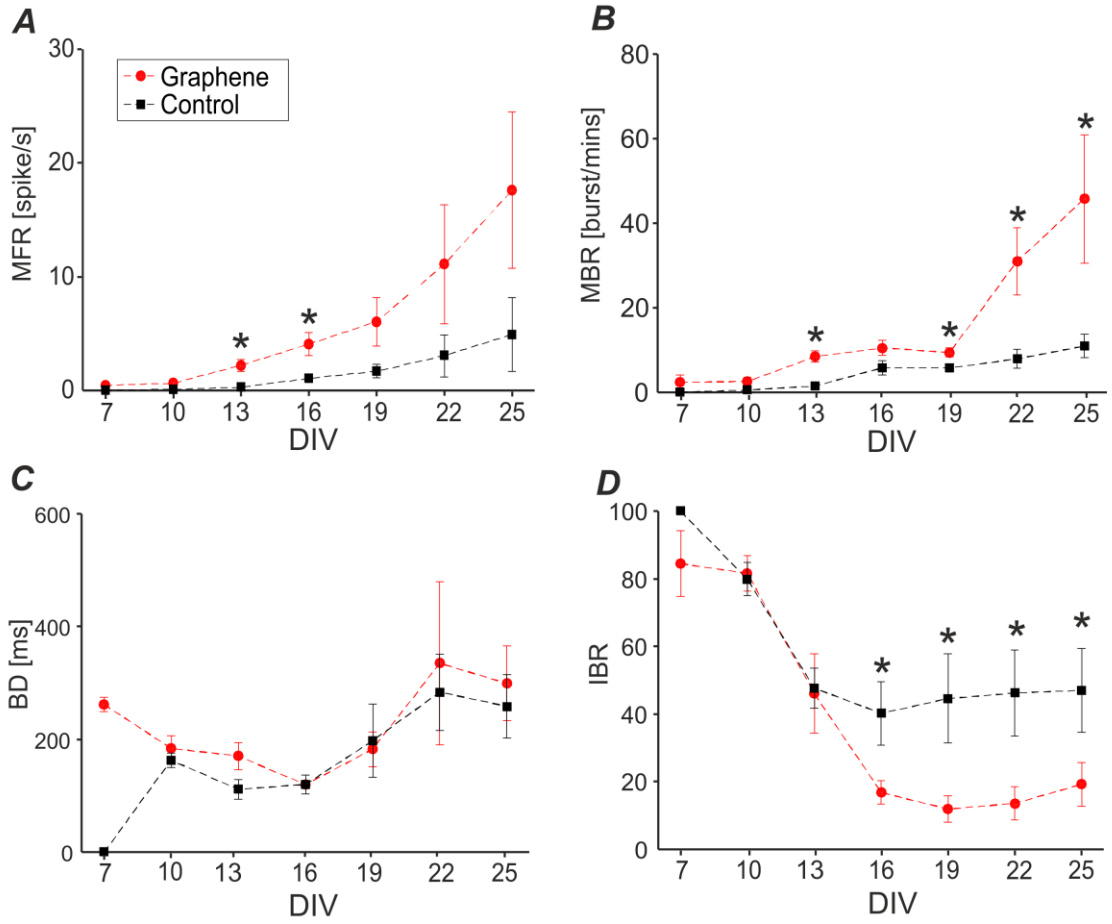

*Figure 1.7 Developmental profiles of hippocampal networks cultured on graphene-transferred MEA (red) and conventional MEA (black). A) Mean firing rate (spikes/s) of 5 cultures on graphene-transferred MEA and 5 cultures on conventional MEA. This parameter differed significantly in the two groups at 13 and 16 DIV. B) Mean bursting rate (bursts/min) differed significantly in the two groups at 13, 19, 22 and 25 DIV. C) No statistically significant difference in burst duration (in ms) was found between the two groups. D) Percentage of spikes outside burst (IBR): this parameter was significantly different between the two groups from 16 to 25 DIV. All data are presented as the mean +/- SEM. Statistical analysis was performed using the two-sample t-test (*p<0.05). (from El Merhie et al., 2018)*

The analysis of the cross-correlation showed higher C_{peak} values compared to the control MEA beginning at 13 DIV (**Figure 1.8 A**), indicating stronger correlation of the activity. Longer latencies were observed in the control MEA, suggesting a greater delay in activity propagation compared to the LG-SLG MEA cultures (**Figure 1.8 B**). At the later developmental stages (i.e., from 21 DIV), the strength of the activity correlation remained higher for the LG-SLG-MEA, possibly due to the higher number of bursting events in the graphene MEAs. In contrast, the latency was similar in the control and LG-SLG MEA cultures at late developmental stages, indicating that the level of synchronization also increased with time in the control MEA, as shown by previous results (Chiappalone et al., 2006).

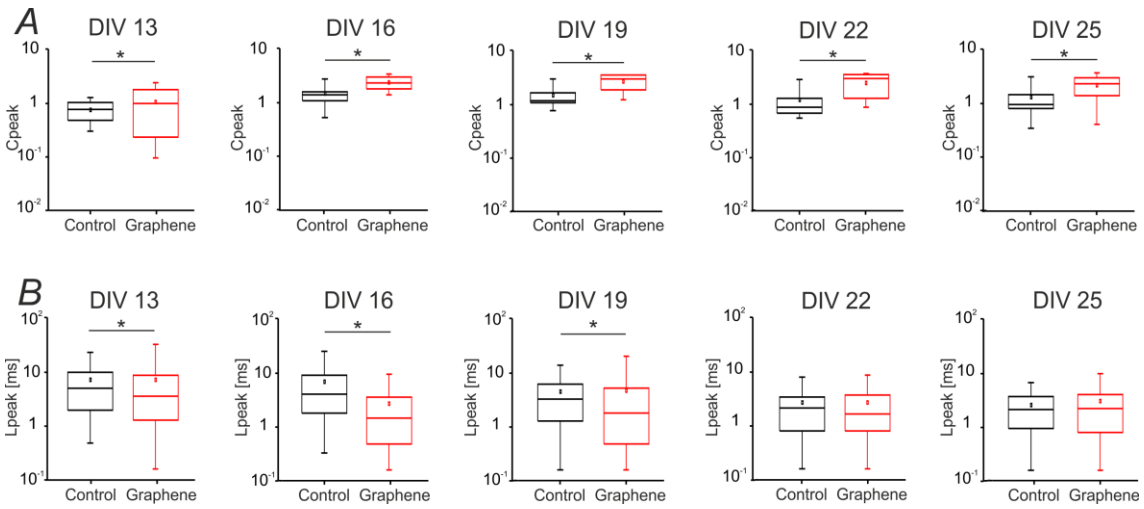

Figure 1.8 Cross-correlation analysis. A) Box plots of the 100 highest C_{peak} values for the control group (black box) and the graphene group (red box) at developmental time points 13, 16, 19, 22, and 25 DIV. We excluded the early developmental stages 7 and 10 DIV since the level of activity at those time points was low. B) Box plots of the corresponding peak latency values (L_{peak}) of the preselected 100 strongest C_{peak} values. We considered only peak latency values smaller than 50 ms. For each box plot in A and B,, the small square indicates the mean, the central line illustrates the median, and the box limits indicate the 25th and 75th percentiles. (From El Merhie et al., 2018).

Hence, earlier and more highly synchronized neuronal network development was observed on LG-SLG-MEA compared to control cultures. The earlier detection of network activity is consistent with our previous observation of earlier synaptogenesis on SLG compared to the control (Keshavan et al., 2018) ; little or no synaptogenesis was detected in the control until 9 DIV, whereas on SLG a slight increase in the postsynaptic current frequency was observed beginning on DIV 7. In the current investigation, we also showed that the number of neurons was generally higher in LG-SLG than in control cultures; this affected the cell density and thus the functional properties of developing networks (Ichikawa et al., 1993;Chiappalone et al., 2008). Together with the earlier synaptogenesis that was previously demonstrated (Keshavan et al., 2018) , this observation suggests better coupling of the neurons to the LG-SLG substrate, with the final effect of accelerating the developmental processes respect to the control MEA. The detection of increased levels of electrophysiological activity and improved cell/electrode coupling is consistent with earlier reports in the literature of a strengthening of cell-to-cell coupling on graphene-based interfaces (Heo et al., 2011;Akhavan and Ghaderi, 2013). In conclusion, the higher survival rate, the increased number of adherent cells and the increased firing activity of the cells indicate not only that LG-SLG devices are compatible with the physiological functionality of neuronal networks but that they also have improved detection capabilities, possibly due to better neuron/substrate coupling.

1.2 Acute brain slices

An alternative approach to the use of dissociated cells is represented by brain slices in which the 3D structure of the intact brain is partially maintained *in vitro*. The term "brain slice" has come to refer to thin (100-700 μm) sections of brain regions that are prepared from adult mammals, maintained for many hours *in vitro* (acute slices) or in culture for days/weeks (organotypic slice cultures) and used in electrophysiological or biochemical studies. The main advantage of these techniques is the possibility of preserving the network architecture and some of the anatomical and physiological properties of the brain in a very controlled environment. The intact brain can be dissected in various ways depending on the position of the regions of interest (i.e., hippocampal slices can be prepared alone or together with entorhinal cortex, cerebellum, cortex, striatum, etc.). At the beginning of the 1990s, many scientists used retina slices from small animals as a model for their experiments. Most initial brain slice studies were metabolic studies; a few notable exceptions used brain explants from frogs, which were shown to have spontaneous activity (Libet and Gerard, 1939) , and one study investigated the properties of brain slices obtained from the cerebral cortex of cats (Burns, 1950). Brain slices were not used in electrophysiological studies until Li and McIlwain recorded resting membrane potentials in isolated neocortical tissue very similar in magnitude to those observed in the brain in situ. Their later studies, including the first report of pair-pulsed facilitation, focused on synaptic transmission (Yamamoto and McIlwain, 1966). In the ensuing years, many novel methods were developed, making it possible to concomitantly measure the output of neurotransmitters and the metabolic or electrical status of the tissue when slices were exposed to a variety of substrates and inhibitors (McIlwain and Snyder, 1970;Heller and McIlwain, 1973).

In the early 1980s, the use of brain slices became mainstream; at this point, many scientists began to express concerns regarding the physiological state of acute slices (Dingledine, 1984;Steriade, 2001). Much effort has been made to improve the conditions used in acute-slice recordings. These improvements include modification of the slicing technique, the addition of micronutrients or antibiotics to sustain tissue quality for longer recordings and the modification of perfusion chambers to improve tissue quality (Garthwaite et al., 1979;Haas et al., 1979;Lynch and Schubert, 1980;Nicoll and Alger, 1981;Koerner and Cotman, 1983). Depending on the experimental needs, several variants of these techniques have been developed and are being used. One distinction between the variants concerns the thickness of the slices. The "thin slice" technique was developed to allow visualization of individual cells in slices less than 250 μm thick, while the thick slice technique is used when connectivity and maintenance of normal dendritic structure are crucial for the study. For electrophysiological studies, slices 300 to 400 μm thick are usually used to balance the need for a

robust network and complete oxygenation of the tissue.

One alternative to the acute slice preparation is the culturing of organotypic brain slices. This method is based on earlier work on explant cultures derived from various anatomical regions (Crain, 1976). The method became increasing popular following the development of the roller-tube technique by Gahwiler in 1981 (Gähwiler, 1981), and later with the development of interface cultures by Stoppini in 1991(Stoppini et al., 1991;Noraberg et al., 1999;De Simoni and Lily, 2006).

Although acute brain slices can be maintained for only a short time, slices can be routinely prepared from mature adult tissue; in contrast, organotypic brain slices can be maintained for longer periods of time in culture, but they are typically prepared from postnatal (P0-P7) rats and mice (Figure 1.9).

Today, brain slices are used in many types of studies, including studies of synaptic plasticity and development, network oscillations, intrinsic and synaptic properties of defined neuronal populations, and many others (Kettenmann and Grantyn, 1992). Due to its very well-defined layered organization, the hippocampus is one of the best-studied regions of the mouse brain.

Hippocampal/cortical slices have also been coupled to planar MEAs (Egert et al., 1998;Jahnsen et al., 1999;Egert et al., 2002;Beggs and Plenz, 2003;Wirth and Lüscher, 2004;Baudry et al., 2006;Colgin, 2006;Soussou et al., 2006;Ferrea et al., 2012), thus allowing long-term extracellular measurements of defined neuronal circuits. In the following, we briefly describe the morphological architecture of hippocampal slices.

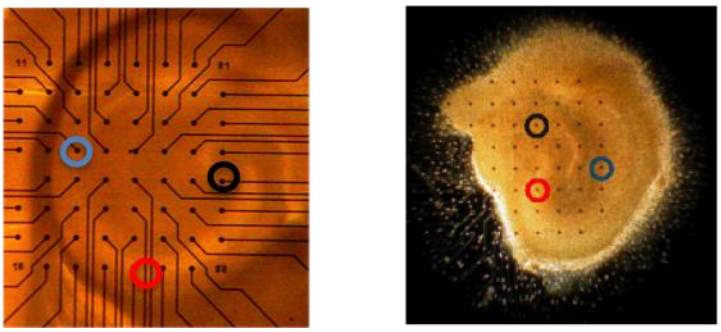

Figure 1.9 Comparison of an acute hippocampal slice and an organotypic slice. A) Hippocampal-entorhinal slices over MEA. B) Image of a hippocampal slice cultured on an MEA for 10) days in vitro (DIV (from Chong et al*., 2018). The black, red, and blue electrodes record the signals in the DG, CA3, and CA1 regions, respectively.*

Hippocampus layers and principal neurons

The hippocampus is one of the best-studied regions of the mammalian central nervous system. One reason for this is that it possesses structures that are distinctive and identifiable at the histological level. The hippocampus is perfectly laminated, i.e., both neuronal cell bodies and the zone of

connectivity are arranged in orderly layers. A second reason is that since the 1950s it has been known that the hippocampus plays a fundamental role in some forms of learning and memory. The hippocampus has been implicated in many neurological and psychiatric diseases such as epilepsy, Alzheimer's disease and schizophrenia. Because of the important role of the hippocampus in learning, memory and synaptic plasticity, it is not surprising that Down syndrome patients also present hippocampal deficits. As part of this thesis work, we performed experiments using hippocampal slices obtained from Down syndrome mice (see Chapter 8).

The hippocampus is composed of the cornus ammonis (CA) region and the dentate gyrus (DG). The first presents three different subregions, CA1, CA2, and CA3 (Lorente de No, 1934), while the second consists of the fascia dentata and the hilus (**Figure 1.10 A**).

In the following, we briefly describe the different layers and neurons that make up the hippocampal circuitry. The surface of all hippocampal fields is formed by the alveus, a thin sheet of outgoing and incoming fibers. There are four principal cell layers in the cornus ammonius (CA), as depicted in **Figure 1.10 B**:

1. *Stratum oriens*: consists of the layers occupied by basal dendrites of the pyramidal cells and receives input from other pyramidal neurons, especially those in CA2-CA1.
2. *Pyramidal cell layer*: one of the most visible strata, it is also visible to the naked eye. It contains the cell bodies of the pyramidal cells, which are the principal excitatory neurons in the hippocampus. These neurons have elaborate dendrites that extend perpendicular to the cell layer in both directions and are therefore called multipolar neurons. The CA3 region also contains synapses from the mossy fibers and the cell bodies of many interneurons.
3. *Stratum radiatum*: contains the apical dendrites of the pyramidal cells and the Shaffer collateral fibers.
4. *Stratum lacunosum moleculare*: the most superficial layer; it contains performant path fibers and the apical dendrites of the pyramidal cells.

The dentate gyrus contains three layers, namely, the granular cell layer, the molecular layer and the diffusely cellular polymorphic layer. The granule cell dendrites extend perpendicular to the granule cell layer into the overlying molecular layer, where they receive synaptic connections from several sources. Since their dendrites emerge only from the top or apical portion of the cell body, granule cells are considered monopolar neurons.

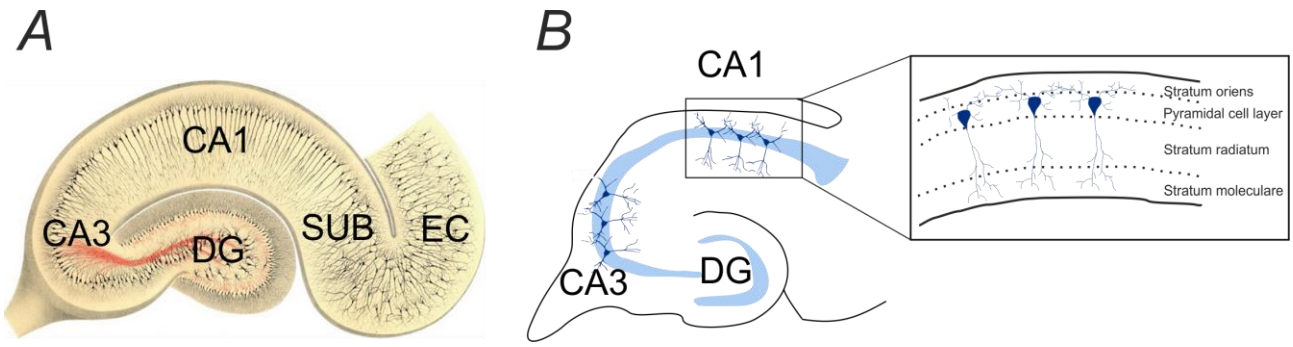

Figure 1.10 Drawings of the hippocampus by Camillo Golgi showing the cytoarchitectonic divisions (from Opera Omnia, 1903). The hippocampus is divided into the cornus ammonis (CA3, CA2 and CA1 regions) and the dentate gyrus. B) Schematic drawing of a hippocampal slice with an enlargement of the molecular layer: stratum oriens (o), pyramidal cell layer (p), stratum radiatum (r) and stratum lacunosum moleculare (l-m).

Hippocampus–EC slices circuitry

Three common slicing angles are employed in experiments investigating hippocampal circuitry, namely, transverse slices, coronal slices and hippocampal-entorhinal cortex slices (HEC). These three types of slice preparation have been widely used to investigate hippocampal circuitry because they preserve the major afferent hippocampal pathways, including the perforant path (PP), the mossy fibers (MFs) and the Schaffer collaterals (SCs). The choice of slicing plane determines which afferent and/or efferent connections are best preserved. HEC slices offer the most suitable slice preparation for studies of hippocampal-EC interaction because they preserve all three of the major pathways within the hippocampus (PP, MFs and SCs) (Xiong et al., 2017).

The brain structures included in hippocampal/EC slices are part of a group of structures called the *hippocampal formation*. In particular, it includes the dentate gyrus (DG), the hippocampus, the subiculum (SUB), and the entorhinal cortex (EC), as shown in **Figure 1.11**.

The intrinsic flow of information in the *hippocampal formation* follows unidirectional and glutamatergic (excitatory) pathways that create a closed circuit called the *trisynaptic circuitry* (Anderson et al. 1971). The *hippocampal formation* receives highly processed multimodal information mainly from the EC. Neurons located in layer II of the EC project to the DG and the hippocampus though the *perforant path*. The *perforant path* travels caudally from the EC via the angular bundle to SUB and terminates both in the DG and in the stratum lacunosum moleculare of the CA3 field of the hippocampus. The CA3 pyramidal cells, in turn, project to other levels of CA3 as well as to CA1 through *Shaffer collateral projections*.

The recurrent connections of the CA3 region are formed by so-called autoassociative fibers and may facilitate the completion of incomplete input patterns (called pattern completion) (Guzowski et al., 2004). On the other hand, CA1 pyramidal cells give rise to connections both to the SUB and to the deeper levels of the EC (layer IV-VI). Moreover, neurons located in layer III of the EC project directly

to CA1 and SUB and finally back to the neurons located in layers IV-VI of EC. Thus, the information flow in the EC travels along the hippocampus and ultimately returns to the area from which it originates. The transformation that takes place in the hippocampal circuitry is essential for storing and preserving the information in long-term memory. In the following, we briefly describe the different layers and neurons.

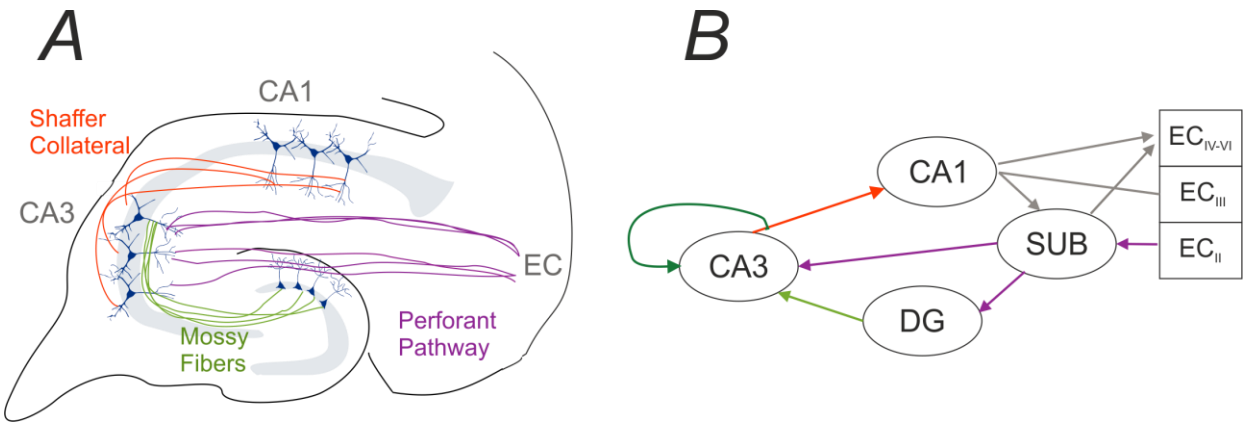

Figure 1.11 Hippocampal-EC circuitry. A) Drawing of neuronal pathways that connect the EC-CA3-CA1 regions. B) Scheme of the unidirectional and glutamatergic (excitatory) pathways showing the perforant path, mossy fibers and Shaffer collateral projections.

Related publications and/or conference abstracts

El Merhie*, A., Ito, D.*, **Colombi, I**., Keshavan, S., Mishra, N., Miseikis, V., Diaspro, A., Coletti, C., Chiappalone, M., and Dante, S. (2018). Single layer graphene functionalized MEA for enhanced detection of neuronal network development. Sensors and Actuators B: Chemical 277, 224-233.

* First equal

References

Akhavan, O., and Ghaderi, E. (2013). Differentiation of human neural stem cells into neural networks on graphene nanogrids. *Journal of Materials Chemistry B* 1**,** 6291-6301.

Akum, B.F., Chen, M., Gunderson, S.I., Riefler, G.M., Scerri-Hansen, M.M., and Firestein, B.L. (2004). Cypin regulates dendrite patterning in hippocampal neurons by promoting microtubule assembly. *Nature neuroscience* 7**,** 145.

Augusti-Tocco, G., and Sato, G. (1969). Establishment of functional clonal lines of neurons from mouse neuroblastoma. *Proceedings of the National Academy of Sciences* 64**,** 311-315.

Banker, G., Goslin, K., and Stevens, C.F. (1998). *Culturing nerve cells.* MIT press.

Banker, G., and Waxman, A. (1988). Hippocampal neurons generate natural shapes in cell culture. *Intrinsic determinants of neuronal form and function***,** 61-82.

Baudry, M., Taketani, M., and Krause, M. (2006). "Applications of Multi-Electrode Array System in Drug Discovery Using Acute and Cultured Hippocampal Slices," in *Advances in Network Electrophysiology*. Springer), 355-376.

Beggs, J.M., and Plenz, D. (2003). Neuronal avalanches in neocortical circuits. *Journal of neuroscience* 23**,** 11167-11177.

Ben-Ari, Y. (2001). Developing networks play a similar melody. *Trends in neurosciences* 24**,** 353-360.

Bi, G.-Q., and Poo, M.-M. (1998). Synaptic modifications in cultured hippocampal neurons: dependence on spike timing, synaptic strength, and postsynaptic cell type. *Journal of neuroscience* 18**,** 10464-10472.

Bi, G.-Q., and Poo, M.-M. (1999). Distributed synaptic modification in neural networks induced by patterned stimulation. *Nature* 401**,** 792.

Biffi, E., Regalia, G., Menegon, A., Ferrigno, G., and Pedrocchi, A. (2013). The influence of neuronal density and maturation on network activity of hippocampal cell cultures: a methodological study. *PloS one* 8**,** e83899.

Brüggemann, D., Wolfrum, B., Maybeck, V., Mourzina, Y., Jansen, M., and Offenhäusser, A. (2011). Nanostructured gold microelectrodes for extracellular recording from electrogenic cells. *Nanotechnology* 22**,** 265104.

Burns, B.D. (1950). Some properties of the cat's isolated cerebral cortex. *The Journal of physiology* 111**,** 50-68.

Carrel, A., and T Burrows, M. (1910). Cultivation of adult tissues and organs outside of the body. *Journal of the American medical association* 55**,** 1379-1381.

Chiappalone, M., Bove, M., Vato, A., Tedesco, M., and Martinoia, S. (2006). Dissociated cortical networks show spontaneously correlated activity patterns during in vitro development. *Brain Res* 1093**,** 41-53.

Chiappalone, M., Massobrio, P., and Martinoia, S. (2008). Network plasticity in cortical assemblies. *European Journal of Neuroscience* 28**,** 221-237.

Cohen, E., Ivenshitz, M., Amor-Baroukh, V., Greenberger, V., and Segal, M. (2008). Determinants of spontaneous activity in networks of cultured hippocampus. *Brain research* 1235**,** 21-30.

Colgin, L.L. (2006). "Investigation of network phenomena in hippocampal slices using multi-electrode recording arrays," in *Advances in Network Electrophysiology*. Springer), 425-453.

Convertino, D., Luin, S., Marchetti, L., and Coletti, C. (2018). Peripheral neuron survival and outgrowth on graphene. *Frontiers in neuroscience* 12**,** 1.

Crain, S.M. (1976). *Neurophysiologic studies in tissue culture.* Raven Press.

De Simoni, A., and Lily, M. (2006). Preparation of organotypic hippocampal slice cultures: interface method. *Nature protocols* 1**,** 1439.

Dingledine, R. (1984). "Hippocampus," in *Brain slices*. Springer), 87-112.

Dotti, C.G., Sullivan, C.A., and Banker, G.A. (1988). The establishment of polarity by hippocampal neurons in culture. *Journal of Neuroscience* 8**,** 1454-1468.

Dowell-Mesfin, N., Abdul-Karim, M., Turner, A., Schanz, S., Craighead, H., Roysam, B., Turner, J., and Shain, W. (2004). Topographically modified surfaces affect orientation and growth of hippocampal neurons. *Journal of neural engineering* 1**,** 78.

Du, X., Wu, L., Cheng, J., Huang, S., Cai, Q., Jin, Q., and Zhao, J. (2015). Graphene microelectrode arrays for neural activity detection. *Journal of biological physics* 41**,** 339-347.

Egert, U., Heck, D., and Aertsen, A. (2002). Two-dimensional monitoring of spiking networks in acute brain slices. *Experimental Brain Research* 142**,** 268-274.

Egert, U., Schlosshauer, B., Fennrich, S., Nisch, W., Fejtl, M., Knott, T., Muller, T., and Hammerle, H. (1998). A novel organotypic long-term culture of the rat hippocampus on substrate-integrated multielectrode arrays. *Brain Res Brain Res Protoc* 2**,** 229-242.

El Merhie, A., Ito, D., Colombi, I., Keshavan, S., Mishra, N., Miseikis, V., Diaspro, A., Coletti, C., Chiappalone, M., and Dante, S. (2018). Single layer graphene functionalized MEA for enhanced detection of neuronal network development. *Sensors and Actuators B: Chemical* 277**,** 224-233.

Ferrea, E., Maccione, A., Medrihan, L., Nieus, T., Ghezzi, D., Baldelli, P., Benfenati, F., and Berdondini, L. (2012). Large-scale, high-resolution electrophysiological imaging of field potentials in brain slices with microelectronic multielectrode arrays. *Frontiers in neural circuits* 6**,** 80.

Frega, M., Van Gestel, S.H., Linda, K., Van Der Raadt, J., Keller, J., Van Rhijn, J.-R., Schubert, D., Albers, C.A., and Kasri, N.N. (2017). Rapid neuronal differentiation of induced pluripotent stem cells for measuring network activity on micro-electrode arrays. *Journal of visualized experiments: JoVE*.

Gähwiler, B. (1981). Organotypic monolayer cultures of nervous tissue. *Journal of neuroscience methods* 4**,** 329-342.

Garthwaite, J., Woodhams, P., Collins, M., and Balazs, R. (1979). On the preparation of brain slices: morphology and cyclic nucleotides. *Brain Res* 173**,** 373-377.

Geim, A.K., and Novoselov, K.S. (2010). "The rise of graphene," in *Nanoscience and Technology: A Collection of Reviews from Nature Journals*. World Scientific), 11-19.

Granville Harrison, R. (1910). The development of peripheral nerve fibers in altered surroundings. *Development Genes and Evolution* 30**,** 15-33.

Guzowski, J.F., Knierim, J.J., and Moser, E.I. (2004). Ensemble dynamics of hippocampal regions CA3 and CA1. *Neuron* 44**,** 581-584.

Haas, H., Schaerer, B., and Vosmansky, M. (1979). A simple perfusion chamber for the study of nervous tissue slices in vitro. *Journal of neuroscience methods* 1**,** 323-325.

Harrison, R.G. (1912). The cultivation of tissues in extraneous media as a method of morpho‐genetic study. *The Anatomical Record* 6**,** 181-193.

Harrison, R.G. (1924). Neuroblast versus sheath cell in the development of peripheral nerves. *Journal of Comparative Neurology* 37**,** 123-205.

Harrison, R.G., Greenman, M., Mall, F.P., and Jackson, C. (1907). Observations of the living developing nerve fiber. *The Anatomical Record* 1**,** 116-128.

Heller, I., and Mcilwain, H. (1973). Release of [14C] adenine derivatives from isolated subsystems of the guinea pig brain: Actions of electrical stimulation and of papaverine. *Brain research* 53**,** 105-116.

Heo, C., Yoo, J., Lee, S., Jo, A., Jung, S., Yoo, H., Lee, Y.H., and Suh, M. (2011). The control of neural cell-to-cell interactions through non-contact electrical field stimulation using graphene electrodes. *Biomaterials* 32**,** 19-27.

Ichikawa, M., Muramoto, K., Kobayashi, K., Kawahara, M., and Kuroda, Y. (1993). Formation and maturation of synapses in primary cultures of rat cerebral cortical cells: an electron microscopic study. *Neuroscience research* 16**,** 95-103.

Ivenshitz, M., and Segal, M. (2010). Neuronal density determines network connectivity and spontaneous activity in cultured hippocampus. *Journal of neurophysiology* 104**,** 1052-1060.

Jahnsen, H., Kristensen, B.W., Thiébaud, P., Noraberg, J., Jakobsen, B., Bove, M., Martinoia, S., Koudelka-Hep, M., Grattarola, M., and Zimmer, J. (1999). Coupling of organotypic brain slice cultures to silicon-based arrays of electrodes. *Methods* 18**,** 160-172.

Kandel, E.R., Schwartz, J.H., Jessell, T.M., Biochemistry, D.O., Jessell, M.B.T., Siegelbaum, S., and Hudspeth, A. (2000). *Principles of neural science.* McGraw-hill New York.

Keshavan, S., Naskar, S., Diaspro, A., Cancedda, L., and Dante, S. (2018). Developmental refinement of synaptic transmission on micropatterned single layer graphene. *Acta biomaterialia* 65**,** 363-375.

Kettenmann, H., and Grantyn, R. (1992). *Practical electrophysiological methods.* Wiley-Liss.

Koerner, J.F., and Cotman, C.W. (1983). A microperfusion chamber for brain slice pharmacology. *Journal of neuroscience methods* 7**,** 243-251.

Kriegstein, A.R., and Dichter, M.A. (1983). Morphological classification of rat cortical neurons in cell culture. *Journal of Neuroscience* 3**,** 1634-1647.

Li, N., Zhang, X., Song, Q., Su, R., Zhang, Q., Kong, T., Liu, L., Jin, G., Tang, M., and Cheng, G. (2011). The promotion of neurite sprouting and outgrowth of mouse hippocampal cells in culture by graphene substrates. *Biomaterials* 32**,** 9374-9382.

Libet, B., and Gerard, R. (1939). Control of the potential rhythm of the isolated frog brain. *Journal of Neurophysiology* 2**,** 153-169.

Lynch, G., and Schubert, P. (1980). The use of in vitro brain slices for multidisciplinary studies of synaptic function. *Annual review of neuroscience* 3**,** 1-22.

Mcilwain, H., and Snyder, S. (1970). Stimulation of piriform‐and neo‐cortical tissues in an in vitro flow‐system: Metabolic properties and release of putative neurotransmitters. *Journal of neurochemistry* 17**,** 521-530.

Mescola, A., Canale, C., Prato, M., Diaspro, A., Berdondini, L., Maccione, A., and Dante, S. (2016). Specific neuron placement on gold and silicon nitride-patterned substrates through a two-step functionalization method. *Langmuir* 32**,** 6319-6327.

Morin, F.O., Takamura, Y., and Tamiya, E. (2005). Investigating neuronal activity with planar microelectrode arrays: achievements and new perspectives. *Journal of bioscience and bioengineering* 100**,** 131-143.

Nakai, J. (1956). Dissociated dorsal root ganglia in tissue culture. *American Journal of Anatomy* 99**,** 81-129.

Nakai, J. (1960). Studies on the mechanism determining the course of nerve fibers in tissue culture. *Zeitschrift für Zellforschung und mikroskopische Anatomie* 52**,** 427-449.

Nicoll, R., and Alger, B. (1981). A simple chamber for recording from submerged brain slices. *Journal of neuroscience methods* 4**,** 153-156.

Noraberg, J., Kristensen, B.W., and Zimmer, J. (1999). Markers for neuronal degeneration in organotypic slice cultures. *Brain research protocols* 3**,** 278-290.

Novoselov, K.S., Geim, A.K., Morozov, S.V., Jiang, D., Zhang, Y., Dubonos, S.V., Grigorieva, I.V., and Firsov, A.A. (2004). Electric field effect in atomically thin carbon films. *science* 306**,** 666-669.

Ostrovsky, S., Hahnewald, S., Kiran, R., Mistrik, P., Hessler, R., Tscherter, A., Senn, P., Kang, J., Kim, J., and Roccio, M. (2016). Conductive hybrid carbon nanotube (CNT)–polythiophene coatings for innovative auditory neuron-multi-electrode array interfacing. *RSC Advances* 6**,** 41714-41723.

Peterson, E.R., and Murray, M.R. (1955). Myelin sheath formation in cultures of avian spinal ganglia. *American Journal of Anatomy* 96**,** 319-355.

Pomerat, C., Hendelman, W., Raiborn Jr, C.W., and Massey, J. (1967). Dynamic activities of nervous tissue in vitro. *The Neuron***,** 119-178.

Previtera, M.L., Langhammer, C.G., and Firestein, B.L. (2010). Effects of substrate stiffness and cell

density on primary hippocampal cultures. *Journal of bioscience and bioengineering* 110**,** 459-470.

Soussou, W., Gholmieh, G., Han, M., Ahuja, A., Song, D., Hsiao, M.-C., Wang, Z., Tanguay, A.R., and Berger, T.W. (2006). "Mapping spatio-temporal electrophysiological activity in hippocampal slices with conformal planar multi-electrode arrays," in *Advances in Network Electrophysiology*. Springer), 127-152.

Steriade, M. (2001). *The intact and sliced brain.* MIT press.

Stoppini, L., Buchs, P.-A., and Muller, D. (1991). A simple method for organotypic cultures of nervous tissue. *Journal of neuroscience methods* 37**,** 173-182.

Taylor, A.M., Blurton-Jones, M., Rhee, S.W., Cribbs, D.H., Cotman, C.W., and Jeon, N.L. (2005). A microfluidic culture platform for CNS axonal injury, regeneration and transport. *Nature methods* 2**,** 599.

Valor, L.M., Charlesworth, P., Humphreys, L., Anderson, C.N., and Grant, S.G. (2007). Network activity-independent coordinated gene expression program for synapse assembly. *Proceedings of the National Academy of Sciences* 104**,** 4658-4663.

Wirth, C., and LüScher, H.-R. (2004). Spatiotemporal evolution of excitation and inhibition in the rat barrel cortex investigated with multielectrode arrays. *Journal of neurophysiology* 91**,** 1635-1647.

Xiong, G., Metheny, H., Johnson, B.N., and Cohen, A.S. (2017). A comparison of different slicing planes in preservation of major hippocampal pathway fibers in the mouse. *Frontiers in neuroanatomy* 11**,** 107.

Yamamoto, C., and Mcilwain, H. (1966). Potentials evoked in vitro in preparations from the mammalian brain. *Nature* 210**,** 1055.

Yli‐Rantala, E., Pasanen, A., Kauranen, P., Ruiz, V., Borghei, M., Kauppinen, E., Oyarce, A., Lindbergh, G., Lagergren, C., and Darab, M. (2011). Graphitised carbon nanofibres as catalyst support for PEMFC. *Fuel Cells* 11**,** 715-725.

Chapter 2

Microelectrode arrays & data analysis tools

Recent technological advances allow researchers to sample neuronal networks both *in vivo* and *in vitro* from several locations in parallel using multielectrode arrays. Actually, many researchers have been seeking a multichannel approach to bridge the gap in understanding single-cell properties and population coding in cellular networks. Due to advances in electronic technology, commercial systems based on the microelectrode array (MEA) methodology are readily available.

In particular, the use of MEAs for electrophysiological experiments typically produces a huge quantity of data due to the high number of recording channels, high sampling frequency, and long-term recordings. This creates a need for smart software that can autonomously manage the high-dimensional recordings and apply the necessary analysis repeatedly to different sets of data.

2.1 State-of-the-art of the microelectrode array electrophysiological technique: an historical perspective

The first electrophysiological recording from cultured cells in which a planar microelectrode array was used was reported in 1972 when Thomas et al. (Thomas Jr et al., 1972) published the first paper describing the development of the technology. In their introduction, they said:

"*Perhaps the most interesting questions to be asked of such cultures are those dealing with the development and plasticity of electrical interactions among the cultured elements (tissues or single cells). Exploration of these questions would be greatly facilitated by a convenient non-destructive method for maintaining electrical contact with an individual culture, at a large number of points, over periods of days or weeks*."

More than 40 years ago, these investigators charted a course for the years to come, identifying which directions to pursue and delineating different possible methods. The array used in this study (**Figure 2.1**) consists of two rows containing 15 electrodes each, spaced 100 μm apart. The array was on glass, with gold electrodes (15-μm dimension) and leads over an adhesion layer, insulated with photoresistant material. To reduce the impedance, they coated the electrodes with platinum black (Gesteland et al., 1959;Robinson, 1968).

These investigators first performed experiments using chick dorsal root ganglion neurons but without any success.

Turning to dissociated chick myocytes, they recorded robust signals of between 20 and 1000 microvolts after the myocytes had formed a confluent contracting layer over the electrodes (**Figure 2.2**). They concluded that single cells or small groups of cells do not produce a localized change in potential near the electrode that is large enough to be detectable.

Five years later, in 1977, Guenter Gross and his collaborators proposed the idea of a multielectrode array, without knowledge of the previous work (Gross, 1977). The array consisted of 36 gold electrodes 10 μm in diameter that were insulated with a thermosetting polymer and spaced 100 or 200 μm apart. The authors recorded single action potentials from an isolated snail ganglion with amplitude up to 3 mV depending upon cell size. Few year later, in 1980, Pine reported the first successful recordings from single dissociated neurons using a multielectrode array consisting of two parallel lines of 16 gold electrodes that had been platinized and insulated with silicon dioxide (**Figure 2.3**) (Pine, 1980). The electrodes were 10 μm square and spaced 250 μm apart. In this work, rat superior cervical ganglion neurons were cultured for one to three weeks on a fibrous collagen substrate 3 to 5 μm thick. The cells were approximately 20 μm in diameter and were usually 25 μm from the electrodes. Pine recorded electrophysiological signals with an average amplitude of 50 μV from 19 cells (9 cultures).

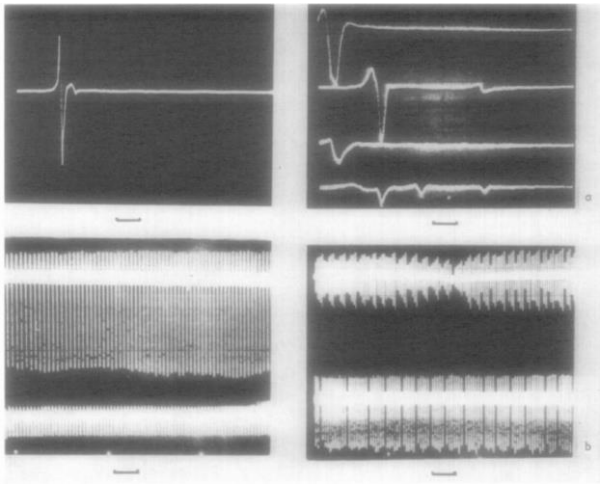

Figure 2.1 Examples of recordings obtained from cultured embryonic chick heart cells (Thomas et al. 1972)

Moreover, Pine used the electrodes to stimulate the cultures with voltage pulses of 0.5 volts with a duration of 1 millisecond. The question then posed by the author was: *how can we know whether the results are compatible with what is to be expected from known neuron's properties*?

The neuronal action potential is typically generated by current flow into the axon hillock, which would represent a point sink (Angelides et al., 1988;Stuart and Sakmann, 1994) (Claverol-Tinture and Pine, 2002). The voltage generated for a point current sink or outside a spherical sink is equal to $I\rho/4\pi r$ (where I is the current, ρ is the resistivity of the medium, and r is the distance from the center

of the current sink). Therefore, a current of 16 nA at the peak of the action potential recorded from neurons at distance of 25 µm would produce a signal of 50 µV, similar to the observed signals. These three works represent a milestone in this field and mark the beginning of *in vitro* network electrophysiology using MEAs.

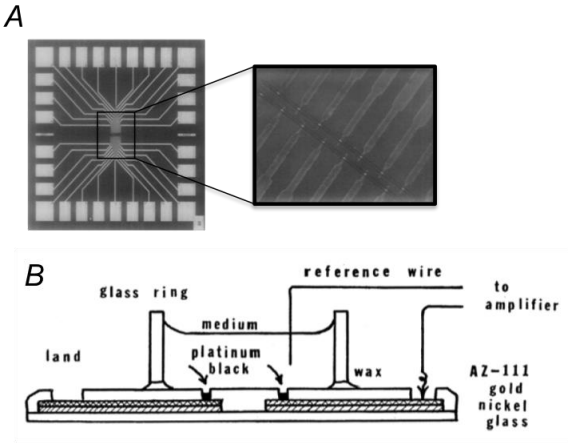

Figure 2.2 A. Planar view of the microelectrode array. On the right, a direct enlargement of the array pattern master plate is shown. B. Schematic diagram of the MEA structure. (Adapted from Thomas et al.*, 1972)*

In the 1980s, many studies in which MEAs were employed for different purposes were reported. For example, in 1982 Gross (Gross et al., 1982) used such an array to record from dissociated spinal cord cultures. He attempted to exploit new tools to investigate the network activity in these cultures. He found a relationship between the level of activity and the temperature at which the cultures were maintained during recording; a good level of activity was obtained at 30 °C, but activity decreased rapidly at room temperature.

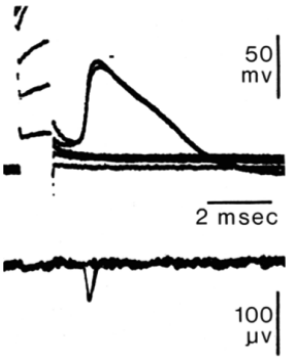

Figure 2.3 Five superimposed intracellular oscilloscope traces are shown at the top. Action potential signals are seen for the largest two traces. Extracellular recordings obtained simultaneously with the intracellular recordings are shown below. The two recordings that are below baseline are from the action potentials and are too similar to resolve (from Pine, 1980.)

Generally, synchronized bursty activity was recorded from these cultures as shown in **Figure 2.4**

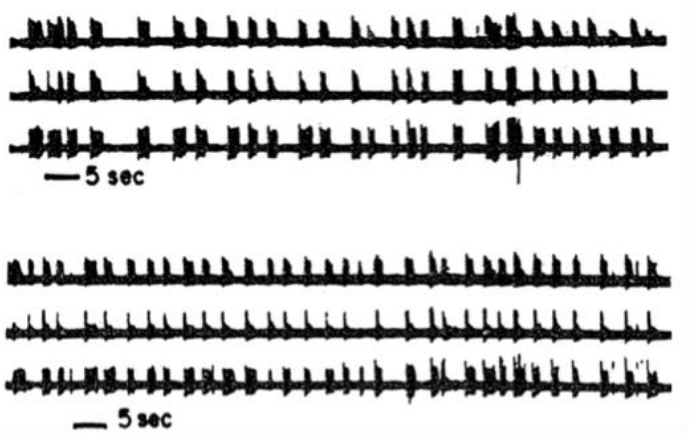

Figure 2.4 Simultaneous recordings obtained using three widely spaced electrodes in a monolayer cortical culture approximately four weeks in vitro (from Gross et al*., 1982).*

Another example is the work of Wheeler and Novak in 1986 in which they performed source density analysis of field potential recordings from hippocampal slices coupled to MEA (Wheeler and Novak, 1986;Novak and Wheeler, 1988). They used a custom MEA with an 8x4 layout of electrodes. The electrodes were 20 μm in diameter, and the distance between electrodes was 200 μm. This allowed them to stimulate the Shaffer collaterals while recording from the CA1 region. **Figure 2.5** shows the response during spontaneous phases; the array is well able to detect the regions of the dendrites and cell bodies of these neurons.

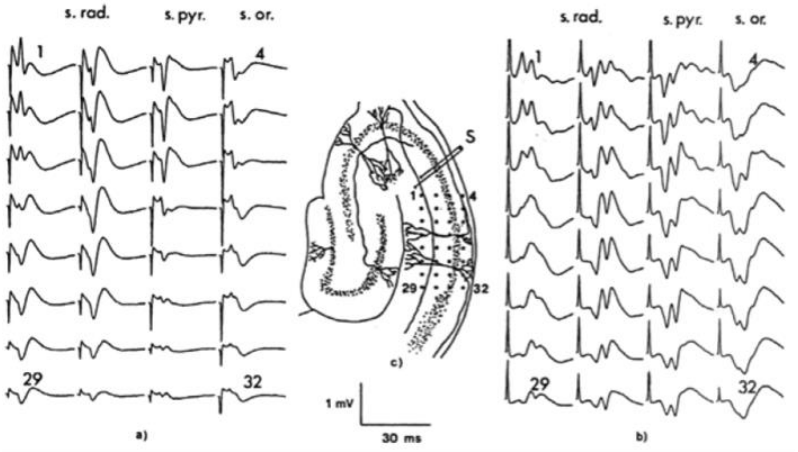

Figure 2.5 Responses of a hippocampal slice to stimulation of the Shaffer collaterals. The center of the figure shows the slice, the stimulating electrode, and the 32 recording electrodes. At left are the normal responses; at right, the result when picrotoxin was added to the bath to reduce inhibitory transmission (from Novak and Wheeler, 1988).

At the end of the 1980s, Regehr et al. studied invertebrate neurons using a 61-electrode array fabricated on a thin glass coverslip to facilitate observation of cells at high magnification with a short

working distance lens and an inverted microscope (**Figure 2.6 A**) (Regehr et al., 1989). The goal of these experiments was to determine whether it was possible to record from a variety of invertebrate neurons in snails, *Aplysia*, and leeches. Not surprisingly, the activity of these large neurons produced large potentials. Depending on the proximity of the electrodes to the neurons, the neurons showed different types of electrophysiological signals (as shown in **Figure 2.6 B**).

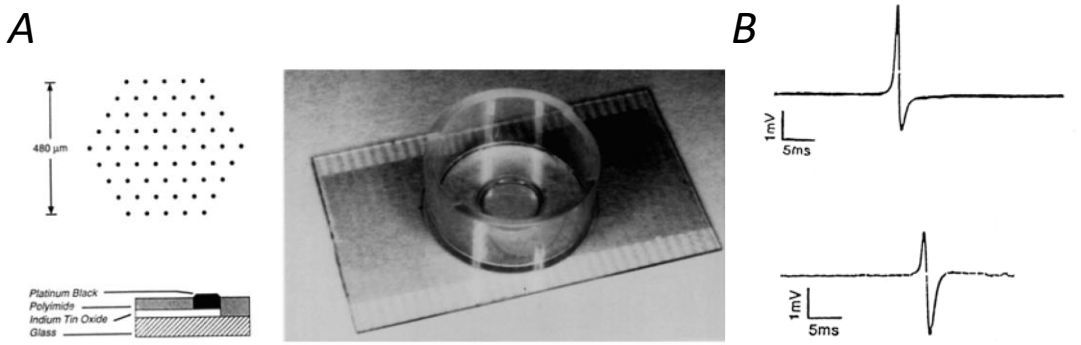

Figure 2.6 A) The 61-electrode array built in the Pine lab. At left, the electrode structure, and at right a completed MEA. B) Signals recorded from two different electrodes: the shape of signals is related to the proximity of the electrodes to the neurons (From Meister et al., 1994 and Regehr et al., 1989.)

In 1989, Meister et al. recorded spontaneous and light-evoked bursts of activity from an explanted salamander retina positioned over the array (Meister et al., 1989;Meister et al., 1994).

At the beginning of the 1990s, the combination of an MEA (for stimulation) and voltage-sensitive dyes (for recording) was exploited to allow the detection and measurement of subthreshold synaptic potentials, which are otherwise impossible to measure by recording extracellular electrical signals (Chien and Pine, 1991). Four years later, Welsh et al. recorded for more than 72 hours in an attempt to monitor the circadian rhythm of dissociated suprachiasmatic neurons (Welsh et al., 1995). These investigators successfully demonstrated that cultured networks did not show synchronized activity and that each neuron maintained independently oscillatory activity with a period of 24 hours. Thus, each neuron maintained its own circadian rhythm generator.

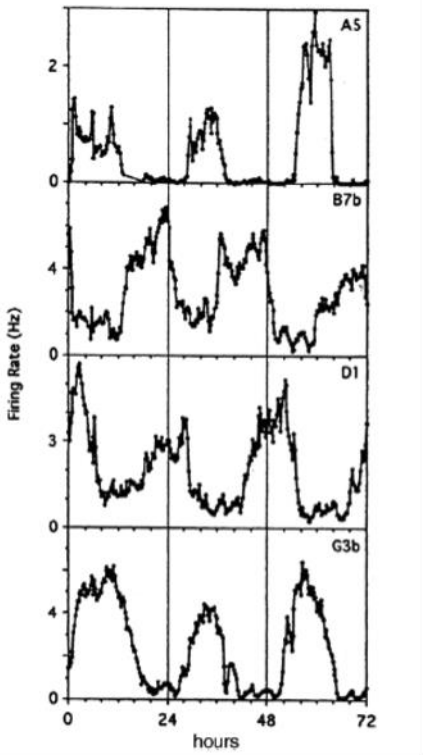

Figure2.7 Spontaneous activity of suprachiasmatic neurons in culture. The diurnal variation of firing rate is large and unsynchronized. (From Welsh et al., 1995.)

At the same time, progress was also made in developing technologies for recording brain slices over MEAs. In 1997, Thiébaud's group constructed the first 3D perforated MEA (pMEA) (Thiebaud et al., 1997). They used a perforated silicon substrate connected to a reservoir of cell culture medium to maintain the viability of the slices. The electrodes, which were either platinum bumps or silicon pyramids 45 μm high, were arranged in a three-dimensional configuration to improve contact with the cells of the slice. The authors were able to record the activity of slices in culture for up to 15 DIVs; they also monitored acute slices for eight hours. A diagram of their system is shown in **Figure 2.8**.

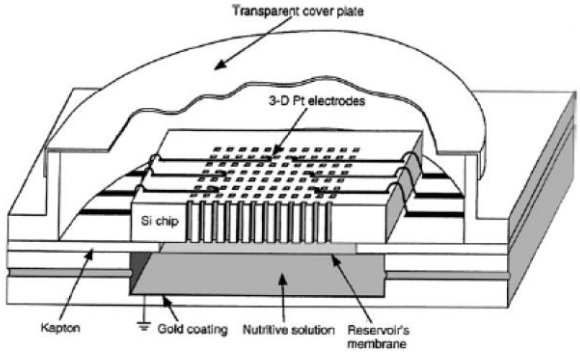

Figure 2.8 Schematic view of a slice measurement setup in which a perforated silicon substrate is used (from Thiébaud et al., 1997.)

During the late 1990s, the research questions most often addressed using MEAs involved network development and plasticity. These are the main goals pursued in the 1990s by groups in Japan at the

Matsuhita and NTT laboratories led by Taketani and Kawana. These investigators fabricated 64-electrode MEAs for use in slice experiments (Oka et al., 1999) and with cultures of dissociated cortical neurons (Maeda (Maeda et al., 1995).). A rocking device that could be used to keep cultured organotypic slices alive for many weeks was developed so that the development of the cultures could be observed over time (Kamioka, 1997). For cortical cultures, the experiments probed the plasticity of connections as a result of tetanic stimulation (Jimbo et al., 1999).

In the following year, the study of synchronous bursting activity attracted the attention of the scientific community. In 2000, Jimbo et al. began to study the dynamics of high-density cortical cultures in detail; the group demonstrated that network burst activity could be produced by a single stimulus even when the stimulus was delivered to a single neuron (**Figure 2.9**) (Jimbo et al., 2000). The work performed by Jimbo and collaborators inspired the development of new protocols for inducing network plasticity. In the following year, Steven Potter's group attempted to understand and control these dish-wide bursts as a means of studying network plasticity (Wagenaar et al., 2001;Madhavan et al., 2003). Similarly, Shahaf and Maron focused their attention on the possibility of inducing learning in dense cortical cultures (Shahaf and Marom, 2001).

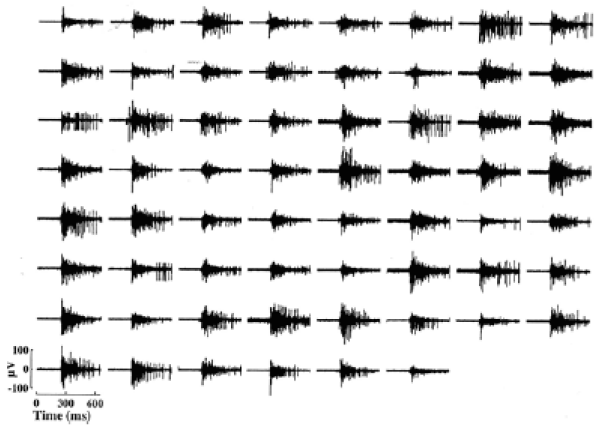

Figure 2.9 Network bursting in a dense cortical culture. (From Jimbo et al., 2000.)

However, since the 1990s (Gross et al., 1995) neuronal networks grown on planar MEAs have been considered a promising tool for drug screening and neurotoxicity studies (Gramowski et al., 2000;Keefer et al., 2001;Gramowski et al., 2004). This approach has proven to be useful in quantifying changes in network activity in response to various neuroactive compounds (Gross, 1977;Streit, 1993;Gramowski et al., 2000;Morefield et al., 2000;Martinoia et al., 2005) Keefer (Keefer et al., 2001;Xia et al., 2003;Parviz and Gross, 2007;Novellino et al., 2011;Colombi et al., 2013;Vassallo et al., 2017).

In summary, during the past thirty years a great variety of explorations have addressed the possibilities provided by MEAs. At present, these technologies represent a powerful tool that can be used to

evaluate the long-term effects of drug compounds on neurons. Findings from these studies could have significant implications for the treatment of human diseases such as congenital malformations, epilepsy, stroke and Alzheimer's disease (Hofmann et al., 2006;Görtz et al., 2009;Gullo et al., 2014). MEA devices offer several advantages over traditional electrophysiological techniques, including making it possible to conduct extracellular recording and to stimulate a neural network in many different locations at once, which in turn allows correlation of electrophysiological activity over a large area. In conclusion, MEAs coupled to neuronal networks (i.e., brain slices or primary cell cultures) represent a reliable model that can be used to study the effects of new therapeutic compounds, especially in pathologies for which there are as yet no cures.

2.2 Microelectrode array technology: standard devices

MEAs consist of cell-sized electrodes (10-30 μm diameter) attached to a glass substrate. The electrodes, which are typically made of gold, indium-tin oxide (ITO), titanium nitride (TiN), or black platinum, must be biocompatible and long-lasting and should preferably have low impedance (less than 500 kΩ at 1 kHz) to reduce thermal noise.

The nonsensitive surface of the MEA and the electrode leads are coated with biocompatible insulators (e.g., polyamide or silicon nitride/oxide) that prevent short circuits with the electrolyte bath. These insulators, which are also coated with adhesion-promoting molecules such as polylysine and/or laminin, allow and promote the coupling of the neuron to the device surface. The low impedance of the electrodes and the choice of an appropriate voltage range to avoid the generation of neurotoxic redox complexes make it possible to use them to deliver external stimuli. The fabrication of MEAs is based on film technology (Elshabini-Riad and Barlow, 1998) and is conducted in a clean room using standard photolithographic techniques. The rapid success met by MEAs in the neuroscience research field moved some electronic companies to develop commercial systems for performing electrophysiological measurements using MEAs. At present, at least two complete acquisition systems based on MEAs are on the market, namely, the MED System produced by Panasonic (www.med64.com, Osaka, Japan) and the MEA System produced by Multi Channel Systems (www.multichannelsystems.com, Reutlingen, Germany). Other companies, such as 3Brain (https://www.3brain.com/, Wädenswil, Switzerland), Plexon (www.plexoninc.com, Dallas, USA) and Axion Biosystem (https://www.axionbiosystems.com/products, Atlanta, USA) have developed microelectrode devices for several different applications (cultures, slices, cardiomyocytes, retinal cells, pharmacological screening, etc.). Figure 2.10 shows four of the products offered by Multi

Channel Systems, Panasonic and Ayanda.

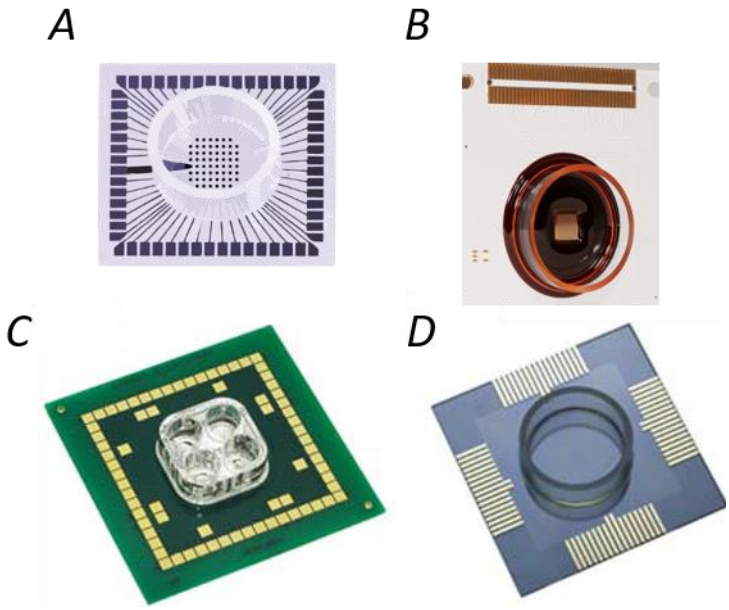

Figure 2.10 MEAs produced by different companies. (A) MEA 30/200 made by Multi Channel Systems for use with dissociated neuronal cultures. (B) High-density MEA from 3Brain. C) Multiwell chip for pharmacological applications. (D) MED60 made by Panasonic.

All the experimental results involving standard commercial devices presented in this thesis were obtained from recordings performed using MEAs manufactured by NMI (Natural and Medical Science Institute, Reutlingen, Germany) and developed by Multi Channel Systems. The following sections describe various design approaches and discuss current development around the MEA chip by NMI.

2.2.1 MCS microelectrode array design

The requirement for specific layouts of MEAs for use in answering specific biological questions has prompted the NMI to develop new custom-designed layouts. Here, we will briefly describe the standard MEA layouts used in this PhD project.

Standard layout MEAs

Multi-Channel Systems (MCS) provides different types of MEAs with varying electrode size and interelectrode spacing.

The MEAs used in this thesis consist of 60 round electrodes made of TiN. The tracks and contact pads are made of titanium or ITO, and the insulation material is silicon nitride (Si_3N_4). The electrodes are positioned in an 8x8 layout grid (the four corner electrodes are not present) or in a rectangular layout (**Figure 2.11**). ITO contact pads and tracks are transparent to allow a perfect view of the

specimen under the microscope. In this study, we used arrays of 30-µm electrodes spaced 200 µm apart.

MEAs are equipped with an internal reference electrode that is used to minimize the possibility of pollution caused by the introduction of an external reference electrode. A glass ring is placed at the center of the device, surrounding the recording area, to contain the culture medium. In this way, when placed in an incubator, the culture can survive for several weeks.

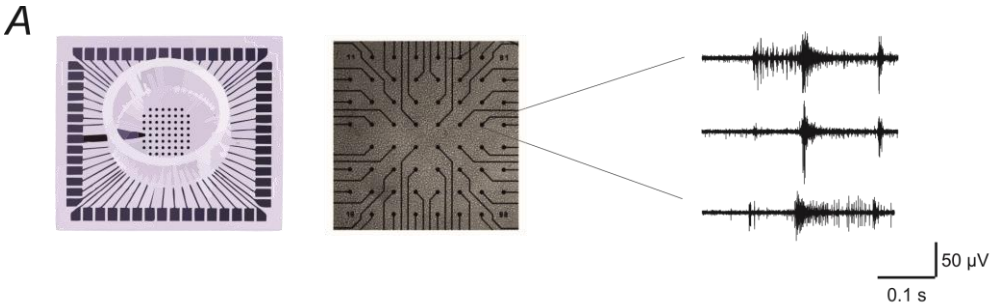

Figure 2.11 Standard 8x8 microelectrode layout from Multi Channel Systems. The array consists of 59 electrodes with one internal reference. On the right are three typical extracellular signals recorded from three different electrodes.

6 Well MEA

In the work described in this thesis, we also used 6-well MEAs that allow simultaneous recording from six independent chambers that are separated by a Makrolon ring. Inside each well, 9 electrodes are placed with one reference electrode. The electrodes, which are made of titanium nitride (TiN), are 30 µm in diameter and are separated by a distance of 200 µm.

The main advantage of using this type of MEA is that it allows the investigator to perform 6 experiments at the same time using the same external condition. Therefore, 6-well MEAs are perfectly suited for neuropharmacological experiments involving the testing of different drugs in the same cultures.

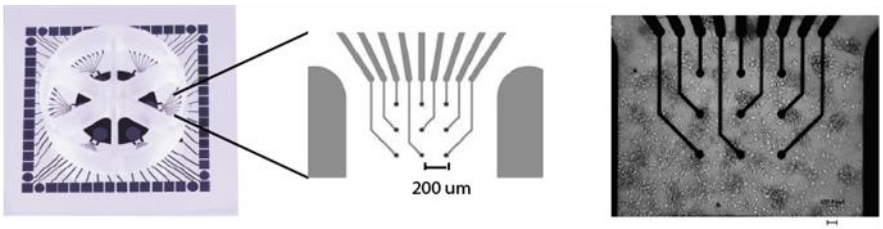

Figure 2.12. A 6-well MEA device with six independent culture chambers divided by a Makrolon separator. Inside each well, nine electrodes and one large internal reference electrode allow recording of electrophysiological activity from cultures of dissociated neurons.

2.2.2 The MCS MEA60 System

All the experiments performed during this PhD project are performed with the MCS MEA60 System developed by Multi Channel System (Reutlingen, Germany, www.multichannelsystems.com).

The MCS MEA60 set-up is made up of the following components, usually contained within a Faraday cage in order to reduce electromagnetic interferences:

1. MEA 1060-Up-Standard Amplifier;
2. PCI-based acquisition board;
3. Acquisition software;
4. Temperature controller;

In an improved version of the MEA60 System, up to four amplifiers, each hosting an MEA device, can be connected to the data acquisition card and 120 out of a potential 240 MEA electrodes can be monitored simultaneously. This allows the parallel recording of more than one sample, particularly useful if one wants to compare the effects of the same experimental protocol on different cultures at the same time. This scalable MEA60 System has been designed by MCS to answer the ever-growing demand in basic research and pharmaceutical applications for automation of experimental and data analysis procedures. In our lab at the Italian Institute of Technology (IIT), we used an MEA120 System to record up to two cultures of dissociated neurons (or brain slices) at the same time and double the number of monitored samples. More details on the complete MEA60 System are available in (Whitson et al., 2006) and references therein. Further technical specifications and data sheets can be found on www.multichannelsystems.com.

In that follow we briefly describe each components as depicted in **Figure 2.13.**

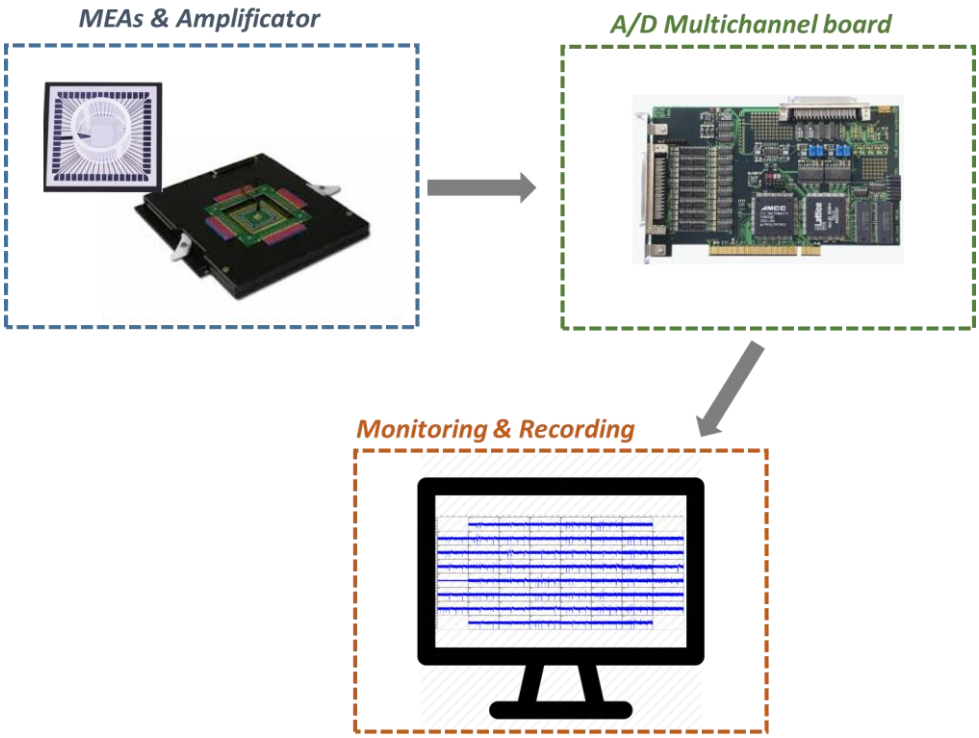

Figure 2.13 Schematic representation of the experimental setup. Signal from MEA was amplifier and acquired with a PCB card and then monitored on a personal computer.

1. Amplifier

An amplifier stage for multi-electrode recording has to meet two main requirements: *i)* eliminating the cables connecting the electrodes and *ii)* coping with the interference (cross-talk phenomenon) among channels. The MEA1060 60-channel amplifier has a compact design (165 X 165 X 19 mm) and, due to the surface-mounted technology (SMD) of pre- and filter-amplifier, the complete circuit and amplifier hardware was built into a single housing: this ensures optimal signal-to-noise ratio of the recording, because no further cables are necessary other than a single SCSI-type cable connecting the amplifier to the data acquisition card. This results in an overall low noise level of the complete amplifier chain (1200, 12-bit resolution, 10 Hz to 3 kHz) of +-3 uV, which is well within the -+5 to 10 uV noise level of the MEA TiN electrode. Given the low noise of the recording system single units in the lower range of 20 to 30 µV can be readily detected. Hence, the MEA sensor is placed directly inside the amplifier and settled so as to fit the standard microscopes.

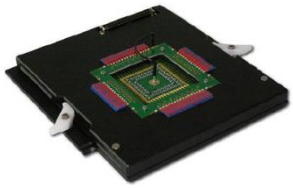

2. PCI-based acquisition board

Standard PC technology is used as the backbone of high-speed multi-channel data acquisition. The data acquisition card is based on PCI-bus technology and allows the simultaneous sampling of up to 128 channels at a sampling rate of 50 kHz per channel. Three analog channels and a digital I/O port are accessible, allowing the simultaneous acquisition of analog data such as current traces from a patch clamp amplifier or temperature together with the MEA electrode data. The digital I/O port features trigger IN/trigger OUT functionality. This is an important feature when, for instance, a stimulator is set up to elicit a stimulation pulse to one or more MEA electrodes.

3. Acquisition software

The MC Rack software allows to record simultaneously the electrophysiological activity from the 60 electrodes of the MEA and monitor the raw data in a real-time mode. Different parameters can be extracted from the data streams and the results can be plotted, saved, and exported to other programs for further analysis.

4. Stimulus generator

The MCS stimulus generator (STG2004) is a general purpose stimulator which generates pulses to be delivered to stimulating electrodes (up to 4 for this model and up to 8 for upgraded models). Complex stimulus waveforms (both current and voltage) of arbitrary duration are designed by using the provided MCS stimulus software and then stored in the stimulus generator connected to the MEA. Stimuli are “tailored" by the user by specifying the desired pulse waveform defining parameters into a worksheet. The pulse waveform is then displayed and the stimulus protocol is downloaded to the stimulus generator via a serial communication port. The stimulus generator operates in both voltage and current mode, and it is equipped with separate voltage and current outputs for each channel.

5. Temperature controller

The MCS temperature controller (TC02) uses a Proportional Integrative Derivative (PID) based technology. The MEA temperature can vary in the range from room temperature to +50 C. The set-point temperature is reached within a range of 30 s to 5 minutes, depending on the recording system configuration.

6. PH01 Canula

The heating canula PH01 from Multichannel System was used for maintaining the temperature during the perfusion system. The programmable fluid temperature is controlled by a temperature controller TC01/02 (see before). A titanium wire inserted into the cannula results in a turbulent flow that ensures that the temperature of the liquid is constant across the flow stream. The heating cannula should be covered by beveled polytetrafluoroethylene (PTFE) tubing to reach the recording chamber inlet port and to minimize noise due to the metallic material of the cannula. The flow rates range from 500 µl to 4.5 ml per minute.

2.2.3 Custom fittings for the MCS MEA60 System

Mini Incubator for recording from cultures

Within the incubator the temperature (37 °C), the relative humidity (90-95%) and the CO_2 concentration (5%) are controlled so as to maintain the culture medium pH of 7.4 and the osmolarity of 230 mOsm. In fact, large variations in these parameters strongly affect the network activity and, if permanent, can cause the culture death. Hence, the optimal recording conditions would be provided by the incubation environment, but it is not possible to store the MCS MEA1060 amplifier in a highly humidified atmosphere, as that of the incubator. This is the reason why we designed and realized a custom recording chamber, which, coupled to the use of a PDMS lid, allows the recording of cultures in safe conditions. The custom chamber (shown in **Figure 2.14**) consists of a metallic box, sized 13x13x4 cm (WxLxH), heated on the topside through planar high-power ceramic resistors (BI Technologies, www.bitechnologies.com, Fullerton, CA, USA) and providing an inlet for a constant gas flow. In fact, the chamber is connected through PTFE/FEP tubing (Legris, www.legris.com, Rennes, France) to a gas cylinder containing a mix of 5% CO_2 - 20% O_2 - 75% N_2, practically the composition of air with 5% CO_2: a constant slow flow of this gas mix into the metallic box covering the MEA during the experiment has been demonstrated to prevent the medium's pH to drift towards more basic values (up to 9 -10 pH units) (Brewer et al., 1993;Brewer, 1997).

Moreover, using this recording chamber, the MEA device containing the culture is not only heated bottom up by the amplifier's warming plate driven by the MCS temperature controller, but also top down through the ceramic resistors heating the metallic box. In fact, when supplied with a suitable voltage, they constantly heat the conducting metallic surface of the chamber so as to provide a surrounding environment for the MEA whose temperature (37 C) is homogeneous. This, together with the PDMS lid and with the fact that the gas is made bubble in water before being fed into the

incubator, strongly reduces the evaporation and maintain the medium's osmolarity constant during the experiment. The recording chamber features a hole on the topside, to let the observation of the culture either using a microscope or to the naked eye, and a lateral hole, to let optional perfusion tubing in or out of the box. These holes are hermetically sealed during normal operation, to limit leakage and keep the 5% CO_2 concentration and temperature as constant as possible inside the chamber.

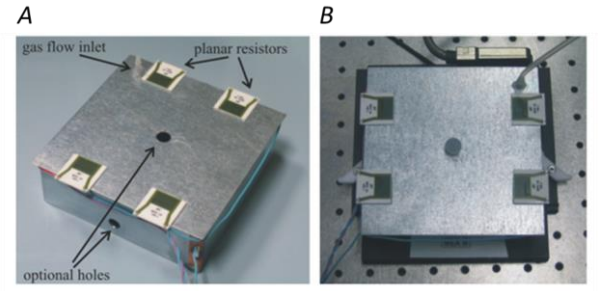

Figure 2.14 Custom recording chamber for MEA recordings. (A) Image of the recording chamber, highlighting the main features, and (B) image of the same chamber during normal operation over an MEA1060 amplifier.

2.3 Signal processing tools for MEAs

2.3.1 Types of signals detected using standard microelectrode arrays

Microelectrode arrays have been developed and used to characterize and analyze the activity of cultured neuronal networks (Thomas Jr et al., 1972;Pine, 1980;Gross et al., 1982;Chiappalone et al., 2007;Novellino et al., 2011): in this type of work, neurons are cultured for weeks *in vitro* on a planar array that is capable of sensing electrical signals.

The typical extracellularly acquired signals from a local network of neurons are local field potentials (LFPs) and multi-unit activity (MUA). The LFPs, which constitute the low-frequency components (<300 Hz) of the raw signal, are believed to be generated by neuronal membrane currents in the local neighborhood of the recording electrode. MUA, which constitutes the high-frequency portion (>300 Hz) of the raw signal, represents the spiking of local neurons situated near the recording electrode (Burns et al., 2010;Buzsaki et al., 2012). The principle of conventional extracellular recording is based on extracellular field theory (Humphrey and Schmidt, 1990). The microelectrode detects electric potential changes in a conductive extracellular field generated by current flow of active neurons. The dimensions of a single electrode are usually 10-30 μm, comparable to the size of a single cell; current originates in a specific part of the neuron (usually the axon hillock or soma) and spreads over the dendrites. Using multiple recording techniques along the dendritic axis, it is possible to

localize the approximate site of generation of the electrical response using a technique called *source density analysis* (Haberly and Shepherd, 1973).). The sink can be localized near the axon hillock (or soma), and the source may be distributed along the dendrites. The polarity of the recorded signal depends strongly on the location of the electrode with respect to the spatial distribution of sources and sinks. The extracellular potential (V_e) at a particular point P can be calculated as follows:

$$V_e(P) = \frac{1}{4\pi\sigma} * \frac{\sum J_i}{r_i} * \Delta S_i$$

where σ is the conductivity of the extracellular medium, Ji is the current density over the i^{th} segment (positive for source, negative for sink), r_i is the distance from the i^{th} segment to point P and ΔS_i is the surface area of the i^{th} segment.

Spike shape is influenced by both the size and the geometry of the cell, i.e., larger membrane currents imply stronger field potential (V_e proportional to Je). Therefore, in cultured neuronal networks, the majority of the recorded signals are somatic spikes since the axon is very small in diameter (i.e., 1 μm) and therefore has high impedance (Nam and Wheeler, 2011). The position of the electrodes relative to the sink and the source also determines the waveform of the recorded signal (Nam and Wheeler, 2011;Obien et al., 2015):); axon spikes are mostly negative biphasic spikes, while dendritic spikes are positive biphasic spikes. Biphasic events include an initial rapid depolarization from the soma followed by a rebound when the soma acts as a source for other, later depolarizing elements. In neuronal cultures, the majority of the spikes (approximately 80%) present negative waveforms, while the remainder (approximately 20%) are positive (Nam and Wheeler, 2011). Unfortunately, it is not easy to determine from which part of the neuron the recording originates; a predominance of negative spike waveforms may indicate that many electrodes are coupled to the excitable soma. Moreover, it is possible to observe changes in the amplitude, width and waveform of the recorded signals due to morphological maturation of the neuronal network during culture development.

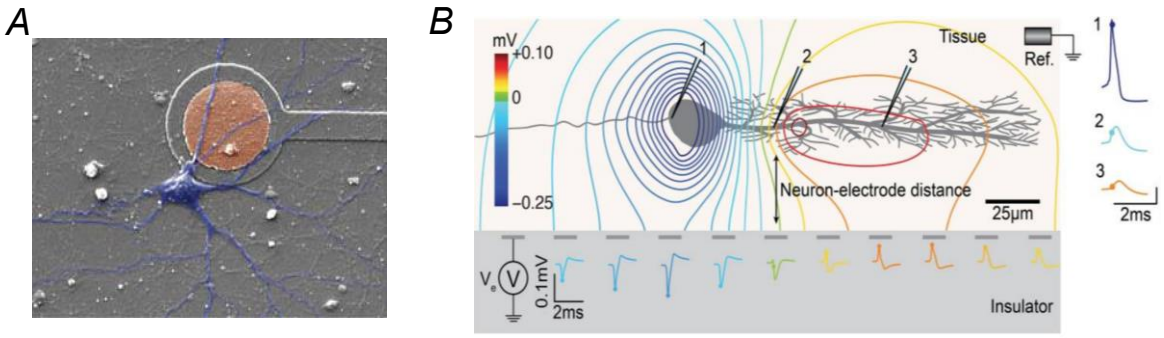

Figure 2.15 A) Neuron-electrode coupling in a culture over MEA at DIV 11 (from Nam and Wheeler, 2011). B) Generalized neuron-electrode interface. The potential at the electrode sites can be calculated using volume conductor theory. The MEA surface is assumed to be an insulator such that the method of images can be applied using Coulomb's law to solve the potential at any point on the MEA surface. The neuron-electrode distance influences the signal amplitude measured at the electrodes. High spatial resolution allows recording at several locations within a single neuron, with large negative spikes located at the perisomatic area and positive spikes at the dendritic area, i.e.*, return current (from J. Obien* et al*. 2015).*

The use of brain slices over MEA permits recording of the extracellular field potential in a 3D environment. Electrophysiological parameters can be visualized relative to the spatial positions of the electrodes in different structures. Berger and coworkers showed that when a custom-made 60-electrode layout is used it is possible to match the correct orientation of a cell's dendritic axis while reducing the number of recordable structures (Soussou et al., 2006) as shown in **Figure 2.16**.

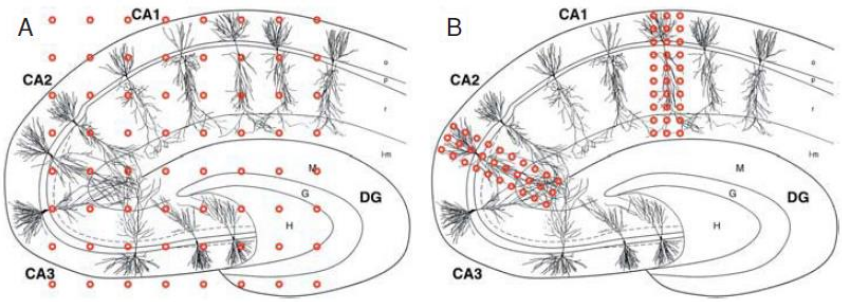

Figure 2.16 Hippocampal brain slices over 60 channels MEAs. A) Drawing of a hippocampal slices placed over a standard 60- channel MEA. B) Custom MEA layout with two high-density 3 ×10 rectangular arrays that allow recording from CA1 and CA3 pyramidal cells (from Soussou et al.*, 2005)*

They performed a current source density analysis of CA1 pyramidal neurons using a custom 20x3 pMEA: hippocampal slice oriented in such a way that the apical CA1 pyramidal dendrites were parallel to the long axis of the array (**Figure 2.17**). Monopolar biphasic stimulation was then delivered through one of the electrodes in the right column of the array, corresponding to the stratum radiatum (marked by a red dot in the figure). They recorded positive evoked field potentials (FPs) in the stratum

oriens (above the cell body layer, the stratum pyramidal) and negative potentials in the strata radiatum and moleculare. The color-coded potential is shown in Fig 2.18 B; positive FPs are depicted in yellow/red, while the blue areas delineate negative excitatory postsynaptic potentials (EPSPs). As shown in the figure, two-dimensional CSD analysis was applied to the recorded voltages (Gholmieh G. et al., 2005). In the FP graph on the left side, the CSD also shows the longitudinal spread of the positive and negative EPSPs. Depending on the electrode density, MEA coupled to brain slices can provide either low-resolution information based on the activity recorded in different slice regions or CSD analysis for accurate mapping of currents and sources in smaller cellular subregions.

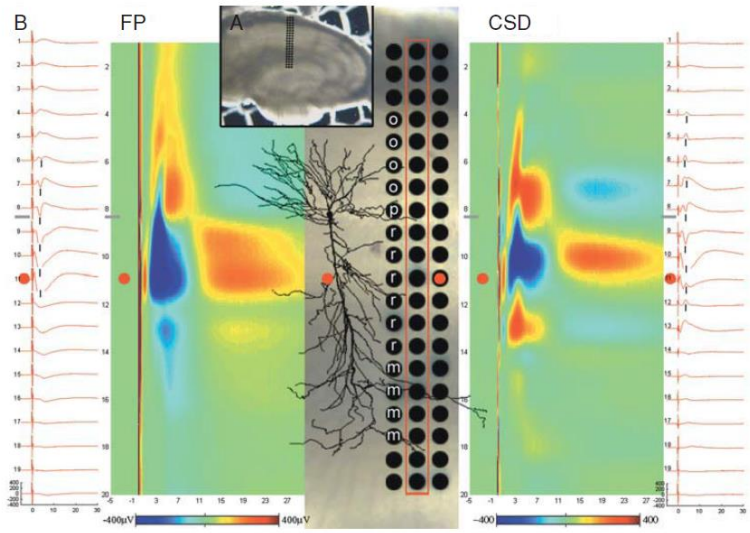

Figure 2.17 FP versus CSD in CA1: B) CA1 laminar profile of the slice shown in (A) in response to stimulation at the electrode marked in red. The color map shows the recorded FPs and the computed CSD values on a color scale and interpolated between electrodes. The trace drawing of a cell illustrates the relative position of the electrodes with respect to the CA1 pyramidal cells. The horizontal gray bars mark the cell layer. The vertical black lines mark the population spike. The stimulation was applied 10 msec after the beginning of the recording. x-axis, 35 msec; y-axis or color range −400 to +400 µV or CSD units. The strata are labeled in the electrodes: oriens (o), pyramidale (p), radiatum (r), and moleculare (m). (from Soussou et al*., 2005)*

2.3.2 SPYCODE: a custom software for the analysis of neuronal cultures

The use of MEAs for electrophysiological experiments is likely to produce a huge quantity of data (high number of recording channels, high sampling frequency, long recordings), thus urging upon the need for a smart software which could autonomously search for the experiments to be analysed, recognize them and apply the needed analysis, several times, to different sets of data.

In the last years, a Matlab-based software has been developed, named Spycode, collecting several basic and advanced tools for the analysis of multichannel recordings: this tool is the output of the joint efforts of several members of our research group (**Figure. 2.18**). Starting from a basic version of the software already implemented in Matlab,(Vato et al., 2004) the concept of “multiple analysis" has been introduced, namely allowing the autonomous repetition of the same 'multiple' computational

operations to 'multiple' data without the intervention of the researcher (except for the setting of the parameters needed to retrieve the experiments) (Bologna et al., 2010).

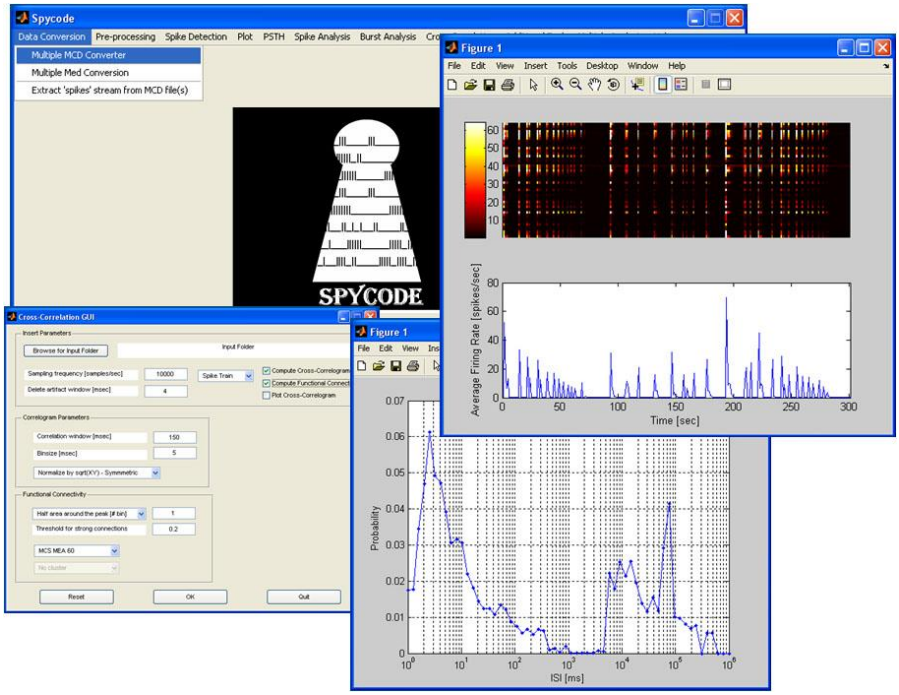

Figure 2.18. Running Spycode. The main Graphical User Interface (GUI) is depicted during a working session of the software. Additional GUIs for data input are shown to the user before launching each computation. The output of an analysis session is provided through a series of figures (.fig or .jpg format) or results files (.mat or ASCII format).

Figure. 2.19 schematically shows the organization of the software, which includes a block for data conversion, one for data filtering (optional) and the cascade of analysis that can be done once spike detection has been performed: spike analysis, burst detection and analysis, post-stimulus time histogram, inter-spike interval (ISI), inter-event interval (IEI) distributions and cross-correlation.

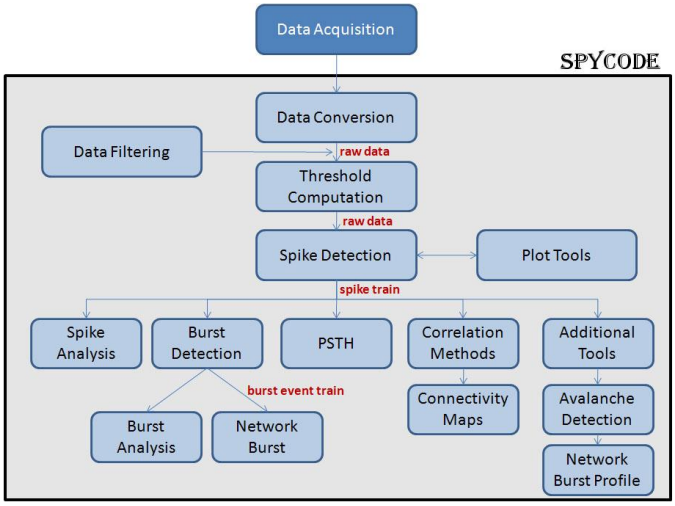

*Figure 2.19 Schematic overview of the data analysis procedure implemented within Spycode. The functional blocks show the main computational and algorithmic options offered by the software. The data flow starts with the data conversion procedure, after which raw data are available in Matlab internal format (i.e. *.mat), then a filter can be applied to de-noise the data (optional).*

In the following paragraphs, we will give a brief description of the standard algorithms used for characterizing the spontaneous and evoked activity of neuronal networks *in vitro*.

Data pre-processing: spike detection.

Extracellularly recorded signals are embedded in biological and thermal noise and spikes can be detected by means of threshold-based spike detection algorithms. In this study, we used for MCS MEAs a spike detection method named Precise Timing Spike Detection (PTSD) which is an evolution of the one previously used, being more precise in detecting the exact timing of spikes (Maccione et al., 2009). Briefly, the method used three parameters: (1) a differential threshold (DT) set independently for each channel and computed as 8-fold the standard deviation (SD) of the noise of the signal; (2) a peak lifetime period (PLP) set to 2 ms; (3) a refractory period set to 1 ms.

The algorithm scans the raw data to discriminate the relative minimum or maximum points. Once a relative minimum point is found, the nearest maximum point is searched within the following PLP window (or vice versa). If the difference between the two points is larger than DT, a spike is identified and its timestamp saved. Then, to characterize the activity level of the analyzed networks, we computed the mean firing rate (MFR), which is defined as the mean number of spikes per second, computed over the total recording time. We considered active electrodes as those presenting a firing rate higher than 0.01 spikes per second. The low threshold guarantees to exclude only those electrodes that are not covered by cells or with very few spikes, keeping all the others.

Burst Detection

Neuronal networks plated on MEA show both random and spiking activity, in large majority, bursting behavior (Brewer, 1997;Leondopulos et al., 2012). Bursts consist of packages of spikes distributed over a range of a few milliseconds, which generally last from hundreds of milliseconds up to seconds, and are separated by long quiescent periods. Spontaneous bursting activity was detected using a custom burst detection method developed in our laboratory (Chiappalone et al., 2005;Turnbull et al., 2005). According to those algorithms, in order to detect bursts, two thresholds were fixed: the first one was the maximum ISI allowed for spikes within a burst (maxISI, usually set at 100 ms); the second one was defined as the minimum number of consecutive spikes belonging to a burst (minSpikes, usually set at 5).

Once spike and burst detection procedures were performed, usually we extracted several parameters describing the electrophysiological patterns, such as mean bursting rate (MBR) [bursts/min], burst duration (BD) [ms], Mean Frequency Intra burst (MFIB,spike/sec), Burstiness Index, and the Inverse Burst Ratio (IBR) (which represents the percentage of random spikes, i.e., spikes outside the bursts).

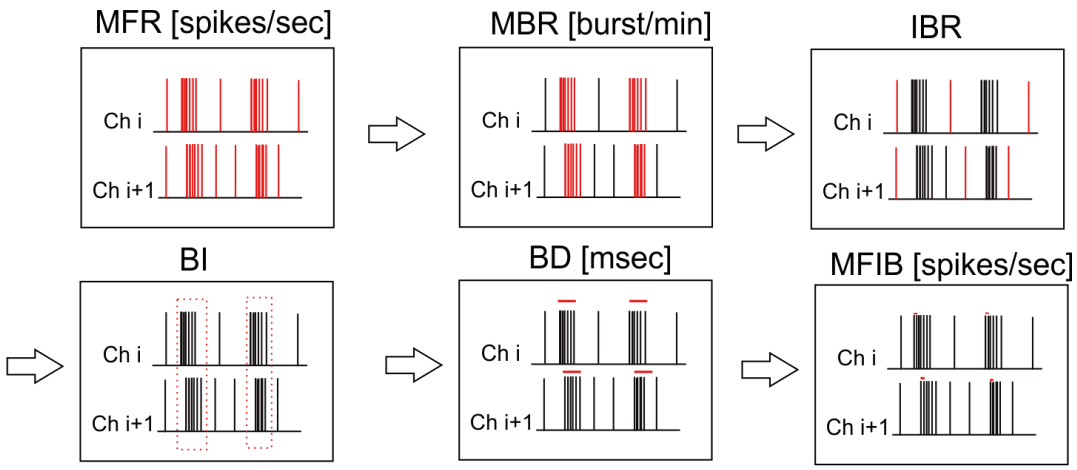

Figure 2.20 Electrophysiological parameters used for describing the electrophysiological patterns such as the level of firing rate (i.e. MFR [spikes/sec]), the level of bursting rate (i.e. MBR (burst/min)), the percentage of spikes outside the burst (i.e. IBR), the Burstiness Index (index between 0 and 1 that indicate the level of burstiness of the networks), the duration for each burst (BD, msec), the mean frequency of the spikes inside each burst (MFIB, spikes/sec).

Cross-correlation

To characterize the synchronization among multi-unit recordings, the correlation analysis was applied to spike trains (Chiappalone et al., 2007). The cross-correlation function was built by considering the spike trains of two recording sites (le Feber et al., 2014), and it is a measure of the frequency at which a spike was recorded in one recording site relative to the spike firing in another recording site, as a function of time. This function was evaluated considering each pair of spike trains recorded from active channels (i.e. with MFR>0.01 spike/s). The correlation function represents the average value of the product of two random processes, which are spike trains, but, mathematically, it reduces to a simple probability. In particular, the Cross Correlation function represents the probability of observing a spike in one channel *i* at time (t+τ, τ=3 ms) given that there is a spike in a second channel *i*+1 at time t.

The cross-correlation (CC) function CXY (τ) was obtained by a normalization procedure, according to the following formula:

$$C_{XY}(\tau) = \frac{1}{\sqrt{N_X N_Y}} \sum_{t_i=(\tau-\frac{\Delta\tau}{2})}^{\tau+\frac{\Delta\tau}{2}} X(t_s)Y(t_s - t_i)$$

where ts indicates the timing of an event in the X train, NX and NY represent the total number of events in the X and in the Y train respectively, Δt is the bin size. The mathematic equation yields the symmetry between CXY (τ) and CYX (τ) (i.e. CXY (τ) = CYX (-τ)) ((Eytan and Marom, 2006). In order to quantify the strength of correlation between each couple of electrodes, we evaluated the

Correlation peak (C_{peak}). We select only the first 100 C_{peak} values to identify only the most significant correlations. Finally, we analyzed the latency from the peak (L_{peak}) and we considered the corresponding peak latency values of the pre-selected 100 strongest C_{peak} values (Bisio et al., 2014). We are confident that this method underestimates the number of significant connections, but it did not include in the analysis non-statistically significant connections (Garofalo et al., 2009;Maccione et al., 2012).

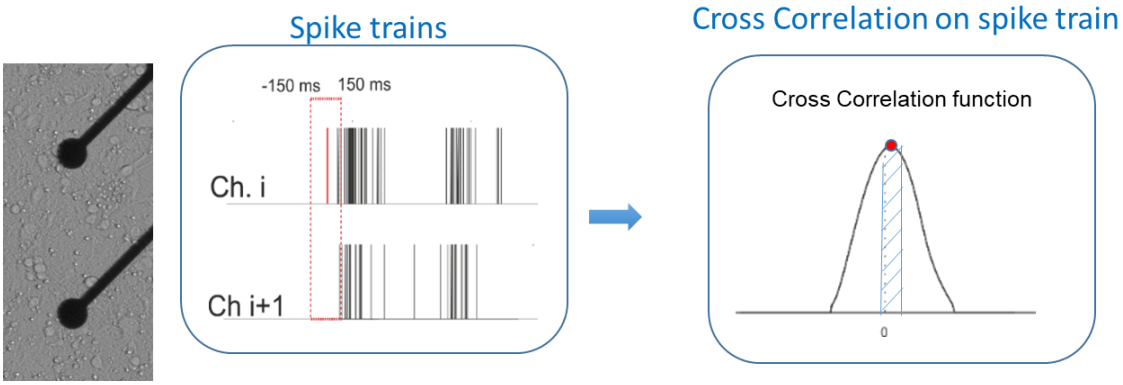

Figure 2.21 Cross Correlation function scheme.

Spike time tiling coefficients - STTCs

To characterize the degree of synchronization within each neuronal network, another method, the spike time tiling coefficient (STTC, Cutts et al. 2014), was used. Since in our experiments we altered the level of firing rate we want to test the level of synchronization with a parameter that is not confounded by the level of firing rate. Briefly, when considering two spike trains A and B, the STTC method looks for spikes in A that fall within ±Δt of a spike that occurs in B. In this method, we account for the amount of correlation expected by chance by making the minimal assumption that we expect the proportion of spikes from A falling within ±Δt of a spike from B by chance to be the same as the proportion of the total recording that falls within ±Δt of a spike from B. Any additional spikes in A that have this property are indicative of positive correlation. We therefore use the quantity $P_A - T_B$ (**Figure 2.20** shows definitions), which is positive if the spikes in train A are correlated with the spikes from train B and negative if there is less correlation than is expected by chance. The authors required the coefficient to be equal to +1 for autocorrelation, to be −1 when $P_A = 0$, $T_B = 1$ and to have a range of [-1, 1]. The normalization factor $(1 - P_A T_B)$ ensures that the insensitivity to firing rate is maintained.

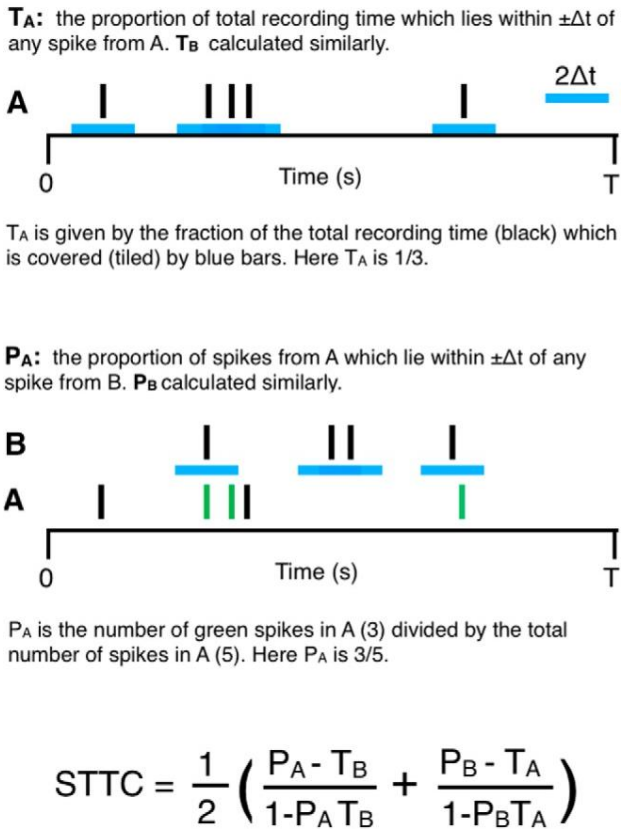

Figure 2.20 STTC diagram depicting the steps in computing the parameter (from Cutts et al.*)*

References

Angelides, K.J., Elmer, L.W., Loftus, D., and Elson, E. (1988). Distribution and lateral mobility of voltage-dependent sodium channels in neurons. *The Journal of cell biology* 106**,** 1911-1925.

Bisio, M., Bosca, A., Pasquale, V., Berdondini, L., and Chiappalone, M. (2014). Emergence of bursting activity in connected neuronal sub-populations. *PloS one* 9**,** e107400.

Bologna, L.L., Pasquale, V., Garofalo, M., Gandolfo, M., Baljon, P.L., Maccione, A., Martinoia, S., and Chiappalone, M. (2010). Investigating neuronal activity by SPYCODE multi-channel data analyzer. *Neural Netw* 23**,** 685-697.

Brewer, G.J. (1997). Isolation and culture of adult rat hippocampal neurons. *Journal of neuroscience methods* 71**,** 143-155.

Brewer, G.J., Torricelli, J., Evege, E., and Price, P. (1993). Optimized survival of hippocampal neurons in B27‐supplemented neurobasal™, a new serum‐free medium combination. *Journal of neuroscience research* 35**,** 567-576.

Burns, S.P., Xing, D., and Shapley, R.M. (2010). Comparisons of the dynamics of local field potential and multiunit activity signals in macaque visual cortex. *J Neurosci* 30**,** 13739-13749.

Buzsaki, G., Anastassiou, C.A., and Koch, C. (2012). The origin of extracellular fields and currents--EEG, ECoG, LFP and spikes. *Nat Rev Neurosci* 13**,** 407-420.

Chiappalone, M., Novellino, A., Vajda, I., Vato, A., Martinoia, S., and Van Pelt, J. (2005). Burst detection algorithms for the analysis of spatio-temporal patterns in cortical networks of neurons. *Neurocomputing* 65**,** 653-662.

Chiappalone, M., Vato, A., Berdondini, L., Koudelka-Hep, M., and Martinoia, S. (2007). Network dynamics and synchronous activity in cultured cortical neurons. *International journal of neural systems* 17**,** 87-103.

Chien, C.-B., and Pine, J. (1991). Voltage-sensitive dye recording of action potentials and synaptic potentials from sympathetic microcultures. *Biophysical journal* 60**,** 697.

Claverol-Tinture, E., and Pine, J. (2002). Extracellular potentials in low-density dissociated neuronal cultures. *Journal of neuroscience methods* 117**,** 13-21.

Colombi, I., Mahajani, S., Frega, M., Gasparini, L., and Chiappalone, M. (2013). Effects of antiepileptic drugs on hippocampal neurons coupled to micro-electrode arrays. *Front Neuroeng* 6**,** 10.

Eytan, D., and Marom, S. (2006). Dynamics and effective topology underlying synchronization in networks of cortical neurons. *The Journal of neuroscience* 26**,** 8465-8476.

Garofalo, M., Nieus, T., Massobrio, P., and Martinoia, S. (2009). Evaluation of the performance of information theory-based methods and cross-correlation to estimate the functional connectivity in cortical networks. *PloS one* 4**,** e6482.

Gesteland, R.C., Howland, B., Lettvin, J.Y., and Pitts, W.H. (1959). Comments on microelectrodes. *Proceedings of the IRE* 47**,** 1856-1862.

Görtz, P., Opatz, J., Siebler, M., Funke, S.A., Willbold, D., and Lange-Asschenfeldt, C. (2009). Transient reduction of spontaneous neuronal network activity by sublethal amyloid β (1–42) peptide concentrations. *Journal of neural transmission* 116**,** 351-355.

Gramowski, A., Juègelt, K., Weiss, D.G., and Gross, G.W. (2004). Substance identification by quantitative characterization of oscillatory activity in murine spinal cord networks on microelectrode arrays. *European Journal of Neuroscience* 19**,** 2815-2825.

Gramowski, A., Schiffmann, D., and Gross, G. (2000). Quantification of acute neurotoxic effects of trimethyltin using neuronal networks cultured on microelectrode arrays. *Neurotoxicology* 21**,** 331-342.

Gross, G. (1977). A new fixed-array multimicroelectrode system designed for long-term recording of long-term recording. *Neurosci Lett* 6**,** 101-105.

Gross, G.W., Rhoades, B.K., Azzazy, H.M., and Wu, M.-C. (1995). The use of neuronal networks on multielectrode arrays as biosensors. *Biosensors and Bioelectronics* 10**,** 553-567.

Gross, G.W., Williams, A.N., and Lucas, J.H. (1982). Recording of spontaneous activity with photoetched microelectrode surfaces from mouse spinal neurons in culture. *Journal of neuroscience methods* 5**,** 13-22.

Gullo, F., Manfredi, I., Lecchi, M., Casari, G., Wanke, E., and Becchetti, A. (2014). Multi-electrode array study of neuronal cultures expressing nicotinic β2-V287L subunits, linked to autosomal dominant nocturnal frontal lobe epilepsy. An in vitro model of spontaneous epilepsy. *Frontiers in neural circuits* 8.

Haberly, L.B., and Shepherd, G.M. (1973). Current-density analysis of summed evoked potentials in opossum prepyriform cortex. *Journal of Neurophysiology* 36**,** 789-802.

Hofmann, F., Feil, R., Kleppisch, T., and Schlossmann, J. (2006). Function of cGMP-dependent protein kinases as revealed by gene deletion. *Physiological reviews* 86**,** 1-23.

Humphrey, D.R., and Schmidt, E.M. (1990). "Extracellular single-unit recording methods," in *Neurophysiological techniques*. Springer), 1-64.

Jimbo, Y., Kawana, A., Parodi, P., and Torre, V. (2000). The dynamics of a neuronal culture of dissociated cortical neurons of neonatal rats. *Biological cybernetics* 83**,** 1-20.

Jimbo, Y., Tateno, T., and Robinson, H. (1999). Simultaneous induction of pathway-specific potentiation and depression in networks of cortical neurons. *Biophysical journal* 76**,** 670-678.

Kamioka, H. (1997). Planar electrode arrays for long-term measurement of neuronal firings in cultured cortical slices. *J. Cellular Engineering*.

Keefer, E.W., Gramowski, A., Stenger, D.A., Pancrazio, J.J., and Gross, G.W. (2001). Characterization of acute neurotoxic effects of trimethylolpropane phosphate via neuronal network biosensors. *Biosensors and Bioelectronics* 16**,** 513-525.

Le Feber, J., Stoyanova, I.I., and Chiappalone, M. (2014). Connectivity, excitability and activity patterns in neuronal networks. *Physical biology* 11**,** 036005.

Leondopulos, S.S., Boehler, M.D., Wheeler, B.C., and Brewer, G.J. (2012). Chronic stimulation of cultured neuronal networks boosts low-frequency oscillatory activity at theta and gamma with spikes phase-locked to gamma frequencies. *J Neural Eng* 9**,** 026015.

Maccione, A., Gandolfo, M., Massobrio, P., Novellino, A., Martinoia, S., and Chiappalone, M. (2009). A novel algorithm for precise identification of spikes in extracellularly recorded neuronal signals. *Journal of neuroscience methods* 177**,** 241-249.

Maccione, A., Garofalo, M., Nieus, T., Tedesco, M., Berdondini, L., and Martinoia, S. (2012). Multiscale functional connectivity estimation on low-density neuronal cultures recorded by high-density CMOS micro electrode arrays. *Journal of neuroscience methods* 207**,** 161-171.

Madhavan, R., Wagenaar, D.A., and Potter, S.M. (Year). "Multisite stimulation quiets bursts and enhances plasticity in cultured networks", in: *Society for Neuroscience Annual Meeting*), 45-56.

Maeda, E., Robinson, H., and Kawana, A. (1995). The mechanisms of generation and propagation of synchronized bursting in developing networks of cortical neurons. *The Journal of neuroscience* 15**,** 6834-6845.

Martinoia, S., Bonzano, L., Chiappalone, M., Tedesco, M., Marcoli, M., and Maura, G. (2005). In vitro cortical neuronal networks as a new high-sensitive system for biosensing applications. *Biosensors and Bioelectronics* 20**,** 2071-2078.

Meister, M., Pine, J., and Baylor, D. (1989). Multielectrode recording from the vertebrate retina. *Invest Ophthalmol Vis Sci* 30**,** 859-864.

Meister, M., Pine, J., and Baylor, D.A. (1994). Multi-neuronal signals from the retina: acquisition and analysis. *Journal of neuroscience methods* 51**,** 95-106.

Morefield, S., Keefer, E., Chapman, K., and Gross, G. (2000). Drug evaluations using neuronal networks cultured on microelectrode arrays. *Biosensors and bioelectronics* 15**,** 383-396.

Nam, Y., and Wheeler, B.C. (2011). In vitro microelectrode array technology and neural recordings.

Critical Reviews™ in Biomedical Engineering 39.
Novak, J.L., and Wheeler, B.C. (1988). Multisite hippocampal slice recording and stimulation using a 32 element microelectrode array. *Journal of neuroscience methods* 23**,** 149-159.
Novellino, A., Scelfo, B., Palosaari, T., Price, A., Sobanski, T., Shafer, T.J., Johnstone, A.F., Gross, G.W., Gramowski, A., and Schroeder, O. (2011). Development of micro-electrode array based tests for neurotoxicity: assessment of interlaboratory reproducibility with neuroactive chemicals. *Frontiers in neuroengineering* 4**,** 4.
Obien, M.E.J., Deligkaris, K., Bullmann, T., Bakkum, D.J., and Frey, U. (2015). Revealing neuronal function through microelectrode array recordings. *Frontiers in neuroscience* 8**,** 423.
Oka, H., Shimono, K., Ogawa, R., Sugihara, H., and Taketani, M. (1999). A new planar multielectrode array for extracellular recording: application to hippocampal acute slice. *Journal of neuroscience methods* 93**,** 61-67.
Parviz, M., and Gross, G. (2007). Quantification of zinc toxicity using neuronal networks on microelectrode arrays. *Neurotoxicology* 28**,** 520-531.
Pine, J. (1980). Recording action potentials from cultured neurons with extracellular microcircuit electrodes. *Journal of neuroscience methods* 2**,** 19-31.
Regehr, W.G., Pine, J., Cohan, C.S., Mischke, M.D., and Tank, D.W. (1989). Sealing cultured invertebrate neurons to embedded dish electrodes facilitates long-term stimulation and recording. *Journal of neuroscience methods* 30**,** 91-106.
Robinson, D.A. (1968). The electrical properties of metal microelectrodes. *Proceedings of the IEEE* 56**,** 1065-1071.
Shahaf, G., and Marom, S. (2001). Learning in networks of cortical neurons. *Journal of Neuroscience* 21**,** 8782-8788.
Soussou, W., Gholmieh, G., Han, M., Ahuja, A., Song, D., Hsiao, M.-C., Wang, Z., Tanguay, A.R., and Berger, T.W. (2006). "Mapping spatio-temporal electrophysiological activity in hippocampal slices with conformal planar multi-electrode arrays," in *Advances in Network Electrophysiology*. Springer), 127-152.
Streit, J. (1993). Regular oscillations of synaptic activity in spinal networks in vitro. *Journal of Neurophysiology* 70**,** 871-878.
Stuart, G.J., and Sakmann, B. (1994). Active propagation of somatic action potentials into neocortical pyramidal cell dendrites. *Nature* 367**,** 69.
Thiebaud, P., De Rooij, N., Koudelka-Hep, M., and Stoppini, L. (1997). Microelectrode arrays for electrophysiological monitoring of hippocampal organotypic slice cultures. *IEEE Transactions on biomedical engineering* 44**,** 1159-1163.
Thomas Jr, C., Springer, P., Loeb, G., Berwald-Netter, Y., and Okun, L. (1972). A miniature microelectrode array to monitor the bioelectric activity of cultured cells. *Experimental cell research* 74**,** 61-66.
Turnbull, L., Dian, E., and Gross, G. (2005). The string method of burst identification in neuronal spike trains. *Journal of neuroscience methods* 145**,** 23-35.
Vassallo, A., Chiappalone, M., Lopes, R.D.C., Scelfo, B., Novellino, A., Defranchi, E., Palosaari, T., Weisschu, T., Ramirez, T., and Martinoia, S. (2017). A multi-laboratory evaluation of microelectrode array-based measurements of neural network activity for acute neurotoxicity testing. *Neurotoxicology* 60**,** 280-292.
Vato, A., Bonzano, L., Chiappalone, M., Cicero, S., Morabito, F., Novellino, A., and Stillo, G. (2004). Spike manager: a new tool for spontaneous and evoked neuronal networks activity characterization. *Neurocomputing* 58**,** 1153-1161.
Wagenaar, D., Demarse, T., Potter, S., and Pine, J. (2001). Development of complex activity patterns in cortical networks cultured on microelectrode arrays. *Ann. Mtg. Soc. Neurosci*.
Welsh, D.K., Logothetis, D.E., Meister, M., and Reppert, S.M. (1995). Individual neurons dissociated from rat suprachiasmatic nucleus express independently phased circadian firing rhythms. *Neuron* 14**,** 697-706.

Wheeler, B.C., and Novak, J.L. (1986). Current source density estimation using microelectrode array data from the hippocampal slice preparation. *IEEE transactions on biomedical engineering*, 1204-1212.

Whitson, J., Kubota, D., Shimono, K., Jia, Y., and Taketani, M. (2006). "Multi-electrode arrays: enhancing traditional methods and enabling network physiology," in *Advances in Network Electrophysiology*. Springer), 38-68.

Xia, Y., Gopal, K.V., and Gross, G.W. (2003). Differential acute effects of fluoxetine on frontal and auditory cortex networks in vitro. *Brain research* 973, 151-160.

Part II

Sleep-related activity in neuronal cultures in physiological and pathological conditions

Chapter 3

Introduction

Sleep is a universal phenomenon that is classically defined as a reversible state of reduced responsiveness to external stimuli and relative inactivity accompanied by a loss of consciousness (Rasch and Born, 2013). The research conducted so far strongly supports the finding that sleep is essential for the brain.

Over the last few years, it has been proposed that electrophysiological markers for sleep cycles can also be derived from *in vitro* neuronal networks similar to those present *in vivo* (Sengupta et al., 2011;Hinard et al., 2012).

As mentioned earlier (see Chapter 1, paragraph 1.1), cortical cultures coupled to MEAs represent a simplified and easily accessible *in vitro* model that can be used to study the principles of neurodynamics and neural coding (Marom and Shahaf, 2002;Chiappalone et al., 2008) ; they also represent a valid method for reducing animal experimentation.

Since neuronal assemblies plated on MEAs present synchronized, low frequency firing patterns similar to *in vivo* slow wave oscillations (Hinard et al., 2012), we used these preparations to study sleep properties. However, neuronal cultures lack the characteristic high-frequency waves of wakefulness, but it is possible to modulate their spontaneous firing patterns through the administration of specific neurotransmitters to suppress the sleep features (Corner, 2008;Corner, 2010;Saberi-Moghadam et al., 2018){Corner, 2013 #331).

In this introductory chapter, we will briefly describe the following: (i) the major patterns that characterize sleep architecture, which are discriminated by electroencephalogram (EEG) combined with electromyogram (EEG) in vivo (see paragraph 3.1); (ii) the main processes that are involved in regulation of the sleep-wake cycle (see paragraph 3.2); (iii) the state of the art regarding the study of sleep features *in vitro* (see paragraph 3.3); (iv) possible modulation strategies that could be used to modify sleep properties (see paragraph 3.4).

3.1 Measuring sleep-wake waves in humans and in animal models

Sleep is characterized by the alternation of two different physiological and behavioral states, each of which possesses distinct electrophysiological features that alternate cyclically. These two states are referred to as non-rapid eye movement (NREM) sleep and rapid eye movement (REM) sleep (**Figure**

3.1).

The stages of sleep in humans are as follows:

- **NREM sleep**: also called slow-wave sleep (SWS) is divided into 4 stages, corresponding to increasing depth of sleep. In human nocturnal sleep, non-REM sleep is predominant during the early part of the sleep period and decreases in intensity and duration across the sleep period (Rasch and Born, 2013). NREM sleep constitutes about approximately 80% of the total time spent in sleep and is characterized by the regular occurrence of local and global slow cortical oscillations (Vyazovskiy and Harris, 2013). The characteristic oscillatory waveforms of non-REM sleep include sleep spindles (sigma frequency, 12–15 Hz), the K-complex waveform, (0–1 Hz) and high-amplitude slow-wave activity (SWA at approximately 0.5–4.5 Hz) (Steriade, 2001).

  SWA is usually used as a marker of non-REM sleep intensity and to determine sleep pressure (Tononi (Cirelli et al., 2006;Vyazovskiy and Harris, 2013). For instance, the longer a subject has been awake, the higher is the spectral power in the slow wave range of the EEG in subsequent sleep; the power in this range decreases during the course of sleep (Achermann and Borbély, 2003). Moreover, it has been proposed that SWA is mainly involved in the restorative processes of sleep (Cirelli et al., 2006;Vyazovskiy and Harris, 2013).

1. **REM sleep**: also known as paradoxical sleep, constitutes approximately 20% of the total time spent in sleep. In human nocturnal sleep, REM sleep becomes more intense and extensive towards the end of the sleep period (Rasch and Born, 2013). REM sleep is defined by the presence of desynchronized (low-voltage, high-frequency) brain wake-like, tonically activated EEG. There are electrophysiological similarities between awaking states and REM sleep (also defined as “paradoxical sleep”); these states include additional features (e.g., muscle atonia and metabolic/thermoregulatory alterations) that allow their distinction. During REM sleep, the EEG pattern (**Figure 3.1**) is characterized by theta activity (5-8 Hz) and slow alpha activity, which arise mostly from the hippocampus.

- **Wakefulness**: During the awake state, neurons in the cerebral cortex fire irregularly, and EEG recording displays low-amplitude, high-frequency fluctuations with consequent activation of muscle tone (Brown et al., 2012).

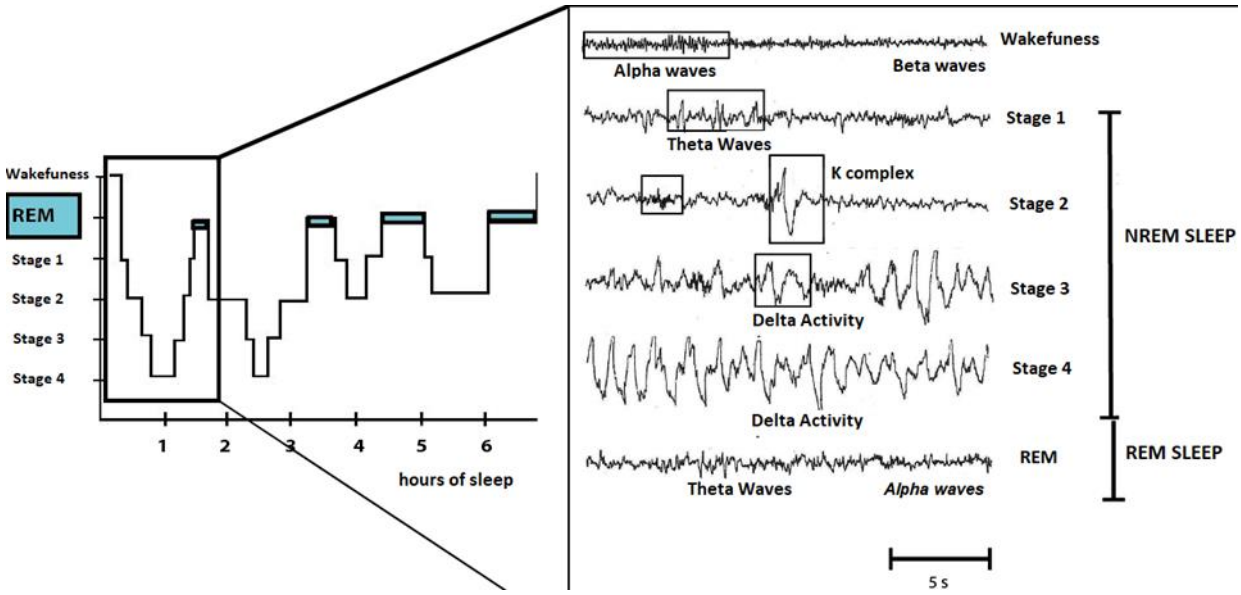

Figure 3.1 EEG signal capture different sleep stages during NREM and REM sleep in human.

Despite our knowledge of the different stages of the sleep-wake cycle, the function or functions of sleep are still unresolved. However, significant progress has been made in understanding the brain mechanisms that control sleep and wakefulness thanks to the use of animal models. Historically, the use of animals in the study of sleep disorders has been extremely useful in discovering the underlying mechanisms of sleep disorders such as narcolepsy (Chemelli et al., 1999;Lin et al., 1999). Animals represent an emerging model that can be used in studies of the physiology of sleep, in identification and validation of the causes and mechanisms of sleep disorders, and in the development and preliminary testing of new therapeutic approaches.

While sleep architecture is conserved across species, humans and rodents display several differences in sleep architecture due to the differences in the complexity of their central nervous systems. First, the organization of the sleep-wake cycle is opposite in phase in rodents and humans. Specifically, rodents are nocturnal animals; they are awake during the dark phase and asleep during the light phase. Moreover, humans have monophasic sleep, meaning that sleep is usually taken in one session during a 24-h period (i.e., during the night). Conversely, rodent sleep is polyphasic and relatively fragmented (Paterson et al., 2011;Toth and Bhargava, 2013). Lastly, NREM sleep in humans is conventionally divided into 3 stages, whereas in rodents this distinction is not used (Rasch and Born, 2013).

However, there are common shared traits among species, such as specific properties associated with the frequency spectrum of distinct sleep states (Lo et al., 2004;Phillips et al., 2010) (Brown et al., 2012). In particular, EEG activity during sleep is characterized by two different patterns, namely, slow oscillations in the delta frequency range (1-4 Hz) during deep sleep (NREM) and rapid, low-voltage waves such as beta (11-30 Hz) and gamma (30-120 Hz) during wakefulness and REM sleep.

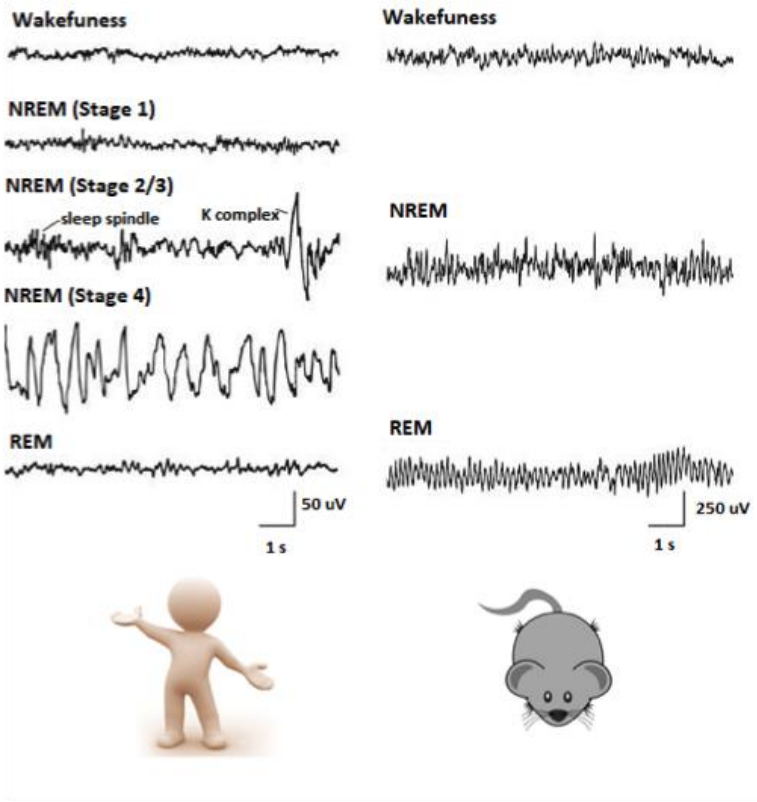

Figure 3.2 Comparison of EEGs in humans and rodents. In rodents, NREM sleep is usually not parsed into separate stages.(adapted from Brown et al*., 2012)*

3.2 Regulation of the sleep-wake cycle: circadian rhythm & sleep-wake homeostasis

Sleep is regulated by two separate but interacting processes, namely, an intrinsic sleep-independent circadian process (Process C) and a sleep-dependent process (Process S) (Borbely, 1982).

The circadian process is a self-sustaining cycle of approximately 24 hours that is mainly related to cell-autonomous mechanisms. Its clock governs the daily cycle of many biological activities such as the control of body temperature and hormone secretion (Stokkan et al., 2001;Reppert and Weaver, 2002). One of the first observations of the existence of circadian rhythmicity was reported by Jacques De Mairan in 1729 (de Mairan, 1729); he observed that the opening and closing of the leaves of plants followed a circadian periodicity of 24 hours even under dark conditions at a controlled temperature. Therefore, he deduced that an internal time-measuring mechanism that regulates that phenomenon must exist, i.e., an endogenous biological clock. The modern-day study of circadian rhythms began in the 1950s with the work of Colin Pittendrigh, who found that the timing of eclosion (emergence of adult flies from the larval case) in *Drosophila* was maintained under conditions of constant darkness (Pittendrigh, 1954). Another pioneer in the study of circadian rhythms, Jürgen Aschoff, demonstrated

circadian rhythms in human activity by placing subjects in a bunker in constant darkness (Aschoff, 1965). The biological rhythm maintained under conditions of constant temperature and light is called *free-running* (Edmunds Jr, 1983). The existence and conservation of *free-running* circadian rhythmicity is due to the presence of a highly specialized endogenous mechanism that is able to regenerate for 24 hours and is called the circadian *biological clock*. It resides in the suprachiasmatic nucleus (SCN) of the hypothalamus, a master pacemaker that regulates circadian rhythms in the brain and body (Franken et al., 2001). The biological clock is designed for the central coordination of the rhythmic cadence of some biological functions at the organism level, as they allow both individual cells and the organism to synchronize in relation to the day / night period and environmental variations.

A circadian biological system is generally made up of the following three fundamental components:

1. A signal from the environment (input) such as light/dark alternation
2. The biological clock (pacemaker) located inside each cell
3. that cause changes in cell behavior related to the periodicity of the oscillator (output) such as hormone secretion, daily temperature variation and food assumption.

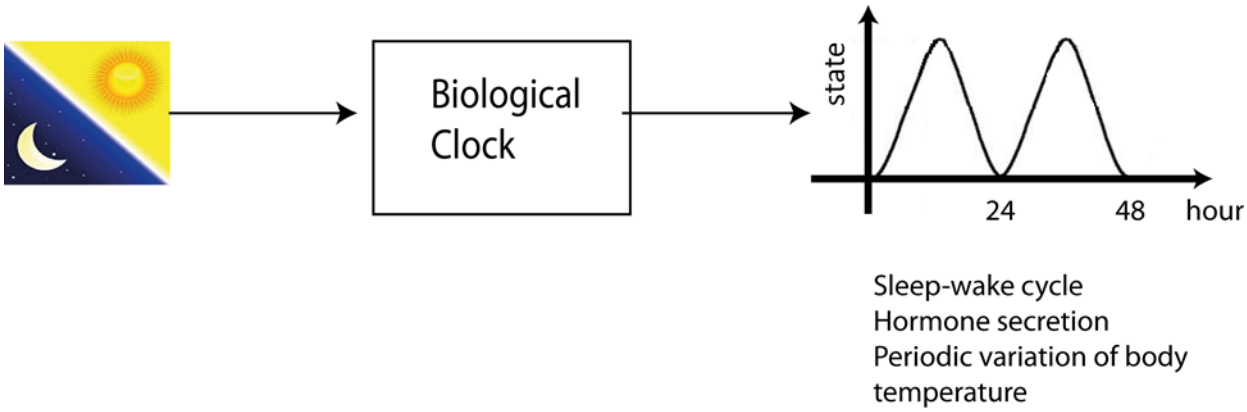

Figure 33 Scheme of regulation of the circadian rhythm.

In mammals, the input and the pacemaker are located in different structures; the light stimulus (input) is transmitted to the circadian clock, which is located in the suprachiasmatic nucleus (SCN), through the retino-hypothalamic tract.

The SCN was identified as the circadian pacemaker in mammals; it is responsible for the coordination and synchronization of oscillators located in other areas of the brain and peripheral organs. Lesions of the SCN in hamsters cause changes in the regulation of the sleep-wake cycle; in particular, surgical removal of more than 75% of the SCN results in loss of the circadian rhythmicity of locomotion, food intake, body temperature and the secretion of some hormones such as melatonin without any recovery in time (Ralph and Menaker, 1988).

The circadian system is made up of a multiplicity of self-driven oscillators, called *Zeitebergs,* which are interconnected and can in turn be synchronized by environmental factors. To understand how the biological circadian clocks are able to regenerate and maintain their periodicity of 24 h, it is necessary to identify the molecular mechanism that allows the system to oscillate; the cells require a complex network of proteins and interacting genes to regulate the internal clock responsible for the control of metabolism, cell division, hormone production and the sleep-wake cycle.

Within each cell is a molecular circadian clock mechanism that acts as a timekeeper that coordinates cellular function and animal physiology with the external environment. The regulatory system consists of a transcription-transduction network with a feedback loop that has a duration of 24 hours. The core of this self-sustained molecular oscillation consists of positive and negative elements.

- Positive elements:
  1. CLOCK (Circadian locomotor output cycle kaput)
  2. BMAL1 (Brain and muscle Arnt-like protein 1)
- Negative elements:
  1. CRY (Cryptochrome)
  2. PER (Period)

The positive elements bind to a unique protein heterodimer, CLOCK:BMAL1, which is characterized by the presence of a specific region for the binding of the DNA at the level of the E box sequence.

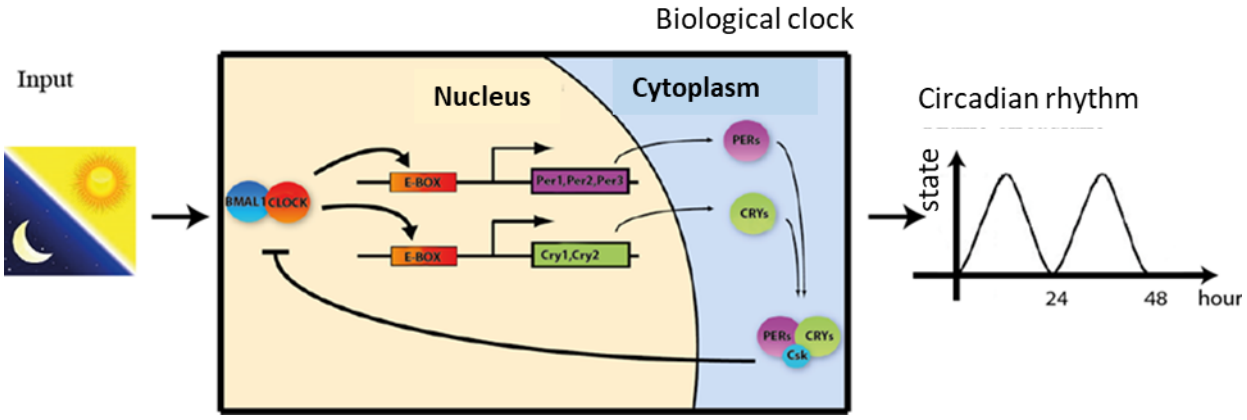

Figure 3.4 Regulatory system of a transcription-transduction network with a feedback loop with a duration of 24 hours..

In the nucleus, the CLOCK:BMAL1 heterodimer initiates the transcription of target genes containing E-box sequences, including PERIOD and CRYPTOCHROME and the relative proteins Per1, Per2, Per3 and Cry1, Cry2. Protein synthesis leads to an accumulation of CRY in the cytoplasm and to the formation of another protein heterodimer, CRY:PER. The negative feedback is provided by PER:CRY heterodimers, which translocate back to the nucleus where they repress their own transcription by acting on CLOCK:BMAL1 heterodimers. After this inhibition, CRY:PER is deactivated by

specialized eukaryotic proteins of the Fbox family (Fbxl3) through ubiquitination. This permits the initiation of a new ~24-hour cycle and contributes significantly to the precision of the mammalian clock.

The importance of these core clock genes in circadian rhythm generation has been demonstrated by constructing mice that carry targeted disruptions in one or a combination of these genes (Lowrey and Takahashi, 2011).

In addition to circadian control, sleep is also regulated by a homeostatic process (Cirelli et al., 2006;Tononi and Cirelli, 2006;2014). The main postulate of sleep homeostasis is ‘‘*the longer we are active (and, perhaps, the more we are active), the deeper our subsequent sleep”* (Daan et al., 1984). In other words, sleep need (or ‘‘sleep pressure’’) increases in proportion to the preceding duration of wakefulness and then dissipates during the ensuing sleep in proportion to sleep duration and intensity. In mammals and birds, sleep SWA is high in early sleep and decreases progressively during sleep, reaching low levels several hours later (Tobler and Borbely, 1986). It can be modeled by a mathematical function that increases during wakefulness and decreases during sleep, thereby describing the pressure for sleep across a circadian cycle (Borbely, 1982;Daan et al., 1984;Franken et al., 2001;Mölle et al., 2004;Marshall et al., 2006) (**Figure 3.5**).

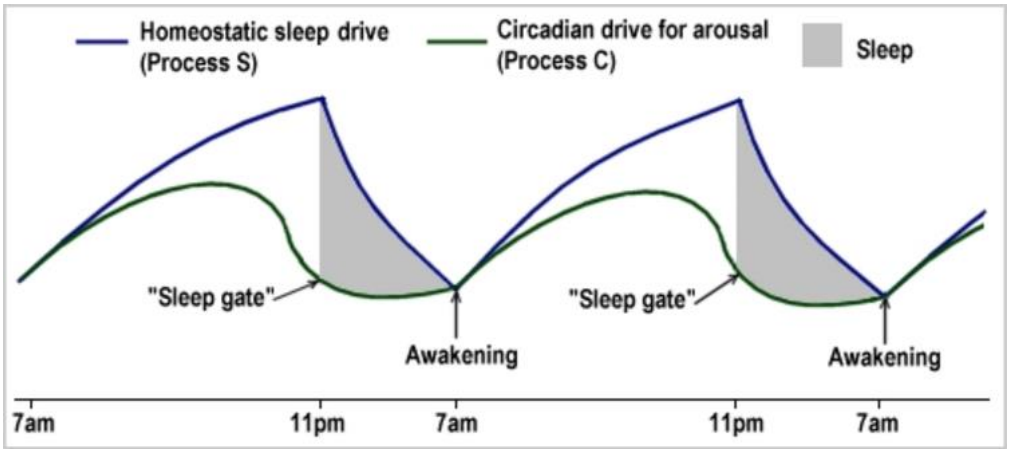

Figure 3.5 Homeostatic and circadian regulation of the sleep-wake cycle (Borbely, 1982)

A highly reliable index of the homeostatic process is provided by the amplitude and prevalence of delta (1-4-Hz) oscillations in the electroencephalogram (EEG) of nonrapid eye movement (NREM) sleep. Delta power is high at sleep onset and decreases during wakefulness. Acute sleep reduction or deprivation normally causes a homeostatic response during the next sleep opportunity; this response is characterized by an increase in NREM sleep, which is also referred to as slow-wave sleep (SWS), during which the EEG reveals slow-wave activity (SWA; 0.75-4.5 Hz). EEG delta power during NREM sleep has been shown to play a critical role in learning-induced plasticity (Mölle et al., 2004;Huber et al., 2006;Marshall et al., 2006;Tononi and Cirelli, 2014)ref.

Waking and sleep are associated with systematic changes in the expression and/or release of a variety of molecules that are directly or indirectly involved in synaptic plasticity as well as in many other essential cellular functions. Sleep need, as indexed by the EEG delta power, is under genetic control (Franken et al., 2001), explaining the inter-individual variation in vulnerability to sleep loss in human subjects (Van Dongen et al., 2004;Tucker et al., 2007). Among the classes of genes affected by sleep deprivation it was demonstrated that in the brain, Homer1a expression best reflects the response to sleep loss(Maret et al., 2007;Diering et al., 2017).

Many studies have demonstrated a strong interplay between circadian and homeostatic components of sleep (Franken et al., 2001). Knocking out one or more of the main clock genes not only changes or disables the circadian clock but also modifies sleep homeostatic markers in animal models. Interestingly, among the core clock genes, PER2 has been shown to play a dual role in that it affects both the cellular clock machinery and the homeostatic control of sleep. Many mouse studies have demonstrated that Per genes control slow wave activity following sleep loss (Kopp et al., 2002;Shiromani et al., 2004). Moreover, new molecular targets and epigenetic regulatory mechanisms are emerging as novel players in the control of sleep and its homeostasis (Tinarelli et al., 2014). In the following chapter, we investigate in more detail recent findings obtained during the study of sleep-like features *in vitro*.

3.3 Sleep features in primary cultures

The investigation of a neural network's dynamic properties during sleep states is difficult when studying *in vivo* experimental systems due to the complexity of the mammalian brain. The complexity of defining the minimal network size required for a sleep-like state has limited our understanding of sleep regulation and sleep function (Krueger et al., 2008). Moreover, sleep has always been thought of as a global feature; for that reason, humans or whole animal studies have been preferred.

Recent clinical evidence suggests that sleep can be a property of something less than the whole brain. In 2005, Mahowald and Schenck (Mahowald and Schenck, 2005) described patients with parasomnias (e.g. sleep walking) who simultaneously displayed features of wakefulness (evidenced by their ability to negotiate around objects) and sleep (indicated by their lack of awareness of their actions). A few days after the occurrence of survivable stroke or other acute damage to the brain, sleep re-emerges; despite millions of such cases, no instance of complete insomnia has been observed. This finding suggests that sleep is a robust fundamental self-organizing property of any surviving group of neurons (Krueger et al., 2008).

The EEG oscillations that occur during sleep and arousal are generated in the thalamus and cerebral

cortex, two regions that are linked by reciprocal connections. The thalamus is the major gateway for the flow of information to the cerebral cortex and the first station at which external signals can be blocked by synaptic inhibition during sleep. This mechanism contributes to the shift that the brain undergoes as it changes from a state of arousal in which it is open to signals from the outside to the closed state of sleep (Steriade et al., 1993). During the NREM phase, thalamic and cortical neurons display burst-pause action potential firing patterns that last 500 ms and are separated by 500 ms of silence. When an animal is going to sleep, these burst patterns synchronize with each other and lead to a slow-frequency component of the EEG signal (Vyazovskiy et al., 2011).

A recent study in cats demonstrated that cortical islands prepared surgically in such a way that they retain their blood flow but not their thalamic input showed local field potentials over periods of 10-20 minutes through episodes with high-amplitude EEG delta waves (Kristiansen and Courtois, 1949). Data from Steriade and colleagues indicated that there is an EEG slow-wave component in the delta frequency range (0.5–1.5 Hz) that originates locally in the cortex (Steriade et al. 2003). These data suggested that sleep, or at least correlates of sleep such as EEG delta wave power, is a regional phenomenon of the brain

Moreover, Pigarev et al. performed experiments with monkeys in transition between sleep and wakefulness and showed that some neurons in the visual cortex display sleep firing patterns even when the animal is still performing a visual discrimination task. Although the animal is awake, the cellular process characteristic of NREM sleep is present, suggesting that there are local islands of sleep(Pigarev et al., 1997).

Repeated single-whisker stimulation and analysis of evoked response potential patterns in the cortical columns of rats demonstrate that it is possible to distinguish between awake-like and sleep-like states (Rector et al., 2005). The sleep-like state is characterized by evoked response potentials of greater magnitude than the evoked potentials that are observed during wakefulness (Timofeev et al., 2001). Although most columns display an evoked response pattern that is consistent with the state of the animal (lower during wakefulness and high during sleep episodes), some columns are in the opposite state, suggesting that sleep is a property of local neuronal networks.

In vitro cultures are simple in comparison to whole brains, yet neuronal cultures exhibit electrical properties that are similar to those used to characterize sleep *in vivo* (Sengupta et al., 2011;Hinard et al., 2012). These properties spontaneously develop and emerge as networks mature and are influenced by stimulation that similarly affects the state of the whole animal (Jewett et al., 2015). Indeed, neuronal assemblies plated on MEA show spontaneously synchronized, low frequency firing patterns (Figure 3.6) (Van Pelt et al., 2004;Chiappalone et al., 2007;Corner, 2008), resembling the slow wave

oscillations that characterize NREM sleep in vivo (Steriade et al., 1993;Rector et al., 2005). These network-wide bursts (i.e. synchronized bursting activity presented simultaneously on several channels) are less frequent and more stereotyped than those observed in the intact brain, an observation that might be expected given the smaller size and lower connection density of these networks as well as the lack of reentrant pathways (Timofeev et al., 2000;Timofeev et al., 2001;Chauvette et al., 2010;Constantinople and Bruno, 2011;Harris and Thiele, 2011).

While the forms of synchrony observed *in vitro* differ in many respects from those associated with low arousal levels in the intact brain, their underlying biophysical mechanisms share important similarities. Current studies *in vivo* (Constantinople and Bruno, 2011;Harris and Thiele, 2011) and *in vitro* (Robinson et al., 1993;Maeda et al., 1995a;Eytan and Marom, 2006;Cohen et al., 2008;Cohen and Segal, 2011;Orlandi et al., 2013) as well as modeling studies (Timofeev et al., 2000;Bazhenov et al., 2002;Hill and Tononi, 2005;Holcman and Tsodyks, 2006), suggest that these forms of synchrony are not imposed by external circuitry, pacemaker cells or global inhibition, but probably depend on the interplay of spontaneous synaptic activity, refractoriness and network-wide synaptic depression (Harris and Thiele, 2011).

Unfortunately, the lack of an awake state counterpart has limited the investigation of the main physiological aspects of sleep. To overcome this problem, a combination of chemical and electrical stimulation was recently proposed (Hinard et al., 2012;Krueger et al., 2013).

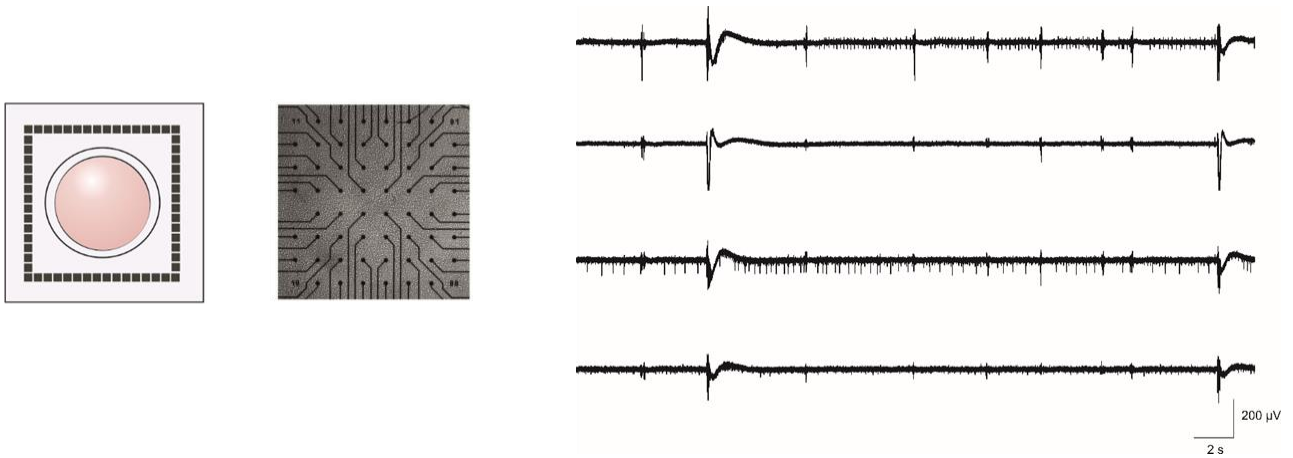

Figure 3.6 Rat cortical cultures over MEAs at DIV 30 displays low-frequency firing patterns similar to those observed in sleeping animals.

Indeed, with appropriate stimulation, such cultures can transition into a more “wake-like state” or “deeper sleep-like state” depending upon the specific stimuli applied. Low-frequency electrical stimulation (0.05-0.2 Hz) of such cultures recruits more active channels to participate in the network-burst state, enhancing the spontaneous activity and suggesting a deeper sleep-like state.

In contrast, higher-frequency stimulation (4-10 Hz) induces more random firing with fewer bursts

compared to the basal condition (Wagenaar et al., 2005;Chiappalone et al., 2007;Krueger et al., 2013). In 2012 Tafti and colleagues (Hinard et al., 2012) showed that the default sleep pattern could be transformed into a tonic firing pattern similar to that observed in wakefulness by stimulating cortical cultures with a cocktail of excitatory neurotransmitters (hereinafter called "CCK" and including monoaminergic, glutamatergic, cholinergic, and orexinergic neurotransmitters or agonists). Moreover, they showed that the stimulated cultures exhibited a transcriptome similar to that of cortical cells harvested from sleep-deprived mice. The expression of immediately early genes (IEGs) was similarly affected in *vitro* and in *vivo* and indicated a sleep-deprived state. *Homer 1a, Arc, Dbp, Per,* and *Fos* were all overexpressed after administration of the cocktail *in vitro* and after sleep deprivation *in vivo*.

Oxygen consumption was monitored *in vivo* in a calorimetric chamber over a 24-hour period. Oxygen consumption *in vivo* was 40% higher during wakefulness compared to the sleep period. Cortical cultures stimulated with the cocktail showed a 30-40% increase in the oxygen consumption rate (OCR), indicating a sustained metabolic increase. Moreover, the investigators found that the same metabolic pathways undergo similar changes *in vitro* and in living animals

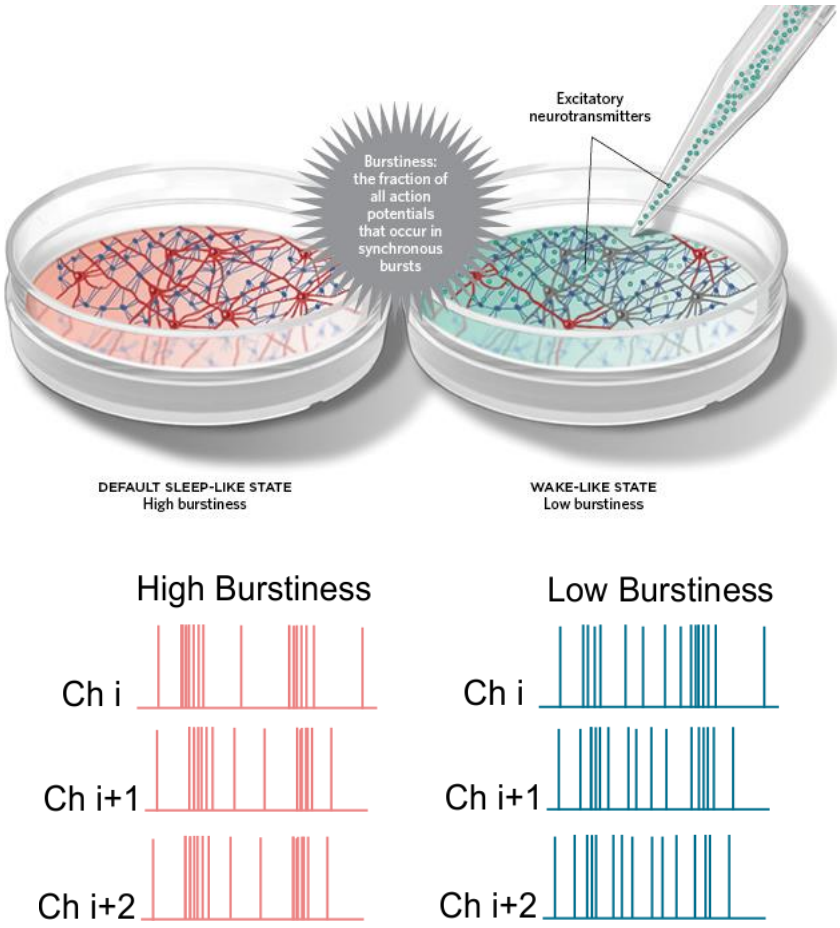

Figure 3.7 Scheme of cortical cultures under a default sleep-like state and upon treatment with a cocktail of excitatory neurotransmitters (from Hinard 2012).

Recently, Kruger's group characterized sleep-like states in cultured neurons and glia during development by stimulating the cultures electrically with the addition of tumor necrosis factor alpha (TNF) (Jewett et al., 2015). They showed that TNF enhanced the synchronicity among networks and the amplitude of the slow oscillatory activity (SWA), suggesting the induction of a deeper sleep-like state similar to the state observed *in vivo* during NREM sleep (Krueger et al., 2008;Jewett et al., 2015). Electrical stimulation reversed the deeper TNF sleep-like state and induced a sleep-like state with a more irregular firing pattern and lower SWA power. Recording of the stimulated cultures after 24 hours showed a rebound of the sleep-like state, suggesting network homeostasis *in vitro*. Recovery of the sleep state depended on the stimulus pattern applied 24 hours earlier, suggesting that network dynamics, connectivity and excitability *in vitro* are dependent upon past patterns of activity. These findings are consistent with the interpretation that the cultured cells can achieve functional plasticity (Maeda et al., 1995a;Jimbo et al., 1999;Tateno and Jimbo, 1999;Shahaf and Marom, 2001;Chao et al., 2007).

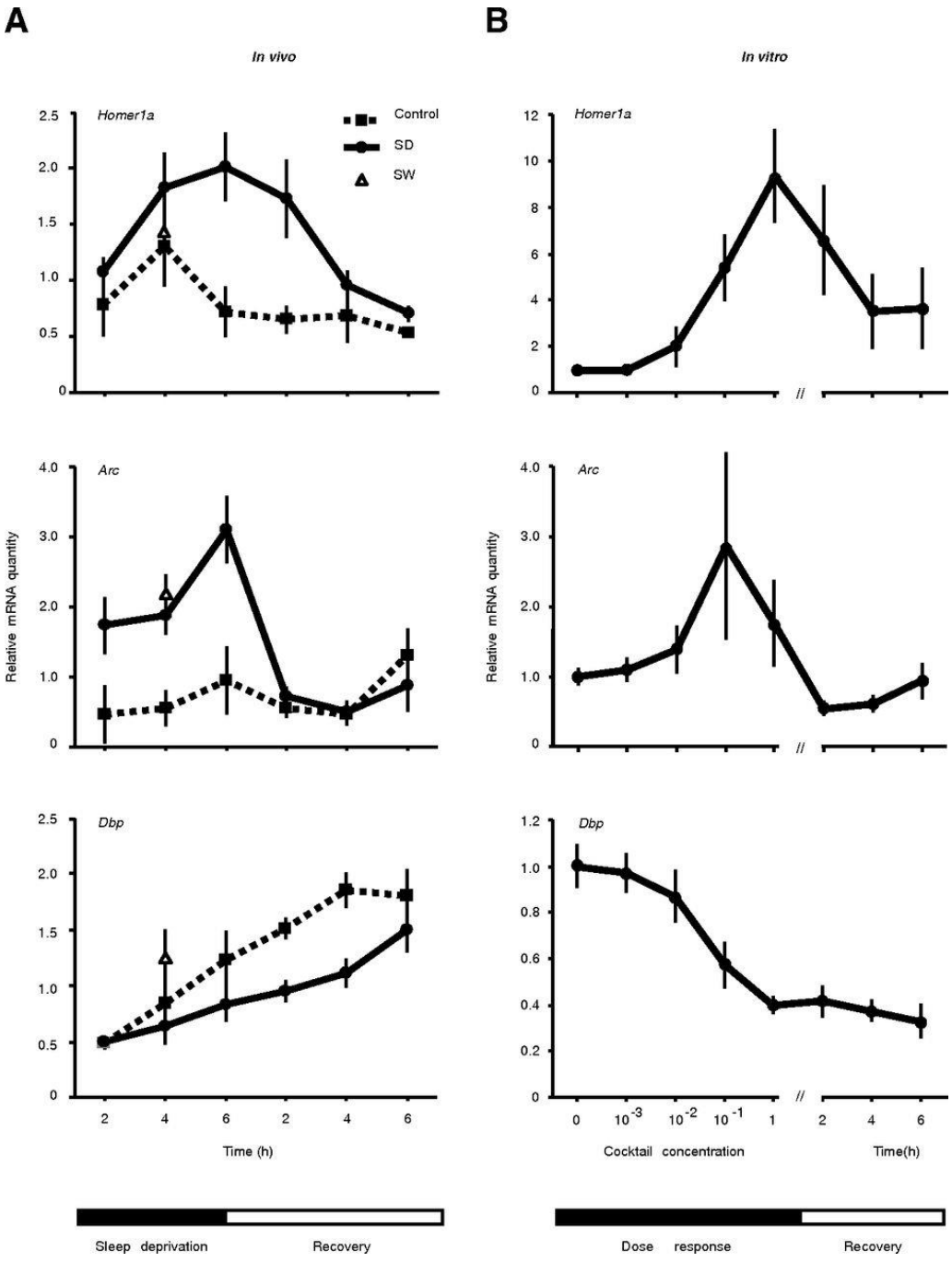

Figure 3.8 Comparison of the time course of gene expression in vivo (A) and in vitro (B). The time course of gene expression in sleep-deprived (SD) mice (n = 4 for each time point) was followed in vivo for 2, 4, and 6 h. Undisturbed home-cage controls were also assessed at the same time points (Control). Homer1a is overexpressed in proportion to the time the animals were kept awake and decreases slowly during the recovery period, while Arc expression shows rapid recovery after 6 h of sleep deprivation. Dbp expression is decreased by sleep deprivation, and the recovery is slow. To show the similarity in the time course of gene expression, primary cortical cultures (n = 3 measured in triplicates) were stimulated by the application of the indicated concentrations of our waking cocktail; cultured cells stimulated for 3 h with 1× cocktail were allowed 2, 4, or 6 h of recovery (right) (from Hinard 2012).

Following these results, M. Tafti's group investigated the behavior of the network 24 hours after cocktail stimulation, when the slow waves reappeared (Saberi-Moghadam et al., 2018). The goal of this work was to determine whether it is possible to observe homeostatic changes similar to those observed in living animals during sleep. They found that the interburst interval is decreased during

recovery, whereas the burst duration is increased (**Figure 3.9 b-c**). These findings suggest that higher homeostatic pressure *in vitro* results in an increased incidence of bursts (UP state) and a decreased interburst interval (DOWN state). The power spectral density at low frequencies was increased, as was the slope of the UP and DOWN states. The authors showed a dose-dependent effect during the recovery; stronger stimulation resulted in larger differences, similar to the manner in which longer wakefulness duration leads to larger sleep changes *in vivo*.

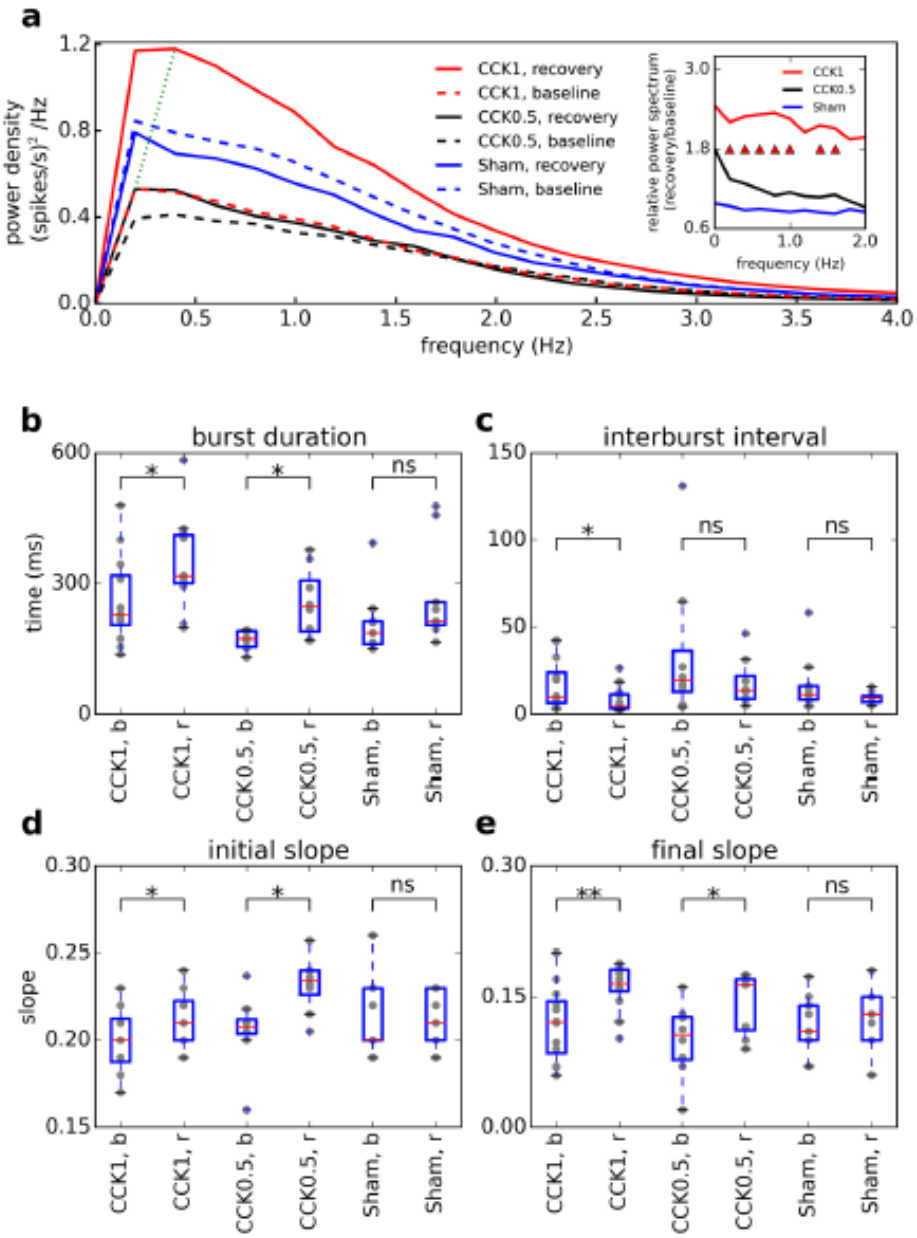

Figure 3.9 Spectral and burst properties of in vitro cortical networks at baseline and during recovery after neuromodulatory or sham stimulation. (a) Spectral power density of bursting activity of cultures during baseline (blue lines) and recovery (black lines) for 1 CCK (n = 12), 0.5 CCK (n = 8), and sham stimulation (n = 9). The inset indicates the relative changes in power densities during recovery (b) Burst duration (BD) is significantly longer and (c) the interburst interval (IBI) is shorter during recovery for 1 CCK and 0.5 CCK, while there is no change in sham-stimulated cultures. (d) Initial and (e) final slopes are significantly increased after 1 CCK and 0.5 CCK stimulation, while no change

*is observed after sham stimulation. Each dot represents a single culture. Bb: baseline; r: recovery; ns: nonsignificant. *p < 0.05, **p < 0.01; paired t-test on relative values (to the sham condition). (Saberi-Moghadam et al., 2018).*

The foregoing results show that the default slow oscillation could be regulated by homeostatic processes; however, whether the homeostatic mechanisms are cell-autonomous or properties of networks remains controversial (Slomowitz et al., 2015;Hengen et al., 2016).

The *in vitro* studies strongly favor the network hypothesis; high-density MEAs based on CMOS technology (with 4096 microelectrodes) revealed a high level of random firing activity, while the overall behavior of the network was driven by synchronized bursts(Lonardoni et al., 2015).Excitatory cortical neurons are known to form privileged synaptic connections to form clusters (Perin et al., 2011). Using a simulation network, Tafti and coworkers showed that as a cell culture matures, connections are formed between neurons and stronger connections are maintained by synaptic plasticity. Prolonged chemical stimulation for 24 h forces neurons to discharge at higher rates and may affect the structural connectivity between neurons (Saberi-Moghadam et al., 2018). This leads to the formation of new clusters or to the collapse of existing clusters and results in modification of the oscillatory activity with respect to the basal condition before stimulation.

Taken together, the current results are consistent with theories that propose that sleep is an emergent property of small neuronal-glial networks (KRUEGER and OBÄL JR, 1993;Benington and Heller, 1995)& Heller, 1995; Mahowald (Mahowald and Schenck, 2005;Cirelli et al., 2006;Krueger et al., 2008;Krueger et al., 2013).

Due to its simplicity and its ability to control the intensity of the emergent state properties, the *in vitro* system offers a novel experimental platform for study of the genetic, molecular, and electrical causality mechanisms of sleep states (Kruger 2013).

The "*CCK*" cocktails used by Tafti M. in the works described above (Hinard et al., 2012;Saberi-Moghadam et al., 2018) contained more than ten excitatory neurotransmitters; thus, it is difficult to know whether a specific neurotransmitter is responsible for the "awake" state. Recently, this group assessed the individual contribution of each neurotransmitter in their original waking cocktail by stimulating cortical cultures with each neurotransmitter and analyzing the expression of the three major candidate genes *Homer 1a, Dbp*, and *Arc* (Mikhail et al., 2017). As demonstrated in microarray experiments in mice and rats, during wakefulness the expression of *Arc, Bdnf, Egr*, and *Homer 1a* increases, whereas *Cirbp* and *Dbp* expression decreases (Cirelli et al., 2004;Terao et al., 2006;Mackiewicz et al., 2007;Maret et al., 2007). Conversely, during REM sleep and after sleep deprivation the expression of all of the above genes is upregulated (Cirelli et al., 2006;Mikhail et al., 2017). It was found that AMPA, norepinephrine (NE), histamine, dopamine (DA), and serotonin [5-hydroxytryptamine (5-HT)] alone had inducing effects similar to that of the cocktail on *Homer 1a*

expression (**Figure 3.10B**). A similar pattern of expression of *Arc* was also observed (**Figure 3.10A**).

Unlike the above IEGs, *Dbp* showed decreased expression in comparison to the control experiments only for the cocktail and for norepinephrine (Ne) (**Figure 3.10C**). The investigators postulated that NE alone could reproduce the effect of the complete cocktail on the expression of the selected candidate genes, confirming the essential role of NE in wakefulness and associated neuronal plasticity (Shepard et al., 2015). Noradrenergic neurons are activated during waking, decrease their firing rate during slow wave sleep, and become silent during rapid eye movement (REM) sleep (Hobson et al., 1975;Aston-Jones and Bloom, 1981). Therefore, the use of CCK cocktails in cultures is limited to inducing a state similar to wakefulness and not similar to the REM state.

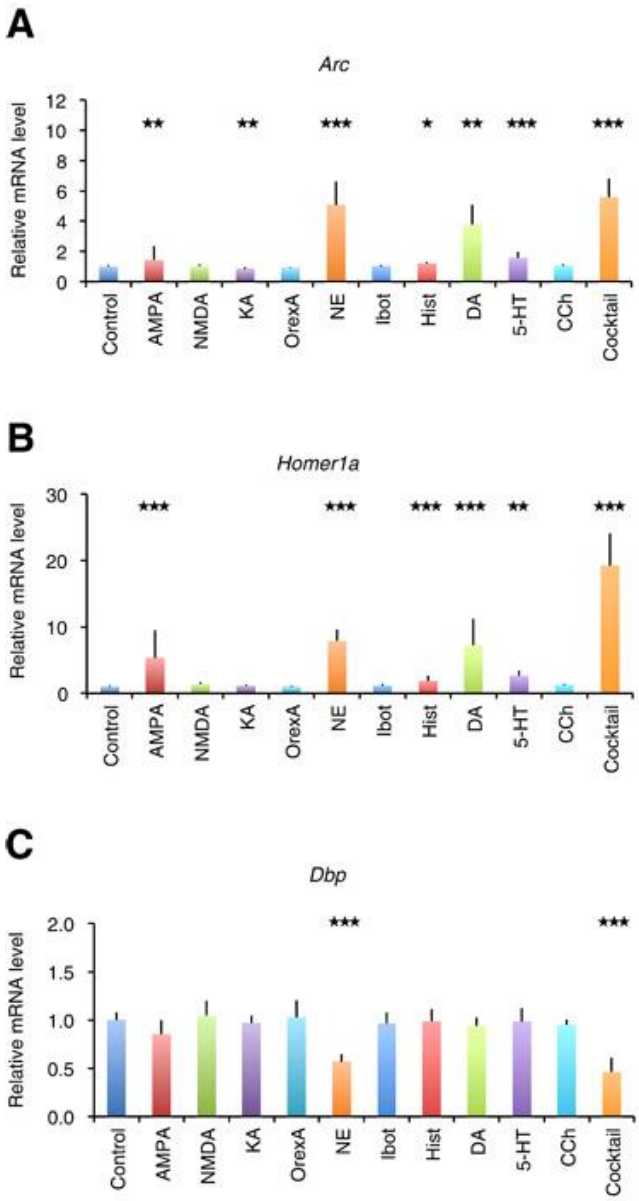

Figure 3.10 Candidate gene expression in cultured neurons after stimulation with individual constituents of the waking cocktail. (A to C) Three dishes from three independent cultures were stimulated for 3 hours with the neuromodulators

*NMDA, AMPA, kainic acid (KA), ibotenic acid (Ibot), serotonin (5-HT), histamine (Hist), DA or NE (each 1 mM), carbachol (CCh, 10 mM), or orexin A (OrexA, 0.01 mM). The data represent the mean normalized mRNA expression + SD relative to sham-stimulated cultures (Control)from six to nine independent experiments. *P <0.05, **P < 0.01, ***P < 0.001 versus control (t tests with Holm correction). ((Mikhail et al., 2017)*

REM sleep activity depends mainly on cholinergic mechanisms; for that reason, we used the cholinergic agonist carbachol (CCh, 20 μM), which is known to induce an increase in neuronal excitability and desynchronization of the activity similar to that observed in the REM sleep phase (Tateno et al., 2005a;Tateno et al., 2005b;Kaufman et al., 2012;Corner, 2013).

Comparing our approach with that used by Tafti's group, we administered twice the concentration of CCh (20 μM) to cultures to achieve the correct efficacy.

In the following paragraph we will describe in details the state of the art of using CCh on neuronal cultures.

3.4 Modulation of sleep in cultures: targeting the cholinergic system

Cortical neurons *in vivo* receive continuous synaptic input as a result of the spontaneous activity of cortical networks (Destexhe et al., 2003). This activity *in vivo* causes large conductance changes in the membrane and large-amplitude membrane potential fluctuation (Steriade, 2001) that modulate not only the response variability of spike trains but also the signal detection sensitivity of neural responses (Hô and Destexhe, 2000). The membrane excitability and firing properties of cortical neurons can be significantly modulated by neuromodulators such as acetylcholine (McCormick et al., 1993;Tateno et al., 2005a;Tateno et al., 2005b;Corner, 2013) and dopamine (Eytan et al., 2004).

Cholinergic neurons in the basal forebrain provide diffuse innervation to all cortical regions, and their activation modulates neuronal activity in the cortex (Richardson, 1991). This activity has been implicated in a number of important physiological functions, including arousal (Steriade and Timofeev, 2003), sensory processing (Juliano, 1998), memory (Hasselmo and Bower, 1992;Kirkwood et al., 1999)), as well as in the development of the cortex (Hohmann and Berger-Sweeney, 1998). Moreover, the cholinergic system promotes high-frequency oscillatory activity typical of wakefulness and REM sleep (Brown et al., 2012).

Indeed, noradrenergic and cholinergic neurons in the brainstem and the basal forebrain that project to cortical regions strongly regulate synchronization in the intact brain (Jones, 2005;Platt and Riedel, 2011;Berridge et al., 2012;Lee and Dan, 2012). Specifically, the activation of this neuromodulatory system suppresses network synchrony and promotes asynchronous firing patterns that are typical of arousal and REM sleep. In contrast, during periods of NREM sleep the activity of these systems is reduced, together with the prominent appearance of network synchrony as defined above.

As stated above, this form of synchronicity and its modulation by acetylcholine (ACh) and noradrenaline is not limited to the intact cortex; similar activity patterns occur in organotypic cortical preparations (Sanchez-Vives and McCormick, 2000;Beggs and Plenz, 2003;Baker et al., 2006;Johnson and Buonomano, 2007;Wester and Contreras, 2013) and even in networks of dissociated cortical neurons (Maeda et al., 1995b;Canepari et al., 1997;Kamioka, 1997;Van Pelt et al., 2004;Wagenaar et al., 2006;Hinard et al., 2012;Kaufman et al., 2012).

In agreement with *in vivo* results (Szerb, 1967;Steriade et al., 1991;Steriade et al., 1993), cholinergic agonists suppressed network synchronicity in cell culture and slice preparations, shifting the activity to tonic firing (Tateno and Jimbo, 1999;Tateno et al., 2005b;Kaufman et al., 2012;Corner, 2013). The synchronization patterns were partially restored after 24 hours (**Figure 3.11**) (Kaufman et al., 2014).

Moreover, prolonged exposure to CCh is associated with the gradual growth of excitatory synapses and, intriguingly, with the gradual reemergence of synchrony, as shown in **Figure 3.11** (Kaufman et al., 2012).

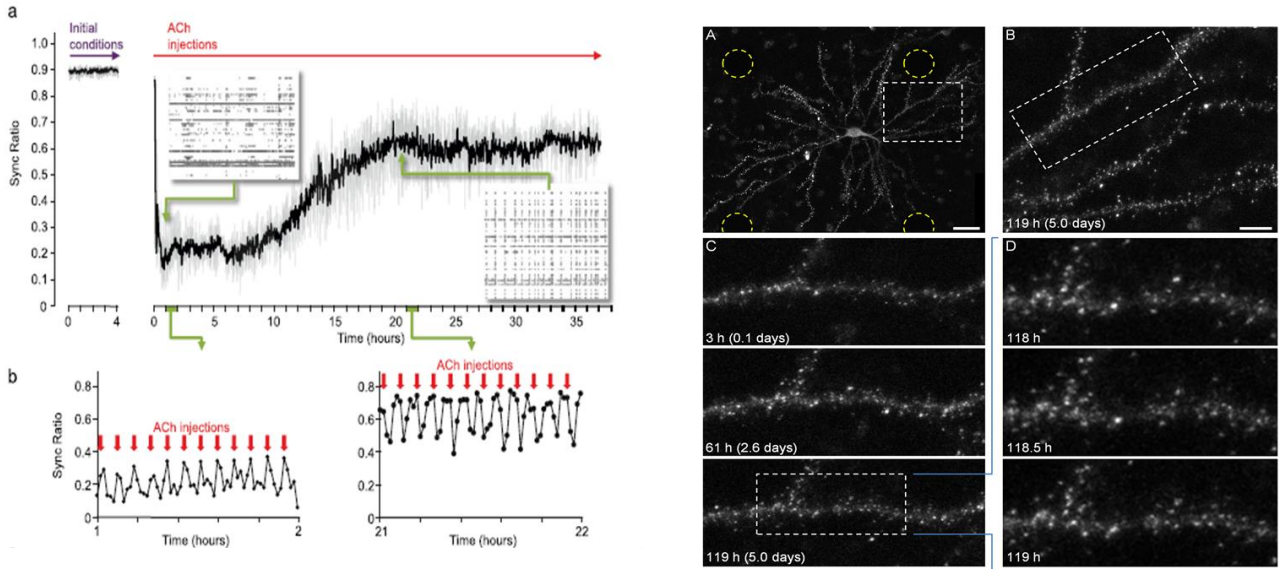

Figure 3.11

- *Left panel) Analysis of synchronous activity during prolonged (>24 hours) ACh application. a) Sync Ratio over time in one experiment performed in an open-loop regime (from M. Kaufman, 2014)*
- *(Right panel) A) Long-term imaging of postsynaptic sites. Single neuron expressing PSD-95:EGFP. Fluorescent puncta represent postsynaptic sites formed on dendritic spines and shafts. B) An enlarged portion of the image in A (region enclosed in rectangle) showing the typical field of view (site) imaged in these time-lapse recordings. C-D) A 10-day time-lapse series (30-min intervals, 48 images/day) of the dendrite enclosed in a rectangle in B (from M. Kaufman, 2012)*

Thus, while networks of cultured cortical neurons do not fully replicate the complex behavior of the intact brain, the similarities in the "default" slow wave pattern and the comparable effects of

neuromodulation on synchronicity suggest that this preparation is a useful model system for studying the basic features of sleep.

References

Achermann, P., and Borbély, A.A. (2003). Mathematical models of sleep regulation. *Front Biosci* 8**,** S683-S693.

Aschoff, J. (1965). Circadian rhythms in man. *Science* 148**,** 1427-1432.

Aston-Jones, G., and Bloom, F. (1981). Activity of norepinephrine-containing locus coeruleus neurons in behaving rats anticipates fluctuations in the sleep-waking cycle. *Journal of Neuroscience* 1**,** 876-886.

Baker, R.E., Corner, M.A., and Van Pelt, J. (2006). Spontaneous neuronal discharge patterns in developing organotypic mega-co-cultures of neonatal rat cerebral cortex. *Brain research* 1101**,** 29-35.

Bazhenov, M., Timofeev, I., Steriade, M., and Sejnowski, T.J. (2002). Model of thalamocortical slow-wave sleep oscillations and transitions to activated states. *Journal of neuroscience* 22**,** 8691-8704.

Beggs, J.M., and Plenz, D. (2003). Neuronal avalanches in neocortical circuits. *Journal of neuroscience* 23**,** 11167-11177.

Benington, J.H., and Heller, H.C. (1995). Restoration of brain energy metabolism as the function of sleep. *Progress in neurobiology* 45**,** 347-360.

Berridge, C.W., Schmeichel, B.E., and España, R.A. (2012). Noradrenergic modulation of wakefulness/arousal. *Sleep medicine reviews* 16**,** 187-197.

Borbely, A.A. (1982). A two process model of sleep regulation. *Hum Neurobiol* 1**,** 195-204.

Brown, R.E., Basheer, R., Mckenna, J.T., Strecker, R.E., and Mccarley, R.W. (2012). Control of sleep and wakefulness. *Physiological reviews* 92**,** 1087-1187.

Canepari, M., Bove, M., Maeda, E., Cappello, M., and Kawana, A. (1997). Experimental analysis of neuronal dynamics in cultured cortical networks and transitions between different patterns of activity. *Biological cybernetics* 77**,** 153-162.

Chao, Z.C., Bakkum, D.J., and Potter, S.M. (2007). Region-specific network plasticity in simulated and living cortical networks: comparison of the center of activity trajectory (CAT) with other statistics. *Journal of Neural Engineering* 4**,** 294.

Chauvette, S., Volgushev, M., and Timofeev, I. (2010). Origin of active states in local neocortical networks during slow sleep oscillation. *Cerebral cortex* 20**,** 2660-2674.

Chemelli, R.M., Willie, J.T., Sinton, C.M., Elmquist, J.K., Scammell, T., Lee, C., Richardson, J.A., Williams, S.C., Xiong, Y., and Kisanuki, Y. (1999). Narcolepsy in orexin knockout mice: molecular genetics of sleep regulation. *Cell* 98**,** 437-451.

Chiappalone, M., Massobrio, P., and Martinoia, S. (2008). Network plasticity in cortical assemblies. *European Journal of Neuroscience* 28**,** 221-237.

Chiappalone, M., Vato, A., Berdondini, L., Koudelka-Hep, M., and Martinoia, S. (2007). Network dynamics and synchronous activity in cultured cortical neurons. *International journal of neural systems* 17**,** 87-103.

Cirelli, C., Faraguna, U., and Tononi, G. (2006). Changes in brain gene expression after long‐term sleep deprivation. *Journal of neurochemistry* 98**,** 1632-1645.

Cirelli, C., Gutierrez, C.M., and Tononi, G. (2004). Extensive and divergent effects of sleep and wakefulness on brain gene expression. *Neuron* 41**,** 35-43.

Cohen, D., and Segal, M. (2011). Network bursts in hippocampal microcultures are terminated by exhaustion of vesicle pools. *Journal of Neurophysiology* 106**,** 2314-2321.

Cohen, E., Ivenshitz, M., Amor-Baroukh, V., Greenberger, V., and Segal, M. (2008). Determinants of spontaneous activity in networks of cultured hippocampus. *Brain research* 1235**,** 21-30.

Constantinople, C.M., and Bruno, R.M. (2011). Effects and mechanisms of wakefulness on local cortical networks. *Neuron* 69**,** 1061-1068.

Corner, M. (2013). From Neural Plate to Cortical Arousal—A Neuronal Network Theory of Sleep Derived from in Vitro “Model” Systems for Primordial Patterns of Spontaneous Bioelectric Activity in the Vertebrate Central Nervous System. *Brain sciences* 3**,** 800-820.

Corner, M.A. (2008). Spontaneous neuronal burst discharges as dependent and independent variables in the maturation of cerebral cortex tissue cultured in vitro: a review of activity-dependent studies in live 'model' systems for the development of intrinsically generated bioelectric slow-wave sleep patterns. *Brain Res Rev* 59**,** 221-244.

Corner, M.A. (2010). The sleep-like nature of early mammalian behavioral rhythms: Theoretical comment on Todd et al.(2010).

Daan, S., Beersma, D., and Borbély, A.A. (1984). Timing of human sleep: recovery process gated by a circadian pacemaker. *American Journal of Physiology-Regulatory, Integrative and Comparative Physiology* 246**,** R161-R183.

De Mairan, J.D. (1729). Observation botanique. *Histoire de l'Académie Royale des Sciences Paris*.

Destexhe, A., Rudolph, M., and Paré, D. (2003). The high-conductance state of neocortical neurons in vivo. *Nature reviews neuroscience* 4**,** 739.

Diering, G.H., Nirujogi, R.S., Roth, R.H., Worley, P.F., Pandey, A., and Huganir, R.L. (2017). Homer1a drives homeostatic scaling-down of excitatory synapses during sleep. *Science* 355**,** 511-515.

Edmunds Jr, L.N. (1983). Chronobiology at the cellular and molecular levels: models and mechanisms for circadian timekeeping. *American journal of anatomy* 168**,** 389-431.

Eytan, D., and Marom, S. (2006). Dynamics and effective topology underlying synchronization in networks of cortical neurons. *The Journal of neuroscience* 26**,** 8465-8476.

Eytan, D., Minerbi, A., Ziv, N., and Marom, S. (2004). Dopamine-induced dispersion of correlations between action potentials in networks of cortical neurons. *Journal of neurophysiology* 92**,** 1817-1824.

Franken, P., Chollet, D., and Tafti, M. (2001). The homeostatic regulation of sleep need is under genetic control. *The Journal of Neuroscience* 21**,** 2610-2621.

Harris, K.D., and Thiele, A. (2011). Cortical state and attention. *Nature reviews neuroscience* 12**,** 509.

Hasselmo, M.E., and Bower, J.M. (1992). Cholinergic suppression specific to intrinsic not afferent fiber synapses in rat piriform (olfactory) cortex. *Journal of neurophysiology* 67**,** 1222-1229.

Hengen, K.B., Pacheco, A.T., Mcgregor, J.N., Van Hooser, S.D., and Turrigiano, G.G. (2016). Neuronal firing rate homeostasis is inhibited by sleep and promoted by wake. *Cell* 165**,** 180-191.

Hill, S., and Tononi, G. (2005). Modeling sleep and wakefulness in the thalamocortical system. *Journal of neurophysiology* 93**,** 1671-1698.

Hinard, V., Mikhail, C., Pradervand, S., Curie, T., Houtkooper, R.H., Auwerx, J., Franken, P., and Tafti, M. (2012). Key electrophysiological, molecular, and metabolic signatures of sleep and wakefulness revealed in primary cortical cultures. *J Neurosci* 32**,** 12506-12517.

Hô, N., and Destexhe, A. (2000). Synaptic background activity enhances the responsiveness of neocortical pyramidal neurons. *Journal of neurophysiology* 84**,** 1488-1496.

Hobson, J.A., Mccarley, R.W., and Wyzinski, P.W. (1975). Sleep cycle oscillation: reciprocal discharge by two brainstem neuronal groups. *Science* 189**,** 55-58.

Hohmann, C., and Berger-Sweeney, J. (1998). Cholinergic regulation of cortical development and plasticity. New twists to an old story. *Perspectives on developmental neurobiology* 5**,** 401-425.

Holcman, D., and Tsodyks, M. (2006). The emergence of up and down states in cortical networks. *PLoS computational biology* 2**,** e23.

Huber, R., Ghilardi, M.F., Massimini, M., Ferrarelli, F., Riedner, B.A., Peterson, M.J., and Tononi, G. (2006). Arm immobilization causes cortical plastic changes and locally decreases sleep slow wave activity. *Nature neuroscience* 9**,** 1169.

Jewett, K.A., Taishi, P., Sengupta, P., Roy, S., Davis, C.J., and Krueger, J.M. (2015). Tumor necrosis

factor enhances the sleep‐like state and electrical stimulation induces a wake‐like state in co‐cultures of neurons and glia. *European Journal of Neuroscience* 42**,** 2078-2090.
Jimbo, Y., Tateno, T., and Robinson, H. (1999). Simultaneous induction of pathway-specific potentiation and depression in networks of cortical neurons. *Biophysical journal* 76**,** 670-678.
Johnson, H.A., and Buonomano, D.V. (2007). Development and plasticity of spontaneous activity and Up states in cortical organotypic slices. *Journal of Neuroscience* 27**,** 5915-5925.
Jones, B.E. (2005). From waking to sleeping: neuronal and chemical substrates. *Trends in pharmacological sciences* 26**,** 578-586.
Juliano, S.L. (1998). Mapping the sensory mosaic. *Science* 279**,** 1653-1654.
Kamioka, H. (1997). Planar electrode arrays for long-term measurement of neuronal firings in cultured cortical slices. *J. Cellular Engineering*.
Kaufman, M., Corner, M.A., and Ziv, N.E. (2012). Long-term relationships between cholinergic tone, synchronous bursting and synaptic remodeling. *PLoS One* 7**,** e40980.
Kaufman, M., Reinartz, S., and Ziv, N.E. (2014). Adaptation to prolonged neuromodulation in cortical cultures: an invariable return to network synchrony. *BMC biology* 12**,** 83.
Kirkwood, A., Rozas, C., Kirkwood, J., Perez, F., and Bear, M.F. (1999). Modulation of long-term synaptic depression in visual cortex by acetylcholine and norepinephrine. *Journal of Neuroscience* 19**,** 1599-1609.
Kopp, C., Albrecht, U., Zheng, B., and Tobler, I. (2002). Homeostatic sleep regulation is preserved in mPer1 and mPer2 mutant mice. *European Journal of Neuroscience* 16**,** 1099-1106.
Kristiansen, K., and Courtois, G. (1949). Rhythmic electrical activity from isolated cerebral cortex. *Electroencephalography and clinical neurophysiology* 1**,** 265-272.
Krueger, J.M., Huang, Y.H., Rector, D.M., and Buysse, D.J. (2013). Sleep: a synchrony of cell activity‐driven small network states. *European Journal of Neuroscience* 38**,** 2199-2209.
Krueger, J.M., and Obäl Jr, F. (1993). A neuronal group theory of sleep function. *Journal of sleep research* 2**,** 63-69.
Krueger, J.M., Rector, D.M., Roy, S., Van Dongen, H.P., Belenky, G., and Panksepp, J. (2008). Sleep as a fundamental property of neuronal assemblies. *Nature Reviews Neuroscience* 9**,** 910.
Lee, S.-H., and Dan, Y. (2012). Neuromodulation of brain states. *Neuron* 76**,** 209-222.
Lin, L., Faraco, J., Li, R., Kadotani, H., Rogers, W., Lin, X., Qiu, X., De Jong, P.J., Nishino, S., and Mignot, E. (1999). The sleep disorder canine narcolepsy is caused by a mutation in the hypocretin (orexin) receptor 2 gene. *Cell* 98**,** 365-376.
Lo, C.-C., Chou, T., Penzel, T., Scammell, T.E., Strecker, R.E., Stanley, H.E., and Ivanov, P.C. (2004). Common scale-invariant patterns of sleep–wake transitions across mammalian species. *Proceedings of the National Academy of Sciences of the United States of America* 101**,** 17545-17548.
Lonardoni, D., Di Marco, S., Amin, H., Maccione, A., Berdondini, L., and Nieus, T. (Year). "High-density MEA recordings unveil the dynamics of bursting events in Cell Cultures", in: *Engineering in Medicine and Biology Society (EMBC), 2015 37th Annual International Conference of the IEEE*: IEEE), 3763-3766.
Lowrey, P.L., and Takahashi, J.S. (2011). "Genetics of circadian rhythms in Mammalian model organisms," in *Advances in genetics*. Elsevier), 175-230.
Mackiewicz, M., Shockley, K.R., Romer, M.A., Galante, R.J., Zimmerman, J.E., Naidoo, N., Baldwin, D.A., Jensen, S.T., Churchill, G.A., and Pack, A.I. (2007). Macromolecule biosynthesis: a key function of sleep. *Physiological genomics* 31**,** 441-457.
Maeda, E., Robinson, H., and Kawana, A. (1995a). The mechanisms of generation and propagation of synchronized bursting in developing networks of cortical neurons. *The Journal of neuroscience* 15**,** 6834-6845.
Maeda, E., Robinson, H., and Kawana, A. (1995b). The mechanisms of generation and propagation of synchronized bursting in developing networks of cortical neurons. *Journal of Neuroscience* 15**,** 6834-6845.

Mahowald, M.W., and Schenck, C.H. (2005). Insights from studying human sleep disorders. *Nature* 437**,** 1279.
Maret, S., Dorsaz, S., Gurcel, L., Pradervand, S., Petit, B., Pfister, C., Hagenbuchle, O., O'hara, B.F., Franken, P., and Tafti, M. (2007). Homer1a is a core brain molecular correlate of sleep loss. *Proceedings of the National Academy of Sciences* 104**,** 20090-20095.
Marom, S., and Shahaf, G. (2002). Development, learning and memory in large random networks of cortical neurons: lessons beyond anatomy. *Quarterly reviews of biophysics* 35**,** 63-87.
Marshall, L., Helgadóttir, H., Mölle, M., and Born, J. (2006). Boosting slow oscillations during sleep potentiates memory. *Nature* 444**,** 610.
Mccormick, D.A., Wang, Z., and Huguenard, J. (1993). Neurotransmitter control of neocortical neuronal activity and excitability. *Cerebral cortex* 3**,** 387-398.
Mikhail, C., Vaucher, A., Jimenez, S., and Tafti, M. (2017). ERK signaling pathway regulates sleep duration through activity-induced gene expression during wakefulness. *Sci. Signal.* 10**,** eaai9219.
Mölle, M., Marshall, L., Gais, S., and Born, J. (2004). Learning increases human electroencephalographic coherence during subsequent slow sleep oscillations. *Proceedings of the National Academy of Sciences* 101**,** 13963-13968.
Orlandi, J.G., Soriano, J., Alvarez-Lacalle, E., Teller, S., and Casademunt, J. (2013). Noise focusing and the emergence of coherent activity in neuronal cultures. *Nature Physics* 9**,** 582.
Paterson, L.M., Nutt, D.J., and Wilson, S.J. (2011). Sleep and its disorders in translational medicine. *Journal of psychopharmacology* 25**,** 1226-1234.
Perin, R., Berger, T.K., and Markram, H. (2011). A synaptic organizing principle for cortical neuronal groups. *Proceedings of the National Academy of Sciences***,** 201016051.
Phillips, A.J., Robinson, P.A., Kedziora, D.J., and Abeysuriya, R.G. (2010). Mammalian sleep dynamics: how diverse features arise from a common physiological framework. *PLoS Comput Biol* 6**,** e1000826.
Pigarev, I.N., Nothdurft, H.-C., and Kastner, S. (1997). Evidence for asynchronous development of sleep in cortical areas. *Neuroreport* 8**,** 2557-2560.
Pittendrigh, C.S. (1954). On temperature independence in the clock system controlling emergence time in Drosophila. *Proceedings of the National Academy of Sciences* 40**,** 1018-1029.
Platt, B., and Riedel, G. (2011). The cholinergic system, EEG and sleep. *Behavioural brain research* 221**,** 499-504.
Ralph, M.R., and Menaker, M. (1988). A mutation of the circadian system in golden hamsters. *Science* 241**,** 1225-1227.
Rasch, B., and Born, J. (2013). About sleep's role in memory. *Physiological reviews* 93**,** 681-766.
Rector, D.M., Topchiy, I.A., Carter, K.M., and Rojas, M.J. (2005). Local functional state differences between rat cortical columns. *Brain research* 1047**,** 45-55.
Reppert, S.M., and Weaver, D.R. (2002). Coordination of circadian timing in mammals. *Nature* 418**,** 935-941.
Richardson, P.M. (1991). Neurotrophic factors in regeneration. *Current opinion in neurobiology* 1**,** 401-406.
Robinson, H., Kawahara, M., Jimbo, Y., Torimitsu, K., Kuroda, Y., and Kawana, A. (1993). Periodic synchronized bursting and intracellular calcium transients elicited by low magnesium in cultured cortical neurons. *Journal of neurophysiology* 70**,** 1606-1616.
Saberi-Moghadam, S., Simi, A., Setareh, H., Mikhail, C., and Tafti, M. (2018). In vitro Cortical Network Firing is Homeostatically Regulated: A Model for Sleep Regulation. *Scientific reports* 8**,** 6297.
Sanchez-Vives, M.V., and Mccormick, D.A. (2000). Cellular and network mechanisms of rhythmic recurrent activity in neocortex. *Nature neuroscience* 3**,** 1027.
Sengupta, P., Davis, C., Clinton, J., Roy, S., and Krueger, J. (Year). "Networks of cultured neurons show oscillatory dynamics", in: *Sleep*: AMER ACAD SLEEP MEDICINE ONE

WESTBROOK CORPORATE CTR, STE 920, WESTCHESTER, IL 60154 USA), A36-A37.
Shahaf, G., and Marom, S. (2001). Learning in networks of cortical neurons. *Journal of Neuroscience* 21**,** 8782-8788.
Shepard, K.N., Liles, L.C., Weinshenker, D., and Liu, R.C. (2015). Norepinephrine is necessary for experience-dependent plasticity in the developing mouse auditory cortex. *Journal of Neuroscience* 35**,** 2432-2437.
Shiromani, P.J., Xu, M., Winston, E.M., Shiromani, S.N., Gerashchenko, D., and Weaver, D.R. (2004). Sleep rhythmicity and homeostasis in mice with targeted disruption of mPeriod genes. *American Journal of Physiology-Regulatory, Integrative and Comparative Physiology* 287**,** R47-R57.
Slomowitz, E., Styr, B., Vertkin, I., Milshtein-Parush, H., Nelken, I., Slutsky, M., and Slutsky, I. (2015). Interplay between population firing stability and single neuron dynamics in hippocampal networks. *Elife* 4**,** e04378.
Steriade, M. (2001). *The intact and sliced brain.* MIT press.
Steriade, M., Dossi, R.C., and Nunez, A. (1991). Network modulation of a slow intrinsic oscillation of cat thalamocortical neurons implicated in sleep delta waves: cortically induced synchronization and brainstem cholinergic suppression. *Journal of Neuroscience* 11**,** 3200-3217.
Steriade, M., Mccormick, D.A., and Sejnowski, T.J. (1993). Thalamocortical oscillations in the sleeping and aroused brain. *Science* 262**,** 679-685.
Steriade, M., and Timofeev, I. (2003). Neuronal plasticity in thalamocortical networks during sleep and waking oscillations. *Neuron* 37**,** 563-576.
Stokkan, K.-A., Yamazaki, S., Tei, H., Sakaki, Y., and Menaker, M. (2001). Entrainment of the circadian clock in the liver by feeding. *Science* 291**,** 490-493.
Szerb, J. (1967). Cortical acetylcholine release and electroencephalographic arousal. *The Journal of physiology* 192**,** 329-343.
Tateno, T., and Jimbo, Y. (1999). Activity-dependent enhancement in the reliability of correlated spike timings in cultured cortical neurons. *Biological cybernetics* 80**,** 45-55.
Tateno, T., Jimbo, Y., and Robinson, H. (2005a). Spatio-temporal cholinergic modulation in cultured networks of rat cortical neurons: spontaneous activity. *Neuroscience* 134**,** 425-437.
Tateno, T., Jimbo, Y., and Robinson, H.P. (2005b). Spatio-temporal cholinergic modulation in cultured networks of rat cortical neurons: evoked activity. *Neuroscience* 134**,** 439-448.
Terao, A., Wisor, J., Peyron, C., Apte-Deshpande, A., Wurts, S., Edgar, D., and Kilduff, T. (2006). Gene expression in the rat brain during sleep deprivation and recovery sleep: an Affymetrix GeneChip® study. *Neuroscience* 137**,** 593-605.
Timofeev, I., Grenier, F., Bazhenov, M., Sejnowski, T., and Steriade, M. (2000). Origin of slow cortical oscillations in deafferented cortical slabs. *Cerebral cortex* 10**,** 1185-1199.
Timofeev, I., Grenier, F., and Steriade, M. (2001). Disfacilitation and active inhibition in the neocortex during the natural sleep-wake cycle: an intracellular study. *Proceedings of the National Academy of Sciences* 98**,** 1924-1929.
Tinarelli, F., Garcia-Garcia, C., Nicassio, F., and Tucci, V. (2014). Parent-of-origin genetic background affects the transcriptional levels of circadian and neuronal plasticity genes following sleep loss. *Philos Trans R Soc Lond B Biol Sci* 369**,** 20120471.
Tobler, I., and Borbely, A. (1986). Sleep EEG in the rat as a function of prior waking. *Electroencephalography and clinical neurophysiology* 64**,** 74-76.
Tononi, G., and Cirelli, C. (2006). Sleep function and synaptic homeostasis. *Sleep medicine reviews* 10**,** 49-62.
Tononi, G., and Cirelli, C. (2014). Sleep and the price of plasticity: from synaptic and cellular homeostasis to memory consolidation and integration. *Neuron* 81**,** 12-34.
Toth, L.A., and Bhargava, P. (2013). Animal models of sleep disorders. *Comparative medicine* 63**,** 91-104.

Tucker, A.M., Dinges, D.F., and Van Dongen, H.P. (2007). Trait interindividual differences in the sleep physiology of healthy young adults. *Journal of sleep research* 16**,** 170-180.

Van Dongen, P., Baynard, M.D., Maislin, G., and Dinges, D.F. (2004). Systematic interindividual differences in neurobehavioral impairment from sleep loss: evidence of trait-like differential vulnerability. *Sleep* 27**,** 423-433.

Van Pelt, J., Wolters, P.S., Corner, M.A., Rutten, W.L., and Ramakers, G.J. (2004). Long-term characterization of firing dynamics of spontaneous bursts in cultured neural networks. *Biomedical Engineering, IEEE Transactions on* 51**,** 2051-2062.

Vyazovskiy, V.V., Cirelli, C., and Tononi, G. (2011). "Electrophysiological correlates of sleep homeostasis in freely behaving rats," in *Progress in brain research*. Elsevier), 17-38.

Vyazovskiy, V.V., and Harris, K.D. (2013). Sleep and the single neuron: the role of global slow oscillations in individual cell rest. *Nature Reviews Neuroscience* 14**,** 443.

Wagenaar, D.A., Madhavan, R., Pine, J., and Potter, S.M. (2005). Controlling bursting in cortical cultures with closed-loop multi-electrode stimulation. *J Neurosci* 25**,** 680-688.

Wagenaar, D.A., Pine, J., and Potter, S.M. (2006). An extremely rich repertoire of bursting patterns during the development of cortical cultures. *BMC neuroscience* 7**,** 11.

Wester, J.C., and Contreras, D. (2013). Differential modulation of spontaneous and evoked thalamocortical network activity by acetylcholine level in vitro. *Journal of Neuroscience* 33**,** 17951-17966.

Chapter 4

Abolishment of the synchronous activity and alteration of the sleep-like electrophysiological properties in physiological condition

In this chapter, we firstly show that neuronal assemblies plated on Micro Electrode Arrays starting from two weeks *in vitro* present synchronized, low frequency firing patterns similar to in vivo slow wave oscillations, which are a key parameter of sleep-like state. Then, we stimulated the cortical cultures with an agonist of acetylcholine receptor, Carbachol, which caused a desynchronization of the spontaneous firing of the cultures. We recorded and monitored the cultures for a period of over 31 hours. We analyzed the electrophysiological signals by exploiting novel methodological approaches, taking into account the different temporal scales of the recorded signals, and considering both spikes and local field potentials. Supporting the electrophysiological analysis results, gene expressions of targeted genes showed the activation of specific markers involved in sleep-wake rhythms. Our results demonstrate that the Carbachol treatment induces desynchronization of neuronal activity, altering sleep-like properties in an in vitro model. These results was published in Frontiers in Neuroscience in 2016 (Colombi et al., 2016).

4.1 Materials and Methods

4.1.1 Cell culture

Dissociated neuronal cultures were obtained from cortices of embryonic rats at gestational day 18 (pregnant Sprague-Dawley female rats delivered by Charles River Laboratories, Lecco, Italy). All experimental procedures and animal care were conducted in conformity with institutional guidelines, in accordance with the European legislation (European Communities Directive of 24 November 1986, 86/609/EEC) and with the NIH Guide for the Care and Use of Laboratory Animals. The procedures for preparing neuronal cultures are described in detail in previous studies (Frega et al., 2012;Colombi et al., 2013). Briefly, the cerebral cortices of 4-5 embryos were dissected out from the brain and dissociated by enzymatic digestion in 5 ml of trypsin 0.125% and HBSS, diluted DNAsi 0.25 mg/ml (Sigma-Aldrich, Saint Louis, Missouri, USA) at 37°C for 30 min. Trypsin digestion was blocked using 5 ml of Neurobasal Medium (Thermo Fisher Scientific, Waltham, MA, USA) containing 2% of

B27 supplement, 1% penicillin/streptomycin, 1% L-glutamine (Thermo Fisher Scientific, Waltham, MA, USA), plus 10% of heat inactivated FBS (Thermo Fisher Scientific, Waltham, MA, USA). Cells were centrifuged 5 min at 1200 rpm and then resuspended by pipetting in 2-3 ml of complete Neurobasal medium plus FBS. Cells debris was removed centrifuging at 700 rpm for 7 min. Neurons were then resuspended in complete culture medium without FBS and counted with trypan blue dye (Sigma-Aldrich). Cells were plated onto 60-channel MEAs previously coated with poly-D-lysine and laminin to promote cell adhesion (final density around 1200 cells/mm^2) and maintained with 1 ml of nutrient medium (i.e. serum-free Neurobasal medium supplemented with B27 and Glutamax-I). Cells were finally placed in a humidified incubator having an atmosphere of 5% CO2-95% air at 37 °C. Half of the medium was replaced weekly.

4.1.2 Micro-Electrode Array recordings

Planar microelectrodes are arranged in an 8×8 layout, excluding corners and one reference electrode, for a total of 59 TiN/SiN planar round recording electrodes (30 µm diameter; 200 µm center-to-center inter electrode distance) (Multichannel Systems, MCS, Reutlingen, Germany) (**Figure 1A**). One recording electrode was replaced by a bigger ground electrode. The activity of all cultures was recorded by means of the MEA60 System (MCS). The signal from each channel was sampled at 10kHz and amplified using a Multichannel System amplifier with a bandwidth of 1 Hz-3kHz. Each recorded channel was acquired through the data acquisition card and on-line monitored through MC_Rack software (MCS). To reduce thermal stress of the cells during the experiment, MEAs were kept at 37 °C by means of a controlled thermostat (MCS) and covered by PDMS caps to avoid evaporation and prevent changes in osmolarity.

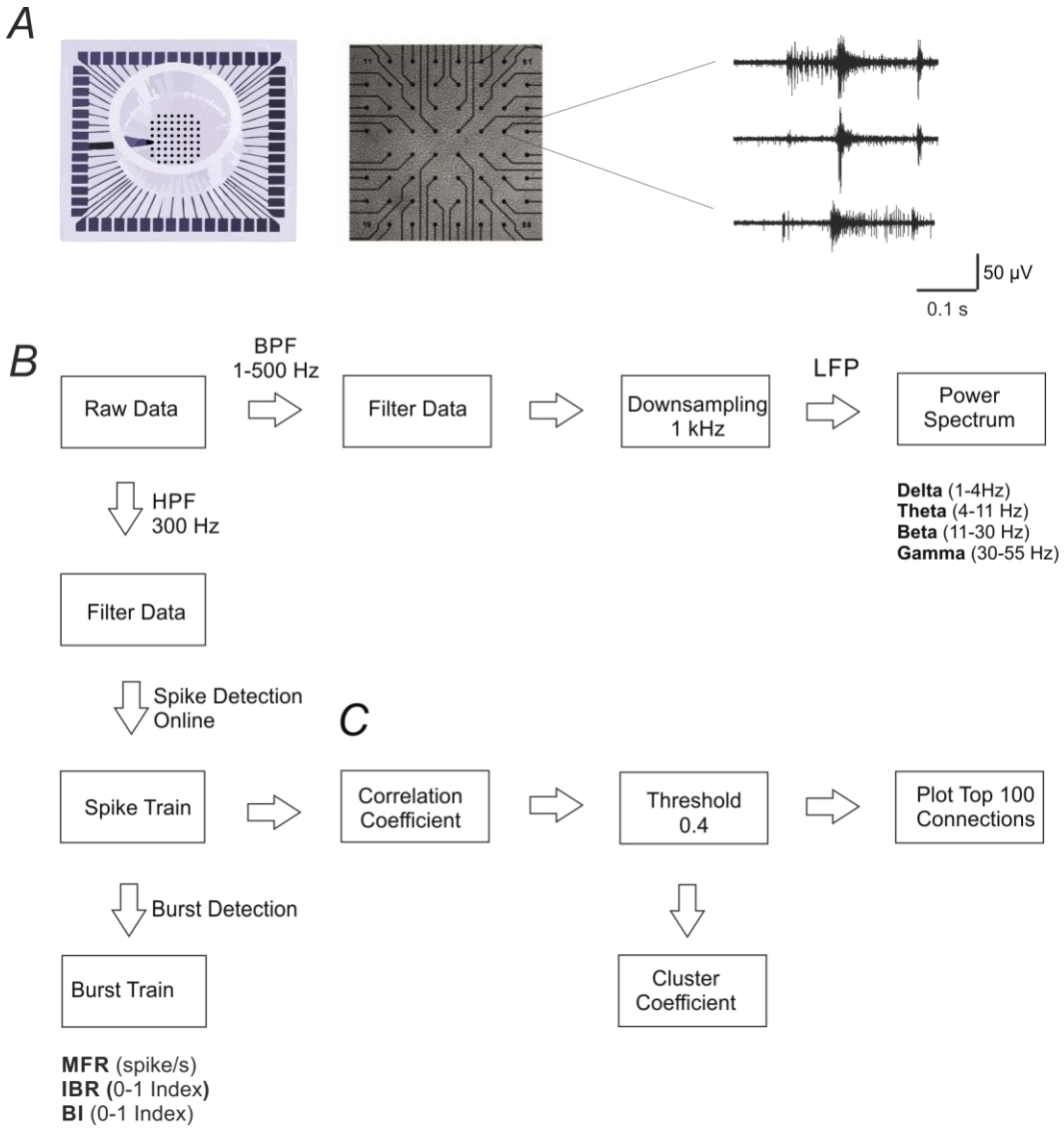

Figure 4.1 MEA electrodes layout and data analysis. (A) A 60-channel-MEA (Multichannel Systems MCS, Reutlingen, Germany) with the standard electrode layout (8 × 8) plated with cortical cultures. On the right, typical traces recorded from three microelectrodes upon high pass filtering at 300 Hz, to selectively consider MUA only. (B) Scheme of the data analysis workflow. We performed spike and burst detection on the high pass filtered signal using MC_Rack software (MCS). Before computing power spectral density, we down-sampled the signal to 1 KHz, previously filtered using a low pass filter (500 Hz). (C) Scheme of the correlation analysis: we considered only the strongest 100 STTC (Spike Time tiling coefficient) during the basal recording (i.e., 7 h), in order to select only the most significant correlations. Then we calculated the percentage of decrease in the STTC values. Therefore, we plot connectivity maps of the 100 STTCs.

4.1.3 Experimental protocol

The general protocol included 7 hours of recording in culture solution (Neurobasal +2% B27 + 1% Glutamax-I 200 µM + 1% Penicilin-Streptomycin sol.), defined as basal condition (**Figure 4.2 A**). Carbachol (CCh) stock solution (100mM) was prepared and diluted in DMSO-water, in order to obtain a final concentration of 20µM (Tateno et al., 2005;Corner, 2008;Kaufman et al., 2012). The drug was added to the bath solution by directly pipetting in the medium (volume of 1mL). Some of the cultures were exposed to CCh for 24 hours, while for control experiment we recorded neuronal networks in culture solution for the same time temporal window. Since we noticed that mechanical

perturbation due to the pipette injection in the medium could cause a temporary instability of the firing rate, we discarded the first 10 minutes at the beginning of the 24-hour recording phase. The total number of experiments performed by following the above described protocol were: 4 for control (42 ± 5 Days in vitro, DIV) and 7 for CCh (34 ± 2 DIV). The two groups were not statistically different in terms of age of the tested cultures ($p>0.05$, Mann-Whitney's test).

4.1.5 Data analysis

As mentioned in the Chapter 2 (section X) the typical extracellularly acquired signals from a local network of neurons are Local Field Potentials (LFPs) and Multi-Unit Activity (MUA). For these reasons we analyzed the electrophysiological signals by exploiting novel methodological approaches, which can take into account both temporal scales of the recorded signals (i.e. LFPs and MUA). The different steps of the analysis are briefly reported in the following (**Figure 4.1 B**).

MUA analysis

Firstly, extracellular signals were filtered online (MC_Rack software, MCS) by using a second-order Butterworth high-pass filter with cut-off frequency of 300 Hz, in order to select only the MUA component of the signal (**Figure 4.1 B**). The online spike detection was performed (MC_Rack software, MCS) with hard threshold chosen as five times the standard deviation of the noise ($-5\sigma_n$). To check for changes in the noise level during long recordings, we performed a post-hoc test for significant differences in the wide-band raw data standard deviation on a selected subset of control experiments. We found no significant changes in the standard deviation of the noise during the entire duration of the experiments. Afterwards spike trains were analyzed off-line using a custom software developed in Matlab (The Mathworks, Natick, MA, USA), named SpyCode (Bologna et al., 2010), which collects several tools for processing multi-channel neuronal recordings. We performed a custom burst detection as previously described (Chiappalone et al., 2005). Once spikes and bursts were detected, we were able to compute several parameters such as Mean Firing Rate, MFR (mean number of spikes over an interval of time [spike/s]), Inverse Burst Ratio, IBR (percentage of spikes outside bursts) and Burstiness Index, BI, index of the burstiness level of the network, as initially presented in (Wagenaar et al., 2005). The parameters extracted through burst and spike detection were normalized for each experiment with regard to the corresponding value of the reference (basal) activity for direct comparability. The same procedure has been described in previous papers from our group (Colombi et al., 2013).

Correlation analysis

First, we calculated the Spike Time Tiling Coefficient (STTC) (Cutts and Eglen, 2014) between each

pair of spike trains recorded from active channels (i.e. having MFR>0.01 spike/s) every one hour (**Figure 4.1 C**). We only considered the largest 100 STTCs selected during the basal recording (i.e. 7 hours), to identify only the most significant correlations. We then calculated the percentage of STTCs significantly decreasing during the control and the CCh application (i.e. decrease higher than 20%, mean + 3SD of the variations observed during basal recording). Finally, for the sake of clarity, we plotted the top 100 STTCs in the connectivity maps at different time points, both for the control and for the CCh experiments.

LFP analysis

Wide-band signals were first down-sampled to 1 kHz, after low pass filtering below 500 Hz to prevent aliasing (using a Hamming-window FIR filter of order 30) (Leondopulos et al., 2012). Then we computed the power spectral density of the decimated signal ($\mu V^2/Hz$), using Welch method (Windows=5s, overlap=50%; DFT (Discrete Fourier Transform) points=8192; df (frequency resolution)=0.12 Hz; dt (temporal resolution)=8.19 s) (**Figure 4.1 B**). We only considered the lower frequency bands of the signal, which are of particular interest for studying the sleep-wake cycle, in particular delta (1-4 Hz), theta (4-11 Hz), beta (11-30 Hz) and gamma (30-55 Hz) bands. To characterize LFP, we calculated the power in each of those frequency bands.

We also plotted the different waves previously described (i.e. delta, theta, beta and gamma), by filtering the LFP signal using FIR filters with different lengths (Leondopulos et al., 2012): 20000 for delta (1-4 Hz), 10000 for theta (4-11 Hz) and beta (11-30 Hz) and 5000 for gamma (30-55 Hz). All filtering operations were time compensated to account the delay introduced by the filter.

4.1.6 Gene expression

Multi-well plates were coated using Poly-D-lysine 0.1 mg/ml (Sigma-Aldrich) and incubated overnight in a sterile incubator at 37°C and 5% CO2. Neurons were then plated at a concentration of 500,000 cells/well. Primary neurons were treated after DIV 30 (i.e. same age used for the MEA experiments) with 20µM of Carbachol (Sigma-Aldrich) for 24h. A wash out was then performed and the cells were put to recovery with conditioned medium for other 24h prior to harvesting. Neurons were washed three times with ice-cold phosphate-buffered saline solution and lysed with 300 µl of Trizol (Life Technologies), followed by a phenol/chloroform extraction. Cell lysates were collected and 600 ng of RNA was retro-transcribed using ImpromII reverse transcription kit (Promega), according to manufacturer`s specifications. Real Time-PCR was performed and analysed as previously described (Tinarelli et al., 2014) in duplicate for each sample. All samples were normalized

against b-actin. Primers used in the different Real Time-PCR experiments are reported in Table 1.

Gene name	Primer Sense	Primer Reverse
b-actin	TATGGAATCCTGTGGCATC	GTGTTGGCATAGAGGTCTT
Arc	TCTACACTCTCAGACCAT	ACACTTGATTTCTTGACTAC
Dlk-1	AAATAGATATTCGGGCTTGC	ATTCGTACTGGCCTTTCT
Fos	CATTACAGAGAGAAGAAACAAGT	TTCACGCACAGATAAGGT
Homer1b/c	TAACCTGAAGACTCTCCTA	ACGAAGACAGACAGTATC
Per2	CATACCTTCACTGCTTCTT	AGTCTCCTCAAGTCCAAT

4.1.7 Statistics

Data are expressed as mean ± standard error of the mean (SE). Statistical tests were performed to assess the significant difference among the experimental conditions. The normal distribution of data was assessed using Kolmogorov-Smirnov normality test. According to the distribution of data we performed either parametric (e.g. t-test) or non-parametric test (e.g. Mann-Whitney) test and p values<0.05 were considered significant. Statistical analysis was carried out by using OriginPro (OriginLab Corporation, Northampton, MA, USA).

4.2 Results

In the present study we examined the long-term effect of CCh on the spontaneous network activity of mature cortical cultures grown over MEAs (**Figure 4.2 A**). In particular, we compared the behavior of cortical networks with (N=4 cultures) or without treatment (N=7 cultures). In control experiments, the networks revealed a spontaneous, synchronized and low-frequency (0.16-3 Hz) multi –unit burst activity, composed of network-wide brief (50-100 ms) bursts separated by periods of nearly complete quiescence or sparse, asynchronous action potentials (Maeda et al., 1995;Van Pelt et al., 2004;Wagenaar et al., 2005;Eytan and Marom, 2006;Chiappalone et al., 2007), as depicted in **Figure 4.2 B**, left panel. Following CCh application, these activity patterns were strongly altered, in particular at the beginning of the administration. This resulted in a loss of regularity, and in fragmentation of burst structures, with many more isolated spikes, as shown in the raster plot of one representative experiment (**Figure 4.2 B**, right panel) and in the measure of network synchronization described below (**Figure 4.2 D-E**). In fact, with respect to the control, CCh increased significantly the percentage of out-burst spikes (Inverse Burst Ratio) during the entire recording (**Figure 4.2 D).** This behavior is also confirmed by the BI (Burstiness Index) which significantly decreased with respect to the control experiments **(Figure 4.2 E)** In contrast, the overall activity levels expressed by firing rate were significantly affected only in the first hour (**Figure 4.2 C**). These effects are in agreement with previous reports (Tateno et al., 2005;Corner, 2008;Kaufman et al., 2012). The percentage of active channels remained high in both experimental conditions: 88.16 % for the control experiment and 80.20% during CCh treatment. We calculated the percentage changes as follows:

$$\%Values = 100 * \frac{XEnd - Xstart}{Xstart}$$

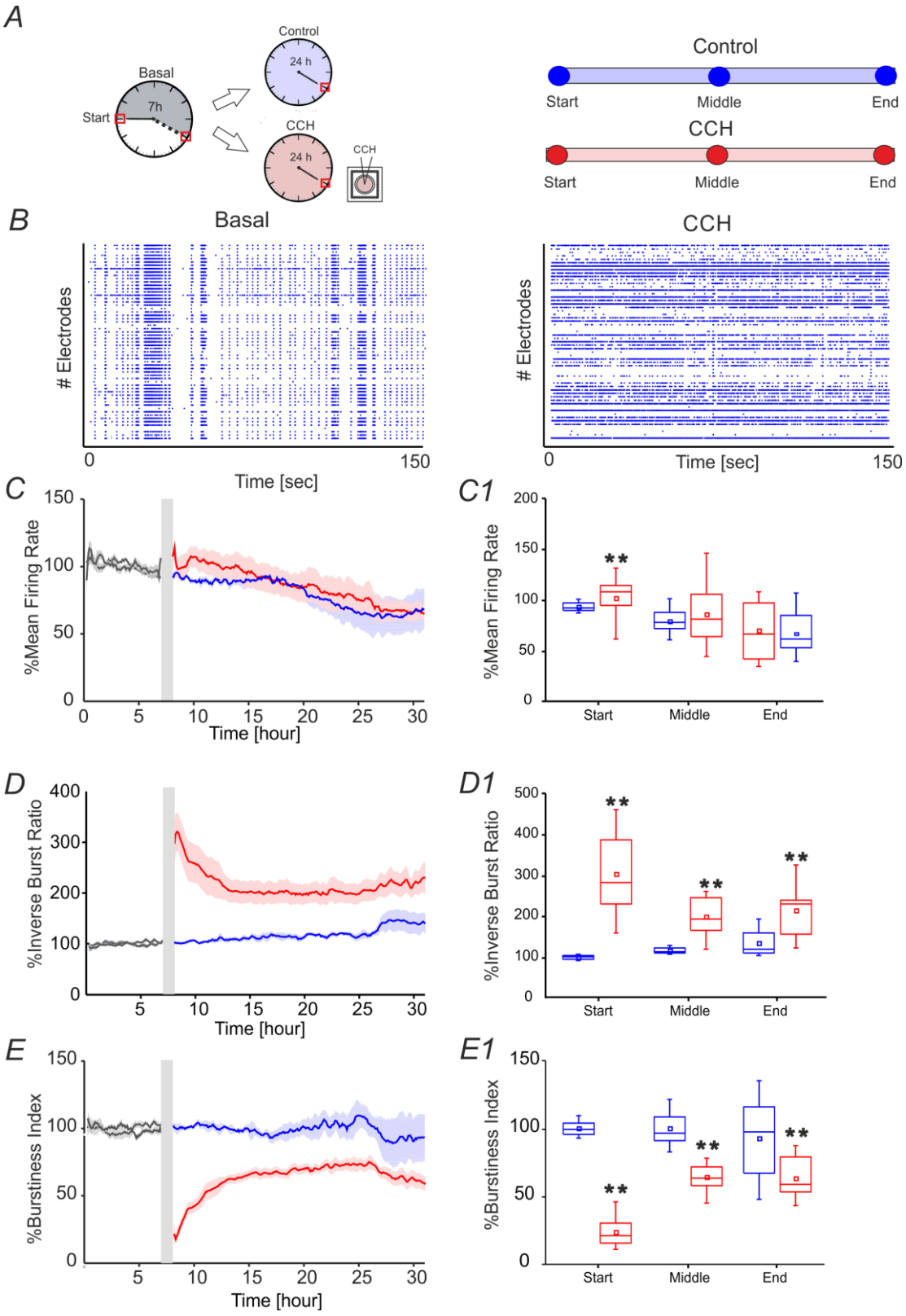

Figure 4.2 MUA analysis. (A) Left panel: Schematic representation of experimental protocol using chronic treatment of Carbachol (CCh). Cortical cultures are recorded for 7 h in basal condition, followed by 24 h of recording, upon addition of 20 µM CCh. Right Panel: Time point of 1 h considered for the evaluation of the networks parameters for each of the two different experimental condition. (B) Raster plots showing 150 s of spontaneous (left) and after CCh application (right) for a representative experiment (each small dot represents a spike, each row an electrode). In the basal condition, the cortical culture shows a synchronized activity completely disrupted after the CCh treatment. (C) MFR of cultures (left) recorded without (blue line: N = 4; cultures age 42 ± 5 DIV) and with stimulation (red line: N = 7; cultures age 34 ± 2 DIV). (C1) Box plot of MFR (right) during control experiments (blue box) and during CCh treatment (red box at three

*different 1-h time intervals: start, middle, and end for each experimental condition. In the analyzed group of experiments, the MFR of cultures upon drug administration changed significantly only in the first 1 h, increasing by 9.55% respect to the control experiments in the same interval of time (D) IBR of cultures (left) recorded without (blue line) and with stimulation (red line). (D1) Box plot of IBR (right) during control experiments (blue box) and during CCh treatment (red box). In the analyzed group of experiments, the IBR of cultures upon drug administration significantly increased compared to the control experiments during the entire recording. In particular, during the first 1 h, IBR increased by 200% compare to the control in the same period of time. (E) BI of cultures (left) recorded without (blue line) and with stimulation (red line). (E1) Box plot of BI (right) during control experiments (blue box) and during CCh treatment (red box). In the analyzed group of experiments, the BI of cultures significantly decreased upon drug administration compared to the control experiments during the entire recording. BI in the first 1 h decreased by 76% respect to the control in the same interval of time. Bold lines and shaded regions (C–E) correspond to mean ± SEM. Gray line corresponds to the basal recording for the two experimental conditions. Gray-shaded area indicates 10 min of recording stop, after CCh addition, to prevent experimental bias due to drug release in the medium. For each box plot (C1–E1), the small square indicates the mean, the central line illustrates the median and the box limits indicate the 25th and 75th percentiles. Whiskers represent the 5th and the 95th percentiles. Statistical Analysis was carried out using Mann–Whitney comparison test, **$p < 0.01$.*

Following the previous results, we analysed the changes of correlation upon CCh administration (see Materials and Methods). The effects of CCh on network activity correlation were visible when comparing the functional connectivity maps at different time points (**Figure 4.3 B).** CCh caused an initial loss of correlation, resulting in 80% decreased of mean STTC values with respect to the basal condition, followed by a partial recovery after a few hours (**Figure 4.3 B**). During the control experiment, only 2% of the STTC values significantly decreased at the end of the recording but the number of links did not change with respect to the basal condition. (**Figure 4.3 C**). In the first few hours following CCh application, the 98% of STTC value significantly decrease with respect to the basal value. Moreover the 5% of the STTC was deleted after the treatment and not recovered after 24 hours.

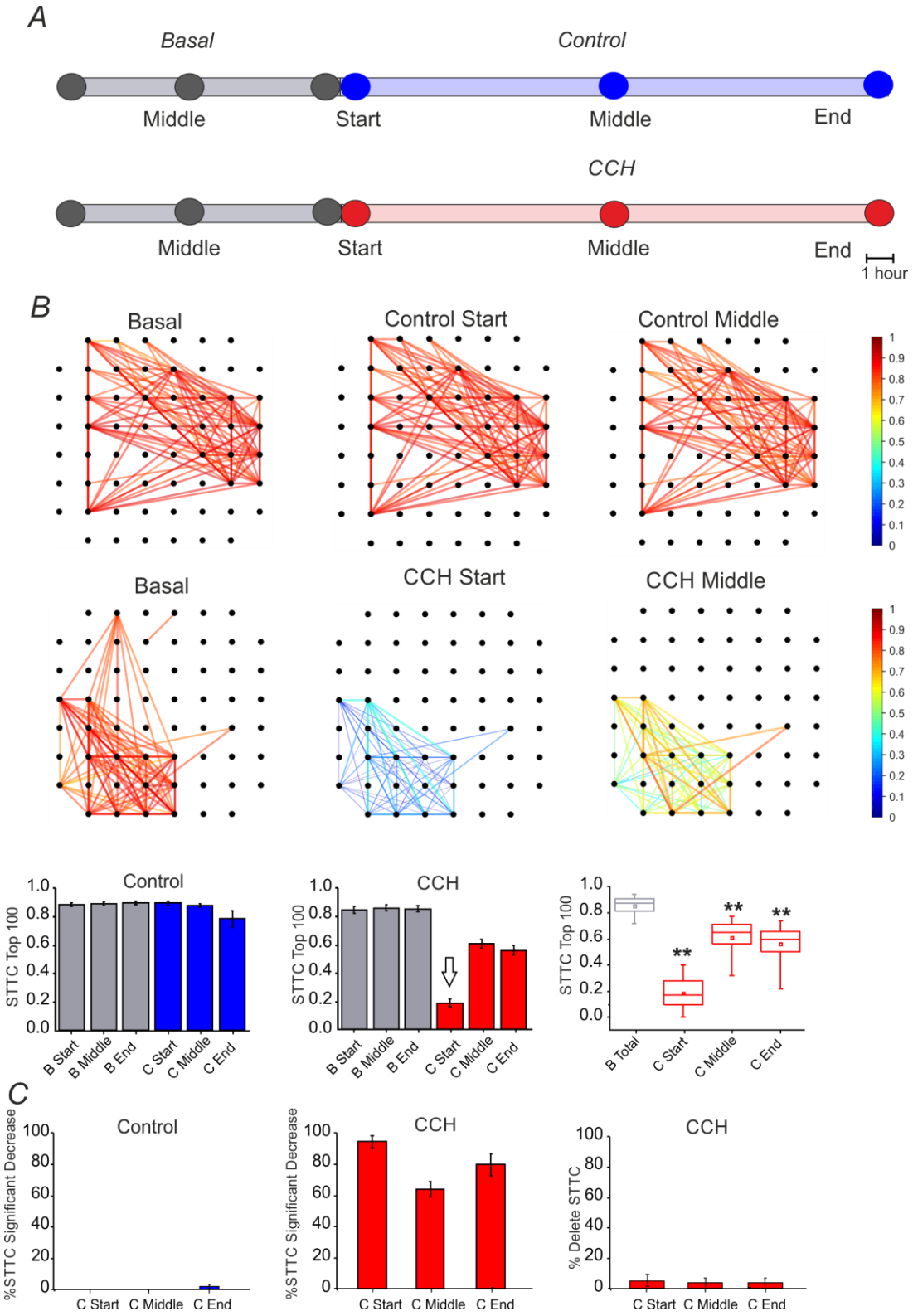

Figure 4.3.Correlation Analysis. (A) One-hour time intervals at three different times considered for the graph of the functional connectivity for each two different experimental conditions. (B) Plot of color-coded functional connectivity of largest 100 values selected during the 7 h of basal recording (i.e., 7 h) for two representative experiments. Top panel: Control experiment did not show variation with respect to the spontaneous condition. In contrast, CCh application caused a complete loss of correlation in the first 1 h with respect to the basal condition, and it did not recover after a few hours (right panels). Bottom panel: Bar plot of largest 100 STTC for non-treated cultures (N = 4) in the basal (gray bar) and in the control (blue bar) condition. Each bar corresponds to one of three different time points of an hour: start, middle, and end for each experimental condition. In the middle, plot of largest 100 STTC for treated cultures (N = 7) in the basal (gray bar) and during the CCh administration (red bar). On the right, box plot of largest 100 STTC for the treated

*experiment evaluated in four different time-point. During the 24 h of CCh application, the SSTC values decreased significantly respect to the 7 h of the basal recording (gray box). White arrow indicates the starting point for CCh treatment. (C) On the left, bar plot of the percentage of STTCs values that significantly decreased (above 20%) respect to the basal in the control condition (blue bar, N = 4) during three different time points (start, middle and end). In the middle, bar plot of the percentage of STTCs values that significantly decreased (above 20%) respect to the basal phase during the CCh administration (red bar, N = 7). On the right, bar plot of the percentage of deleted connections (i.e., STTC) during the CCh application. For box plot (B,C), the small square indicates the mean, the central line illustrates the median and box limits indicate the 25th and 75th percentiles. Whiskers represent the 5th and the 95th percentiles. Statistical Analysis was carried out using Mann–Whitney comparison test, **p < 0.01.*

All main waves (i.e. delta, theta and partly beta), which characterize classical sleep-wake-cycle, are strongly suppressed upon CCh treatment (**Figure 4.4 A**, right panel). Thus we evaluated how the power spectral density (PSD) changed at different time points during both control and CCh protocol **(Figure 4.4 B**). The control experiments indicate that most power is concentrated in the delta frequency band, reflecting very slow oscillations in the LFP that match the appearance of synchronous bursting activity in the MUA (**Figure 4.4 C**, blue line). PSD trend remained stable throughout the recording in the control experiments, whereas CCh application to the culture caused a marked decrease of the low-frequency power in the LFP (especially in the delta and theta range) (**Figure 4.4 C**, red line). The total power in the first hour (i.e. Start) (**Figure 4.4 C**) decreased by 93% in delta, 87% in theta, 50% in beta, and 40% in slow gamma bands with respect to the control experiment. After 12 hours from the treatment (i.e. Middle) **(Figure 4.4 C),** the integrated power in the delta and theta bands shows a partial recovery especially with respect to the first hour: the total reduction drops to 37% for delta and 55% for theta bands. The average PSDs (when considering all phases) globally show marked reduction of power in all frequency bands caused by CCh (62% for delta; 71% for theta; 50% for beta; 43% for gamma).

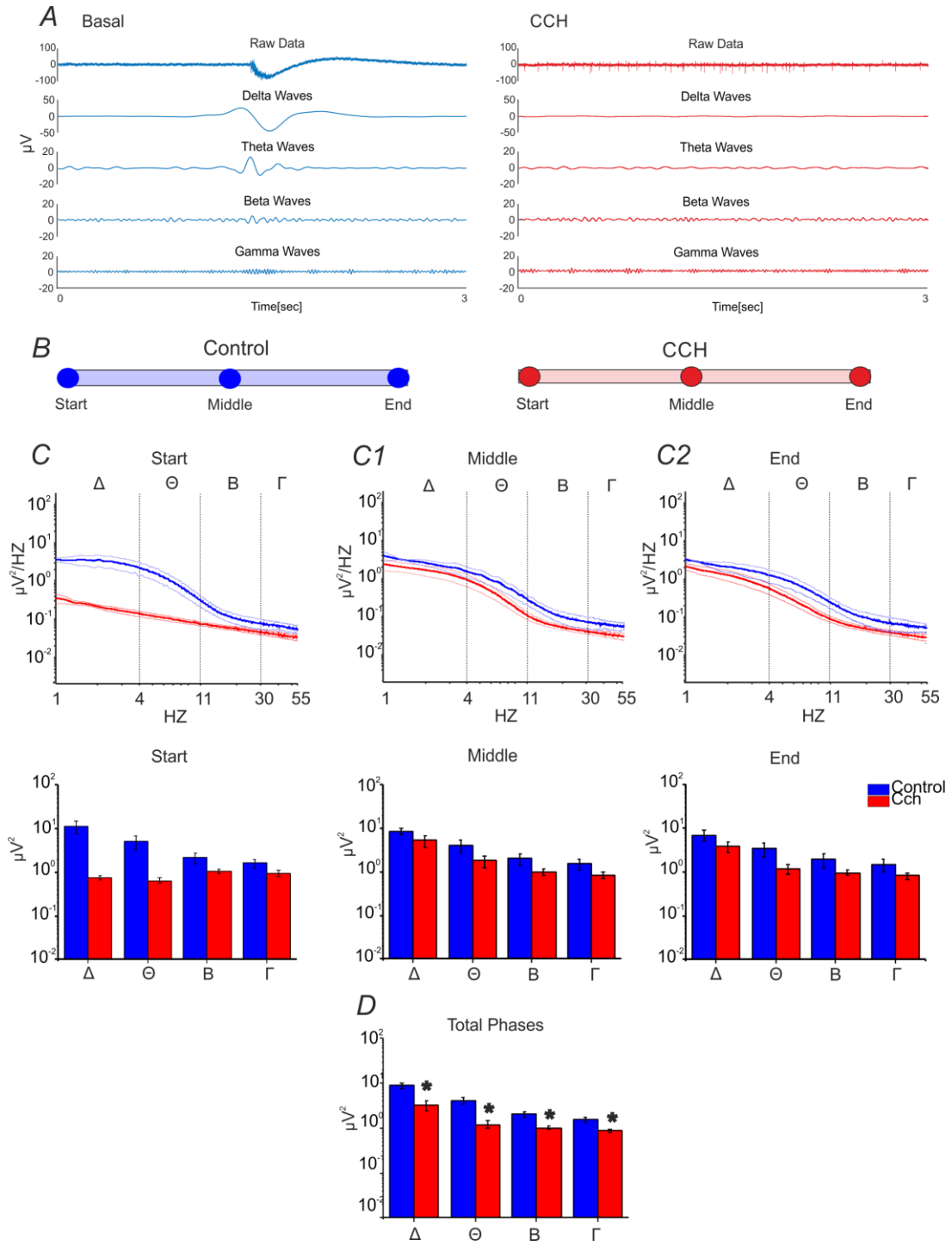

Figure 4.4 LFP analysis. (A) Signal filtered to specific frequency bands involved in the sleep for one channel of a representative experiment. The CCh treatment induced a suppression of the low waves delta (Δ, 1–4 Hz), theta (Θ, 4–11 Hz), beta (B, 11–30 Hz), and gamma (Γ, 30–55 Hz) respect to the control condition. (B) Different time points (1 h long) considered for each two types of experimental condition. (C) PSD during the control phase (N = 2, blue line) and the CCh application (N = 4, red line) in the first 1 h of recording (Top Panel). Bold lines and shaded regions correspond to mean ± SEM. Column bar of integrated PSD per frequency bands in the same time point (Bottom Panel). CCh treatment caused a suppression of the low components of the signal (1–55 Hz). (C1) PSD after 12 h of recording (Top Panel). Column bar of integrated PSD per frequency bands in the same time point (Bottom Panel). (C2) PSD in the last hour of recording (Top Panel). Column bar of integrated PSD per frequency bands in the same time point (Bottom Panel). (D) Column bar of integrated PSD evaluated through the key time points described in (B). The decrease involves in particular the delta and theta frequency bands. (D) Bar plot of the power for all phases in the different frequency ranges for the control experiment (N = 2; Delta Power = 8.87 ± 1.36 μV2; Theta power = 4.15 ± 0.71 μV2; Beta power = 2.03 ± 0.29 μV2; Gamma power = 1.53 ± 0.19 μV2) and for the experiment with the administration of CCh (N = 4; Delta Power = 3.28 ± 0.82 μV2; Theta power = 1.21 ± 0.23 μV2; Beta power = 1.00 ± 0.07 μV2; Gamma power = 0.87 ± 0.07 μV2).

*Statistical analysis was carried out using Mann-Whitney test, *p < 0.01.*

We complemented the electrophysiological study with a gene expression assessment. In particular, we investigated whether the network physiological effects of CCh treatment were corroborated by a gene expression modulation that recapitulated the clock-like and the homeostatic-like aspects of sleep. We performed gene expression analysis of DIV 30 primary rat neurons treated with 20 µM of CCh for 24h and harvested 24h later. Interestingly, two classical immediately early genes (IEG), *Arc* and *Fos* **(Figure 4.5 D),** were upregulated by CCh, *Arc* being significantly overexpressed (p=0.02 control n= 13, CCh treated n=14) **(Figure 4.5 A)**, while *Homer1b/c* was not altered (**Figure 4.5 E**). Moreover, we observed a 50% significant (p=0.02 control n=12, CCh treated n=15) increase of *Per2* gene expression in cultures treated with CCh compared to control cultures (**Figure 4.5 C**). In addition to the classical markers of the circadian and the synaptic homeostasis control of sleep, we tested new genes that play a role in the epigenetic regulatory processes of sleep. In particular, we found that *Dlk1,* a genomic imprinted gene, was significantly (p=0.03 control n=15 CCh treated n=13) downregulated (i.e. by approximately 30%) by Carbachol treatment compared to controls.

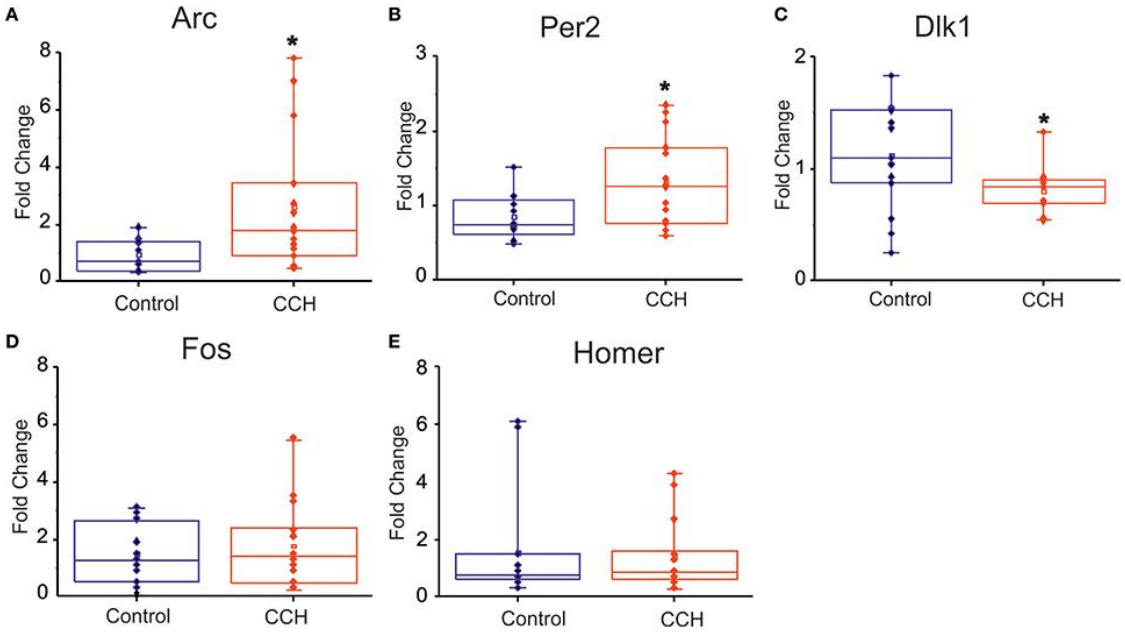

*Figure 4.5 Gene expression analysis following CCh treatment. (A–C) Box plot of Arc, Per2, Dlk1, Fos, Homer1 mRNA levels in primary neuronal rat cultures, treated at DIV 30 with 20 µM of CCh or with normal medium as control. For each box plot (A–E), the small square indicates the mean, the central line illustrates the median and box limits indicate the 25th and 75th percentiles. Whiskers represent the 5th and the 95th percentiles. Raw data are plotted as blue and red dots, respectively for control and CCH treatments. The dots represent data from three different experiments. *p < 0.05 after Student.*

4.3 Discussion

In this study we presented electrophysiological and genetic evidence that primary cortical cultures, usually displaying synchronized low-frequency firing patterns under spontaneous conditions, are able to encompass some essential features of sleep in a controllable way. LFP analysis complemented MUA analysis and allowed us to look for classical sleep electrophysiological signatures (i.e. slow waves) in our simplified *in vitro* experimental model. In fact, we found that under spontaneous condition most LFP power was actually confined to the delta frequency range, as it can be usually observed in the EEG signal during NREM phase in sleeping rodents (Steriade et al., 1993). In addition, *in vivo* these waves were found to be negatively correlated with the response to arousing stimuli (Neckelmann and Ursin, 1993). These observations suggest that cortical cultures are usually characterized by a sleep-like state, confirming recent data from several different laboratories (Sengupta et al., 2011;Hinard et al., 2012). Since cortical cultures spontaneously lack sleep-wake rhythm that occurs in *in vivo* systems, we tested whether we could mimic wake-like states by chemical manipulation, in order to use this as a simplified and easily controllable experimental model to investigate sleep more completely. The application of CCh resulted to be an efficient experimental strategy to suppress classical sleep-like properties of activity, resulting in an asynchronous firing pattern with many isolated spikes. In fact, while the percentage of isolated spikes increased significantly upon CCh stimulation, the burstiness level markedly decreased. Similarly, the correlation of activity dropped in the first one hour after CCh treatment, while the firing rate increased. The value of STTC remained significantly low during the entire recording. The percentages of decreased STTC values remain higher during the 24 hours of the CCh application. Moreover, the administration of CCh induced a suppression of delta and theta waves, a range encompassing the entire spectrum of sleep *in vivo.* These changes testify for a significant alteration of sleep-like states in the network but, surprisingly, beta and low-gamma waves, which are typically present during wakefulness and REM sleep, do not show power variations compared to the low frequency components of the signal. This study demonstrates that wake-like and sleep-like electrophysiological signatures can be dissociated *in vitro* and, possibly studied independently within this experimental model. Furthermore, we demonstrated that CCh alters specific sleep-like signatures.

As a complement of the above conclusions, gene expression profile in our study confirmed an effect on the circadian and the synaptic homeostatic components. Our results demonstrated that CCh exerts a significant role in activating molecular markers of sleep-wake rhythms, for example *Per2* expression. Yet, we showed that classical sleep-dependent IEGs (Cirelli et al., 2006) are also essential in neuronal responses of our in vitro experimental model. However, Homer1b/c, a gene considered as a molecular marker of the synaptic excitability response to stimulation (Ango et al., 2000;Nakano-

Kobayashi et al., 2014;Cao et al., 2015), was not affected by the treatment. Moreover, it raises also a new possibility: can we use in vitro experimental model to dissect molecular markers of synaptic homeostasis and circadian control of sleep? Indeed, PER2 is a marker of the circadian control of sleep (Kopp et al., 2002;Shiromani et al., 2004) while Homer1b/c is an important marker of neuronal excitatory synapses activity. In addition we have shown that *Dlk1* is a molecular marker of sleep-like electrophysiological aspects in vitro, confirming recent evidence *in vivo* (Tinarelli et al., 2014).

Altogether our results demonstrate that our experimental model in cultures is not able to reproduce an awake-like state, however it is a promising model to manipulate and study sleep properties in a very controlled way.

In conclusion, this study shows that MEA recordings coupled to cortical cultures represent a favorable model to investigate the essential neuronal network features of sleep *in vitro*. We envisage that sleep-related electrophysiological phenotypes can be assessed by using *in vitro* experimental models. In particular, the combination of new gene editing technologies such as CRISPR/cas9 system and MEA recordings has the potential to accelerate the investigation of loss or gain of function due to gene mutations in sleep studies.

Related publications and/or conference abstracts

1) **International journals**

- **Colombi, I**., Mahajani, S., Frega, M., Gasparini, L., and Chiappalone, M. (2013). Effects of antiepileptic drugs on hippocampal neurons coupled to micro-electrode arrays. Front Neuroeng 6, 10.
- **Colombi, I.**, Tinarelli, F., Pasquale, V., Tucci, V., and Chiappalone, M. (2016). A simplified in vitro experimental model encompasses the essential features of sleep. Frontiers in Neuroscience 10.

2) **Conference proceeding**

Colombi I, Tinarelli F, Pasquale V, Tucci V, Chiappalone M. Circadian rhythm monitoring and manipulation in neural assemblies. MEA Meeting 2016 | 10th International Meeting on Substrate-Integrated Electrode Arrays, Reutlingen, Germany, 28 Jun - 1 Jul, 2016.

3) **Oral presentations**

- Dissociated *in vitro* cultures recapitulates the main features of sleep *in vivo*. GDR 2904 Multielectrode systems for Neuroscience: 6th annual meeting 5-8 Jan 2016, Grenoble-Autrans, France
- Dissociated *in vitro* cultures recapitulated the essential features of sleep, invited by Dr T. Nieus and Dr Marcello Massimini, 15 March 2017, Ospedale Luigi Sacco

References

Ango, F., Pin, J.-P., Tu, J.C., Xiao, B., Worley, P.F., Bockaert, J., and Fagni, L. (2000). Dendritic and axonal targeting of type 5 metabotropic glutamate receptor is regulated by homer1 proteins and neuronal excitation. *Journal of Neuroscience* 20**,** 8710-8716.

Bologna, L.L., Pasquale, V., Garofalo, M., Gandolfo, M., Baljon, P.L., Maccione, A., Martinoia, S., and Chiappalone, M. (2010). Investigating neuronal activity by SPYCODE multi-channel data analyzer. *Neural Netw* 23**,** 685-697.

Cao, L., Tian, Y., Jiang, Y., Zhang, G.-J., Lei, H., and Di, Z.-L. (2015). Down-regulation of Homer1b/c protects against chemically induced seizures through inhibition of mTOR signaling. *Cellular Physiology and Biochemistry* 35**,** 1633-1642.

Chiappalone, M., Novellino, A., Vajda, I., Vato, A., Martinoia, S., and Van Pelt, J. (2005). Burst detection algorithms for the analysis of spatio-temporal patterns in cortical networks of neurons. *Neurocomputing* 65**,** 653-662.

Chiappalone, M., Vato, A., Berdondini, L., Koudelka-Hep, M., and Martinoia, S. (2007). Network dynamics and synchronous activity in cultured cortical neurons. *International journal of neural systems* 17**,** 87-103.

Cirelli, C., Faraguna, U., and Tononi, G. (2006). Changes in brain gene expression after long‐term sleep deprivation. *Journal of neurochemistry* 98**,** 1632-1645.

Colombi, I., Mahajani, S., Frega, M., Gasparini, L., and Chiappalone, M. (2013). Effects of antiepileptic drugs on hippocampal neurons coupled to micro-electrode arrays. *Front Neuroeng* 6**,** 10.

Colombi, I., Tinarelli, F., Pasquale, V., Tucci, V., and Chiappalone, M. (2016). A simplified in vitro experimental model encompasses the essential features of sleep. *Frontiers in Neuroscience* 10.

Corner, M.A. (2008). Spontaneous neuronal burst discharges as dependent and independent variables in the maturation of cerebral cortex tissue cultured in vitro: a review of activity-dependent studies in live 'model' systems for the development of intrinsically generated bioelectric slow-wave sleep patterns. *Brain Res Rev* 59**,** 221-244.

Cutts, C.S., and Eglen, S.J. (2014). Detecting pairwise correlations in spike trains: an objective comparison of methods and application to the study of retinal waves. *J Neurosci* 34**,** 14288-14303.

Eytan, D., and Marom, S. (2006). Dynamics and effective topology underlying synchronization in networks of cortical neurons. *The Journal of neuroscience* 26**,** 8465-8476.

Frega, M., Pasquale, V., Tedesco, M., Marcoli, M., Contestabile, A., Nanni, M., Bonzano, L., Maura, G., and Chiappalone, M. (2012). Cortical cultures coupled to micro-electrode arrays: a novel approach to perform in vitro excitotoxicity testing. *Neurotoxicol Teratol* 34**,** 116-127.

Hinard, V., Mikhail, C., Pradervand, S., Curie, T., Houtkooper, R.H., Auwerx, J., Franken, P., and Tafti, M. (2012). Key electrophysiological, molecular, and metabolic signatures of sleep and wakefulness revealed in primary cortical cultures. *J Neurosci* 32**,** 12506-12517.

Kaufman, M., Corner, M.A., and Ziv, N.E. (2012). Long-term relationships between cholinergic tone, synchronous bursting and synaptic remodeling. *PLoS One* 7**,** e40980.

Kopp, C., Albrecht, U., Zheng, B., and Tobler, I. (2002). Homeostatic sleep regulation is preserved in mPer1 and mPer2 mutant mice. *European Journal of Neuroscience* 16**,** 1099-1106.

Leondopulos, S.S., Boehler, M.D., Wheeler, B.C., and Brewer, G.J. (2012). Chronic stimulation of cultured neuronal networks boosts low-frequency oscillatory activity at theta and gamma with spikes phase-locked to gamma frequencies. *J Neural Eng* 9**,** 026015.

Maeda, E., Robinson, H., and Kawana, A. (1995). The mechanisms of generation and propagation of synchronized bursting in developing networks of cortical neurons. *The Journal of*

neuroscience 15**,** 6834-6845.
Nakano-Kobayashi, A., Tai, Y., Kasri, N.N., and Van Aelst, L. (2014). The X-linked mental retardation protein OPHN1 interacts with Homer1b/c to control spine endocytic zone positioning and expression of synaptic potentiation. *Journal of Neuroscience* 34**,** 8665-8671.
Neckelmann, D., and Ursin, R. (1993). Sleep stages and EEG power spectrum in relation to acoustical stimulus arousal threshold in the rat. *Sleep* 16**,** 467-477.
Sengupta, P., Davis, C., Clinton, J., Roy, S., and Krueger, J. (Year). "Networks of cultured neurons show oscillatory dynamics", in: *Sleep*: AMER ACAD SLEEP MEDICINE ONE WESTBROOK CORPORATE CTR, STE 920, WESTCHESTER, IL 60154 USA), A36-A37.
Shiromani, P.J., Xu, M., Winston, E.M., Shiromani, S.N., Gerashchenko, D., and Weaver, D.R. (2004). Sleep rhythmicity and homeostasis in mice with targeted disruption of mPeriod genes. *American Journal of Physiology-Regulatory, Integrative and Comparative Physiology* 287**,** R47-R57.
Steriade, M., Mccormick, D.A., and Sejnowski, T.J. (1993). Thalamocortical oscillations in the sleeping and aroused brain. *Science* 262**,** 679-685.
Tateno, T., Jimbo, Y., and Robinson, H.P. (2005). Spatio-temporal cholinergic modulation in cultured networks of rat cortical neurons: spontaneous activity. *Neuroscience* 134**,** 425-437.
Tinarelli, F., Garcia-Garcia, C., Nicassio, F., and Tucci, V. (2014). Parent-of-origin genetic background affects the transcriptional levels of circadian and neuronal plasticity genes following sleep loss. *Philos Trans R Soc Lond B Biol Sci* 369**,** 20120471.
Van Pelt, J., Wolters, P.S., Corner, M.A., Rutten, W.L., and Ramakers, G.J. (2004). Long-term characterization of firing dynamics of spontaneous bursts in cultured neural networks. *Biomedical Engineering, IEEE Transactions on* 51**,** 2051-2062.
Wagenaar, D.A., Madhavan, R., Pine, J., and Potter, S.M. (2005). Controlling bursting in cortical cultures with closed-loop multi-electrode stimulation. *J Neurosci* 25**,** 680-688.

Chapter 5

Measurement of the perturbation complexity index during alteration of sleep-like properties

In the previous chapter, we showed that cell cultures plated over MEA display a spontaneous activity that is characterized by a firing regime that resembles that of the sleep-like state (Hinard et al., 2012;Colombi et al., 2016;Saberi-Moghadam et al., 2018). By treating our cultures with Carbachol, we are able to induce suppression of the sleep state by desynchronizing the neuronal activity and thus alter sleep-like properties in an *in vitro* model (Colombi et al., 2016).

Starting from these findings, we began a collaboration with the group led by Dr. M. Massimini at the *Dipartimento di Scienze Biomediche e Cliniche "L. Sacco"* in Milan. The main goal of the group is to assess the level of consciousness in human subjects during wakefulness, NREM and REM sleep under both physiological and pathological conditions. With this collaboration we aim to understand if Carbachol administration to cortical cultures is sufficient to induce changes in the complexity of the response, similar to those observed in human subjects during REM sleep or wakefulness.

Indeed, 2013, Massimini and coauthors introduced an empirical measure of brain complexity called the perturbation complexity index (PCI) (Casali et al., 2013).PCI is used in human research to quantify the complexity of spatiotemporal responses recorded with EEG to transcranial magnetic stimulation (TMS); it permits assessment of the level of consciousness of human subjects. During sleep, a TMS pulse either evokes a local EEG response (e.g., to a low-amplitude pulse) or a global but stereotypical EEG response across all electrodes (e.g., to a high-amplitude pulse) (Huber et al., 2012).In TMS/EEG experiments, the most striking difference between wakefulness and sleep is found not in the amplitude of the TMS/EEG responses but in the ‘richness’ of the peaks and troughs in the responses observed during wakefulness (Tononi et al., 1998;Massimini et al., 2005).

The PCI aims to summarize the TMS/EEG responses in different brain states using a single number. As a first step, it is necessary to quantify the number of significant activations that occur due to the stimulation. To do this, bootstrap statistics are applied to the pre-stimulus activity to determine the threshold of any significant deviation from baseline activity for each electrode. Second, the response of each electrode is compared to its own threshold, and significant activations are established (1 indicates significant activation, and 0 indicates non significant activation), forming a spatiotemporal binary matrix (S(x,t)). To quantify the ‘complexity’ of the response matrix S(x,t), a Lempel-Ziv

compression algorithm is then used (further details are given in Casali et al. 2013).

According to the mathematical definition, PCI is low when the interaction between cortical areas is low (loss of integration) or when many interacting areas all react to the perturbation in a stereotypical way (loss of differentiation). In contrast, PCI is high if the initial perturbation is transmitted to a large integrated area that subsequently responds differently by generating a spatiotemporal pattern of activation that cannot be easily compressed. Indeed, PCI was found to be high when consciousness is present (i.e., during wakefulness) and low whenever consciousness is lost, for example, during sleep, anesthesia, and coma (Tononi, 2004;Seth et al., 2008;Boly, 2011).

In 2013 Casali et al. (Casali et al., 2013) quantified PCI in a large dataset of TMS/EEG recordings (208 sessions involving 52 subjects) obtained from healthy subjects during wakefulness, NREM sleep and various sedated states (**Figure 5.1**). During wakefulness, PCI was indeed the highest because TMS triggered a widespread and differentiated activity response. Upon loss of consciousness, the complex pattern of causal interactions observed during wakefulness collapsed into a stereotypical slow wave, and PCI decreased.

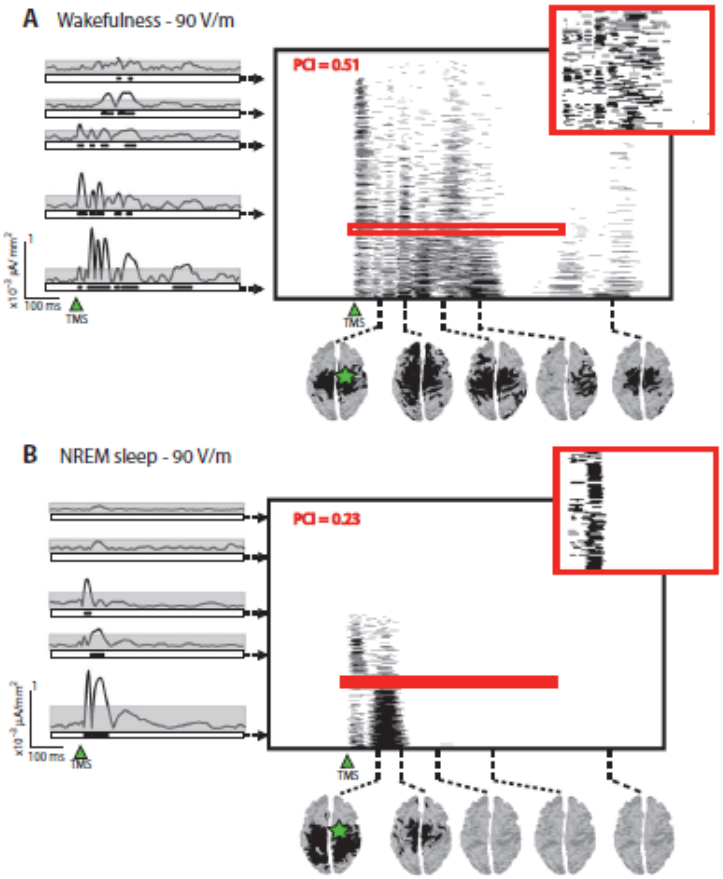

Figure 5.1 PCI measurement during wakefulness and REM sleep captures integration and differentiation of the activity. The green star indicates the site of TMS stimulation (from Massimini et al. *2005)*

These slow waves represent a default pattern of activity that also emerges from cortical networks under conditions of functional or anatomical disconnection (Chapter 3, Paragraph 3.3).

A recent study showed that acute cortical slices can be induced to oscillate between low- and high-complexity states of evoked activity by application of a cocktail of neuromodulators that includes Norepinephrine and Carbachol (D'andola et al., 2017).

Here, we were interested in determining whether we could observe systematic changes in the complexity of the responses in a simplified model of cortical networks, namely cortical cultures. We stimulated the cell cultures using single shocks with an interstimulus interval of 5 seconds (~120 trials) to find the significant component of the response (i.e., the significant response) with respect to the prestimulus activity. To do this, we analyzed the spiking activity and adapted the statistics (see the preceding step 1) to define the S(x,t) matrix in cortical cultures under different conditions (basal *versus* CCh administration).

We demonstrated that PCI could be effectively modulated by pharmacological application of CCh, paving the way for the possibility of studying some features of consciousness using cell culture networks.

5.1 Materials and methods

5.1.2 Cell cultures & Micro-Electrode Array recordings

Cortical cell cultures prepared from embryonic rats at gestational day 18 were plated on 60-channel MEAs (Multi Channel Systems, MCS, Reutlingen, Germany) that had been previously coated with borate buffer and poly-L-lysine to promote cell adhesion (final cell density approximately 1200 cells/mm^2). The details of the procedure used to obtain the cultures are described in section 4.1.1 of Chapter 4. After a period of rest (~30 minutes) outside the incubator to allow the culture to adapt to the new environment and reach a stable level of activity, the spontaneous activity of the culture was monitored and recorded for 30 minutes.

5.1.2 Experimental protocol

The experimental protocol included 30 minutes of basal recording (i.e., in Neurobasal medium) followed by two sessions of electrical stimulation (10 minutes each) at two different sites. We applied CCh (20 μm) by directly pipetting it into the culture medium and recorded from the cultures for 1 hour in the absence of electrical stimulation. Since we observed that mechanical perturbation caused by the addition of CCh to the medium through a pipette can cause temporary instability of the firing rate, we discarded the first 10 minutes of recording following CCh administration. After one hour, we

repeated the electrical stimulation protocol in the presence of CCh, using the same locations for stimulation and performing the stimulation in the same order that was used in the basal recording.

For each stimulation session (duration 10 minutes), a total of 120 trials per stimulation site were collected. The stimulus was the same across all experiments and all experimental phases (biphasic voltage pulse, duration 600 μs, 750 mV half-amplitude every 5 seconds). These parameters have been shown to be the most effective parameters for evoking responses in neurons cultured on MEAs (Wagenaar 2004). A total of 9 experiments were performed using cultures at 34 ± 3 DIVs.

5.1.3 Data analysis

MUA activity

In the high-pass filtered data (f>300 Hz), we detected spikes (i.e., single over-threshold peaks) and bursts (i.e., groups of tightly packed spikes) using custom software developed in our laboratory (Bologna et al., 2010) (see Chapter 2). We then computed the following electrophysiological parameters, which were also used in our previous work (Colombi et al., Chapter 4): Mean Firing Rate (MFR, spikes/sec), Inverse Burst Ratio (IBR, percentage of spike outside the burst) and Burstiness Index (BI, index of the burstiness level of the network).

To investigate the effect of the electrical stimulation on the neuronal activity, we computed the PSTH, which reflects the mean impulse response of each site to the stimulation. The PSTH was calculated by considering 400-ms time windows in the recordings that followed each stimulus. We first divided each time window into 4-ms bins and then counted the number of spikes that occurred in each time bin. Finally, we normalized the spike count per time bin by the number of trial times the bin size (Chiappalone et al., 2008). With this definition, all channels with PSTH area below '1' were removed from the statistical analysis because they were considered to be inactive (i.e., not able to evoke a minimal response to stimulation).

We computed the percentage of variation of the PSTH area as follows:

$$\Delta = \frac{100 * XEnd - Xstart}{Xstart}$$

We defined as significant a channel that displayed changes in PSTH higher or lower than a specific threshold that was defined based on the 'stability' phases. We selected as stability phases the stimulation sessions during the evoked activity without CCh. Specifically, we divided every stimulation session (S1 or S2) into two equal parts of 5 minutes each. For each divided session of 5 consecutive minutes, we computed the histogram of the variation in PSTH area (ΔSTIM1, ΔSTIM2) as depicted in **Figure 5.2**. The threshold was defined as the mean+ 2SD of the PSTH area variation

(i.e., 20%).

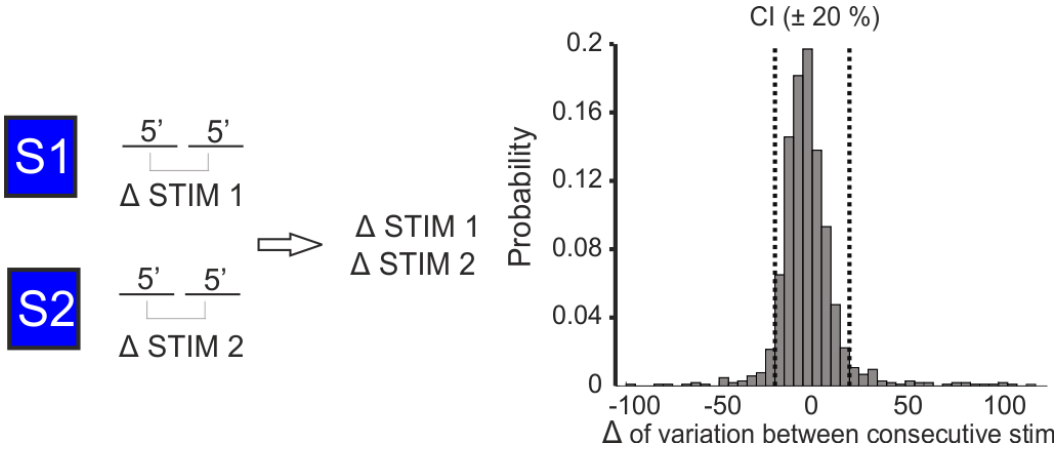

Figure 5.2 Selection of the threshold during the stability phases.

Perturbation Complexity Index

We quantified the perturbation complexity index (PCI) in cortical cell cultures by analyzing the evoked spiking activity.

Compared to the human data, cortical cultures yielded a higher signal-to-noise ratio; therefore, we used a smaller number of trials (60 to 120) and simpler statistics to assess the significant evoked activity.

The activity of each channel was binned (bin size=5 ms or 20 ms) around the stimulation artifact (1000 ms before and 500 ms after the stimulus). As the threshold for significant activation of a channel, we selected the mean+-K*std of the prestimulus activity (K = number of standard deviations). We found that K=1 (i.e., one standard deviation) sufficed to limit the detection of false activations in the baseline ($\sim<10^{-5}$).

We then extracted a binary matrix of significant sources (SS(x,t)) that represents the spatial (channel x) and temporal (time t after stimulation) activations caused by the electrical perturbation (Casali et al. 2013). The channels in the matrix SS(x,t) are sorted from bottom to top on the basis of their total activity during the poststimulus period (i.e., according to the number of activations). To quantify the minimal amount of redundant information contained in the binary matrix S(x,t), the matrix was compressed using the Lempel-Ziv complexity measure. Finally, PCI is defined as the Lempel-Ziv complexity measure normalized between [0,1] to make the PCI comparable across conditions (e.g., carbachol treatment).

LFP Activity

To select the LFP components, we low-pass-filtered the raw data between 1 and 300 Hz. We then

computed the power spectral density of the decimated signal (sampling frequency 1 kHz) ($\mu V^2/Hz$), using the Welch method (Windows=5s, overlap=50%). We considered only the lower frequency bands of the signal, in particular the delta (1-4 Hz), theta (4-11 Hz) and beta (11-30 Hz) bands, which are of particular interest in studies of the sleep-wake cycle. To characterize the LFP, we calculated the power in each of those frequency bands.

For the stimulation phase, we computed the mean response to the stimulation pulse for the top 20 channels for each culture that displayed the highest MFR. We then considered the response to the stimulation (100 ms before and 900 ms after the stimulus) and repeated the analysis described above, computing the power in each frequency band. To eliminate the artifact, we discarded the first 10 ms after the stimulus. PSD was computed using the Pwelch function in MATLAB with the following parameters: win=200 ms, overlap=50%, Fs=1e3 and Max frequency =100 Hz.

5.2 Results

We performed experiments using rat cortical cultures plated on MEA according to the protocol depicted in **Figure 5.3A**. Since we observed that the electrophysiological parameters were not stable during the first 30 minutes after CCh administration (20 uM), we divided the CCh recording phase into CCh 30' and CCh 50' (i.e., the first 30 minutes and the last 20 minutes, respectively). We normalized each experiment with respect to the mean of the selected parameter (i.e., MFR, IBR and BI) during the basal recording.

No significant differences in the level of activity expressed by MFR were observed during the application of the experimental protocol. However, CCh application resulted in an increase in the number of isolated spikes (i.e., higher IBR) and a decrease in the burstiness index (BI) with respect to the basal phase, indicating a loss of bursting activity followed by a loss of synchronicity.

We evaluated the network activity correlation using the STTC method (see Chapter 2, paragraph 2.4.2 REF). As shown in panel E of **Figure 5.3**, during the basal phase (blue box) the STTC was high since the activity was strongly correlated. After administration of CCh, there was a progressive and significant decrease in the STTC values, indicating desynchronization of the activity.

Indeed, the results obtained in cultures treated with CCh are consistent with the results obtained previously using embryonic rat cortical cultures coupled to MEA(Colombi et al., 2016) (Chapter 4 paragraph 4.2).

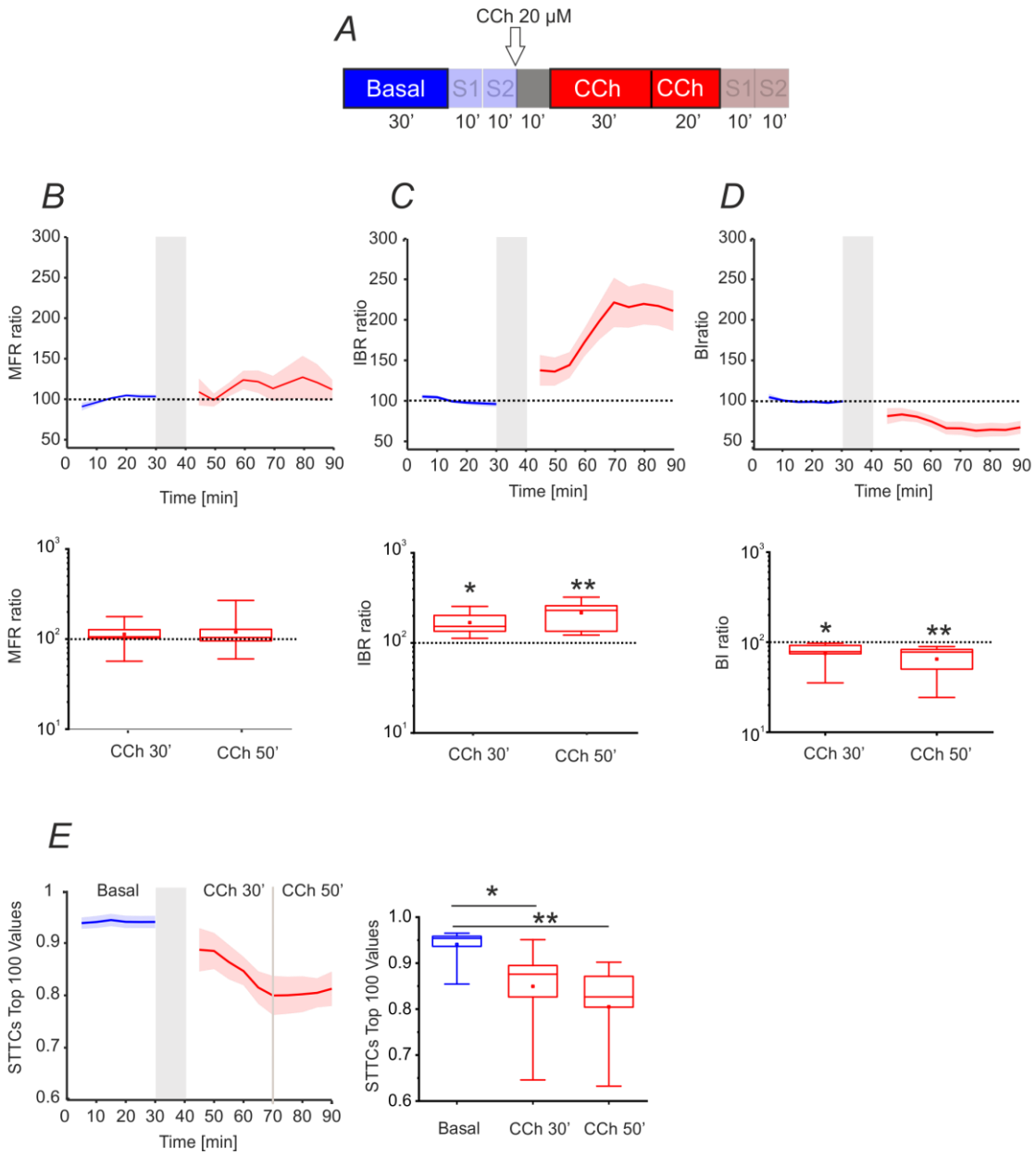

*Figure 5.3. Comparison of the network parameters during basal and CCh administration. A) Experimental protocol adopted in the experiments. The spontaneous phase (*i.e., *without electrical stimulation), which was analyzed here, is highlighted. Cortical cultures were recorded for 30' under basal conditions followed by 1 h of recording after the addition of 20 µM CCh. B) MFR of cultures under basal conditions and during CCh stimulation (n=10). Box plot of MFR (right) during CCh treatment (red box at two different time intervals: the first 30' (CCh 30') and the last 20' (CCh 50'). In the group of experiments analyzed here, the MFR of cultures did not change with respect to the basal phase after drug administration (dotted line in the figure). C) IBR of cultures during basal and CCh stimulation (n=10). Box plot of IBR (right) during CCh treatment (red box at two different time intervals: the first 30' (CCh 30') and the last 20' (CCh 50'). In the analyzed group of experiments, the IBR of the cultures significantly increased after drug administration compared to the basal phase (dotted line in the figure). (D) BI of cultures under basal conditions and during CCh stimulation (n=10). A box plot of BI (right) during CCh treatment (red box) at two different time intervals the first 30' (CCh 30') and the last 20' (CCh 50') is shown. In the analyzed group of experiments, the BI of cultures upon drug administration did not change with respect to the basal phase (dotted line in the figure). E) STTC values of cultures under basal conditions and during CCh stimulation (n=10). A box plot of the STTC values (right) during the basal phase (blue box) and during CCh treatment (red box) at two different time intervals the first 30' (CCh 30') and the last 20' (CCh 50') is shown. In the analyzed group of experiments, the STTCs of the cultures increased significantly after drug administration compared to the basal phase. The bold lines and shaded regions (B-E) correspond to the mean ± SEM. The gray shaded area denotes a 10-min pause in the recording after CCh addition to prevent experimental bias due to drug release into the medium. For each box plot (B-E), the small square indicates the mean, the central line illustrates the median, and the box limits indicate the 25th and 75th percentiles. Whiskers represent the 5th and the 95th percentiles. Statistical analysis was*

*conducted using the Mann-Whitney comparison test; **p < 0.01.*

Next, we analyzed the changes in the effect of electrical stimulation by comparing the PSTH area at baseline with that observed after CCh administration (**Figure 5.4A**). **Figure 5.4B** depicts the network PSTH observed in one representative experiment during the basal (blue line) and CCh phases for both stimulation sites (dark red line). More than 50% of the channels showed a significant decrease in PSTH area compared to the basal condition (**Figure 5.4C**). We did not find any differences in the PSTH area between the two stimulation sessions, indicating that this reduction did not depend on the order of stimulation. The histogram of the percentage of variation of the PSTH area for each active electrode showed a negative median value for both stimulation sites (**Figure 5.4D**).

These effects are consistent with previous reports based on EEG data obtained in humans with TMS stimulation (Massimini, 2005). In fact, TMS-evoked responses during sleep showed higher EEG signals than those recorded during wakefulness.

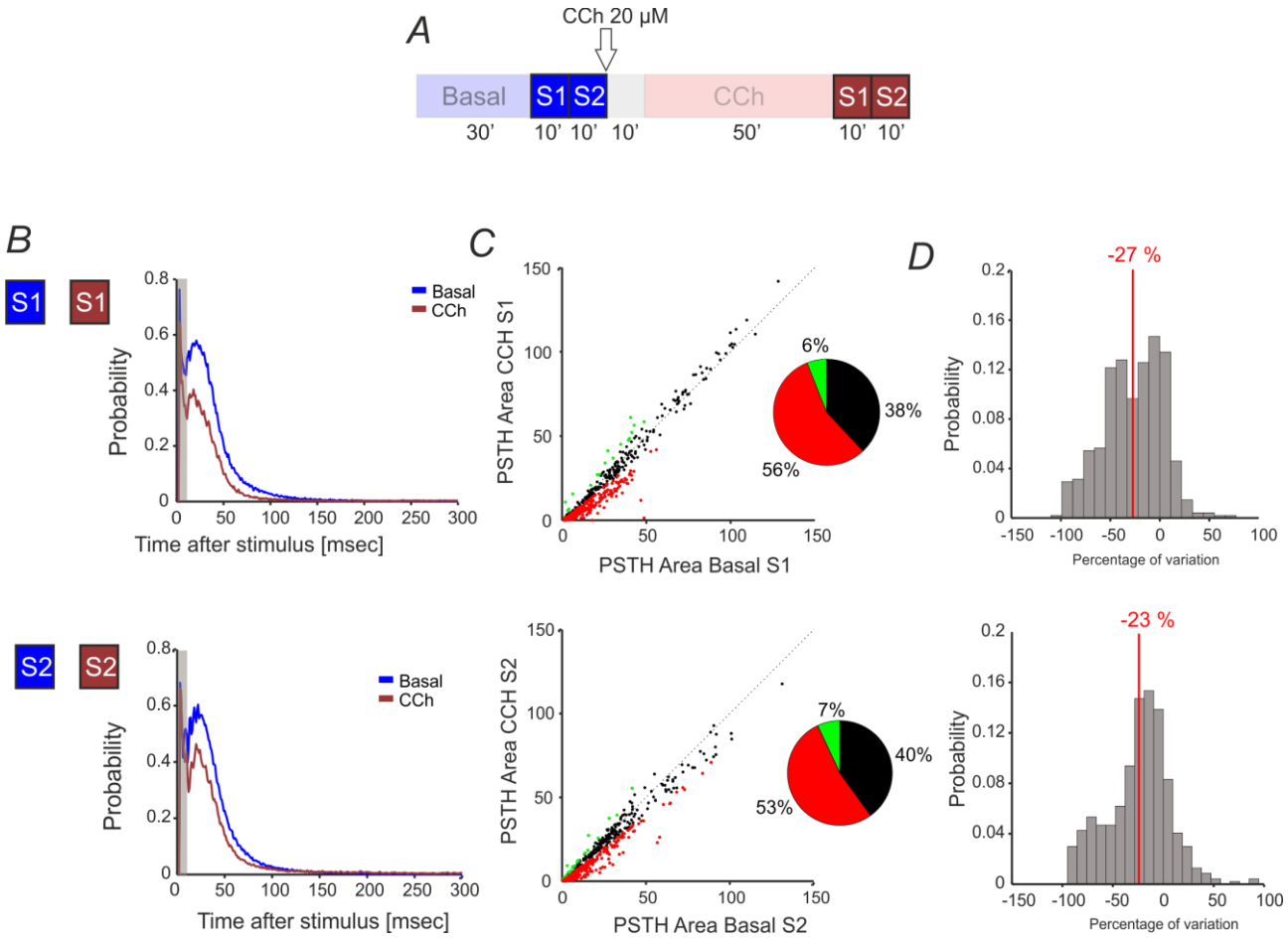

Figure 5.4 PSTH area analysis. A) Experimental protocol adopted for the experiments. Cultures were recorded at 30 DIVs. The stimulation phase analyzed here is highlighted. Cortical cultures were stimulated for 10 minutes at two different sites under basal conditions and after CCh treatment. B) Network PSTH measured in one representative experiment during both stimulation sessions under basal conditions (blue lines) and after CCh treatment (dark red lines). C) The PSTH area for both stimulation sessions showed a higher percentage of channels that decreased relative to the basal level. The variation of each channel was considered significant if it was greater than 20% of the threshold computed by

measuring the variation during the stability phases. Red dots indicate channels that significant decrease with respect to the basal conditions, green dots indicate channels that significant increase and black channels are the ones that did not changed. D) The histogram of the percentage of variation for both stimulation sessions showed a peak centered at -27 for stimulus 1 and a peak centered at -23 for stimulus 2.

As we previously showed in Chapter 4, all of the main waves (i.e., delta, theta and to some extent beta) that characterize the classical sleep-wake cycle are strongly suppressed upon CCh treatment, as shown in **Figure 5.5 B** (left and center panels). We decided to not include the results on gamma bands since we did not found any difference upon CCh administration in the previous chapter (see Chapter 4). Thus, we evaluated how the power spectral density (PSD) changed during the CCh protocol.

Spontaneous activity was characterized by very slow oscillations in the LFP; indeed, most of the power is concentrated in the delta frequency band (**Figure 5.5 C**, blue line). Application of CCh to the cultures resulted in a marked decrease in the low-frequency power in the LFP, especially in the delta and theta ranges (**Figure 5.5 B**, red line). The normalized powers in those frequency bands showed a significant decrease with respect to the basal phase, as indicated by the dashed line in **Figure 5.5 C**. In comparing the variation during the first 30 minutes upon CCh administartion (CCh 30') and the last 20 minutes (CCh 50'), we found a significant decrease in delta and theta power in both phases. Beta power show a decrease of the power but we did not found any statistically difference.

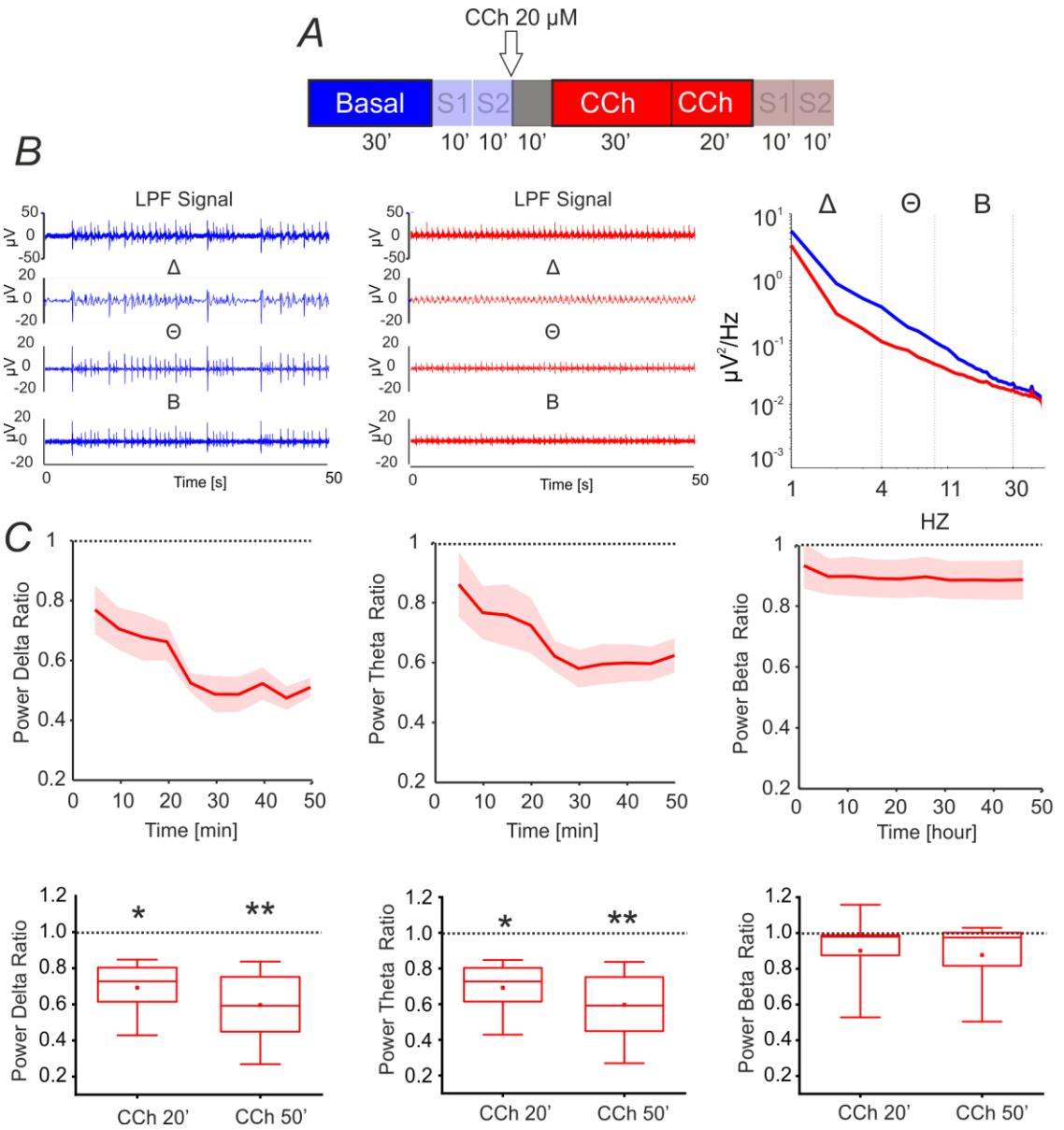

*Figure 5.5Analysis of local field potentials (LFP) during the basal and CCh phases. A) Experimental protocol adopted for the experiments. The spontaneous phase (*i.e.*, without electrical stimulation) analyzed here is highlighted. Cortical cultures were recorded for 30' under basal conditions followed by 1 h of recording after the addition of 20 µM CCh. B) Signal filtered to specific frequency bands involved in sleep for one channel of a representative experiment: Low Pass Filtered signal (LFP signal, 1-300 Hz), delta frequency signal (Δ, 1-4 Hz), theta frequency signal (Θ, 5-9 Hz) and beta frequency signal (B, 10-30 Hz). CCh treatment induced suppression of all low-frequency waves compared to the control condition. C) Time course of the power spectral density ratio computed in delta, theta and beta power. (Below) Box plot comparison of the PSD of each band showing a marked decrease in the delta and theta bands. We did not find any difference in the PSD in the beta bands. The bold lines and shaded regions (C) correspond to the mean ± SEM. In each box plot, the small square indicates the mean, the central line illustrates the median, and the box limits indicate the 25th and 75th percentiles. Whiskers represent the 5th and the 95th percentiles. Statistical analysis was conducted using the Mann-Whitney comparison test; **p < 0.01.*

CCh treatment also caused strong suppression of the power of the LFP evoked response, as shown in the evoked LFP signal of the top 20 channels of one representative experiment under the basal condition (blue lines) and after CCh administration (**Figure 5.6. B**). The top 20 channels were selected on the basis of their firing rates in the spontaneous phase. CCh caused a decrease in the amplitude without any apparent changes in morphology, as shown in the power spectral density

evaluation computed for all channels.

As expected, we found a significant decrease in the power of the delta, theta and beta bands in the first stimulation session. In the second stimulation session, we found no difference between the basal and CCh-evoked responses.

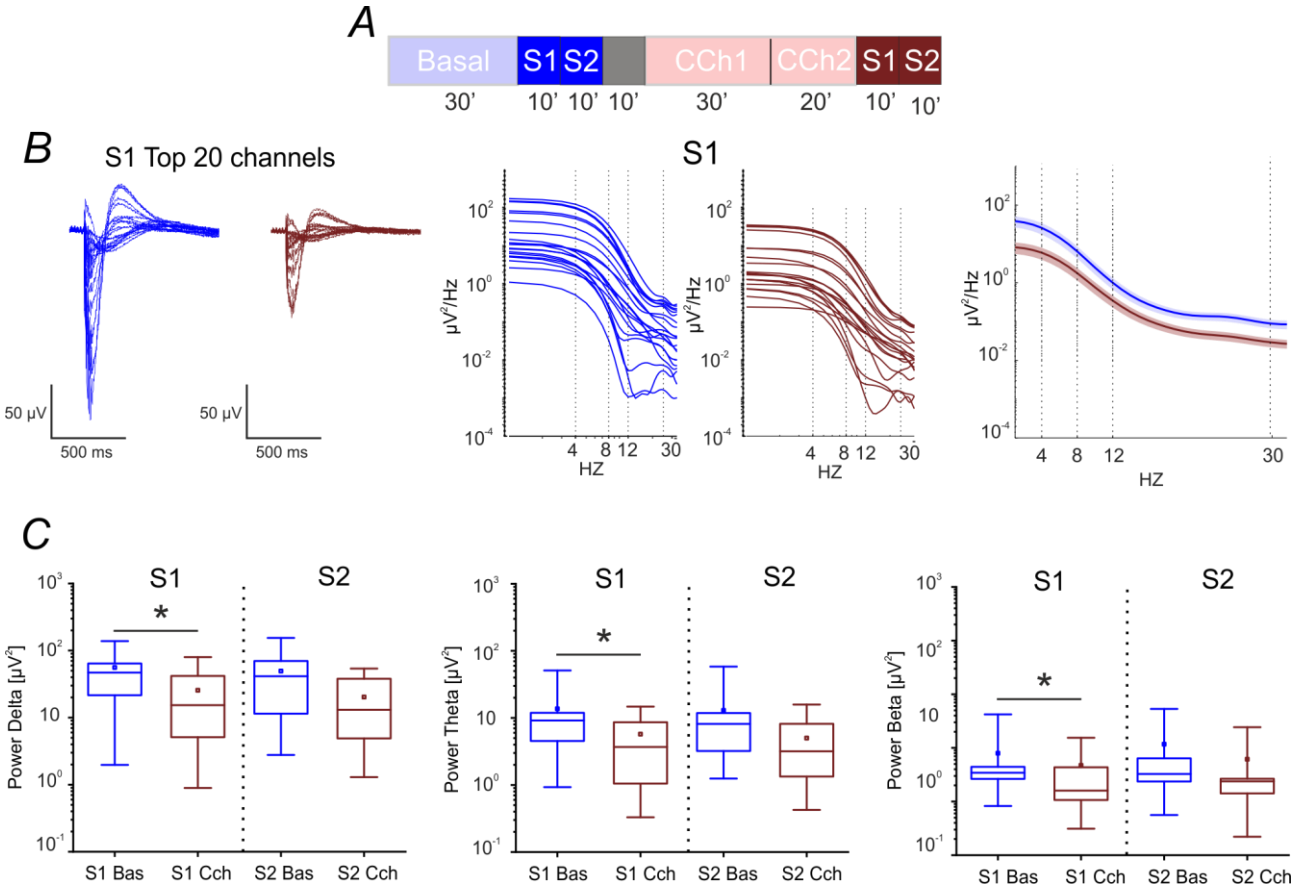

*Figure 5.6 LFP analysis of the evoked response. A) Experimental protocol adopted for the experiments. The electrical stimulation phases analyzed here are highlighted. Cortical cultures were stimulated for 10 minutes at two different sites under basal conditions and after CCh treatment. B) (Left panel) Mean evoked responses of the top 20 channels in one representative experiment during basal conditions and after CCh administration. (Center panel) PSD of the same channels depicted in the left panel. (Right panel) Comparison of the mean PSD of the two different experimental phases. C) Box plot of power in three different bands: delta (1 4 Hz), theta (5-9 Hz) and beta (10-30 Hz) for each stimulation site. We found a significant difference only in the first stimulation phase. The bold lines and shaded regions (B) correspond to the mean ± SEM. For each box plot, the small square indicates the mean, the central line illustrates the median, and the box limits indicate the 25th and 75th percentiles. Whiskers represent the 5th and the 95th percentiles. Statistical analysis was conducted using the Mann-Whitney comparison test; **p < 0.01.*

Indeed, since the most remarkable difference between wakefulness and sleep was in the 'complexity' of the response rather than in its amplitude, we evaluated the PCI index. We compared the PCI observed during the stimulation phase at baseline with that observed after CCh treatment.

After CCh administration, we observed an increase in the PCI values for both sessions of stimulation. Specifically, we found that the PCI for the first stimulation site increased significantly (up to 20%) in 56% of the experiments and that the PCI for the second stimulation site increased in 44% of the experiments (**Figure 5.6 C**).

Next, we determined whether the PCI results depended on the bin size used to bin the activity for each channel. As shown in **Figure 5.6 D**, we found a perfect correlation between the results obtained using bin size 20 and bin size 5 for both stimulation sites. Thus, the PCI results did not depend on the binning dimension.

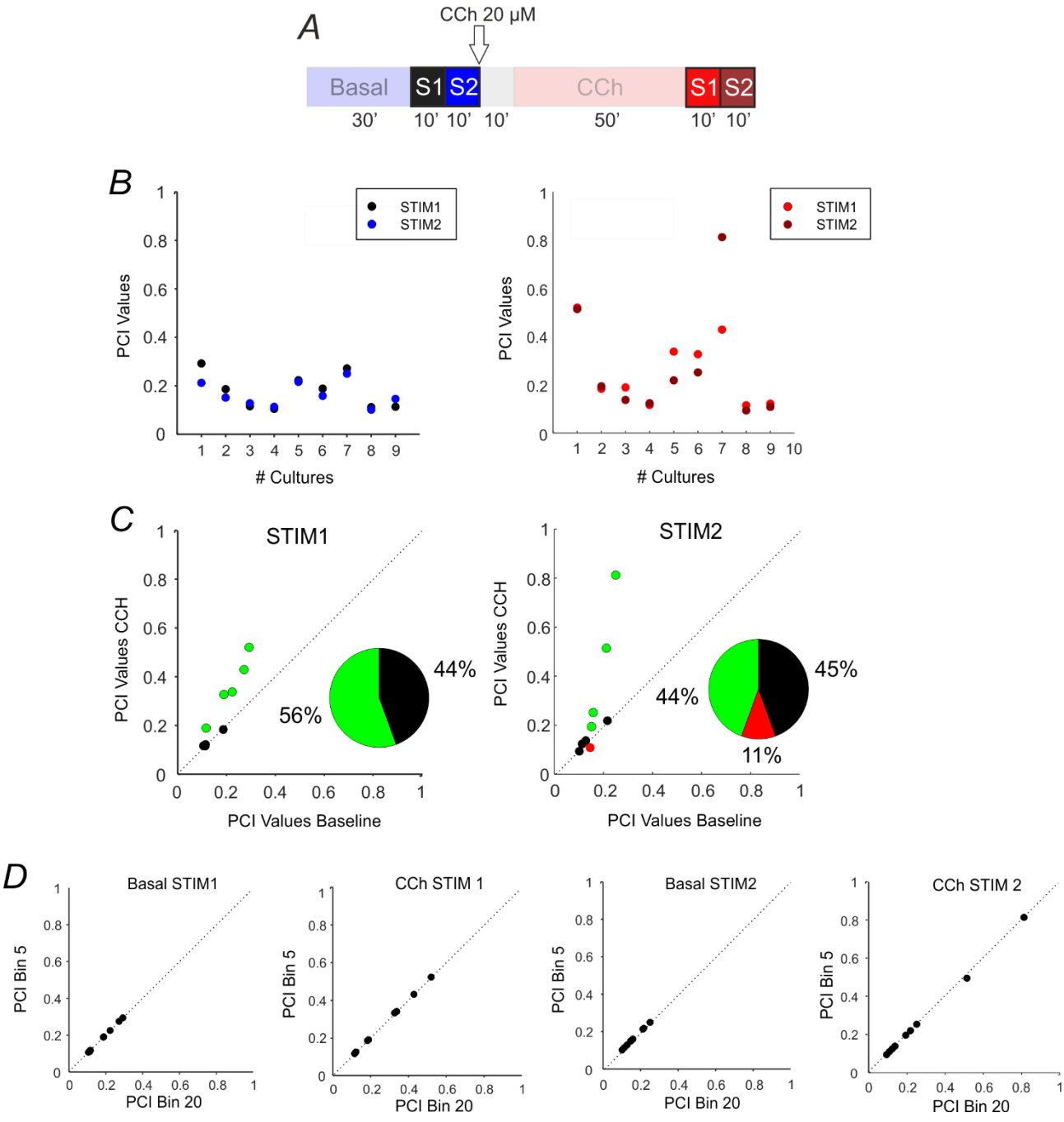

Figure 5.7 Perturbation complexity index (PCI) analysis. A) Experimental protocol adopted for the experiments. The electrical stimulation phases analyzed here are highlighted. B) PCI displayed a low value during the basal phase, similar to that recorded during sleep in humans. After CCh administration, we observed an increase in the PCI, but in the majority of the experiments its value was less than 0.4 (lowest value of consciousness). C) Variation in PCI during the two stimulation sessions. Red dots indicate channels that showed an increase of the PCI higher than 20 %, red dots indicate channels that showed a decrease of the PCI higher than 20 % and black dots represent channels that did not showed variation higher than ± 20 %. In the majority of the experiments (56% for the first stimulation session and 44% for the second stimulation session), the PCI increased after CCh administration. D) PCI variation using two different bin sizes (20 and 5). We found a correlation between the results obtained using the two different bin sizes. Indeed, the results did

not depend on the bin size used for binning the activity for each channel.

Next, we determined whether the sleep-like values recorded during baseline were region-dependent and whether desynchronization per se could explain the higher PCI. We used a dataset available from the SICODE website (www.sicode.eu; {Nieus, 2015 #367) that consists of the spiking activity of hippocampal cell cultures recorded using a high-density 4096-electrode MEA device. The cultures were electrically stimulated under baseline conditions and after the administration of norepinephrine, resulting in desynchronization of the network activity similar to that observed after the administration of CCh. However, unlike the cortical cell cultures, hippocampal cultures showed the highest PCI values under baseline conditions, and the addition of norepinephrine did not induce any significant changes in the PCI (**Figure 5.7**).

The differences in the PCI values observed during stimulation under baseline conditions (i.e., without norepinephrine) could be due to the use of a greater number of recording electrodes compared to the standard 60-channel MEAs. In fact, in HDMEAs, the probability of observing channels that are equally activated by the stimuli is higher. Therefore, since the PCI is computed on the ranked response based on the level of activation, the entropy will increase if is not possible to unequivocally order the responses. The next step will be to evaluate the PCI using a different method of ordering that takes these problems into account.

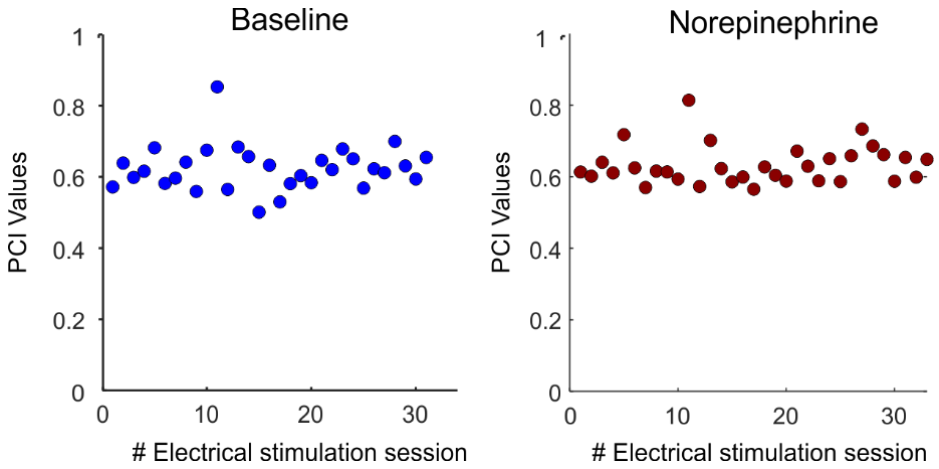

Figure 5.8 PCI analysis under baseline conditions and during norepinephrine stimulation of hippocampal cultures on high-density MEAs. Each dot represents one stimulation session. After norepinephrine addition, we did not observe any significant variation compared to the basal phase.

5.3 Conclusion

In this study, we electrically stimulated our cultures at two different sites before and after the administration of CCh, which we previously showed is able to modulate sleep-like activity in cultures. Our goal is to understand whether the evoked response observed in cortical cultures shares similarities with human data recorded using EEG and TMS stimulation. During sleep in both humans and rodents, network activity is synchronized across brain areas, while during wakefulness it is desynchronized. Therefore, when stimulated with TMS, the human brain responds with larger EEG signals during sleep than during wakefulness.

Consistent with this behavior, CCh caused desynchronization of the activity and suppression of the low-frequency component that appears during sleep (see Chapter 4). The responsiveness of cortical cultures to the stimulation (assessed using the post stimulus-time histogram, PSTH) decreased after CCh administration, consistent with previous observations made using human data.

Interestingly, CCh application resulted in an increase in the complexity of the response with respect to the baseline similar to the increase that is recorded during REM sleep and wakefulness {Casali, 2013 #262}. However, the comparison cannot be extended further since in humans the EEG responses to TMS were visibly different in different brain states.

Next, we compared our results with those obtained from hippocampal cells cultured on high-density MEAs. We found that the addition of norepinephrine caused a desynchronization of the activity comparable to that observed in our experiments with CCh administration (Nieus 2015). The interesting point is that desynchronization per se did not induce a decrease in the PSTH area (data not shown) and an increase in the PCI. These aspects will be evaluated more fully in the coming months.

In the future, it will be of interest to evaluate evoked response synchronization/desynchronization (ERSD) of the different frequency bands. This may allow us to determine whether CCh exerts different effects on the frequency bands used in the LFP analysis. Moreover, since cell cultures are not truly random networks (Lonardoni et al. 2017, Nieus et al. 2018), such cultures represent a reduced and interesting system that can be used to manipulate neuronal growth to obtain a higher PCI.

Related publications and/or conference abstracts

Colombi I. *, Nieus T.*, Chiappalone M. Assessment of the perturbational complexity index in cortical cell cultures studied in basal condition and under carbachol treatment. (**in preparations**)

* First equal

References

Bologna, L.L., Pasquale, V., Garofalo, M., Gandolfo, M., Baljon, P.L., Maccione, A., Martinoia, S., and Chiappalone, M. (2010). Investigating neuronal activity by SPYCODE multi-channel data analyzer. *Neural Netw* 23**,** 685-697.

Boly, M. (2011). Measuring the fading consciousness in the human brain. *Current opinion in neurology* 24**,** 394-400.

Casali, A.G., Gosseries, O., Rosanova, M., Boly, M., Sarasso, S., Casali, K.R., Casarotto, S., Bruno, M.-A., Laureys, S., and Tononi, G. (2013). A theoretically based index of consciousness independent of sensory processing and behavior. *Science translational medicine* 5**,** 198ra105-198ra105.

Chiappalone, M., Massobrio, P., and Martinoia, S. (2008). Network plasticity in cortical assemblies. *European Journal of Neuroscience* 28**,** 221-237.

Colombi, I., Tinarelli, F., Pasquale, V., Tucci, V., and Chiappalone, M. (2016). A simplified in vitro experimental model encompasses the essential features of sleep. *Frontiers in Neuroscience* 10.

D'andola, M., Rebollo, B., Casali, A.G., Weinert, J.F., Pigorini, A., Villa, R., Massimini, M., and Sanchez-Vives, M.V. (2017). Bistability, causality, and complexity in cortical networks: an in vitro perturbational study. *Cerebral Cortex* 28**,** 2233-2242.

Hinard, V., Mikhail, C., Pradervand, S., Curie, T., Houtkooper, R.H., Auwerx, J., Franken, P., and Tafti, M. (2012). Key electrophysiological, molecular, and metabolic signatures of sleep and wakefulness revealed in primary cortical cultures. *J Neurosci* 32**,** 12506-12517.

Huber, R., Mäki, H., Rosanova, M., Casarotto, S., Canali, P., Casali, A.G., Tononi, G., and Massimini, M. (2012). Human cortical excitability increases with time awake. *Cerebral cortex* 23**,** 1-7.

Massimini, M., Ferrarelli, F., Huber, R., Esser, S.K., Singh, H., and Tononi, G. (2005). Breakdown of cortical effective connectivity during sleep. *Science* 309**,** 2228-2232.

Saberi-Moghadam, S., Simi, A., Setareh, H., Mikhail, C., and Tafti, M. (2018). In vitro Cortical Network Firing is Homeostatically Regulated: A Model for Sleep Regulation. *Scientific reports* 8**,** 6297.

Seth, A.K., Dienes, Z., Cleeremans, A., Overgaard, M., and Pessoa, L. (2008). Measuring consciousness: relating behavioural and neurophysiological approaches. *Trends in cognitive sciences* 12**,** 314-321.

Tononi, G. (2004). An information integration theory of consciousness. *BMC neuroscience* 5**,** 42.

Tononi, G., Edelman, G.M., and Sporns, O. (1998). Complexity and coherency: integrating information in the brain. *Trends in cognitive sciences* 2**,** 474-484.

Chapter 6:

Sleep-related pathologies: Prader Willi syndrome

In the previous chapters, we stimulated our *in vitro* neuronal networks using the cholinergic agonist carbachol (CCh, 20 μM) to suppress sleep features. We observed for the first time that CCh treatment affected both the high- and the low-frequency components of the signal, causing suppression of the classical sleep-like properties of the activity. Having observed this, we were interested in understanding how the electrophysiological signal changes in pathologies in which sleep is compromised. There are several diseases in which sleep alterations occur; however, the research group of Dr. V. Tucci and coworkers at the IIT has already characterized sleep alterations in a heterozygous mouse model with paternal deletion of the *Snord116* gene (PWScr m+/p^-) (Lassi et al., 2016b), which represents a good model for studying Prader-Willi syndrome (PWS). For this reason, we focused on this specific pathology.

PWS is a rare imprinted neurodevelopmental disorder that is associated with a paternally expressed genomic imprinting defect within human chromosome region 15q11-13 (Peters, 2014). The syndrome is associated with growth retardation, metabolic abnormalities, hyperphagic behavior, cognitive deficits, and sleep abnormalities. Imprinted genes are often associated with human diseases, particularly disorders affecting cell growth, development, and behaviour (Morison and Reeve, 1998;Falls et al., 1999;Nicholls, 2000). Most of the autosomal genes are expressed from both maternal and paternal alleles. However, imprinted genes are an example of non-Mendelian genetics, in which only one member of the gene pair (from the mother or the father) is expressed and expression is determined by that parent. Thus, genomic imprinting is the differential expression of genetic material depending on the parent of origin (Butler, 2002).

The genetic defects can be quite heterogeneous across patients and include uniparental disomy deletions, and genomic imprinting deficits. One of the candidate genes associated with the syndrome is the gene that encodes small nucleolar ribonucleic acid (RNA)-116 (*SNORD116*, also called HBII-85) , a noncoding molecule that participates in the modification of other small nuclear RNAs and is predominantly expressed in the brain (Skryabin et al., 2007). Clinical single cases of PWS patients revealed microdeletions in the q11.q13 domain of chromosome 15 that included *SNORD116* (Sahoo et al., 2008;de Smith et al., 2009;Duker et al., 2010;Bieth et al., 2015). The authors reported that

deletion of the *SNORD116* gene cluster contributes greatly to generation of the PWS phenotype, whereas deletions of *MKRN3, MAGEL2, NECDIN, SNORD115 or C15ORF2 and SNURF-SNRPN* do not give rise to PWS. Moreover, in the hypothalamus, *SNORD116* gene seems to be developmentally regulated and to play a role in the maturation of feeding circuits and in the control of the sleep-wake cycle (Vgontzas et al., 1996a).

Indeed, PWS patients are often affected by sleep-wake disturbances associated with hypersomnia, fragmented sleep and apnea (Harris and Allen, 1996;Manni et al., 2001;Priano et al., 2006;Camfferman et al., 2008). The disturbances reflect alterations in the architecture of sleep (Vgontzas et al., 1996a;Vgontzas et al., 1996b;Priano et al., 2006;Camfferman et al., 2008), abnormalities in rapid eye movement (REM) sleep cycles (Hertz et al., 1993) and in sleep onset REM periods (SOREMPs) and an increased number of REM episodes(Vgontzas et al., 1996a;Vgontzas et al., 1996b;Manni et al., 2001;Priano et al., 2006).

Some sleep alterations, particularly related to REM sleep, have also been described by the group of V. Tucci at IIT in heterozygous mutant mice carrying a paternal deletion of *Snord116* (PWScr m^+/p^-) at the orthologous locus on mouse chromosome 7C (Figure 6.1 A) (Lassi et al., 2016a;Lassi et al., 2016b). PWScrm^+/p^- heterozygous mutant mice revealed a complete absence of *Snord116* expression in different brain areas whereas it was generally expressed in PWScrm^+/p^+ wild-type animals (Figure 6.1B) (Lassi et al., 2016a).

PWScr $m+/p^-$ mice partially exhibits some of the endophenotypes observed in PWS subjects: i.e. alterations in the sleep-wake cycle, REM sleep dysregulation and temperature instability (Lassi et al., 2016b), dysregulation of several circadian genes (Powell and LaSalle, 2015)neo-natal developmental delays (Ding et al., 2008)and cognitive deficits (Adhikari et al., 2018).

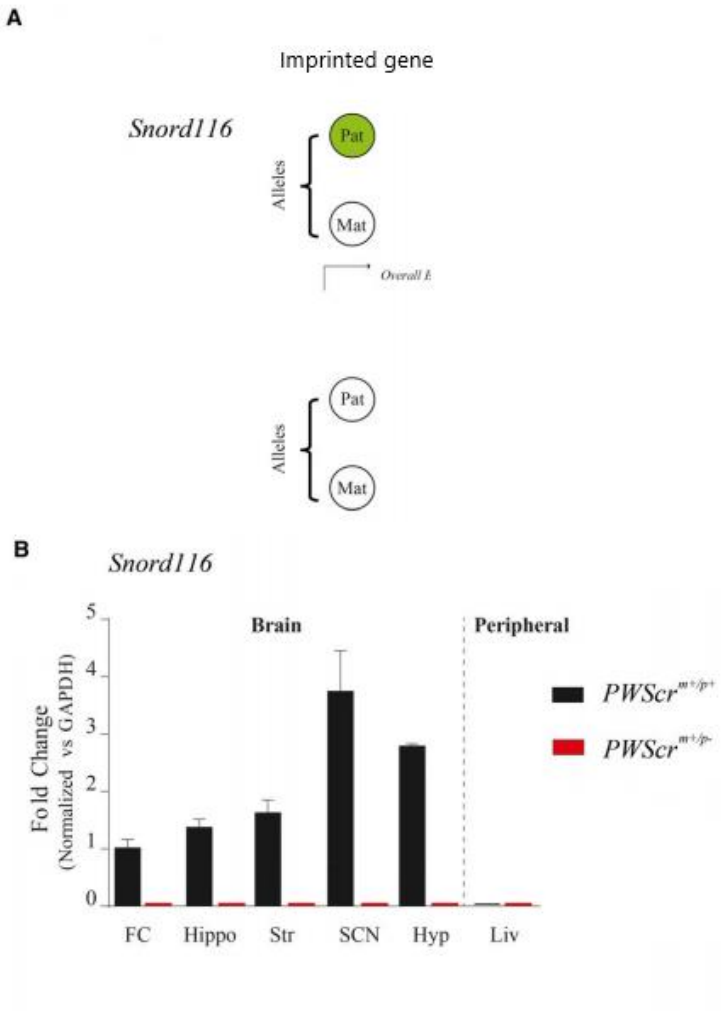

Figure 12 Scheme of the allelic combination of the imprinted gene Snord116 in the WT (PWScr m^+/p^+) and in PWScr m^+/p^-. The allelic combination for both conditions is represented as green filled circles (expressed) or empty circles (not expressed). In PWScr m^+/p^+ mice Snord116 is expressed only in the paternal allele, while in PWScrm+/p− is not expressed at all. (B) Relative Snord116 expression analysis by RT-PCR in PWScrm+/p+ and PWScrm+/p− in mouse brain tissues (n = 3). Liver was used as a negative control. FC, frontal cortex; Hippo, hippocampus; Str, striatum; Hyp, hypothalamus; SNC, suprachiasmatic nucleus of the hypothalamus; Liv, liver. (Adapted from Lassi et al. 2016)

Regarding the sleep disturbances, PWScr m+/p^- mice showed an increase in rapid eye movement (REM) sleep compared with control mice (Lassi et al., 2016b). Moreover, a difference in the theta power of the EEG during REM sleep was also observed (**Figure 6.2**).

Overall, the data suggest that the paternally expressed *Snord116* gene may play a crucial role in the regulation of the microstructure of sleep and that it may be particularly related to REM sleep. In support of these results, a recent study showed that it has an essential role in the regulation of the circadian process (Powell and LaSalle, 2015).

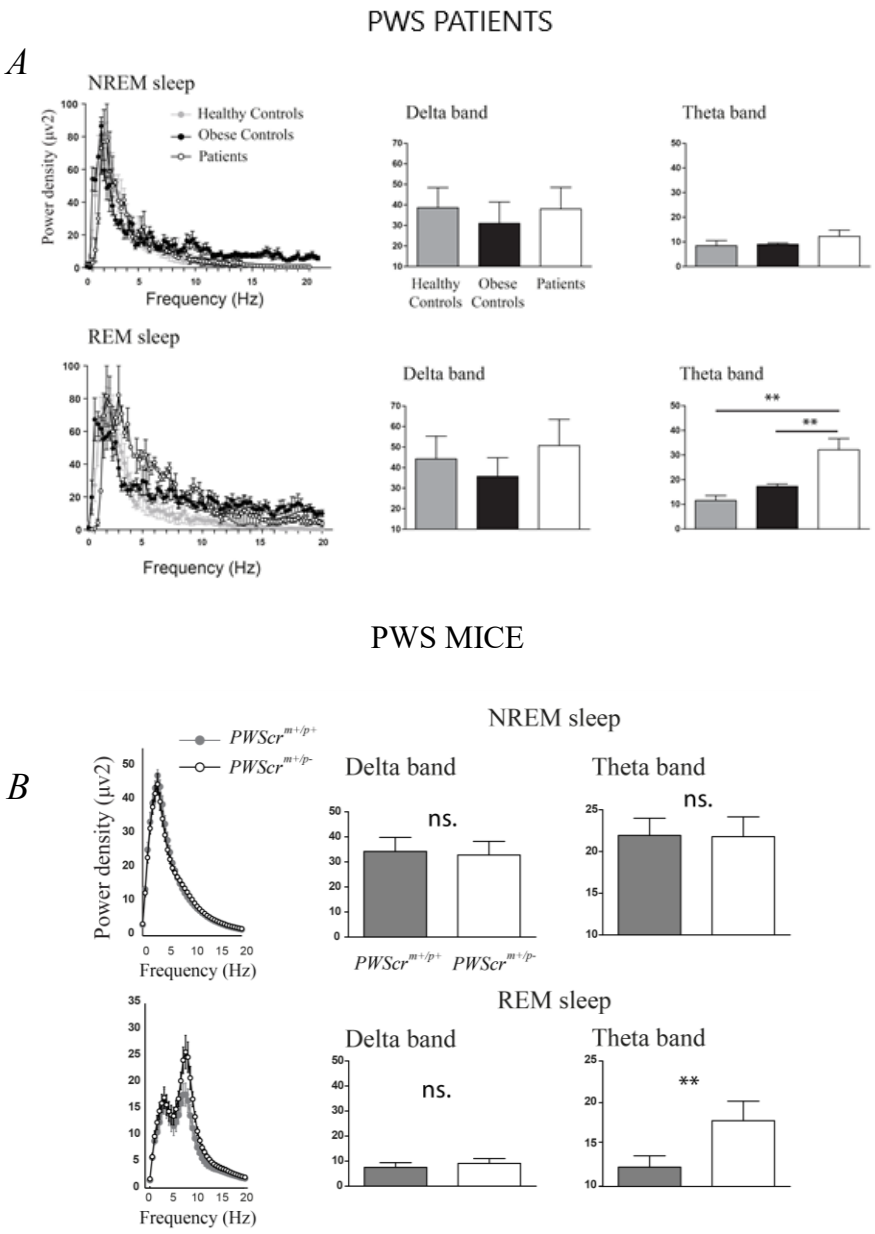

*Figure 6.2 A) Power densities of the whole spectrum of frequencies and detailed histograms for delta and theta electroencephalographic frequencies (µV2) in NREM and REM sleep in patients and in healthy and obese controls. B) Power densities of the whole spectrum of frequencies and detailed histograms for delta and theta EEG frequencies (µV2) in NREM and REM sleep in mutant and control mice during the light phase. Data are presented as the mean ± standard error of the mean; **P < 0.01 (adapted from Lassi et al.,2016).*

As described in Chapter 3, sleep is regulated by two linked biological processes, namely, a circadian process that is independent of sleep-wake history and homeostatic sleep "pressure," which is driven by prior sleep-wake history (Borbely, 1982) (see Chapter 3 paragraph 3.2).

In this context, the changes in sleep microstructure in Snord116 mice might be driven either by alterations in the circadian clock or by alterations in the homeostatic processes. However, to date, whether or not the paternally expressed *Snord116* gene has a role in the control of the homeostatic process remains unknown.

Based on these considerations, the central hypothesis of this project is to understand whether the *Snord116* gene contributes to the control of the sleep homeostatic process. My role in that study focused primarily on determining whether or not the same sleep abnormalities could be observed in a simplified and accessible *in vitro* model.

We thus performed experiments using cortical cultures of PWScr m+/p$^-$ mice to which we applied Carbachol (CCh, 20 µM) to suppress the sleep waves. Interestingly, we found similar alterations in theta waves in wild-type and PWScr m+/p$^-$ mice upon CCh administration. Moreover, by measuring the electrophysiological parameters, we showed that PWS mice are less reactive than wild-type animals to the sleep suppression state induced by CCh. To understand the possible differences in these homeostatic and circadian processes, we complemented the MEA recording by performing gene expression analysis in cortical cultures *in vitro* upon CCh administration.

Then, we compared genes expression results from cortical cultures with the ones obtained from in vivo samples after 6 hours of Sleep-Deprivation (SD). Measurement of the expression levels of specific genes confirmed our hypothesis and showed that the genes involved in sleep deprivation were not altered in PWS after CCh administration. We show that these results are consistent with the results obtained using frontal cortex (FC) and parietal cortex (PC) of WT and PWS mice after sleep deprivation.

6.1 Material and methods

6.1.1 Cell cultures

Cortical cell cultures prepared from embryonic mice at gestational day 18 were plated on 60-channel MEAs (Multi Channel Systems, MCS, Reutlingen, Germany) that had been coated with borate buffer and poly-L-lysine to promote cell adhesion (final density approximately 1200 cells/mm^2). We recorded the activity of neuronal networks between 19 ± 1 DIVs (mean ± SD) for the WT mice (PWScrm+/p+) and 18 ± 1 DIVs for the PWS cultures (PWScrm+/p-). We decided to anticipate the recording date as compared to the projects described in the previous chapters (see Chapter 4-5) because in our experience cortical cultures from mice showed a different developmental profile as compared to rat cortical cultures. In particular, we observed that the survival rate of cultures, especially the PWScrm+/p- cultures, tends to decrease after 21-22 DIVs.

6.1.2 Experimental protocol

We recorded the electrophysiological activity of 12 cultures from mice with paternally inherited

Snord116 deletions (PWScrm+/p-) and 6 wild-type littermate control mice (PWScrm+/p+). For simplicity, these are referred to in the text and figure as PWS and WT, respectively.

The experimental protocol adopted for these experiments included 2 hours of recording in culture solution, which was defined as the basal condition. We then chemically stimulated the cultures with CCh (20 μM) for 2 hours (Figure 3A). We normalized the results obtained in each experiment to the mean of each electrophysiological parameter during basal recording.

6.1.3 Data analysis

Starting from the raw data (i.e., the wide-band signal), we used a dual process to analyze both MUA (multi-unit activity, f>300 Hz) and LFP (local field potential, f<300 Hz) (Figure 1B). To capture only MUA activity, we high-pass-filtered the raw signal. When spikes (i.e., single over-threshold peaks) and bursts (i.e., groups of tightly packed spikes) activity were detected in the MUA recordings, we computed the following parameters for each channel: Mean Firing Rate (MFR, spikes/sec), Mean Bursting Rate (bursts/min), Inverse Burst Ratio (IBR, percentage of spikes outside the burst), Burstiness Index (BI, an index of the burstiness level of the network), Burst Duration (BD, msec), Mean Frequency Intra Burst (MFB, spikes/sec), Interburst Interval (IBI, msec) and Spike Tiling Timing Coefficient (STTC) (**Figure 6.3B**, light blue boxes in the diagram).

We then analyzed the Network Bursts (NB) activity considering any variation in the number (NBR, NB/min), duration (NB Duration, msec) and distance between NBs (Inter NB interval, sec). A ‘network burst’ (NB) consists of densely packed spikes occurring simultaneously at many channels, spread over the entire array. These packages generally last from hundreds of milliseconds up to seconds (burst duration) with long quiescent inter-burst periods (Inter Burst Interval - IBI). A custom burst detection method (Pasquale et al., 2010) was used to detect bursts on single recording channels. The input parameters were directly estimated from the inter-spike interval distribution of each channel. Briefly, the method exploited the logarithmic Inter Spike Interval Histogram (logISIH) to extract the parameters needed for the analysis of each recording channel. Generally, the range of ISI thresholds for our cultures is approximately 200–400 msec.

Finally, we computed the Cross- Correlation between each pair of burst trains recorded from active channels (i.e., with MFR>0.02 spikes/s). For each channel, we considered only the first spike for each burst, and we computed the cross-correlation function that represents the probability of observing a spike in one channel i at time (t+τ, τ=3 ms) given that there is a spike in a second channel i+1 at time t. To quantify the strength of the correlation between each couple of electrodes, we evaluated the correlation peak (C_{peak}). We selected only the first 100 C_{peak} values to identify only the most significant correlations. Finally, we analyzed the latency from the peak (L_{peak}) and considered the

corresponding peak latency values of the preselected 100 strongest C_{peak} values (El Merhie et al., 2018).

To select the LFP components, we low-pass-filtered the raw data between 1 and 300 Hz (Figure 1B, light gray boxes in the diagram). We then computed the power spectral density of the decimated signal (sampling frequency 1 kHz) ($\mu V^2/Hz$) using the Welch method (windows=5s, overlap=50%). We only considered the lower-frequency bands of the signal; these bands, in particular the delta (1-4 Hz), theta (4-11 Hz), and beta (11-30 Hz) bands, are of particular interest in the study of the sleep-wake cycle. To characterize the LFP, we calculated the power in each of those frequency bands.

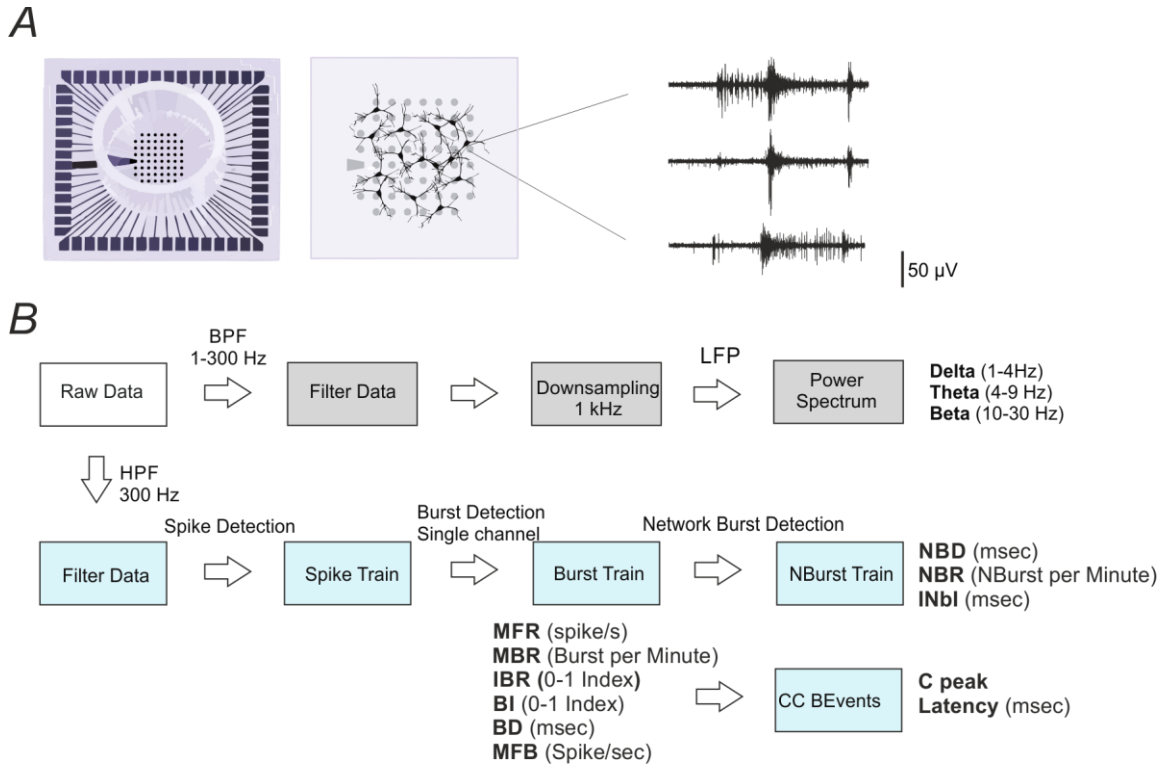

Figure 6.3. Cortical cultures on MEA and data analysis. (A) Cortical cultures were plated on 60-channel MEAs (Multi Channel Systems MCS, Reutlingen, Germany) with the standard electrode layout (8x8). On the right are shown typical traces recorded from three microelectrodes upon high-pass filtering at 300 Hz. (B) Scheme of the data analysis workflow. We applied a high-pass filter to the signal (f>300 Hz) to analyze only MUA activity (light blue boxes in the diagram). We performed spike and burst detection for each channel on the MUA recordings, and we computed and analyzed the following electrophysiological parameters: MFR (Mean Firing Rate), MBR (Mean Bursting Rate), IBR (Inverse Burst Ratio), BI (Burstiness Index), BD (burst duration) and MFB (Mean Frequency Intra Burst). After we performed network burst detection, we analyzed the following parameters: Network Burst Rate (NBR), Network Burst Duration (NB Duration) and Inter Network Burst Interval (IBI). Cross-correlation was computed on burst events, and we measured the strength of the correlation (C_{peak}) and the latency. We also analyzed the LFP (light gray boxes in the diagram). Here, the signal was low-pass-filtered (f<300 Hz), and we computed the power spectral density taking into account only the low-frequency bands of the signal that are associated with sleep: delta (1-4 Hz), theta (4-11 Hz) and beta (11-30 Hz).

6.1.4 In vitro Genes expression

Multi-well plates were coated with poly-D-lysine (0.1 mg/ml, Sigma-Aldrich) and incubated overnight in a sterile incubator at 37 °C and 5% CO_2. Neurons were then plated at a concentration of

500,000 cells/well. Primary neurons were treated at DIV 20 (i.e., the same age interval used in the MEA experiments) with 20 μM of carbachol (Sigma-Aldrich) for 1 h. The neurons were washed three times with ice-cold phosphate-buffered saline solution and lysed with 300 μl of Trizol (Life Technologies) followed by phenol/chloroform extraction. Cell lysates were collected, and 600 ng of RNA was reverse-transcribed using an Improm-II reverse transcription kit (Promega) according to the manufacturer`s instructions. Real-time PCR was performed in duplicate for each sample, and the results were analyzed as previously described (Tinarelli et al., 2014). All samples were normalized against the GAPDH gene.

6.1.4 In vivo sleep deprivation protocol

Total sleep deprivation (SD) was performed using gentle handling techniques that consisted of introducing novel objects into the cage and knocking or shaking the cage when behavioral signs of sleep were observed. Animals were subjected to SD during the first 6 h of the light period. We chose this time because mice are nocturnal animals (they are active at night and sleep during the day) and the sleep pressure is maximal at the beginning of the light period.

6.1.5 In vivo gene expression

Five mice with paternally inherited Snord116 deletions ($PWScr^{m+/p-)}$ and 5 wild-type littermate control mice (PWScrm+/p+) were investigated using qRT-PCR. Two different conditions were analyzed. First, (i) mice treated with 6 h of sleep deprivation (SD); the brains of these animals were extracted 1 h after the end of the treatment (n5= $PWScr^{m+/p-}$_SD and n5= $PWScr^{m+/p+}$_SD). Second, (ii) mice that were not treated with SD but were sacrificed at the same time of day (ZT7) (n5= $PWScr^{m+/p-}$_nSD and n5= $PWScr^{m+/p+}$_nSD).

At the end of the experiments, the mice were sacrificed; the cerebral cortex was divided into frontal and parietal cortex, extracted and stored at -80 °C.

Total RNA was extracted from approximately 0.5 g of snap-frozen PFC and HYP using Qiazol (Qiagen, Hilden, Germany) according to the manufacturer's instructions. RNA samples were quantified using an ND1000 Nanodrop spectrophotometer (Thermo Fisher Scientific Inc., Waltham, MA, USA). Reverse transcription of 0.5 μg of RNA was performed using ImProm-II(TM) Reverse Transcriptase (Promega, Milan, Italy) according to the manufacturer's instructions. RT-qPCR was performed on an Applied Biosystems 7900HT Fast Real-Time PCR System (Applied Biosystems, Foster City, CA, USA) using the QuantiFast SYBR Green PCR Kit (Qiagen, Hilden, Germany) under the following conditions: 5 min at 95 °C followed by 40 cycles of denaturation at 95 °C for 10 sec, annealing at 60 °C for 30 sec and extension at 70 °C for 1 min. Each sample was run to obtain average

Ct values according to the manufacturer's specifications. A list of the primers used is provided below. All samples were normalized against GAPDH as a housekeeping gene. Expression levels relative to the housekeeping gene were determined by the calculation of ΔCt.

6.2 Results

We performed experiments using PWS cultures plated on MEA according to the protocol depicted in **Figure 6.4 A**. We recorded two hours of basal recording (i.e., in Neurobasal medium) followed by 2 hours of CCh stimulation of both groups (WT and PWS cultures). We recorded the activity of neuronal networks between 19 ± 1 DIVs (mean ± SD) for the WT mice (PWScrm+/p+) and 18 ± 1 DIVs for the PWS cultures (PWScrm+/p-).

In the comparison of basal activities, we found no significant differences; thus, the starting level of activity was comparable (**Figure 6.4B**; light blue box and light red box for WT and PWS, respectively). Although we found no statistically significant differences, the activity of PWS cultures seemed to be more desynchronized than that of the WT, as shown by the lower BI (burstiness index) and STTC (spike tiling timing coefficient) values and the higher IBR (inverse burst ratio) value. Moreover, PWS cultures exhibited a different distribution of burst activity during the basal phase, indicated by lower MFB (mean frequency intraburst) and higher BD (burst duration) values compared to the WT cultures.

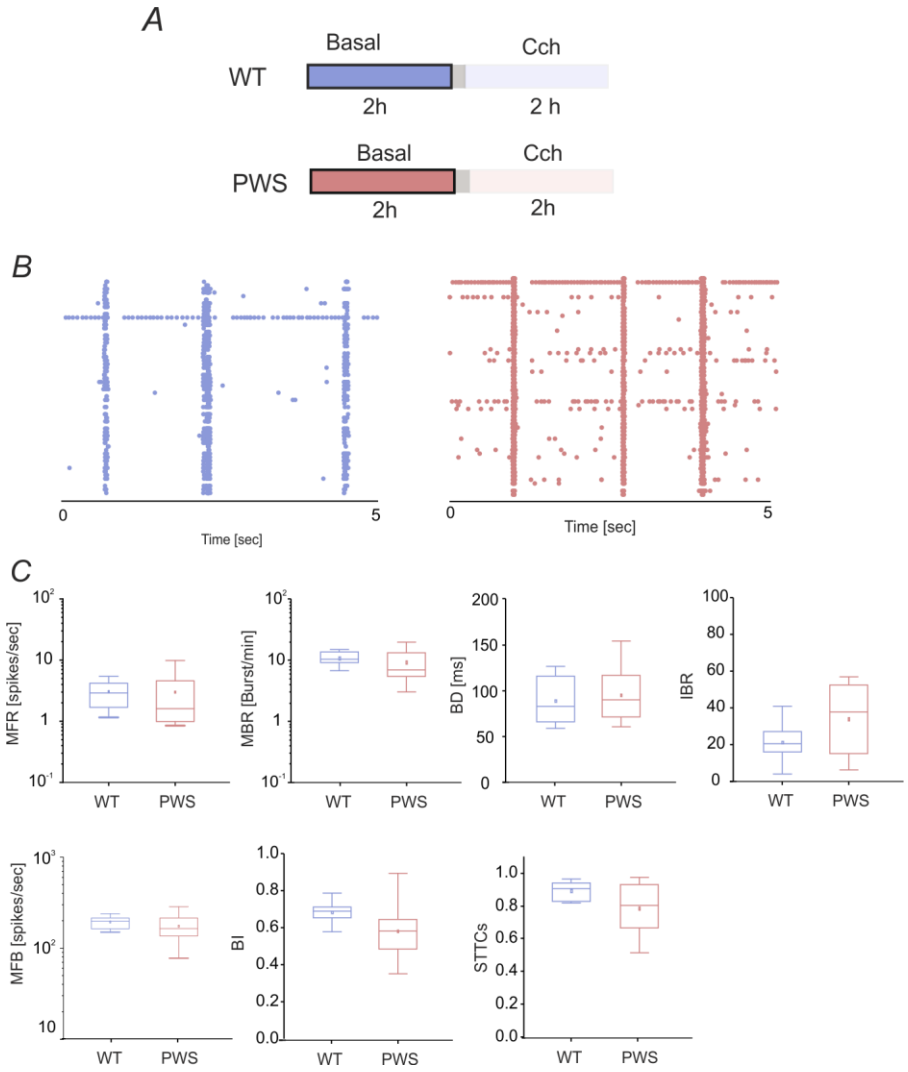

Figure 6.4 MUA analysis of WT and PWS cortical cultures during the basal phase. *A) Experimental protocol adopted for the experiments. The 2 hours of basal recording considered in the analysis are highlighted. B) 5 seconds of raster plot of two representative experiments during the basal phase for WT and PWS culture at DIV 17.C) Box plots showing the MFR, MBR, IBR, BD, IBR, MFB, BI, and STTCs of WT cultures (light blue boxes: N=6; DIV= 19±1, mean ± SD) and PWS cultures (light red boxes: N=12, DIV= 18±1, mean ± SD) during basal recording. The gray shaded area denotes a 10-min break in the recording following CCh addition; this was done to prevent experimental bias due to the release of drug in the medium. In each box plot, the small square indicates the mean, the central line illustrates the median, and the box limits indicate the 25th and 75th percentiles. Statistical analysis was performed using the two-sample t-test [*p<0.05].*

To make it possible to compare the behavior of the cultures during CCh stimulation, we normalized the results of each experiment to the mean values obtained during basal recording. In the WT cultures (**Figure 6.5C**, blue line), the activity level evaluated by means of the MFR increased after CCh administration compared to the basal condition but we did not found any statistical difference. At the same time, CCh application resulted in an increased number of isolated spikes (i.e., a higher IBR value, **Figure 6.5D**) and a decrease in the BI (**Figure 6.5D**) and STTC (**Figure 6.5E**) compared to the basal phase, indicating a loss of bursting activity and of synchronicity. This was confirmed by the increase in the duration of the bursts (i.e., a higher BD value, **Figure 6.5G**) and by the decrease in the frequency of the spikes (i.e., a lower MFB value, **Figure 6.5H**). Indeed, the relative changes of

the analyzed parameters upon CCh administration in WT cultures are consistent with the previous results obtained in cortical cultures from embryonic rats despite the different DIVs of cultures recorded (Colombi et al., 2016).

PWS cultures (**Figure 6.5B**, red line) showed an increase in MFR only in the second hour after CCh treatment. The number of isolated spikes (i.e. IBR) and BI showed an increase after CCh administration compared to the basal condition, especially in the second hour. During the first hour, WT cultures showed higher values of MFR, MBR, BD, IBR and BI than the PWS cultures. Conversely, the BI of WT cultures was lower than that of PWS cultures. In the second hour after CCh administration, the levels of the selected parameters described above were comparable between groups. We found a statistical difference between the two time-points of CCh administration (CCh 60' and CCh 120') for the BI, the STTCs, BD and MFIB only in PWS culture. This suggests that CCh has a delayed effect in PWS cultures despite the fact that the starting level of firing and bursting activity was comparable (**Figure 6.4B).**

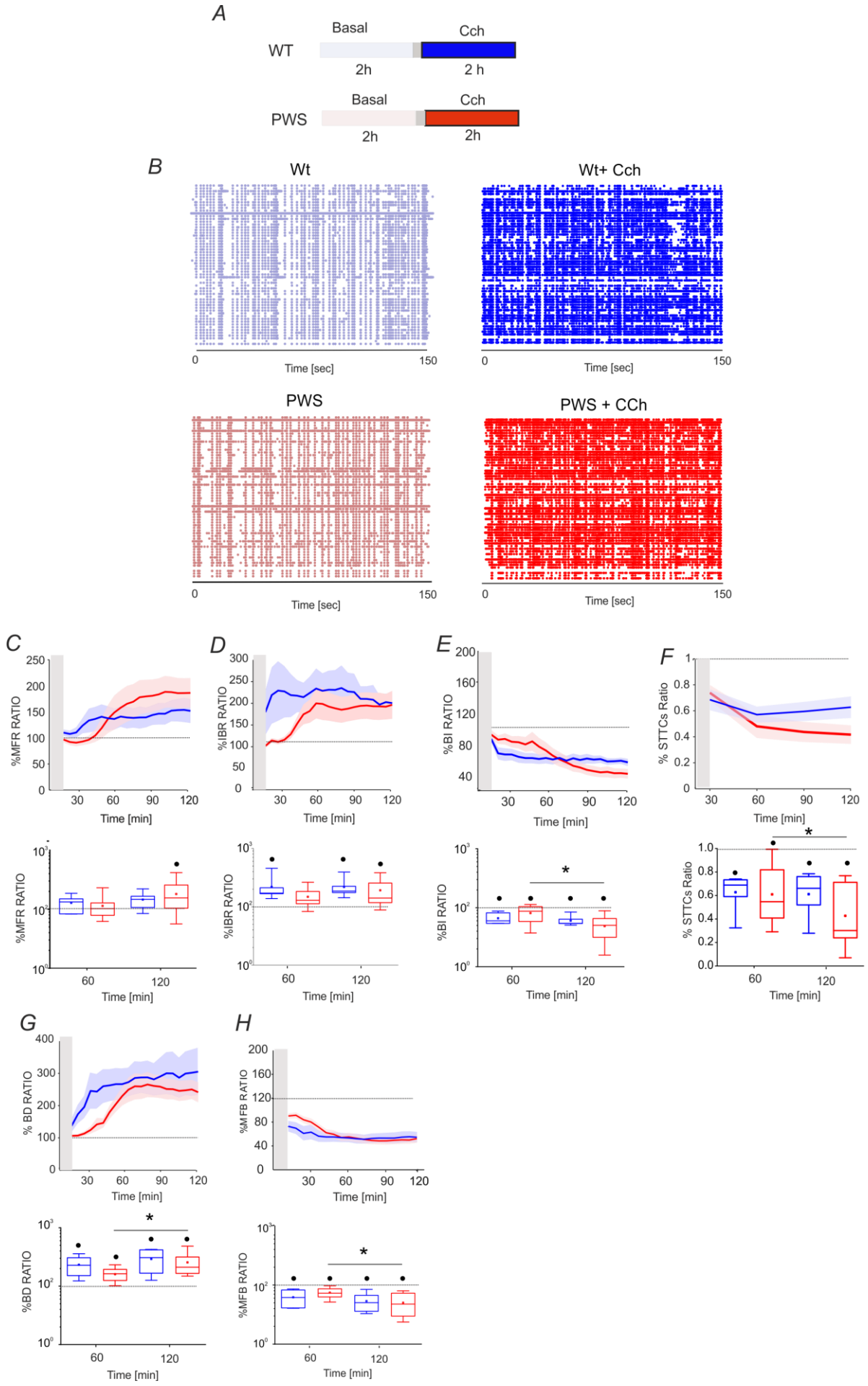
A
Basal
Cch
WT
2h
2 h
Basal
Cch
PWS
2h
2h
B
Wt
Wt+ Cch
PWS
PWS + CCh
0
150
Time [sec]
C
D
E
F
%MFR RATIO
%IBR RATIO
%BI RATIO
% STTCs Ratio
Time [min]
G
H
% BD RATIO
%MFB RATIO
%BD RATIO
*

Figure 6.5 ***MUA analysis of WT and PWS cortical cultures following CCh administration****. A) Experimental protocol adopted for the experiments. The 2 hours of CCh recording used in the analysis are highlighted. We normalized the values for each culture and for each parameter with respect to the basal values. B) 150-s raster plots of cortical cultures at DIV 17 during basal and CCh administration for WT and PWS cultures C) Comparison of MFR in WT (blue line, N=6, DIV= 19±1, mean ± SD) and PWS (red line, N=12, DIV= 18±1, mean ± SD) cultures following CCh administration. We did not find any significant differences in MFR between WT (blue box) and PWS (red box) cultures during the first and second hours of treatment. D) Comparison of IBR in WT (blue line, N=6, DIV= 19±1, mean ± SD) and PWS (red line, N=12, DIV= 18±1, mean ± SD) cultures following CCh administration. CCh caused an increase in spike activity outside the burst in both genotypes. In particular, WT appears to be less correlated during the first hour of treatment. E) Comparison of BI in WT (blue line, N=6, DIV= 19±1, mean ± SD) and PWS (red line, N=12, DIV= 18±1, mean ± SD) cultures following CCh administration. CCh administration resulted in a decrease in the prevalence of burst activity in both genotypes. WT cultures showed lower values of the burstiness index, indicating lower correlation as indicated by the IBR parameter. F) Comparison of the top 100 STTC values obtained for WT (blue line, N=6, DIV= 19±1, mean ± SD) and PWS (red line, N=12, DIV= 18±1, mean ± SD) cultures following CCh administration. CCh caused desynchronization of the activity in both genotypes. The mean values recorded during each of the two hours are comparable. G) Comparison of BD in WT (blue line, N=6, DIV= 19±1, mean ± SD) and PWS (red line, N=12, DIV= 18±1, mean ± SD) cultures following CCh administration. CCh caused an increase in burst duration in both genotypes. We observed a statistically significant difference between WT and PWS only during the first hour. H) Comparison of MFB in WT (blue line, N=6, DIV= 19±1, mean ± SD) and PWS (red line, N=12, DIV= 18±1, mean ± SD) cultures following CCh administration. CCh caused a decrease in the mean frequency of spikes within every burst in both genotypes. This is consistent with the finding that BD:CCh treatment increased the burst duration by increasing the distance between spikes within each burst. The burst duration appeared to decrease less in PWS than in WT. The gray shaded area indicates the 10-min period after CCh addition during which activity was not recorded; this was done to prevent experimental bias due to drug release into the medium. In each box plot (B-H), the small square indicates the mean, the central line indicates the median, and the box limits indicate the 25th and 75th percentiles. All data are presented as the mean +/- SEM. Statistical analysis was performed using Tukey's post hoc test following two-way repeated-measures ANOVA (*p<0.05 indicated statistical difference among the different time points treatment (i.e. CCh 60' and CCh 120') within the same genotype,° p <0.05 indicated statistical difference within the same genotype during Cch administration with respect to the basal condition).*

Then we analyzed the changes in network burst activity by measuring the variation in the number, the duration and the distance for each NB (**Figure 6.6**). During the basal phase, we found no difference in NB duration in the two genotypes. In contrast, PWS showed a reduced number of NB (i.e., a lower level of NBR) separated by a greater distance (i.e., higher IBI) (**Figure 6.6 B**, light blue and light red lines). As shown for the parameters in Figure 6.5 (Panel C-G), WT cultures and PWS cultures showed different behavioral profiles following CCh administration. WT cultures displayed higher NBR and NB duration and significantly lower INbI in the first hour (**Figure 6.6 B**, blue line and red line). With time, NBR and NB duration became comparable in the two genotypes, while the IBI remained higher in PWS. The analysis of the cross-correlation of burst events (**Figure 6.6 C**) revealed a statistically significant difference in the latency of the top 100 connections between the two groups under basal conditions (**Figure 6.6 C).**

We did not find any significant difference in the C_{peak} value. Following CCh administration, we observed an increase in the latency and a decrease in the C_{peak} values for both genotypes. We found a statistically significant difference between WT and PWS cultures only during the second hour. When normalizing the data, we did not find any difference between WT and PWS, indicating that the variation is the same in the two groups (**Figure 6.6 D**).

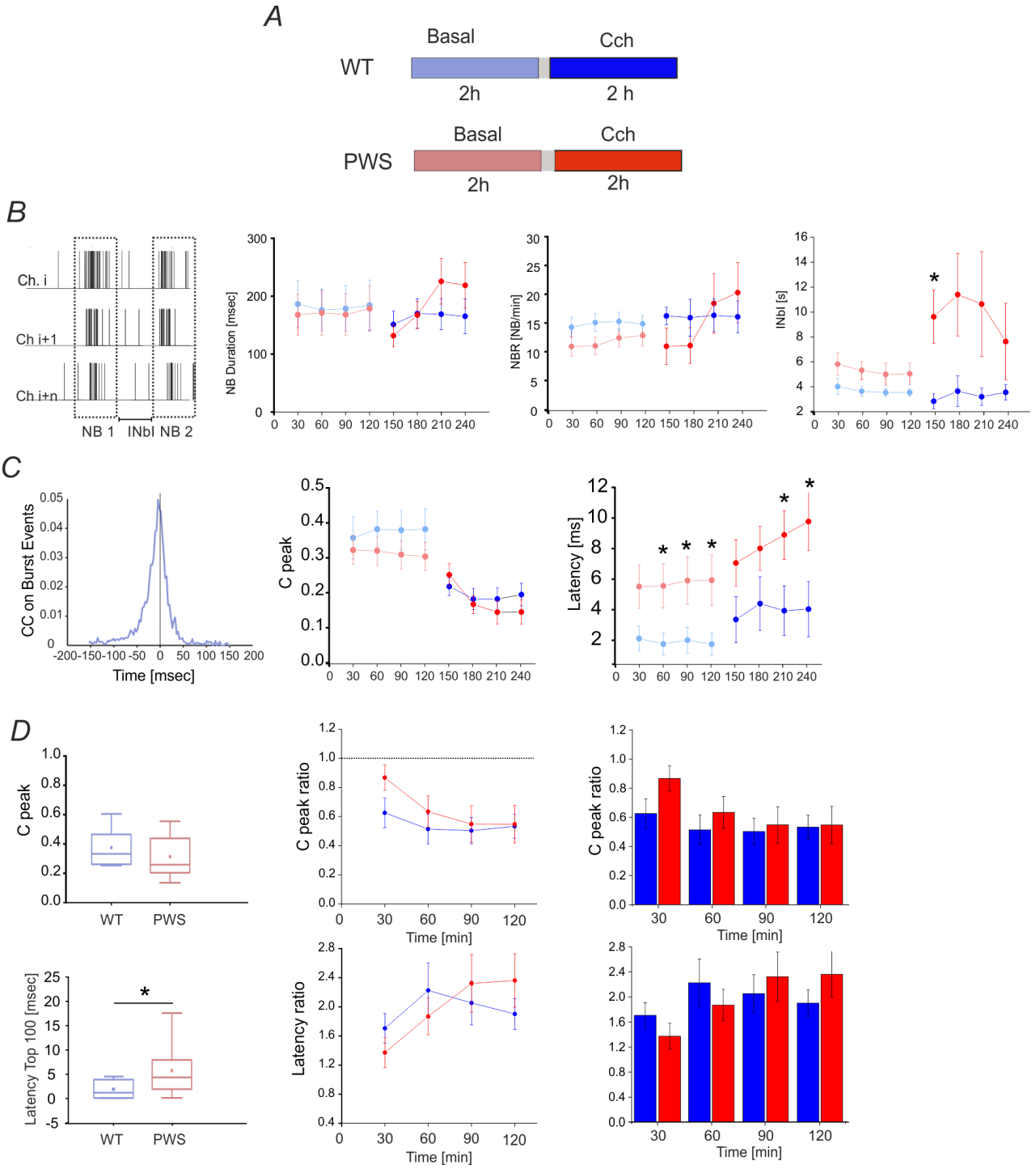

Figure 6.6 ***Network burst analysis and cross-correlation of burst events in WT and PWS cortical cultures****. A) Experimental protocol adopted for the experiments. B) Network burst activity recorded from three representative channels. We did not find any difference in the NB duration or in NBR between WT and PWS cultures. PWS mice showed a higher inter-network burst interval (INbI) during basal recording. After CCh administration, PWS and WT cultures showed two opposite behavioral profiles: the INbI of PWS significantly increased with respect to the basal condition, especially in the first 30 minutes, whereas the INbI of WT decreased. We found a significant difference only during the first 30 minutes of treatment. C) Cross-correlation analysis of burst events. (Middle panel) Plot of the 100 highest C_{peak} values at each 30-minute time point. PWS cultures showed lower C_{peak} values than WT cultures. (Right panel) Plot of the corresponding peak latency values (L_{peak}) of the preselected 100 highest C_{peak} values. PWS cultures showed a higher latency that was maintained during CCh application. D) Box plots of the 100 highest C_{peak} values and the corresponding peak latency values (L_{peak}) of WT (light blue box) and PWS (light red box) cultures during basal recording. We normalized each parameter with respect to the basal recording. We did not find any difference in the variation of the C_{peak} and L_{peak} values. For each box plot (D), the small square indicates the mean, the central line illustrates the median, and the box limits indicate the 25th and 75th percentiles. All data are presented as the mean +/- SEM. Statistical analysis was*

*performed using the two-sample t- test (*p<0.05).*

The analysis of the LFP in WT and PWS mice did not indicate differences between the genotypes during the basal phase (**Figure 6.7 B**). CCh application resulted in strong suppression of all main waves (i.e., delta, theta and to some extent beta) that characterize the classical sleep-wake cycle (**Figure 6.7 C**).

We normalized each power with respect to the basal condition. Following CCh administration, the power of the delta waves decreased by 80% in both sets of cultures (**Figure 6.7 D**). We found a significant difference between the two sets of cultures (i.e., WT and PWS) only in the theta waves after 1 hour of CCh application (**Figure 6.7 E**). The theta power of the WT cultures decreased by 60%, whereas that of the PWS cultures decreased by 30%. These results are consistent with the results of a previous study that revealed abnormalities in theta waves during REM sleep. Beta waves did not show significant differences in the two genotypes.

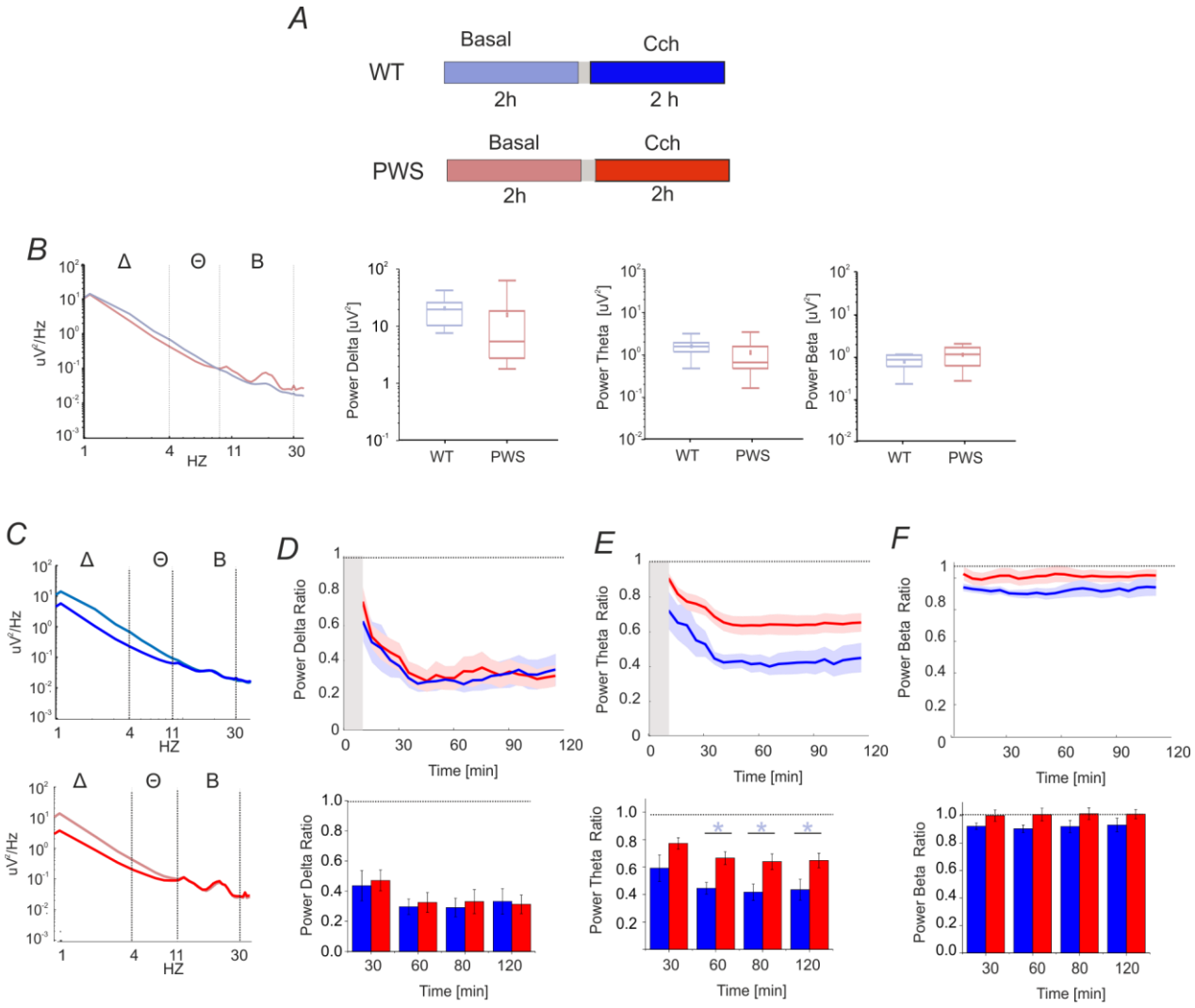

Figure 6.7 LFP analysis of PWS and WT cultures. *A) Experimental protocol adopted for the experiments. B) Power spectral density of basal segments for WT and PWS cultures. We computed the power for each set of bands delta (1-4 Hz), theta (5-9 Hz) and beta (9-13 Hz). We did not find any differences during the basal phase. C) Power spectral density of WT and PWS under baseline conditions and during CCh application. CCh caused suppression of all the low waves considered for both genotypes. D) Delta power following CCh administration. We normalized the power with respect to the basal value (indicated by the dashed line). CCh caused a decrease of 80% for both groups. After dividing the entire recording into 30-minute intervals, we did not find a significant difference between WT and PWS. E) Theta power following CCh administration. We normalized the power with respect to the basal value (indicated by the dashed line). CCh caused a decrease of 60% in WT cultures and a decrease of 30% in PWS cultures. After dividing the entire recording into 30-minute intervals, we found a significant difference between WT and PWS after 1 hour of treatment. F) Beta power following CCh administration. We normalized the power with respect to the basal value (indicated by the dashed line). Beta waves were not affected by the treatment in PWS cultures. WT cultures showed a decrease of 90% compared to the basal values. After dividing the entire recording into 30-minute intervals, we did not find a significant difference between WT and PWS. For each box plot (B), the small square indicates the mean, the central line illustrates the median, and the box limits indicate the 25th and 75th percentiles. All data are presented as the mean +/- SEM. Statistical analysis was performed using the two-sample t- test (*p<0.05).*

The electrophysiological study was complemented by gene expression assessment performed by the group of V. Tucci. In particular, we first determined whether the differences in the network sleep suppression states between PWS and WT cultures identified by MEA recordings are associated with differences in the transcriptome observed *in vivo*.

For the *in vitro* analyses, cortical cultures were stimulated with 20 μM of CCh, and RNA was extracted 1 h later. For the *in vivo* gene expression analyses, mice were sleep-deprived for 6 h, and their brains were collected 1 hour later. Control mice were kept undisturbed in their home cages, and control cultures were sham-stimulated with water. The data were normalized with respect to the control condition both *in vivo* and *in vitro* (dashed green line, **Figure 6.8**).

As expected, two classical immediately early genes (IEGs), Homer 1a (**Figure 6.8 C**), and C- fos **(Figure 6.8A)** were significantly overexpressed after sleep deprivation as well as after CCh stimulation of cell cultures. We are going to check the level of Arc in the following weeks. The relative mRNA levels of Per2 (**Figure 6.8 E**), Dpb (Figure 6.7 B) and Bmal (**Figure 6.8 D**), three circadian genes, were significantly affected by the treatment both *in vitro* and *in vivo*. In contrast, PWS mice and cultures did not show any significant variation after Sleep-deprivation (SD) *in vivo* or after CCh stimulation *in vitro*. Comparing the two genotypes, both circadian and homeostatic genes were found to be differently affected by SD in WT and PWS mice. In particular, PWS cultures did not show any significant variations in the relative mRNA levels upon CCh administration. This suggest that the paternal deletion of the *Snord116* gene could affected both the homeostatic and the circadian genes.

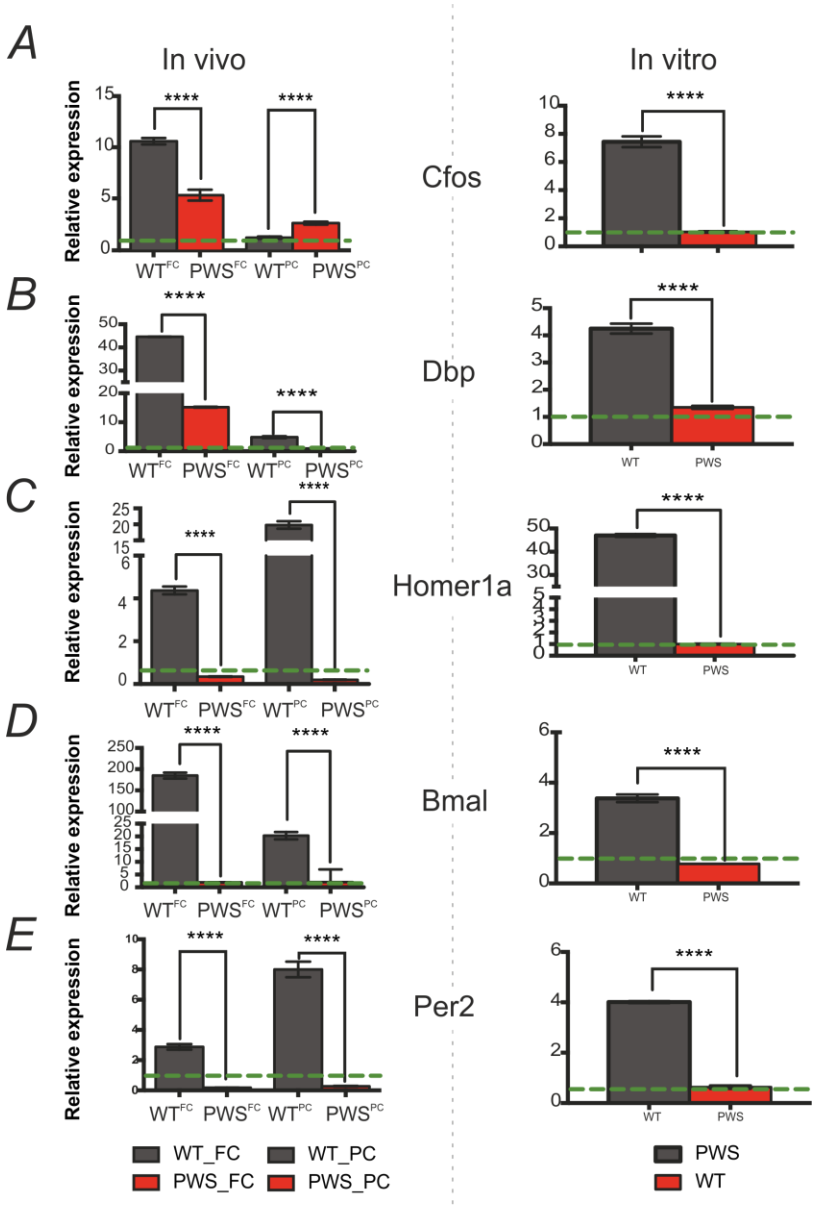

Figure 6.8. Comparison of gene expression in WT and PWS in vitro and in vivo.(Left) In vivo gene expression was measured using frontal cortex (FC) and parietal cortex (PC) from WT (n=5) and PWS mice (n=5). The animals were sacrificed 1 hour after sleep deprivation. The data were normalized with respect to control samples from WT (n=5) or PWS (n=5) mice without sleep deprivation (green dotted line) (Right). In vitro gene expression analysis of cortical cells after 1 hour of CCh administration t WT (n=5) or PWS (n=5) cultures. The data were normalized with respect to control cultures treated with standard medium (green dashed line).

6.3 Conclusion

In this study, we presented electrophysiological evidence indicating that primary cortical cultures that display synchronized low-frequency firing patterns under spontaneous conditions are also able to encompass some essential features of sleep in a pathological model. We presented experiments and analyses suggesting that our results potentially replicate those obtained *in vivo* in animals.

During the spontaneous phase, the starting level of firing and bursting activity is comparable between genotypes. PWS cultures displayed less synchronized activity than the WT cultures, as indicated by their higher IBR, lower BI and lower STTC. However, we did not find significant differences in the spontaneous synchronized activity of PWS and WT cultures.

CCh administration caused evident desynchronization of the activity of both genotypes, but WT and PWS cultures showed different response profiles after CCh treatment. In particular, PWS cultures displayed less reactivity in response to the stimulation, especially during the first hour. After that period, the profiles of the two groups were similar.

To assess possible differences in connectivity, we analyzed the network burst activity and the correlation between burst events. We found no significant difference in the duration of NB events, although PWS exhibited a higher NB rate and longer IBI during basal recording than the WT cultures.

Moreover, the analysis of the cross-correlation during the basal period showed higher C_{peak} values and lower latencies for WT cultures than for PWS cultures. Hence, more strongly synchronized neuronal networks were observed in the WT cultures than in the PWS cultures. These results suggest that there is less neuronal connectivity in PWS cultures than in WT cultures at the same developmental stage. Since one of the phenotypes of Snord116 mice is delayed development, we hypothesize that a similar trend occurs in the neuronal cultures. For confirming that, in the future we will assess morphological changes with immunofluorescence analysis to marker possible difference in the number of neurons, and in the glutamatergic and GABAergic synapses.

The analysis of LFP revealed abnormalities in the theta waves similar to those observed in animals *in vivo* and in PWS patients (Lassi et al., 2016b). No differences in LFP were found between PWS and WT cultures during the sleep-like state (i.e., the basal phase). These results are consistent with the results previously reported by Lassi(Lassi et al., 2016b).

Distinct classes of genes are differentially expressed during sleep and wakefulness (Pompeiano et al., 1994, 1997; Cirelli et al., 1996, 2004, 2006; Cirelli and Tononi, 1999, 2000a,b; Wisor et al., 2002; Terao et al., 2003; Mackiewicz et al., 2007; Maret et al., 2007; Mongrain et al., 2010). One important class of genes that is overexpressed during spontaneous or enforced wakefulness is immediate early

genes (IEG). Recent studies have shown that among the IEGs, Homer1a expression is the most reliable marker for sleep need (Maret et al., 2007; Hinard 2012). We showed that Homer1a and Cfos were significantly overexpressed both *in vivo* and *in vitro* after sleep deprivation in WT animals. Moreover, SD causes a significant increase in the relative levels of Per2 and Bmal. WT cultures treated with CCh showed similar behavior, i.e., all the IEGs examined were overexpressed, as shown in our previous work (Colombi et al., 2016). In PWS, the expression of these genes did not show any rebound after SD, suggesting an alteration in the control of the homeostatic process. These alterations could be due to deletion of the SNORD 116 gene in PWS.

In conclusion, our results showed that MEA recordings coupled to cortical cultures could recapitulate functional and molecular key mechanisms of the complex in-vivo brain networks both in physiological and pathological conditions.

Related publications and/or conference abstracts

1) International Journal

Colombi I. Falappa M. Freschi A. Tucci V*. Chiappalone M. Pace M. Phenotypic characterization of mice with a paternal deletion of the Snord116 gene: A mouse model for Prader Willi Syndrome. **(In preparation)**

*Corresponding author

2) Conference proceeding

Colombi I., Pace M, Tucci V., Chiappalone M. Sleep- related electrophysiological activity of cortical cultures on MEA. MEA Meeting 2018 | 11th International Meeting on Substrate Integrated Microelectrode Arrays, Reutlingen, Germany, 4 Jul - 6 Jul, 2018.

References

Adhikari, A., Copping, N.A., Onaga, B., Pride, M.C., Coulson, R.L., Yang, M., Yasui, D.H., Lasalle, J.M., and Silverman, J.L. (2018). Cognitive Deficits in the Snord116 Deletion Mouse Model for Prader-Willi Syndrome. *Neurobiology of learning and memory*.

Bieth, E., Eddiry, S., Gaston, V., Lorenzini, F., Buffet, A., Auriol, F.C., Molinas, C., Cailley, D., Rooryck, C., and Arveiler, B. (2015). Highly restricted deletion of the SNORD116 region is implicated in Prader–Willi Syndrome. *European Journal of Human Genetics* 23**,** 252.

Borbely, A.A. (1982). A two process model of sleep regulation. *Hum Neurobiol* 1**,** 195-204.

Butler, M.G. (2002). Imprinting disorders: non-Mendelian mechanisms affecting growth. *Journal of pediatric endocrinology & metabolism: JPEM* 15**,** 1279.

Camfferman, D., Mcevoy, R.D., O'donoghue, F., and Lushington, K. (2008). Prader Willi Syndrome and excessive daytime sleepiness. *Sleep medicine reviews* 12**,** 65-75.

Colombi, I., Tinarelli, F., Pasquale, V., Tucci, V., and Chiappalone, M. (2016). A simplified in vitro experimental model encompasses the essential features of sleep. *Frontiers in Neuroscience* 10.

De Smith, A.J., Purmann, C., Walters, R.G., Ellis, R.J., Holder, S.E., Van Haelst, M.M., Brady, A.F., Fairbrother, U.L., Dattani, M., and Keogh, J.M. (2009). A deletion of the HBII-85 class of small nucleolar RNAs (snoRNAs) is associated with hyperphagia, obesity and hypogonadism. *Human molecular genetics* 18**,** 3257-3265.

Ding, F., Li, H.H., Zhang, S., Solomon, N.M., Camper, S.A., Cohen, P., and Francke, U. (2008). SnoRNA Snord116 (Pwcr1/MBII-85) deletion causes growth deficiency and hyperphagia in mice. *PloS one* 3**,** e1709.

Duker, A.L., Ballif, B.C., Bawle, E.V., Person, R.E., Mahadevan, S., Alliman, S., Thompson, R., Traylor, R., Bejjani, B.A., and Shaffer, L.G. (2010). Paternally inherited microdeletion at 15q11. 2 confirms a significant role for the SNORD116 C/D box snoRNA cluster in Prader–Willi syndrome. *European Journal of Human Genetics* 18**,** 1196.

El Merhie, A., Ito, D., Colombi, I., Keshavan, S., Mishra, N., Miseikis, V., Diaspro, A., Coletti, C., Chiappalone, M., and Dante, S. (2018). Single layer graphene functionalized MEA for enhanced detection of neuronal network development. *Sensors and Actuators B: Chemical* 277**,** 224-233.

Falls, J.G., Pulford, D.J., Wylie, A.A., and Jirtle, R.L. (1999). Genomic imprinting: implications for human disease. *The American journal of pathology* 154**,** 635-647.

Harris, J.C., and Allen, R.P. (1996). Is excessive daytime sleepiness characteristic of Prader-Willi syndrome?: The effects of weight change. *Archives of pediatrics & adolescent medicine* 150**,** 1288-1293.

Hertz, G., Cataletto, M., Feinsilver, S.H., and Angulo, M. (1993). Sleep and breathing patterns in patients with Prader Willi syndrome (PWS): effects of age and gender. *Sleep* 16**,** 366-371.

Lassi, G., Maggi, S., Balzani, E., Cosentini, I., Garcia-Garcia, C., and Tucci, V. (2016a). Working-for-food behaviors: A preclinical study in Prader-Willi mutant mice. *Genetics***,** genetics. 116.192286.

Lassi, G., Priano, L., Maggi, S., Garcia-Garcia, C., Balzani, E., El-Assawy, N., Pagani, M., Tinarelli, F., Giardino, D., and Mauro, A. (2016b). Deletion of the Snord116/SNORD116 alters sleep in mice and patients with Prader-Willi syndrome. *Sleep* 39**,** 637-644.

Manni, R., Politini, L., Nobili, L., Ferrillo, F., Livieri, C., Veneselli, E., Biancheri, R., Martinetti, M., and Tartara, A. (2001). Hypersomnia in the Prader Willi syndrome: clinical-electrophysiological features and underlying factors. *Clinical neurophysiology* 112**,** 800-805.

Morison, I.M., and Reeve, A.E. (1998). A catalogue of imprinted genes and parent-of-origin effects in humans and animals. *Human Molecular Genetics* 7**,** 1599-1609.

Nicholls, R.D. (2000). The impact of genomic imprinting for neurobehavioral and developmental disorders. *The Journal of clinical investigation* 105**,** 413-418.

Pasquale, V., Martinoia, S., and Chiappalone, M. (2010). A self-adapting approach for the detection of bursts and network bursts in neuronal cultures. *Journal of computational neuroscience* 29**,** 213-229.

Peters, J. (2014). The role of genomic imprinting in biology and disease: an expanding view. *Nature Reviews Genetics* 15**,** 517.

Powell, W.T., and Lasalle, J.M. (2015). Epigenetic mechanisms in diurnal cycles of metabolism and neurodevelopment. *Human molecular genetics* 24**,** R1-R9.

Priano, L., Grugni, G., Miscio, G., Guastamacchia, G., Toffolet, L., Sartorio, A., and Mauro, A. (2006). Sleep cycling alternating pattern (CAP) expression is associated with hypersomnia and GH secretory pattern in Prader–Willi syndrome. *Sleep medicine* 7**,** 627-633.

Sahoo, T., Del Gaudio, D., German, J.R., Shinawi, M., Peters, S.U., Person, R.E., Garnica, A., Cheung, S.W., and Beaudet, A.L. (2008). Prader-Willi phenotype caused by paternal deficiency for the HBII-85 C/D box small nucleolar RNA cluster. *Nature genetics* 40**,** 719.

Skryabin, B.V., Gubar, L.V., Seeger, B., Pfeiffer, J., Handel, S., Robeck, T., Karpova, E., Rozhdestvensky, T.S., and Brosius, J. (2007). Deletion of the MBII-85 snoRNA gene cluster in mice results in postnatal growth retardation. *PLoS genetics* 3**,** e235.

Vgontzas, A.N., Bixler, E.O., Kales, A., Centurione, A., Rogan, P.K., Mascari, M., and Vela-Bueno, A. (1996a). Daytime Sleepines and Rem Abrormalities in Prader-Willi Syndrome: Evidence of Generalized Hypoarousal. *International Journal of Neuroscience* 87**,** 127-139.

Vgontzas, A.N., Kales, A., Seip, J., Mascari, M.J., Bixler, E.O., Myers, D.C., Vela‐Bueno, A., and Rogan, P.K. (1996b). Relationship of sleep abnormalities to patient genotypes in Prader‐Willi syndrome. *American journal of medical genetics* 67**,** 478-482.

Part III

Central nervous system diseases

Introduction

Central nervous system diseases (CNS) constitute 6.3% of the global burden of disease and impact on quality of life: the problems related to such diseases involve cognitive, psychological and social consequences. There are more than 600 diseases of the nervous system, such as brain tumors, epilepsy, Parkinson's disease and stroke. Therapies for neurological disorders usually include physiotherapy, pain management, and medication. Among the Central nervous system diseases (CNS) during my PhD project I was involved in two different side projects in the field of epilepsy and Down syndrome.

The first project is the Marie Skłodowska-Curie project Re.B.Us (Rewiring Brain Units) granted to Dr G. Panuccio. One of the project's aims was to suppress ictal-like activity of brain slices with specific patterns of electrical stimulation. Currently, drug therapies are the most common approach to alleviate seizures, but unfortunately up to 30% of epilepsy patients do not respond to pharmacological treatment (Pineau et al., 2009). While surgical ablation of the epileptogenic tissue may ameliorate the patient's condition, it is not feasible in all patients and may not guarantee a completely seizure-free life (Tanriverdi et al., 2008). Modulation of epileptic limbic networks by electrical DBS is a promising approach when pharmacological treatment or neurosurgery are not suitable. For this reason starting from the second year, we developed a custom methodology in order to guarantee the maintenance for good and stable ictal-like activity over several hours (Panuccio et al., 2018).

During the third year I then adapted this methodology to record spontaneous activity from hippocampal brain slices. The purpose of these experiments was to validate the effect of Bumetanide on Down syndrome mice both in cultures and in slices (see Chapter 8). Our approaches had significantly improved the feasibility of MEA recording from brain slices, allowing us to record stable activity along different hours.

Chapter 7:

Developing a methodology for brain slice experiments

Rodent brain slices are a valuable tool for studying how neuronal networks function in health and disease (Dingledine, 2013) by means of ex vivo electrophysiological techniques because they preserve, at least in part, the original architecture and connectivity of the brain region(s) of interest (ROI).

MEAs permit the recording of electrical activity generated by neuronal networks from a greater number of observation points compared to conventional extracellular field potential recording, where spatial restrictions limit the number of electrodes that can be accommodated on the surface of the brain slice. Moreover, MEA chips offer the added advantage of known interelectrode distance, which is very useful in tracing impulse propagation and assessing the traveling velocity of recorded signals. Although initially conceived for recording from cultured neurons (Gross et al., 1995;Novellino et al., 2011;Vassallo et al., 2017), MEAs are now also used to characterize the electrophysiological features of acute brain slices obtained from rodents (Reinartz et al., 2014) and humans (Dossi et al., 2014).

However, MEA recording inherently involves technical challenges associated with obtaining or maintaining stable patterns of activity throughout long (several hours) experimental protocols. First, tissue oxygenation may not be adequate within the large, round, submerged-type recording chamber (Hajos et al., 2009;Ivanov and Zilberter, 2011) that is typical of commercially available MEAs, while poor signal-to-noise ratio and temperature instability may affect the quality of the recording when a high perfusion rate (6-10 mL/min) is used to increase the oxygen supply to the brain slice. Second, signals with high-frequency components are rarely observed when submerged-type recording chambers are used (Hajos et al., 2009). To overcome these limitations, several strategies have been proposed by researchers. For example, increasing the perfusion rate (Hajos et al., 2009) while reducing brain slice thickness (≤ 400 μM) and area is crucial in achieving adequate oxygen supply to the tissue. Although the described approaches have significantly improved the feasibility of MEA recording from acute brain slices, they have not been tested in prolonged recording sessions of several hours' duration, which can cause significant stress to brain tissue. For these reasons, we developed a custom methodology that allowed us to record stable and prolonged activity from brain slices (paragraph 7.2).). Moreover, since our laboratory had no previous expertise in analyzing brain slice

signals, I personally developed a custom Graphical User Interface (GUI) for the analysis of signals from different regions of the brain tissue. In this chapter, I will first introduce the user-friendly software that I developed for mapping the electrodes with respect to the ROI in real time. I will then describe the seizure detection algorithm I developed for the analysis of ictal-like activity in the ReBus project.

7.1 Setup for acute brain slices

Hippocampal-EC slices coupled to MEA were employed in the electrophysiological studies. Below, we briefly describe the procedure that was used to record spontaneous activity based on our recent work published in Jove (Panuccio et al., 2018).

Dissection procedure

Adult (4-6-week-old) male CD1 mice were perfused intracardially with ice-cold (0-2 °C) ACSF under deep isoflurane anesthesia and then decapitated. Their brains was quickly removed (within 60 seconds, **Figure 7.1A**) and placed in a small bowl containing equilibrated ice-cold (0-2 °C) cutting ACSF; the ACSF was continuously bubbled with a gas mixture (5% CO_2 and 95% O_2) to equilibrate it at pH 7.35-7.40. The brain was allowed to chill for 90-120 seconds (**Figure 7.1B**, right panel). The cerebellum was removed, and a straight cut was made along the coronal plane to remove the frontal third of the brain (**Figure 7.1C**). The isolated tissue block was glued with cyanoacrylate to the specimen disc of the vibratome (VT1000S, Leica, Germany) with the entorhinal cortex facing the blade and immediately placed in the slicing chamber containing carbogenated (5% CO_2 and 95% O_2) cold (0-2 °C) cutting ACSF (**Figure 7.1D**). Hippocampus-EC slices (400 μm thick) were cut in the horizontal plane. Tissue sections were discarded until the hippocampus was clearly visible (usually ~900 μm). The two hemispheres were separated using a scalpel blade. The brain slices were gently transferred to a beaker using an inverted Pasteur pipette and rinsed twice with standard ACSF solution. The slices were then transferred to a commercial holding chamber (KF Technologies) containing carbogenated ACSF solution and incubated for approximately 20 minutes at 32 °C and then for at least 1 hour at room temperature (**Figure 7.1D**).

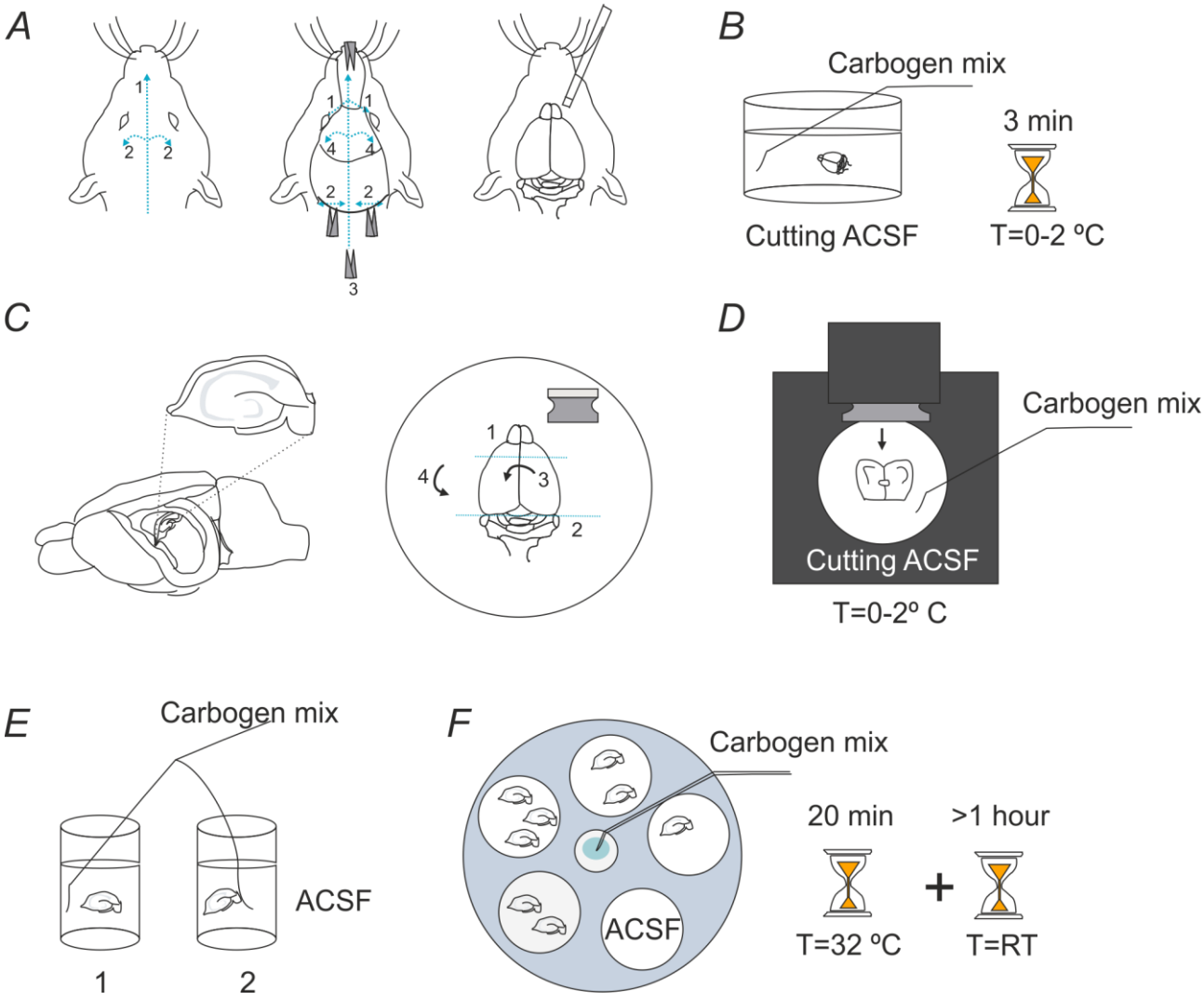

Figure 7.1 Schematic representation of the brain slice preparation. A) Once the head is cut, the scalp is removed using scissors (left panel, 1-2). Using the scissors, two mediolateral cuts are made above the eyes (middle panel, 1); subsequently, two more cuts are made at the base of the head (middle panel, 2). Then, by a postero-anterior cut in the midline of the skull, two skull flaps are formed (middle panel 3). The brain is exposed using scissors, and a small spatula is used to gently extract it from the skull (left panel). C) The brain is immersed in ice-cold ACSF for at least 2-3 min. C) The brain is placed in a cold Petri dish, and the cerebellum and one third of the frontal brain (along the coronal plane) are removed. D) The isolated tissue block is glued with cyanoacrylate to the specimen disc of the vibratome (VT1000S, Leica, Germany) with the entorhinal cortex facing the blade. E) The brain slices are gently transferred to a beaker using an inverted Pasteur pipette and rinsed twice with standard ACSF solution. F) The slices are then transferred to a commercial holding chamber (KF Technologies) containing carbogenated ACSF solution and incubated for approximately 20 min at 32 °C and then for at least 1 hour at room temperature.

Custom chamber and perfusion control system for brain slices

For brain slices, we used a customized recording chamber inspired by the design of the patch-clamp recording chamber; this provides stable and reliable laminar flow that is crucial for the successful MEA recording (**Figure 7.2**). The use of this chamber also allows the thickness of the brain slice to be increased to 400 µm, making it possible to achieve a fair trade-off between tissue viability and intrinsic connectivity. The use of recording chambers with relatively small volume (~1.5 mL) and a high perfusion rate (5-6 mL/min) allows adequate exchange of the perfusion medium (≥3 times/min).

The customized chamber can be obtained from commercial sources (e.g., Crisel Instruments) at an affordable price or produced in-house using 3D printing technology.

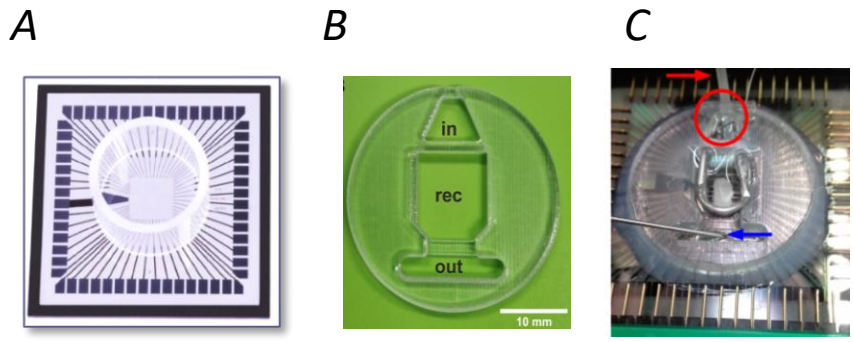

Figure 7.2 A) MEA 30/200 made by Multi Channel Systems with small ring. B) Custom recording chamber. in: inlet reservoir to accommodate the heating cannula and the reference electrode; out: outlet reservoir to accommodate the suction needle; rec: recording chamber. C) Final assembly of the recording chamber mounted on the MEA chip. A brain slice rests on the bottom and is held in place by the anchor. The red arrow indicates the PTFE tubing covering the heating cannula; the red circle indicates the reference electrode, a saturated KCl pellet submerged in ACSF in the inlet reservoir. The blue arrow indicates the suction needle in the outlet reservoir.

The standard MEA electrophysiology setup can also be combined with a perfusion system. Continuous flow of artificial CSF (ACSF) saturated with 95% O_2 and 5% CO_2 is necessary to maintain acute slices in functional condition during the MEA recording. Since in the laboratory of IIT we had no prior experience using acute brain slices on MEA, we tested several arrangements to find the best setup configuration. Initially, we attempted to control the perfusion flow using a peristaltic pump, but we encountered several problems with the resulting noise during the recording and with the level of oxygenation of the brain slice. For these reasons, we decided to control the flow by gravity only. The custom recording chamber described above (**Figure 7.2**) allows exchange of the perfusion medium 6-10 times/min at a flow rate of 2 mL/min. Thus, an adequate oxygen supply to the brain slices is guaranteed even at relatively medium-low perfusion rates while still ensuring a stable recording temperature and high signal-to-noise ratio. **Figure 7.3** depicts the setup used for brain slice recording.

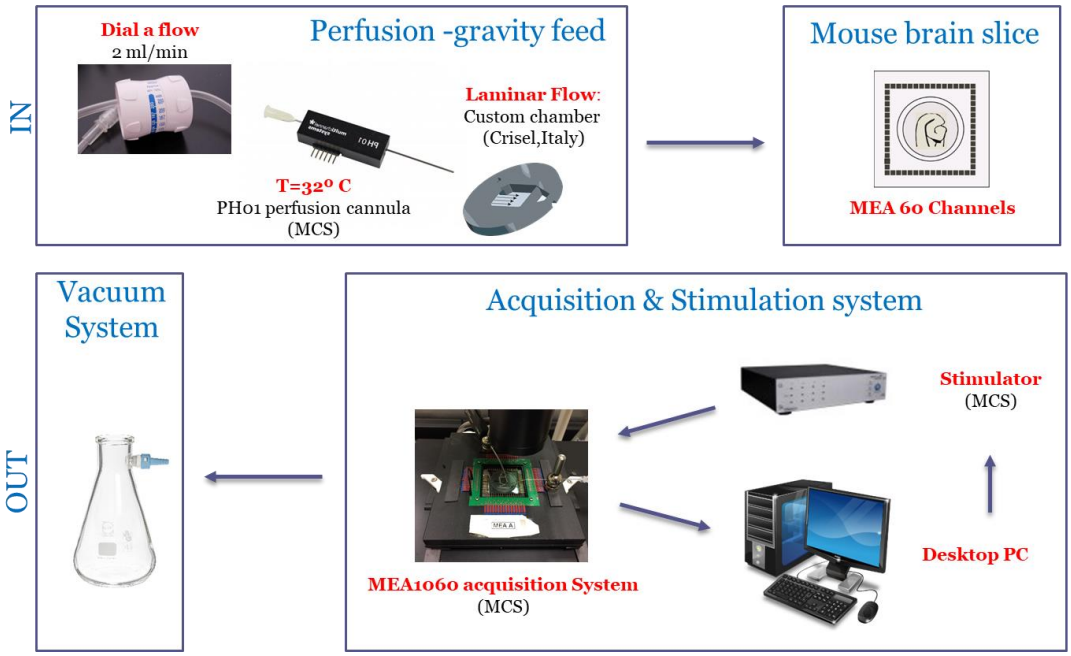

Figure 7.13 Experimental setup used for brain slices experiments

7.2 Data analysis tools for brain slices: sliceGUI

When we began to record from brain slices, we decided to adapt the GUI used for the analysis of culture signals (SpyCode, Chapter 2, paragraph 2.4.2). The new GUI, named SliceGUI, offers tools that focus primarily on analysis of the low-frequency portion of the signals, including filtering, detection and power spectral density estimation. Since I have been involved in the ReBus project focused on epilepsy, I implemented a new seizure detection method with the specific aim of being simple and fast. Several parameters that are often used in EEG analysis, such as energy and the estimation of the fluctuation index, were also implemented.

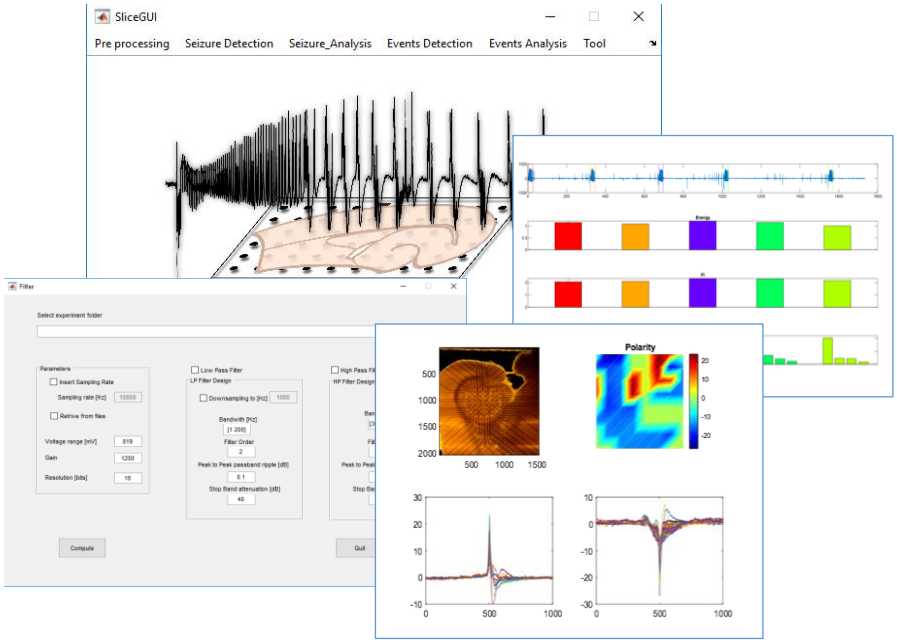

Figure 7.4 Running SliceGUI. The main Graphical User Interface (GUI) is depicted during a working session of the software. Additional GUIs for data input are shown to the user before launching each computation. The output of an analysis session is provided through a series of figures (.fig or .jpg format) or results files (.mat or ASCII format).

Figure 7.5 schematically shows the organization of the software. It includes a block for data conversion, one for mapping the electrodes in different brain structures (optional), and the cascade of analyses that can be performed after data filtering has been performed, i.e., seizure detection, features computation, events detection (both spikes and LFP) and the events analysis, which includes PSD estimation and MFR evaluation.

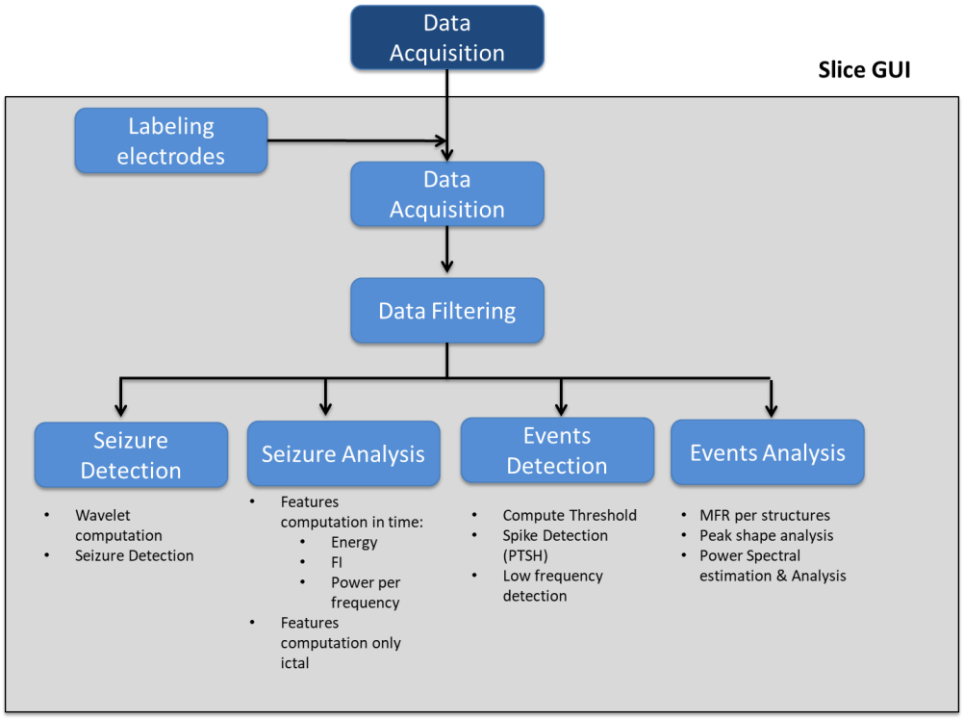

Figure 7.5 Schematic overview of the data analysis procedure implemented within Spycode. The functional blocks show the main computational and algorithmic options offered by the software.

In the following, we briefly describe the GUI used to map the electrodes and the seizure detection algorithm.

7.2.1 Labeling electrodes (MapGUI)

Our user-friendly GUI provides a quick, simple and flexible tool for mapping electrodes in various brain structures. Unlike commercial software, it is possible even for users with only basic programming skills to add custom MEA layouts. Images can be acquired in bright field; thus, any general-purpose camera that has good resolution and fits on a microscope is suitable. An inverted microscope is essential for visualizing the position of the microelectrodes relative to the brain slice, since these would be hidden underneath the tissue if an upright microscope were used. Once a picture of the slice has been obtained and loaded into the GUI, it is possible to select the top and bottom electrodes in the leftmost row of the array to mark the XY coordinates for image straightening using the "Activate Pointer button". Using the numbered pushbuttons below the brain slice image, the user can select the electrodes corresponding to the ROI and click the corresponding pushbutton in the structures panel to assign them (**Figure 7.5B**). By selecting the "Enter New Structures" button, it is possible to customize the structures. The default structures for the horizontal brain slice are depicted in Figure 2A.

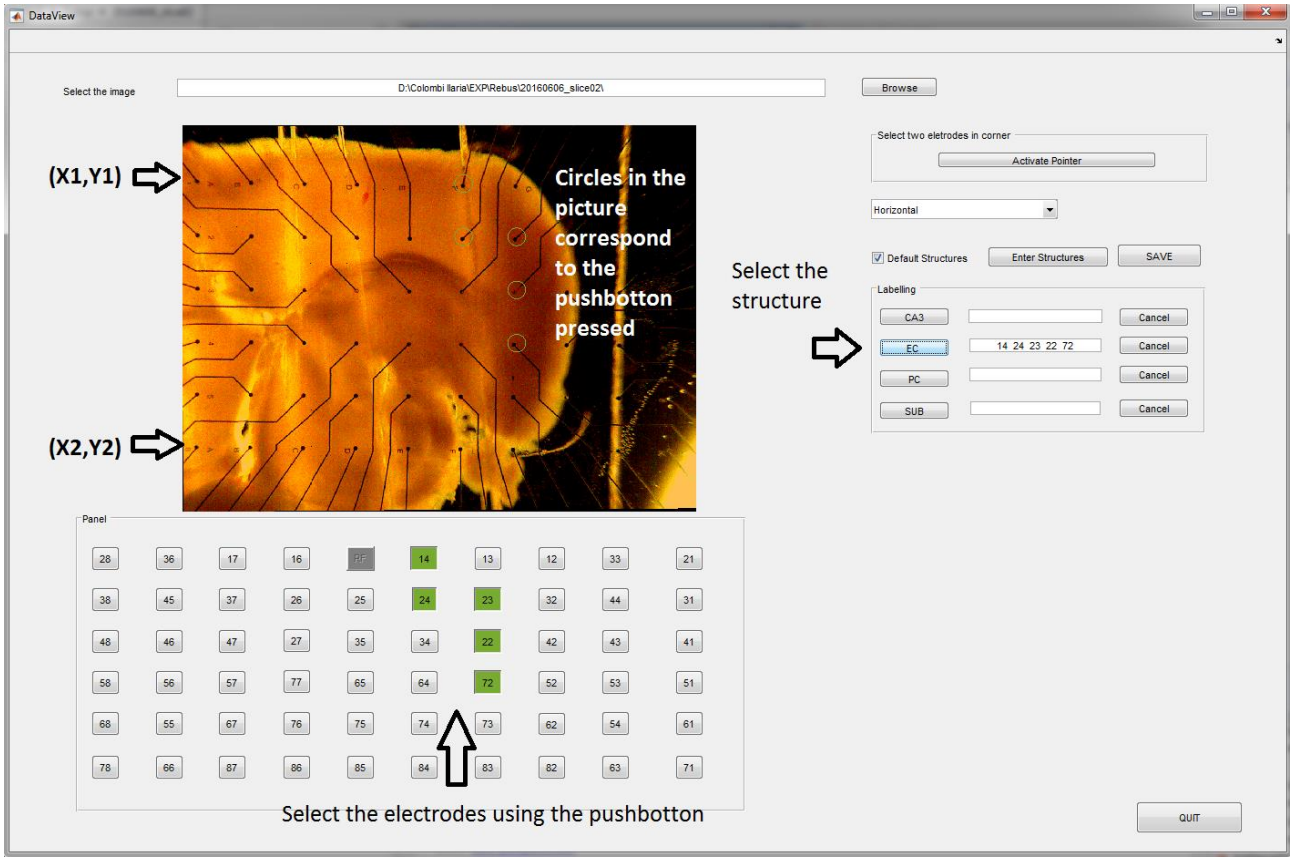

Figure 7.6 ***GUI for live MEA electrode mapping.*** *(A) Schematic representation of the combined hippocampus-EC slice positioned on the MEA. The default structures used for this protocol are the cornu ammonis 3 (CA3), the entorhinal cortex*

(EC), the perirhinal cortex (PC), and the subiculum (SUB). The reference electrode is schematized as a triangle; the electrodes encircled by dotted lines represent the XY coordinates for image straightening. (B) Screen capture of the GUI during live MEA mapping. The flow chart on the left of the capture outlines the step-by-step procedure that is followed.

7.2.2 Seizure detection & analysis

Seizure-like activity can be acutely induced in brain slices by changing the ionic composition of the artificial cerebrospinal fluid (ACSF), for example by decreasing magnesium while increasing potassium (Rutecki et al., 1985;Traynelis and Dingledine, 1988;Huberfeld et al., 2011), or by means of pharmacological manipulations such as blocking inhibitory GABAergic activity (Pitkänen et al., 2017). However, because these models are based on an unbalanced alteration of excitation and inhibition, they do not allow study of the interactions of excitatory and inhibitory networks and their concerted contribution to ictogenesis. Continuous perfusion of brain slices with the convulsant drug 4-AP, a K+ channel blocker (Rudy, 1988) (Rutecki et al., 1987), enhances both excitatory and inhibitory neurotransmission, thus allowing the investigator to study acute ictogenesis while keeping overall synaptic activity intact (Rutecki et al., 1987). The slices were incubated in 4-AP at 32 ºC for at least 1 hour before recording.

The mouse hippocampus-entorhinal cortex (EC) slice presents epileptiform-like activity that is induced by 4-AP and generated in the EC. The hippocampus and the EC are brain structures located in the medial temporal lobe. Pathologically, they play a special role in the development of seizures, especially in the case of temporal lobe epilepsy. The mechanism for controlling epileptogenesis is shown in **Figure 7.6 A,** i.e., ictal discharges form in the EC, propagate to the dentate gyrus via the perforant path, and follow the hippocampal loop to project back to the EC. Interictal discharges form in CA3, propagate to CA1 via the Schaffer collaterals and are projected back to the EC. The role of the re-entrant activity is to prevent rather than to sustain prolonged ictal events (Barbarosie and Avoli, 1997). Cell damage in the CA3 area is frequently found in patients with temporal lobe epilepsy; this type of damage can be simulated by cutting the Schaffer collaterals, represented in Figure 4A by a thick dotted line. This prevents interictal discharges from propagating and thereby increasing the epileptiform activity. As reported in previous work (Pineau et al., 2009), fixed low-frequency (1 Hz) stimulation of the subiculum is known to be effective in suppressing epileptiform activity in this *ex-vivo* model of epilepsy.

Therefore, we recorded specific regions in each slice, i.e., superficial and deeper EC, CA3, and subiculum (SUB), as depicted in **Figure 7.6B.**

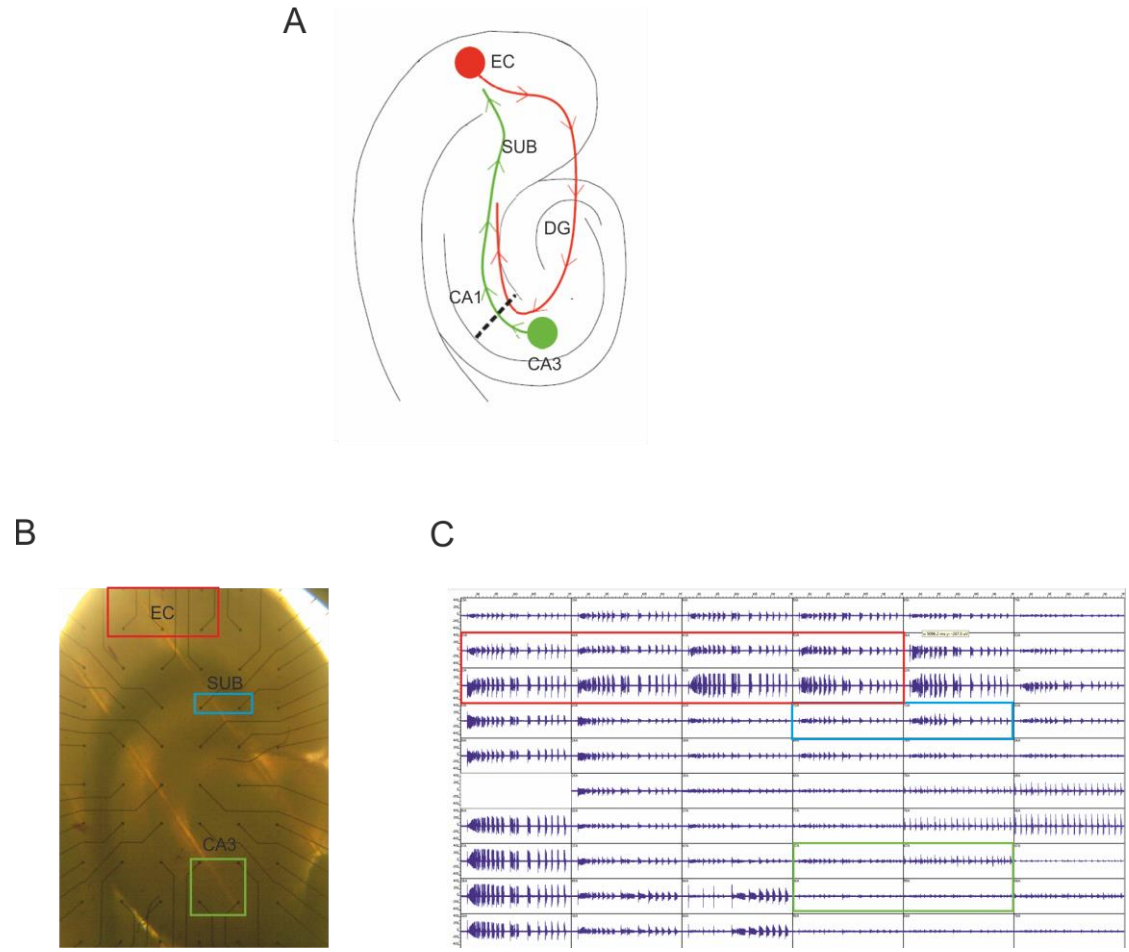

Figure 7.6. A) A schematic of the organization of the hippocampus-EC slice. B) Slice on the 60-channel MEA. C) 60-MEA channel recording using Mc Rack software during epileptic activity induced by 4 AP.

My expertise, which was acquired through the *in vitro* culture experiments (cf. Part II of this thesis), was in the analysis of the electrophysiological signals. The high-frequency activity (i.e., the spiking activity) of these cultures revealed a synchronized pattern of burst events consisting of a sequence of highly packed spikes with features similar to ictal-like activity (**Figure 7.7**). I then adapted the algorithm developed by my group for burst detection(Pasquale et al., 2010), so that it could be used to automatically detect ictal-like discharges in the ex-vivo brain slice assay.

Wide-band signals were first downsampled to 1 kHz; a low-pass filter (cutoff frequency 200 Hz) was then applied using a Hamming-window FIR filter of order 30.

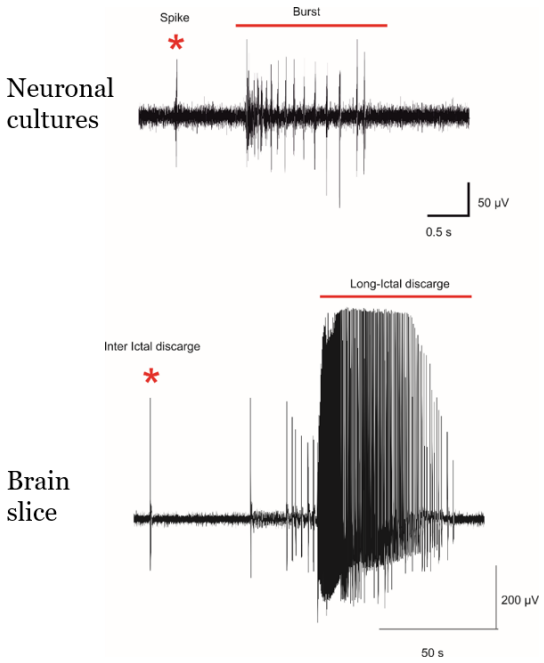

Figure 7.7 Comparison of single burst activity in a neuronal culture and ictal-like activity in a brain slice (recorded using one electrode in the entorhinal cortex)

We then computed the discrete wavelet transformation. Wavelets are mathematical functions that are capable of localizing a function or a set of data in both time and frequency. They are particularly useful for representing various aspects of signals such as trends, discontinuities, and repeated patterns. This method is especially powerful for nonstationary signal analysis.

There are two different wavelet functions, a continuous one (CWS) and a discrete one (DWS). In CWT, the signal to be analyzed is matched and convolved with the wavelet basis function at continuous time and frequency increments. In DWS, the product is taken at discrete points (usually dyadic to ensure orthogonality); the result is a weighted sum of a series of basic functions. In particular, the signal is decomposed using detailed coefficients that represent local details in the original function (such as a high-pass filter) and an approximation coefficient that gives the general trend of the original signal (such as a low-pass filter).

:

Approximation coefficient (A) Detail coefficient (D)

$$f(t) = \sum_{k=-\infty}^{\infty} c_k \phi(t-k) + \sum_{k=-\infty}^{\infty} \sum_{k=-\infty}^{\infty} d_{j,k} \psi(2^j.t-k)$$

Wavelet basic functions are families of functions that satisfy prescribed conditions such as continuity, zero mean amplitude, and finite or near finite duration. The Daubechies family of wavelets (Dhande and Gulhane, 2015)is one of the most commonly used orthogonal wavelets; it satisfies the

admissibility conditions, thus allowing reconstruction of the original signal from the wavelet coefficients.

The Daubechies order 4 wavelet was found to be the most appropriate for analysis of epileptic EEG data(Adeli et al., 2003;Dhande and Gulhane, 2015). As reported in a previous work (Adeli et al., 2003;De Guzman et al., 2004), the ictal activity is centered in a frequency range between 0.3 and 29 Hz, while the ictal onset appears in the theta range (9-11 Hz). To capture this activity, we selected the fifth level that is specific for these frequency ranges (**Figure 7.8**).

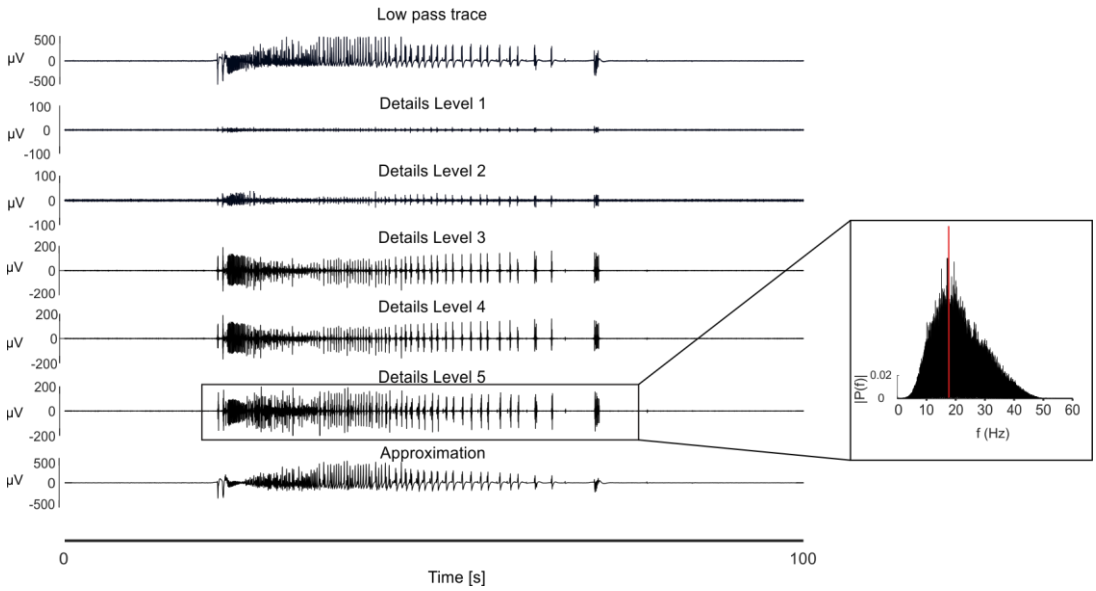

Figure 7.8 Daubechies order 4 decomposition on a single channel from Enthorinal/Cortex of CD1 mouse upon 4AP administration. We selected the fifth level that is specific for capturing the ictal onset (9-11 Hz).

We then performed event detection by setting a hard threshold, chosen as twelve times the standard deviation of the wavelet's noise (-10 σn). To classify different types of events, we computed the histogram of the interevent intervals. The histogram presents two peaks that correspond to high-packed and sparse activity, respectively.

We selected the minimum between these peaks as a threshold to discriminate among

1. Ictal core (tonic) events
2. Short interictal events
3. Long interictal events

The different types of events are depicted in **Figure 7.9.**

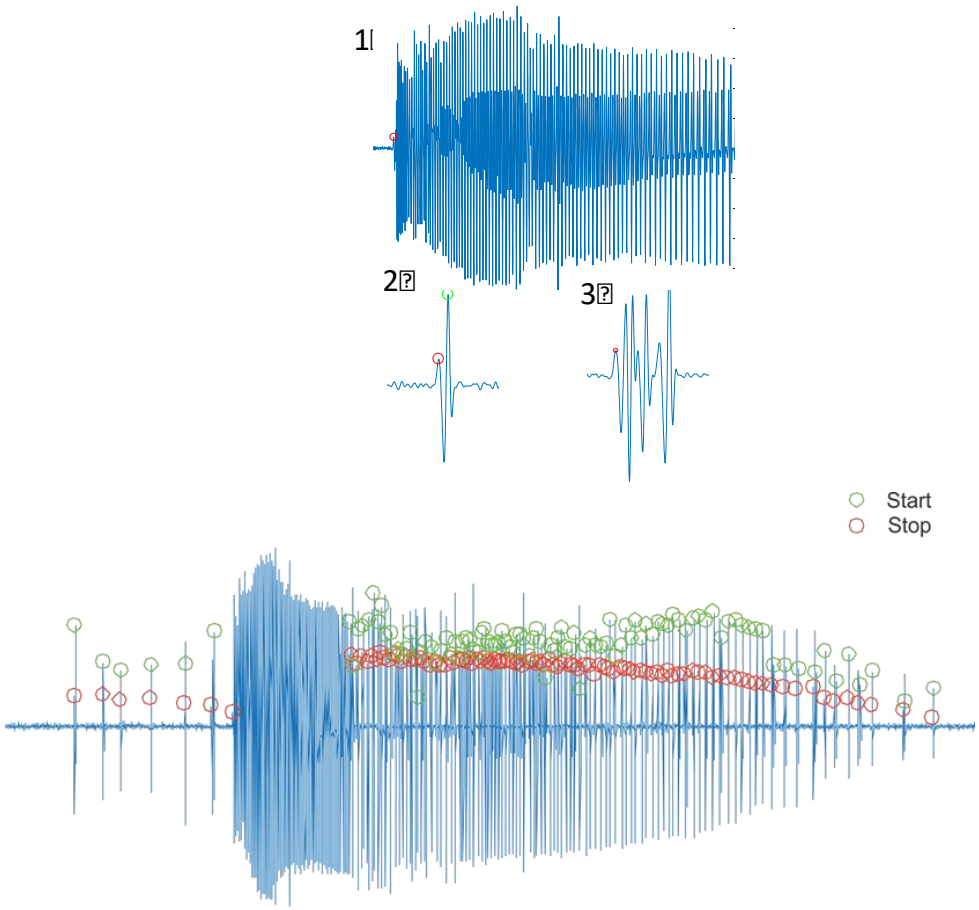

Figure 7.9 Types of events selected using an automatic threshold based on the distribution of events. Zoom of the three different types of events discriminate in the first step of the algorithm: the ictal core (tonic) events (numbered as 1 in the figure), short interictal events (events numbered as 2) and long interictal events (events numbered as 2). Below, one single ictal-like event with the different types of events depicted before.

If the algorithm detected only one peak, the threshold was set as the first value that was less than 10% of the first peak. To discriminate between these three types of events, we computed another histogram showing the duration of all detected events. We found two peaks; the first peak represents the short interictal events, and the second peak represents the ictal core and the long interictal events. We selected as a threshold the first value that was less than 10% of the second peak.

Ictal-like activity consists of a tonic phase that is characteristic of the onset of the activity and a subsequent clonic phase. To identify the clonic phase, we used the interevent distance (IEI), which was calculated as the difference between the end and the start of the next event. If the histogram of IEIs presented two peaks, we selected the minimum; otherwise, we took a percentage (10%) of the first peak as a threshold (min_IEI). If two ictal events were closer than a threshold (equal to min_IEI), they were merged. Ictal-like activities with duration less than 3 s were excluded.

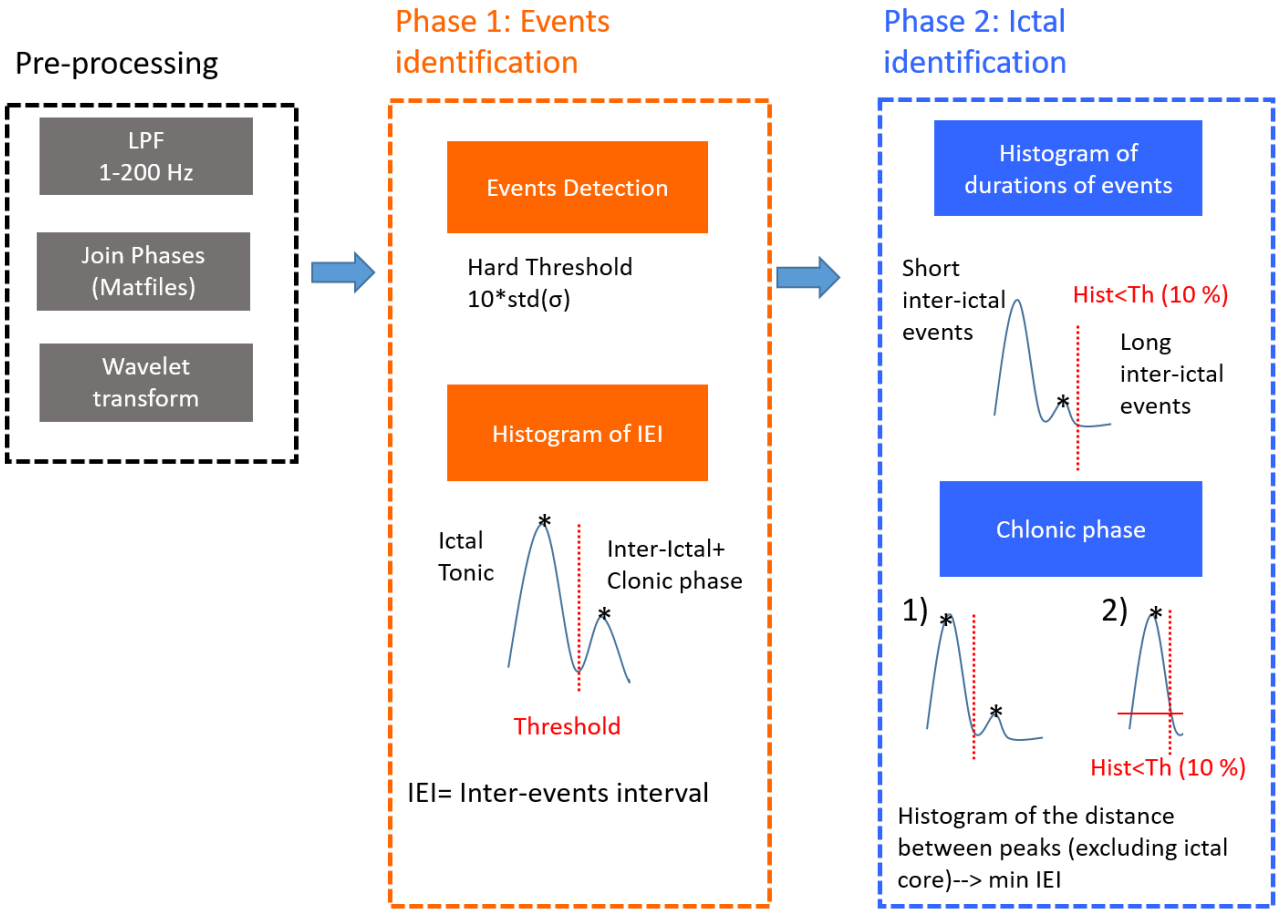

Figure 7.10 Schematic representation of the step of seizure detection algorithm

The seizure detection algorithm is implemented in a GUI that allow the user to compute the analysis in the selected ROI and phase as shown in **Figure 7.11**.

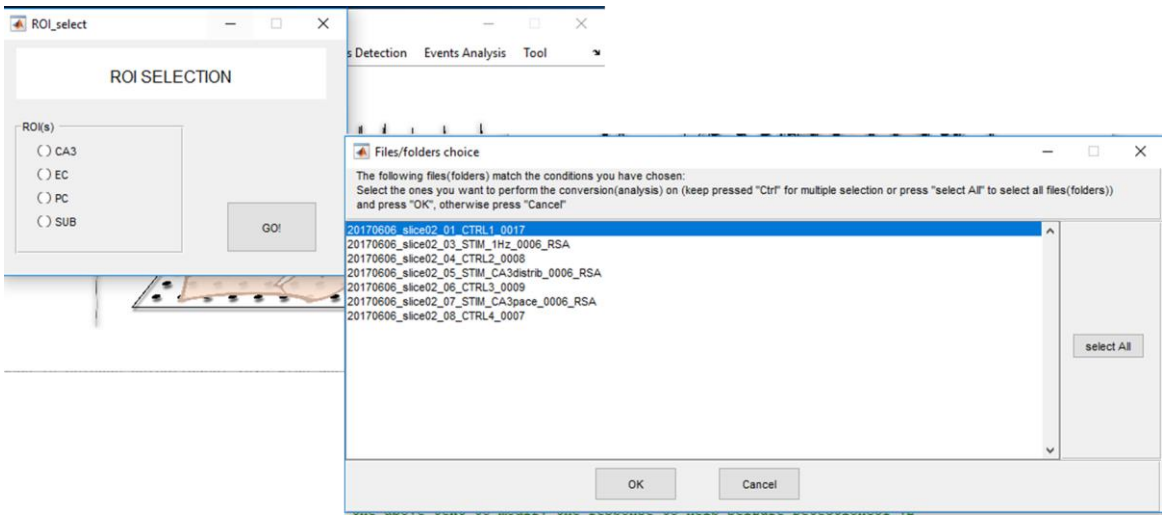

Figure 7.11 Running SeizureDetectionGUI. The main graphical user interface (GUI) is depicted during a working session of the software.

The user can easily insert and modify the parameters required by the software in text form. The computation can be performed for all of the mapped electrodes or for the visualized channel (**Figure**

7.12). Manual labeling was also implemented for false positives and negatives (using the plus or minus button) and for modifying the start or the stop of a detected seizure (using the edit button) (**Figure 7.12**).

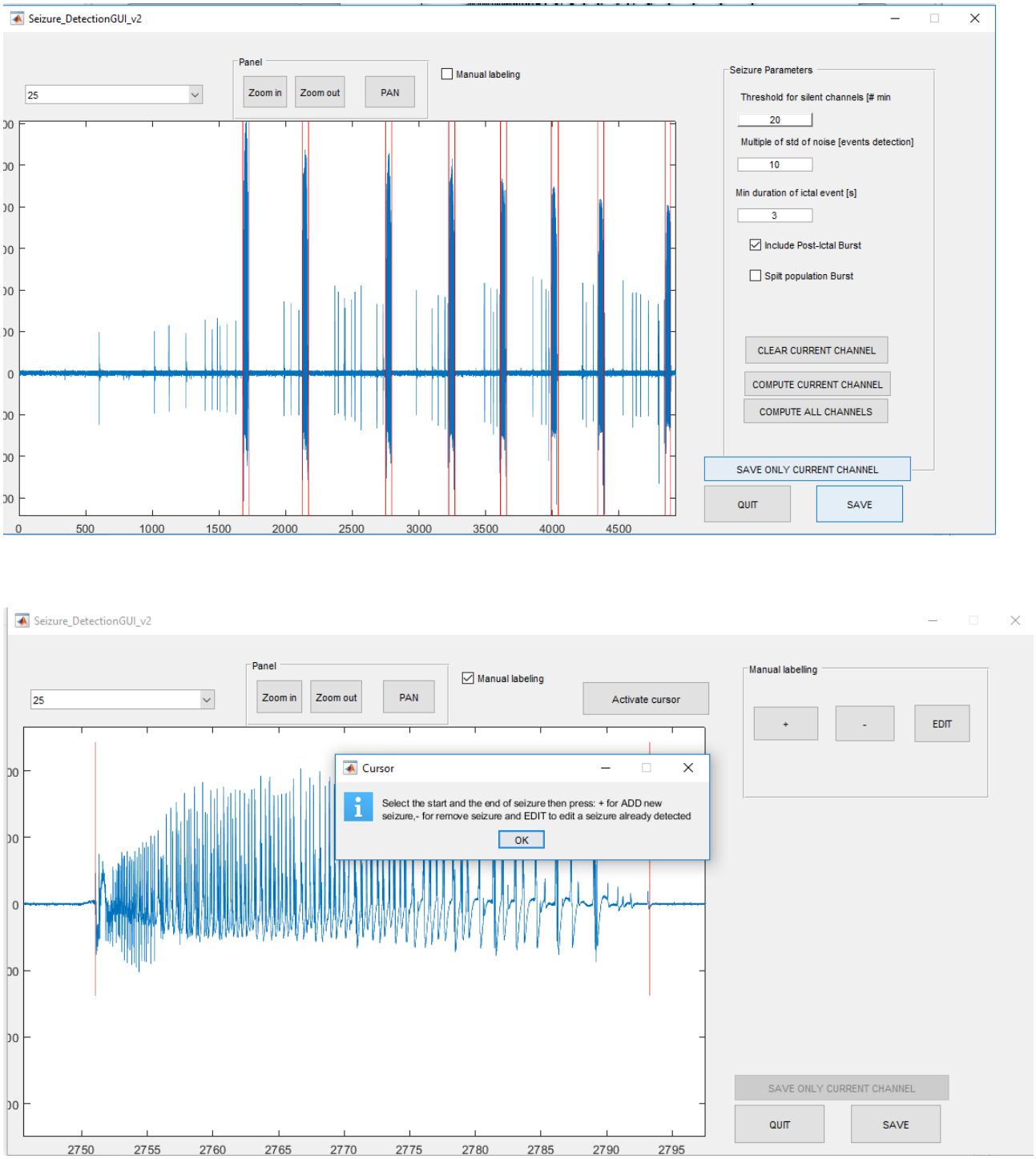

Figure 7.12 Examples of the output of the GUI. (Above) Seizure detection in a representative channel (the red bar indicates the seizure detected by the algorithm). (Below) Manual labeling for seizure correction.

Related publications and/or conference abstracts

Panuccio, G., **Colombi, I.,** and Chiappalone, M. (2018). Recording and Modulation of Epileptiform Activity in Rodent Brain Slices Coupled to Microelectrode Arrays. *Journal of visualized experiments: JoVE*.

References

Adeli, H., Zhou, Z., and Dadmehr, N. (2003). Analysis of EEG records in an epileptic patient using wavelet transform. *Journal of neuroscience methods* 123**,** 69-87.

Barbarosie, M., and Avoli, M. (1997). CA3-driven hippocampal-entorhinal loop controls rather than sustains in vitro limbic seizures. *The Journal of neuroscience* 17**,** 9308-9314.

De Guzman, P., D'antuono, M., and Avoli, M. (2004). Initiation of electrographic seizures by neuronal networks in entorhinal and perirhinal cortices in vitro. *Neuroscience* 123**,** 875-886.

Dhande, J., and Gulhane, S. (Year). "Daubechies wavelet based neural network classification system for biomedical signal", in: *Information Processing (ICIP), 2015 International Conference on*: IEEE), 188-191.

Dingledine, R. (2013). *Brain slices.* Springer Science & Business Media.

Dossi, E., Blauwblomme, T., Nabbout, R., Huberfeld, G., and Rouach, N. (2014). Multi-electrode array recordings of human epileptic postoperative cortical tissue. *Journal of visualized experiments: JoVE*.

Gross, G.W., Rhoades, B.K., Azzazy, H.M., and Wu, M.-C. (1995). The use of neuronal networks on multielectrode arrays as biosensors. *Biosensors and Bioelectronics* 10**,** 553-567.

Hajos, N., Ellender, T.J., Zemankovics, R., Mann, E.O., Exley, R., Cragg, S.J., Freund, T.F., and Paulsen, O. (2009). Maintaining network activity in submerged hippocampal slices: importance of oxygen supply. *European Journal of Neuroscience* 29**,** 319-327.

Huberfeld, G., De La Prida, L.M., Pallud, J., Cohen, I., Le Van Quyen, M., Adam, C., Clemenceau, S., Baulac, M., and Miles, R. (2011). Glutamatergic pre-ictal discharges emerge at the transition to seizure in human epilepsy. *Nature neuroscience* 14**,** 627.

Ivanov, A., and Zilberter, Y. (2011). Critical state of energy metabolism in brain slices: the principal role of oxygen delivery and energy substrates in shaping neuronal activity. *Frontiers in neuroenergetics* 3**,** 9.

Novellino, A., Scelfo, B., Palosaari, T., Price, A., Sobanski, T., Shafer, T.J., Johnstone, A.F., Gross, G.W., Gramowski, A., and Schroeder, O. (2011). Development of micro-electrode array based tests for neurotoxicity: assessment of interlaboratory reproducibility with neuroactive chemicals. *Frontiers in neuroengineering* 4**,** 4.

Panuccio, G., Colombi, I., and Chiappalone, M. (2018). Recording and Modulation of Epileptiform Activity in Rodent Brain Slices Coupled to Microelectrode Arrays. *Journal of visualized experiments: JoVE*.

Pasquale, V., Martinoia, S., and Chiappalone, M. (2010). A self-adapting approach for the detection of bursts and network bursts in neuronal cultures. *Journal of computational neuroscience* 29**,** 213-229.

Pineau, J., Guez, A., Vincent, R., Panuccio, G., and Avoli, M. (2009). Treating epilepsy via adaptive neurostimulation: a reinforcement learning approach. *Int J Neural Syst* 19**,** 227-240.

Pitkänen, A., Buckmaster, P., Galanopoulou, A.S., and Moshé, S.L. (2017). *Models of seizures and epilepsy.* Academic Press.

Reinartz, S., Biro, I., Gal, A., Giugliano, M., and Marom, S. (2014). Synaptic dynamics contribute to long-term single neuron response fluctuations. *Frontiers in neural circuits* 8**,** 71.

Rutecki, P.A., Lebeda, F.J., and Johnston, D. (1985). Epileptiform activity induced by changes in extracellular potassium in hippocampus. *Journal of neurophysiology* 54**,** 1363-1374.

Rutecki, P.A., Lebeda, F.J., and Johnston, D. (1987). 4-Aminopyridine produces epileptiform activity in hippocampus and enhances synaptic excitation and inhibition. *Journal of neurophysiology* 57**,** 1911-1924.

Tanriverdi, T., Poulin, N., and Olivier, A. (2008). Life 12 years after temporal lobe epilepsy surgery: a long-term, prospective clinical study. *Seizure* 17**,** 339-349.

Traynelis, S.F., and Dingledine, R. (1988). Potassium-induced spontaneous electrographic seizures in the rat hippocampal slice. *J Neurophysiol* 59**,** 259-276.

Vassallo, A., Chiappalone, M., Lopes, R.D.C., Scelfo, B., Novellino, A., Defranchi, E., Palosaari, T., Weisschu, T., Ramirez, T., and Martinoia, S. (2017). A multi-laboratory evaluation of microelectrode array-based measurements of neural network activity for acute neurotoxicity testing. *Neurotoxicology* 60**,** 280-292.

Chapter 8

Modulation of electrophysiological activity in neuronal networks of Ts65Dn mice

Down syndrome (DS) is a genetic disorder that causes intellectual disability in children and adults. The disorder results from the presence of an extra copy of human chromosome 21 (HSA21) or of a major portion of this chromosome; hence, it is also referred to as trisomy 21.

The onset of DS-related phenotypes occurs during prenatal development, although some of the manifestations of the disorder may also become apparent in adulthood (Dierssen, 2012). Learning deficits in DS children involve both short-term and long-term memory. DS children perform significantly worse than normal children on explicit memory tasks. However, they show normal learning ability for tasks requiring implicit memory processing, indicating a functional dissociation between implicit and explicit memory. Poor information encoding, impaired retrieval ability and attention deficits have also been demonstrated consistently in adults with DS, accounting for the selective impairment of explicit memory (Contestabile et al., 2010). The early occurrence of neuroanatomical abnormalities suggests that neurodevelopmental impairment is the major determinant of intellectual disability in DS.

Previous studies have demonstrated that trisomic DS mouse models reproduce the main genetic and cognitive disabilities associated with the human syndrome (Dierssen, 2012;Rueda et al., 2012;Aziz et al., 2018). The best-characterized and most widely investigated animal model of DS is the Ts65Dn mouse; it carries an extra copy of the distal segment of mouse chromosome 16, which is syntenic to the long arm of human chromosome 21.

Altered GABAergic signaling through chloride-permeable $GABA_A$ receptors ($GABA_ARs$) seems to play a major role in brain dysfunction and cognitive impairment in DS mouse models. The alteration involves neuronal network dynamics and synaptic inhibitory/excitatory balance in neurons (Kleschevnikov et al., 2004;Contestabile et al., 2017).

In the adult mammalian brain, GABA (γ-aminobutyric acid) is the main inhibitory neurotransmitter through $GABA_ARs$. $GABA_ARs$ are ligand-gated ion channels that are permeable to chloride (Cl^-); however, the flux of Cl^- through these receptors depends on the chloride reversal potential, which in turn depends on the intracellular chloride concentration ($[Cl^-]_i$). $[Cl^-]_i$ is mainly determined by the

opposing actions of the Cl^- importer NKCC1 and the Cl^- exporter KCC2. In the adult brain, neuronal KCC2 expression predominates over NKCC1 expression, resulting in low $[Cl^-]_I$ and hyperpolarizing/inhibitory action of GABA.

During neuronal development, expression of the exporter KCC2 is extremely low; therefore, $[Cl^-]_i$ is low, and GABA exerts a depolarizing/excitatory action (**Figure 1**, from (Ben-Ari, 2017)). This developmental shift in GABA signaling has been observed in a wide range of brain structures including the hippocampus (Berninger et al., 1995;Leinekugel et al., 1995;Khazipov et al., 1997;Ganguly et al., 2001;Gao and Van Den Pol, 2001), the neocortex (Luhmann and Prince, 1991;Owens et al., 1996;Barker et al., 1998;Dammerman et al., 2000;Maric et al., 2001), the hypothalamus (Wang et al., 1994;Chen et al., 1996;Obrietan and van den Pol, 1999), the spinal cord (Reichling et al., 1994;Wang et al., 1994;Serafini et al., 1995;Vinay and Clarac, 1999) and the cerebellum (Yuste and Katz, 1991;Eilers et al., 2001).

Importantly, during development, GABAergic currents arise before glutamatergic currents and provide the first main excitatory input to developing neurons. This early activity is fundamental in organizing early patterns of activity and enabling neurons to fire and form synaptic connections. In particular GABA exerts a depolarizing and mainly excitatory action during early development (until the first or second postnatal week in rodents) (Sernagor et al., 2010;Ben-Ari et al., 2012).

Indeed alteration of the GABAergic system during restricted developmental periods (Meredith, 2015) appears to be a key feature of many neurodevelopmental disorders, including autism spectrum disorders (ASD) (Chen et al., 1996;Coghlan et al., 2012), fragile X syndrome (Tyzio et al., 2014) and Down Syndrome(Lysenko et al., 2018). This result supports the hypothesis that the increased neuronal $[Cl^-]_i$ represents a common feature and a potential target for the treatment of these diseases.

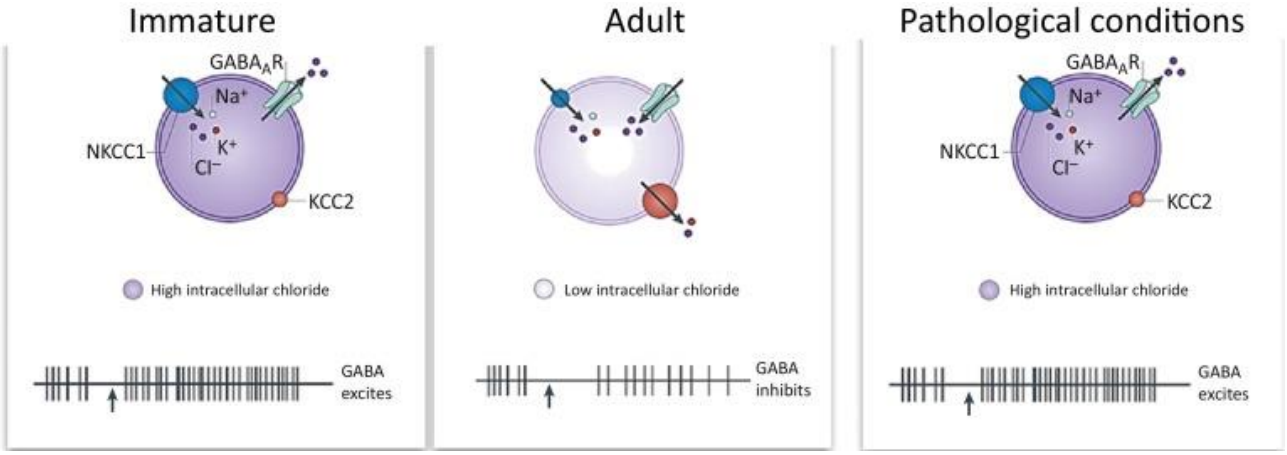

Figure 8.1 GABA switch during development (from Ben-Ari et al 2015)

Remarkably, previous studies have shown that intracellular chloride accumulation depolarizes $GABA_A$Rs-mediated currents in adult Ts65Dn mice (Deidda et al., 2015b). Intracellular chloride accumulation is paralleled by increased expression of the chloride importer NKCC1 in the brains of both Ts65Dn mice and DS patients, while the expression of the chloride exporter KCC2 is unaffected.

Cell-attached patch clamp recording of CA1 pyramidal neurons revealed differences in the electrophysiological behavior of WT and Ts65Dn slices upon application of GABA (a $GABA_A$R agonist) or bicuculline (BIC, a $GABA_A$R antagonist) (**Figure 8.2**, from Deidda 2015).

As shown in Figure 8.2 (adapted from Deidda et al., 2015), upon GABA administration neurons of WT mice showed a dose-dependent decrease in spike frequency. However, application of GABA at the same concentrations elicited a strong increase in spike frequency in neurons from Ts65Dn mice. Conversely, bath application of the $GABA_A$R antagonist BIC caused an increase in spike frequency in neurons from WT mice. However, once again, Ts65Dn neurons showed the opposite behavior, displaying a decrease in spike frequency after the removal of $GABA_A$R-mediated inhibition. These results confirmed that depolarizing GABAergic signaling occurs in Ts65Dn CA1 neurons, possibly due to excessive NKCC1 expression.

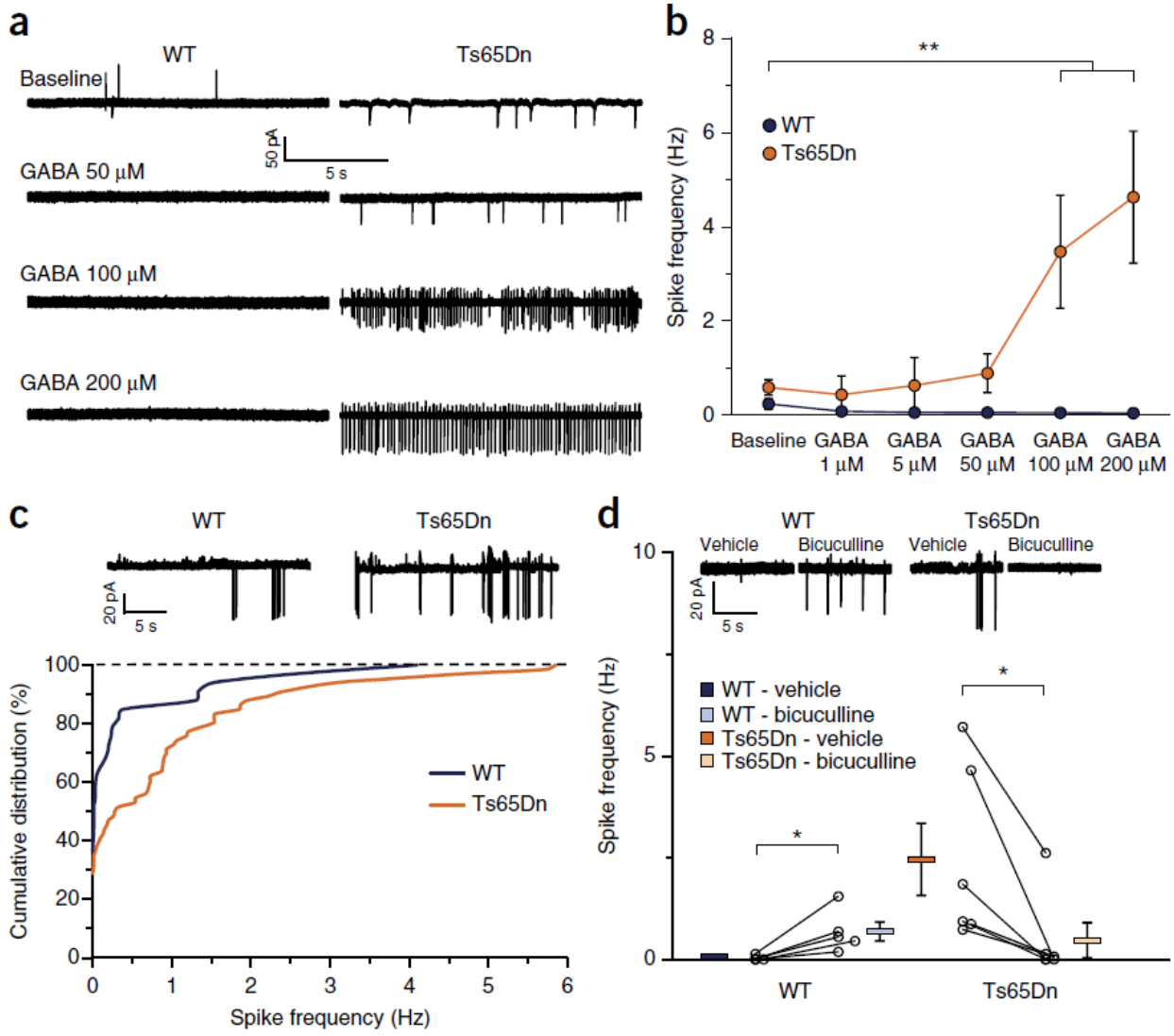

Figure 8.2 Cell-attached patch clamp recording of the activity of CA1 pyramidal neurons upon GABA or BIC administration. WT cells showed a marked decrease in spiking frequency during GABA application, while Ts65Dn neurons showed a dose-dependent increase. Conversely, BIC application induced a marked increase in the firing rate in WT slices, whereas Ts65Dn slices displayed a significant decrease in firing rate after BIC administration (from Deidda et al.*, 2015).*

In fact, pharmacological inhibition of NKCC1 activity using the FDA-approved drug bumetanide restored both intracellular chloride concentration ($[Cl^-]_i$) and $GABA_AR$-mediated hyperpolarizing currents in trisomic neurons. Moreover, *in vivo* treatment of Ts65Dn mice with bumetanide rescued cognitive impairment in several behavioral tasks (Deidda et al., 2015b).

However, the effects of depolarizing $GABA_AR$ signaling and pharmacological NKCC1 inhibition on neuronal network dynamics have never been directly studied in DS models. Under the supervision of Dr. A. Contestabile and Dr. L. Cancedda, we have evaluated the efficacy of pharmacological treatment with bumetanide in restoring GABAergic inhibition in Ts65Dn neurons coupled to MEA.

In the first part of this study, we used a simplified neuronal model consisting of dissociated

hippocampal cultures plated on MEAs. We performed preliminary experiments using brain slices to analyze the effect of the pharmacological NKCC1 inhibition on the hippocampal CA1 network ensemble.

8.1 Materials and Methods

8.1.1 Hippocampal and cortical neuronal cultures

All animal experiments were performed in accordance with the guidelines established by European Community Council Directive 2010/63/EU (September 22, 2010) and were approved by the Italian Ministry of Health. Ts65Dn and WT mice were generated by repeated backcrossing of Ts65Dn females (obtained from the Jackson Laboratory) to C57BL/6JEi × C3SnHeSnJ (B6EiC3) F1 males. Primary neuronal cultures were prepared from WT and Ts65Dn pups at postnatal day 2 (P2) as previously described (Beaudoin et al., 2012;Valente et al., 2016). In brief, brains were dissected under a stereomicroscope in ice-cold Dissection Buffer (DB) composed of Hank's Balanced Salt Solution (HBSS; Gibco) supplemented with 6 mg/mL glucose, 3 mg/mL bovine serum albumin (BSA; Sigma), 5.87 mM $MgSO_4$, 5 μg/mL gentamycin and 10 mM Hepes, pH 7.4. The tissue was minced and enzymatically digested with 0.25% trypsin in HBSS (Gibco) containing 0.6 mg/mL Deoxyribonuclease I (DNAse; Sigma) for 5 min at 37°C. Tissue chunks were washed in DB, incubated for 5 min in DB supplemented with 1 mg/mL of Soybean trypsin inhibitor (Sigma) and mechanically dissociated in DB supplemented with 0.6 mg/mL DNAse. The cells were passed through a 40 μm cell strainer and then centrifuged (*110 x g* for 7 min at 4°C) to remove cellular debris. The cells were plated on MEA coated with poly-L-lysine (Sigma; 0.1 mg/mL in 100 mM borate buffer, pH 8.5). Neurons were maintained in culture medium consisting of Neurobasal medium supplemented with 2% B-27, 1% GlutaMax and 5 μg/mL gentamycin (all from Gibco) at 37 °C in a humidified atmosphere (95% air, 5% CO_2).

.

8.1.2 MEA recording from neuronal cultures

Experimental protocol

For these experiments, cultures 21 DIVs old were pretreated with bumetanide (10 μM) or with the corresponding vehicle (0.01% DMSO) for 1 hour in the incubator prior to each recording session. The cultures were then transferred to the experimental setup, which was equipped with a custom-made incubator chamber (37 °C in a humidified atmosphere consisting of 95% air and 5% CO_2), and kept there for 20 minutes before beginning the recordings to allow the culture to adapt to the new

environment and reach a stable level of activity (Frega et al., 2012;Colombi et al., 2013;El Merhie et al., 2018).

The spontaneous network activity of cultures treated with bumetanide or vehicle was recorded for 30 minutes. We then applied bicuculline (BIC, 20 μM; Sigma) or GABA (100 μM; Sigma) and recorded the activity of the cultures for an additional 30 minutes.

In another set of experiments, we assessed the effect of bumetanide on the spontaneous activity. For this aim, after adapting the culture to the recording setup for 20 minutes as described above, we recorded 30 minutes of basal activity. The cultures were then treated with bumetanide or vehicle as above and after 1 hour were recorded for an additional 30 minutes.

Data analysis

Data analysis was performed off-line using the custom software package SPYCODE (ref, Chapter 2). The steps in the analysis are described briefly below.

Raw traces were high-pass-filtered (>300 Hz) to isolate spikes from the low fluctuation of the signal (LFP). We computed the spike detection as described in Chapter 2.

To characterize the activity level of the analyzed networks, we calculated the mean firing rate (MFR), which is defined as the mean number of spikes per second measured over the total recording time. We considered electrodes active if they recorded a firing rate greater than 0.02 spikes per second. The low threshold guarantees that only electrodes that are not covered by cells and those with very few spikes are excluded and that all others are retained.

We computed the percentage of variation for each active electrode and, using a bootstrap method (ref), we evaluated statistically significant changes with respect to the basal condition. The percentage of variation was computed as follows:

$$\%\, Variation\ Ch = \frac{MFRdrug - MFRbasal}{MFRbasal}$$

For the bootstrap analysis, the peak train for each time segment (basal or drug) was divided into 1-minute bins. The MFRs recorded during each 1-minute bin for the two time segments for each well were randomly shuffled into two groups 10,000 times. The differences between the means of the randomly shuffled groups produced a null distribution (**Figure 8.3**). For each channel, we computed the real difference between the basal and the drug values and assessed whether it fell outside the 95% confidence interval of the null distribution.

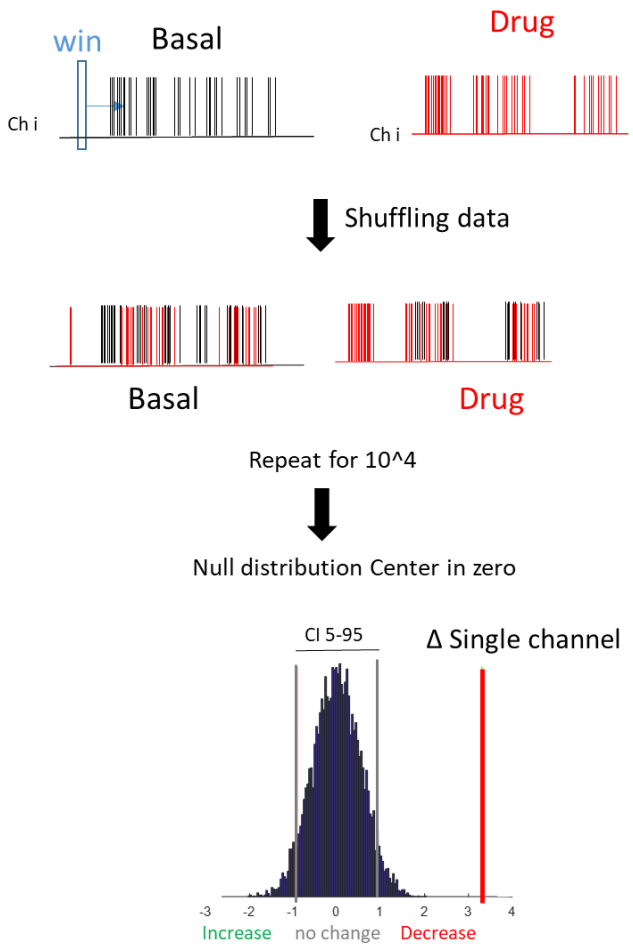

Figure 8.14 Bootstrap analysis method. The spike train for each channel was measured in 1-minute bins and shuffled 10,000 times. The differences between the means of the two randomly shuffled groups produced a null distribution. For each channel, we computed the real difference between the basal and the drug values and assessed whether it fell outside the 95% confidence interval of the null distribution.

To assess changes in the synchronicity of the neuronal networks, we computed the cross-correlation function between each pair of spike trains recorded from active channels. The cross-correlation function represents the probability of observing a spike in one channel i at time (t+τ, τ=3 ms) given that there is a spike in a second channel i+1 at time t. To quantify the strength of correlation between each pair of electrodes, we evaluated the correlation peak (C_{peak}). Then we analyzed changed in the C_{peak} of the Cross Correlation function computed between the first spikes for each burst for all pairs of active channels.

8.1.2 MEA recording from ex vivo acute hippocampal slices

Hippocampal slices preparation

All animal experiments were performed in accordance with the guidelines established by European

Community Council Directive 2010/63/EU (September 22, 2010) and were approved by the Italian Ministry of Health. Ts65Dn and WT mice were generated by repeated backcrossing of Ts65Dn females (obtained from the Jackson Laboratory) to C57BL/6JEi × C3SnHeSnJ (B6EiC3) F1 males. Animals were genotyped by PCR as previously described (Duchon et al., 2011;Deidda et al., 2015b). Animals between 10 and 16 weeks of age were used in the experiments. Only male mice were used in the electrophysiology experiments.

Slices were obtained as described in Chapter 7. Briefly, mice were anesthetized with isoflurane and transcardially perfused with an ice-cold cutting solution (pH 7.4, oxygenated with 95% O_2 and 5% CO_2; see appendix A for the composition of the solutions). The animals were decapitated, and their brains were removed and immersed in ice-cold cutting solution. Combined entorhinal/hippocampal slices (400 μm thick, cut with a VT1000S Leica Microsystems vibratome) were incubated at 32 °C for 20 min in artificial cerebrospinal fluid (ACSF) oxygenated with 95% O_2 and 5% CO_2 (see appendix A for the compositions of the solutions). The slices were then maintained in ACSF solution for at least 1 hour to allow recovery.

Experimental protocol

Slices were pre-incubated with standard ACSF (see appendix A) or with BUME (10 μM) for 45 minutes. As described for the cultures, we adapted slices for 20 minutes on the MEA setup while continuously perfusing them with oxygenated ACSF and then recorded basal spontaneous activity for 30 minutes. We applied bicuculline or GABA (as described above) for the same amounts of time. We discarded the recordings made during the first 15 minutes of drug application to ensure complete exchange of the solution.

Data analysis

Wide-band raw signals were high-pass-filtered (up to 300 Hz) to isolate spikes. We determined the significant variation for each channel before and after the treatment using the bootstrap method described in paragraph 8.1.2. To consider the lower component of the signal, we low-pass-filtered the wide band raw signal between 1 and 200 Hz. The power spectral density was computed as described in Chapter 4.

For the moment, we only considered the lower frequency bands of the signal, namely, the delta (1-4 Hz), theta (4-8 Hz), alpha (8-12 Hz) and beta (12-25 Hz) bands. To characterize the LFP, we calculated the power in each of those frequency bands.

All of the results presented here were obtained from the CA1 area. We are currently analyzing and collecting additional data that will be used to show the behavior of the entire hippocampus.

8.2 Results on hippocampal cultures

In the first part of the present study, we examined the effect of bumetanide on hippocampal neuronal networks coupled to MEA.

As a first step, we assessed whether NKCC1 is overexpressed in Ts65Dn neurons in culture. To this aim, we analyzed the levels of NKCC1 protein in hippocampal and cortical primary neuronal cultures prepared from WT and Ts65Dn mice.

After 15 days *in vitro* (DIV), neurons were lysed, and NKCC1 protein expression was measured by immunoblotting. Consistent with the previous *in vivo* results (Deidda et al., 2015b), immunoblotting analysis showed that overexpression of NKCC1 occurs in both cortical and hippocampal trisomic neuronal cultures (**Figure 8.4**).

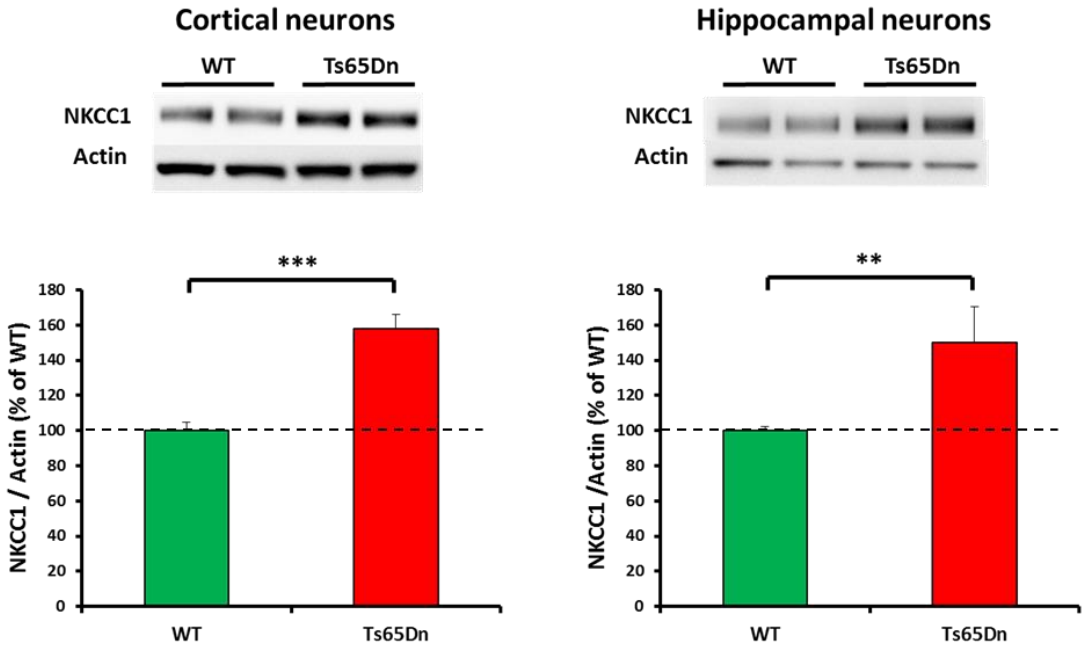

*Figure 8.4 NKCC1 expression in Ts65Dn and WT cortical and hippocampal neuronal cultures measured by immunoblotting at 15 DIV. **p<0.01; *** p<0.001; unpaired Student's t-test.*

Since previous studies have shown that the expression of NKCC1 and KCC2 is developmentally regulated during neuronal maturation (Ben-Ari et al., 2007;Kaila et al., 2014), we next evaluated the expression of both cotransporters in Ts65Dn neurons during *in vitro* development. We found that NKCC1 expression increased in Ts65Dn neurons beginning at 15 DIV and that it persisted afterwards (**Figure 8.5**). Conversely, the developmental increase in KCC2 expression appeared similar in WT and Ts65Dn mice (Ben-Ari, 2002).

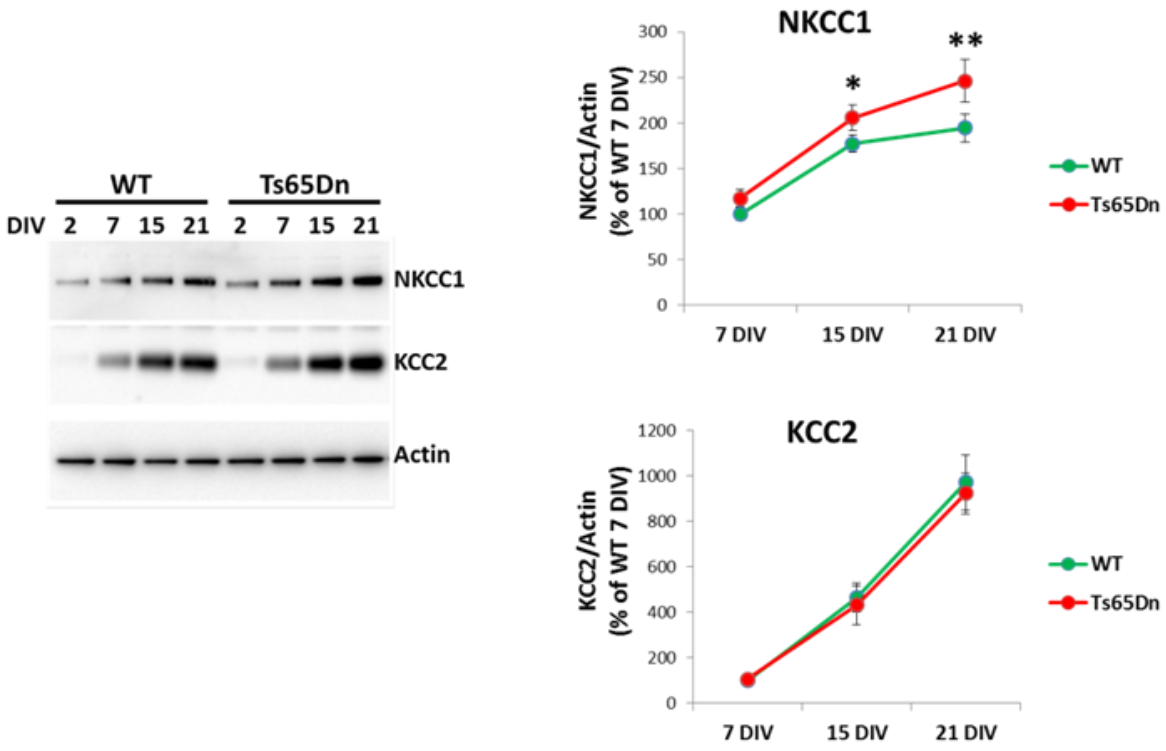

*Figure 8.5 Developmental changes in NKCC1 and KCC2 protein expression in Ts65Dn and WT neuronal cultures. *p<0.05; ** p<0.01; Tukey's post hoc test following two-way ANOVA.*

Because NKCC1 expression appeared to be upregulated in Ts65Dn neurons during *in vitro* maturation, we next evaluated the occurrence and timing of the developmental GABA switch in Ts65Dn cultures. To this aim, we evaluated GABA-induced Ca^{2+} responses in developing neuronal cultures by live imaging with the Ca^{2+}-sensitive dye fluo-4 at four different developmental stages, namely, 2, 7, 15, and 21 DIV. The optical trace for each cell was normalized to baseline (ΔF/F0), and we evaluated the percentage of cells showing GABA-induced Ca^{2+} responses.

As expected, WT neurons showed a progressive decrease in the GABA-induced Ca^{2+} response beginning at 7 DIV that reflects the developmental GABA shift from excitatory to inhibitory (**Figure 6**). Conversely, Ts65Dn neurons displayed an incomplete developmental GABA shift compared to WT cultures. Consistent with the increased NKCC1 expression (Figure 5), we found a statistically significant increase in the number of neurons showing GABA-induced Ca^{2+} responses in Ts65Dn cultures at both 15 and 21 DIV. Then, we measured the GABA-induced Ca^{2+} responses upon Bumetanide application in hippocampal cultures at DIV 15. During the control phase (vehicle phase) we found a statistical difference between Ts65Dn and WT cultures that is completely recover after Bumetanide applications.

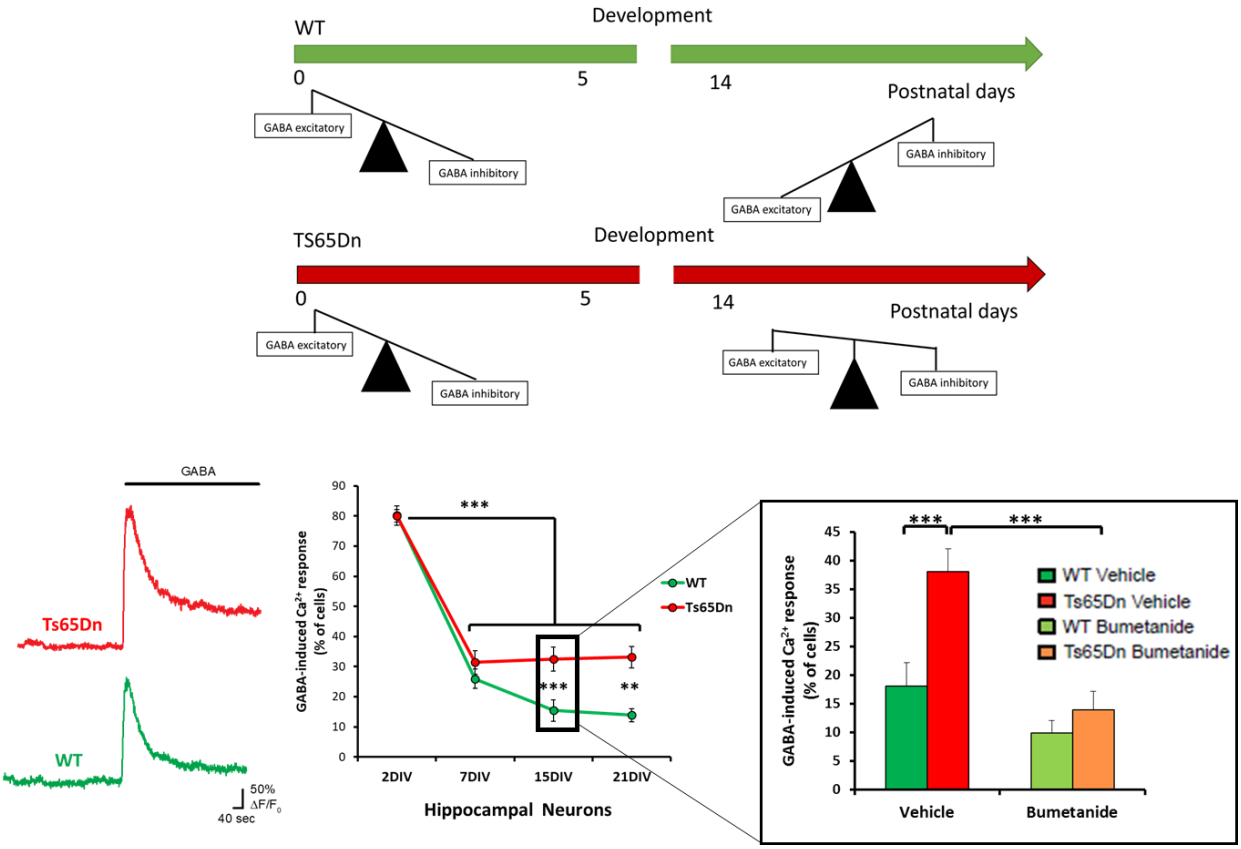

*Figure 8.15 Developmental GABA switch in Ts65Dn and WT neuronal cultures measured by live Ca^{2+} imaging. GABA induced CA2+ response in hippocampal cultures at DIV 15 upon Bumetanide applications. **p<0.01; ***p<0.001; Tukey's post hoc test following two-way ANOVA.*

We next assessed the effect of depolarizing $GABA_AR$ signaling on neuronal network dynamics by means of MEA recordings.

Initially, we performed experiments with the aim of determining whether pharmacological blockade of NKCC1 activity with bumetanide influenced spontaneous neuronal network activity. Although the mean of the firing rates of neurons of the two genotypes were comparable both at baseline and during bumetanide treatment (**Figure 8.7B**), the synchronization levels were affected both at baseline and after bumetanide treatment (**Figure 8.7C**). In fact, bumetanide application resulted in a significant decrease in synchronization for both genotypes. Moreover, the Ts65Dn neuronal network showed lower C_{peak} values than the WT network both at baseline and during bumetanide application (**Figure 8.7 C**). The MBR level of activity was not significant affected by the treatment for both genotypes (**Figure 8.7 D**), although the synchronization between burst events was strongly affected (**Figure 8.7 E**).

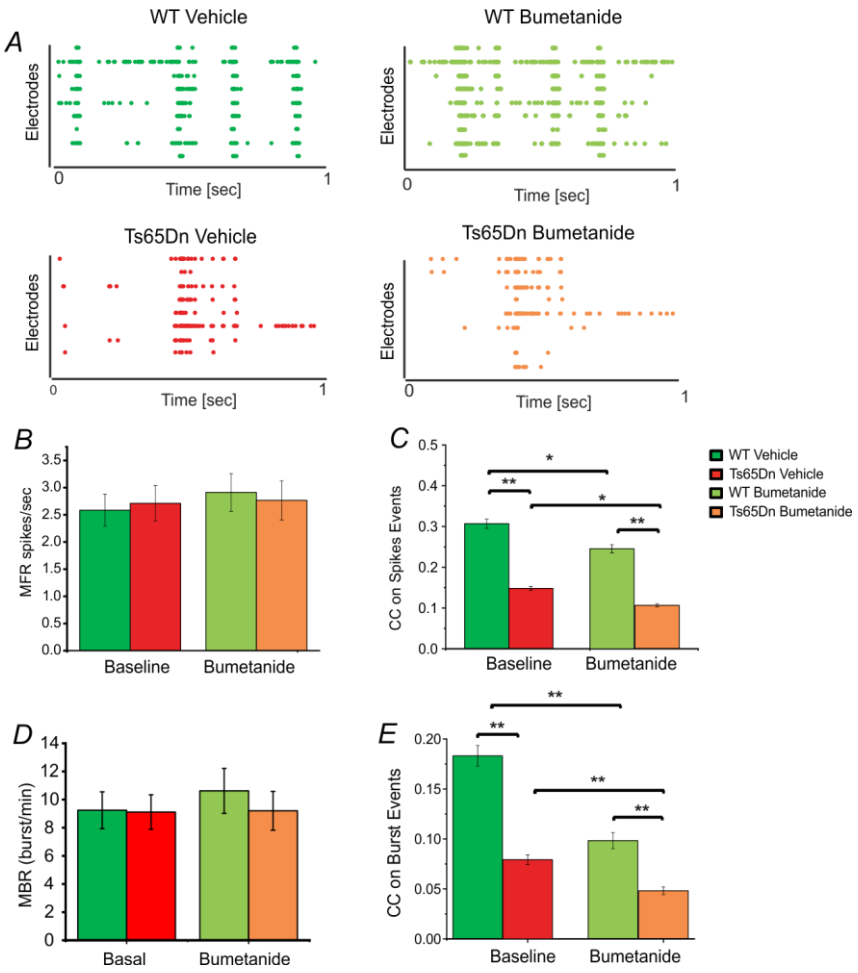

Figure 8.7 MFR and MBR q*uantification and* C_{peak} *comparison computed on spikes and burst train between WT and Ts65Dn cultures. A) 1-second raster plot of WT cultures and Ts65Dn cultures treated with Bumetanide. B) Comparison of the MFR for cultured WT (n=38 cultures, green bar) and Ts65Dn (n=35 cultures, red bar) neurons before and after treatment with bumetanide (BUME, light green bar for WT and red for Ts65Dn). C) Neuronal network synchronization was evaluated by analyzing the* C_{peak} *values for both genotypes during basal conditions and after bumetanide application. D) Neuronal network synchronization on burst activity was evaluated by analyzing the* C_{peak} *values on burst events for both genotypes during basal conditions and after bumetanide application. All data are presented as the mean +/- SEM. *p<0.05; ** p<0.01; Tukey's post hoc test following two-way repeated-measures ANOVA.*

Next, we evaluated the percentage of channels showing changes in MFR after bumetanide application using bootstrap statistics (**Figure 8.8A**; see paragraph 8.1.2 for details). We found that WT cultures exhibited a higher percentage of channels (43%) with increased MFR compared to Ts65Dn cultures (29%) (**Figure 8.8B**, green box). Conversely, Ts65Dn cultures showed a higher percentage of channels (37%) with decreased MFR compared to the WT cultures (25%) (**Figure 8.8B**, red box). A difference of similar magnitude was found by counting the number of experiments that showed higher percentages of channels showing a decrease or an increase in MFR or *vice versa* (**Figure 8.8C**).

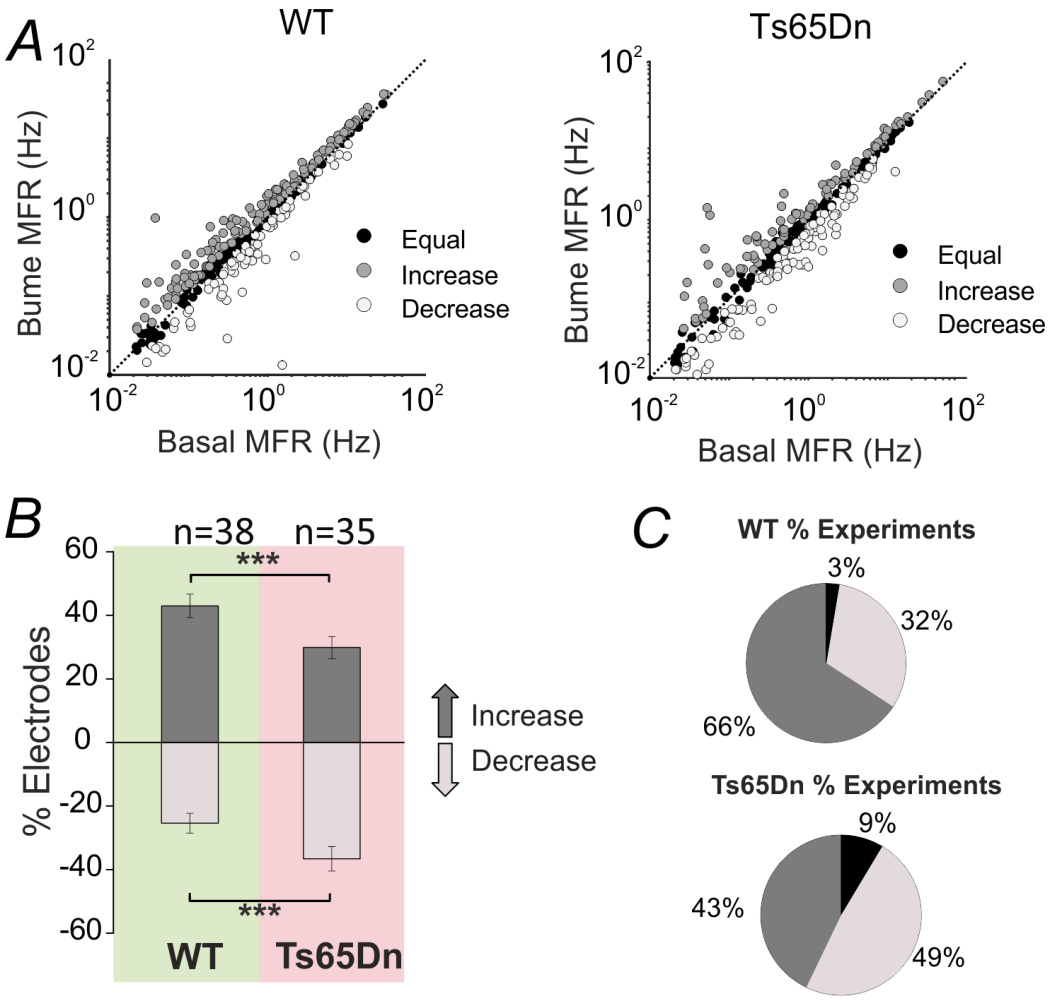

*Figure 8.8 Comparison of MFR before and after bumetanide application to WT and Ts65Dn neurons. A) MFR variation caused by the administration of bumetanide. The gray dots indicate channels that recorded significantly increased MFR compared to the basal level; light gray dots indicate channels that recorded significantly decreased MFR compared to the basal level, and the black dots indicate channels that did not change after bumetanide application. B) Quantification of the percentage of channels that changed significantly upon bumetanide application for WT (n=38) and Ts65Dn (n=35) neurons. C) Quantification of the percentage of experiments showing MFR decreases that were higher than the MFR increases and vice versa. All data are presented as the mean +/- SEM. *** p<0.001, unpaired Student's t-test.*

In another set of experiments, we evaluated the efficacy of bumetanide in restoring the inhibitory GABAergic signal during the administration of bicuculline (a $GABA_AR$ blocker) or GABA ($GABA_AR$ agonist). We normalized the results obtained in each experiment to the mean of each electrophysiological parameter during basal recording. Regarding the WT cultures (**Figure 8.9 A**, green bar) the activity level, evaluated by means of the MFR, increased after BIC administration with respect to the basal condition. WT cultures pre-treated with Bumetanide showed a higher increase after the BIC treatment (**Figure 8.9 A**, green light bar). Regarding Ts65Dn cultures pre-treated with vehicle, we observed a lower increase in the MFR with respect to the WT cultures (**Figure 8.9 A**, red bar). Bumetanide pre-treatment to Ts65Dn cultures caused a significant increase in the MFR with respect to the cultures pretreated with vehicle (**Figure 8.9 A**, orange bar).

In another set of experiments, we examined the effect of the $GABA_AR$ blocker bicuculline. WT cultures treated with vehicle or Bumetanide showed a strong decrease in the MFR after GABA application (**Figure 8.9 B**, green and light green bars). Ts65Dn showed a lower decrease in the MFR with respect to the WT cultures pre-treated with Bumetanide (**Figure 8.9 B**, red bar). We found no significant difference between WT and Ts65Dn pre-treated with Bumetanide during GABA administration.

Regarding bursting activity we found a significant difference between WT and Ts65Dn cultures during BIC treatment: Ts65Dn showed a lower increase in the MBR with respect to the WT cultures (**Figure8.9 C**). The treatment with Bumetanide caused a significant increase in the MBR of Ts65Dn with respect to the vehicle condition. No significant difference was found between WT and Ts65Dn cultures pre-treated with Bumetanide. The analysis of the Cpeak values, computed on the spike trains, revealed an increase in the synchronicity of WT cultures after the removal of GABAA blocker (**Figure 8.9 D**). Ts65Dn cultures, as for the above parameters, displayed a lower increase in the synchronization with respect to the WT cultures. Bumetanide treatment caused a significant increase of C peak valued of Ts65Dn cultures. We observed the same behavior for the Cpeak parameter computed on burst train (**Figure 8.9 E**): WT cultures exhibit a higher increase of the C peak values with respect to the WT that is completely recovery by the Bumetanide application.

Then, we evaluated the percentage of the MFR variations for each active electrodes upon GABA/BIC administration. As expected, administration of GABA caused abrupt suppression of the firing activity in the WT cultures, as shown by the distribution of the percentage MFR variation from all active electrodes, which peaked at -100% (**Figure 8.9A** left, green). On the other hand, after GABA application to Ts65Dn cultures, the distribution of the percentage MFR variation appeared very different from that observed for WT; the data were widely dispersed and even showed increased MFR from some electrodes, indicating reduced efficacy of GABA inhibition and partial excitatory activity (**Figure 8.10 A** left, red). In fact, by bootstrap analysis we found that virtually all (99.7%) active channels in the WT cultures displayed a significant decrease in firing after GABA application (**Figure 8.10 B**, green box). However, in Ts65Dn cultures, only 67% of the active channels showed a decrease in MFR after GABA application, while 7% of the analyzed channels showed an increase (**Figure 8.10 B**, red box).

Interestingly, treatment with bumetanide fully restored inhibitory GABA signaling in Ts65Dn cultures, as demonstrated by the distribution of the percentage MFR variation, which in that case was indistinguishable from that of WT cultures (**Figure 8.10 A**, right). Moreover, after bumetanide pretreatment, all recorded electrodes (100%) in the Ts65Dn cultures showed a GABA-mediated

decrease in firing rate (**Figure 8.10 B**, red box).

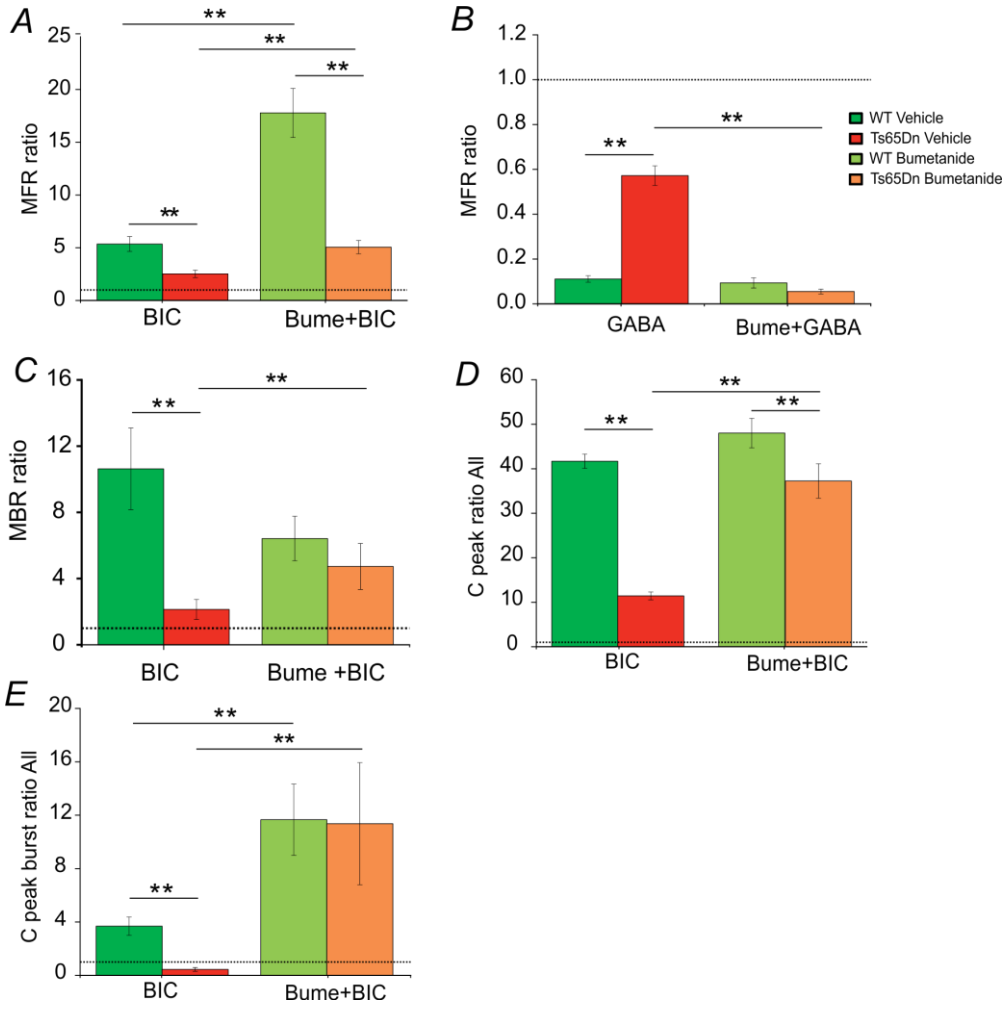

*Figure 8.9. Electrophysiological parameters evaluated during BIC/GABA administration for the WT and Ts65Dn. A) Comparison of the MFR ratio during BIC administration for the cultures pretreated with vehicle (n=9 for WT green bar; n=12 for Ts65Dn red bar) or bumetanide (n=9 for WT light green bar; n=9 for Ts65Dn orange bar). B) Comparison of the MFR ratio during GABA administration for the cultures pretreated with vehicle (n=9 for WT green bar; n=12 for Ts65Dn red bar) or bumetanide (n=9 for WT light green bar; n=9 for Ts65Dn orange bar). C) Comparison of the MBR ratio during BIC administration for the cultures pretreated with vehicle (n=9 for WT green bar; n=12 for Ts65Dn red bar) or bumetanide (n=9 for WT light green bar; n=9 for Ts65Dn orange bar).D) C peak ratio computed on spike trains for every couples of channels for the cultures pretreated with vehicle (n=9 for WT green bar; n=12 for Ts65Dn red bar) or bumetanide (n=9 for WT light green bar; n=9 for Ts65Dn orange bar). E) C peak ratio computed on burst trains for every couples of channels for the cultures pretreated with vehicle (n=9 for WT green bar; n=12 for Ts65Dn red bar) or bumetanide (n=9 for WT light green bar; n=9 for Ts65Dn orange bar). All data are presented as the mean +/- SEM. *p<0.05; ** p<0.01; Tukey's post hoc test following two-way repeated-measures ANOVA.*

Upon removing endogenous GABA-mediated inhibition, the distribution of the percentage MFR variation peaked at +100% in the WT cultures, highlighting the expected firing increase (**Figure 8.10 C**, left, green). Conversely, in Ts65Dn cultures the distribution of the percentage MFR variation showed a bimodal distribution characterized by both positive and negative values, indicative of a

mixed response to bicuculline treatment (**Figure 8.10 C** left, red).

Bootstrap analysis was used to quantify the percentage of channels displaying significant MFR changes upon bicuculline administration. The results showed that in WT cultures 85% of the active channels increased firing, while 6% showed a decrease compared to the basal values. In contrast, in Ts65Dn cultures only 60% of the active channels showed a significant increase in MFR after bicuculline administration, while 23% of channels showed a significant decrease in MFR, indicative of aberrant GABAergic signaling. However, pretreatment of Ts65Dn cultures with bumetanide shifted the distribution of the percentage MFR variation towards higher values, indicating rescue of GABA-mediated inhibition (**Figure 8.10 C** right, red). Accordingly, bumetanide treatment rescued the percentage of active channels showing a significant MFR increase (84%) upon bicuculline administration in Ts65Dn cultures (**Figure 8.10 D**, red box).

These results confirm that depolarizing $GABA_A$ signaling occurs in Ts65Dn neurons. No significant effects of bumetanide were found upon GABA/bicuculline treatment of WT cultures.

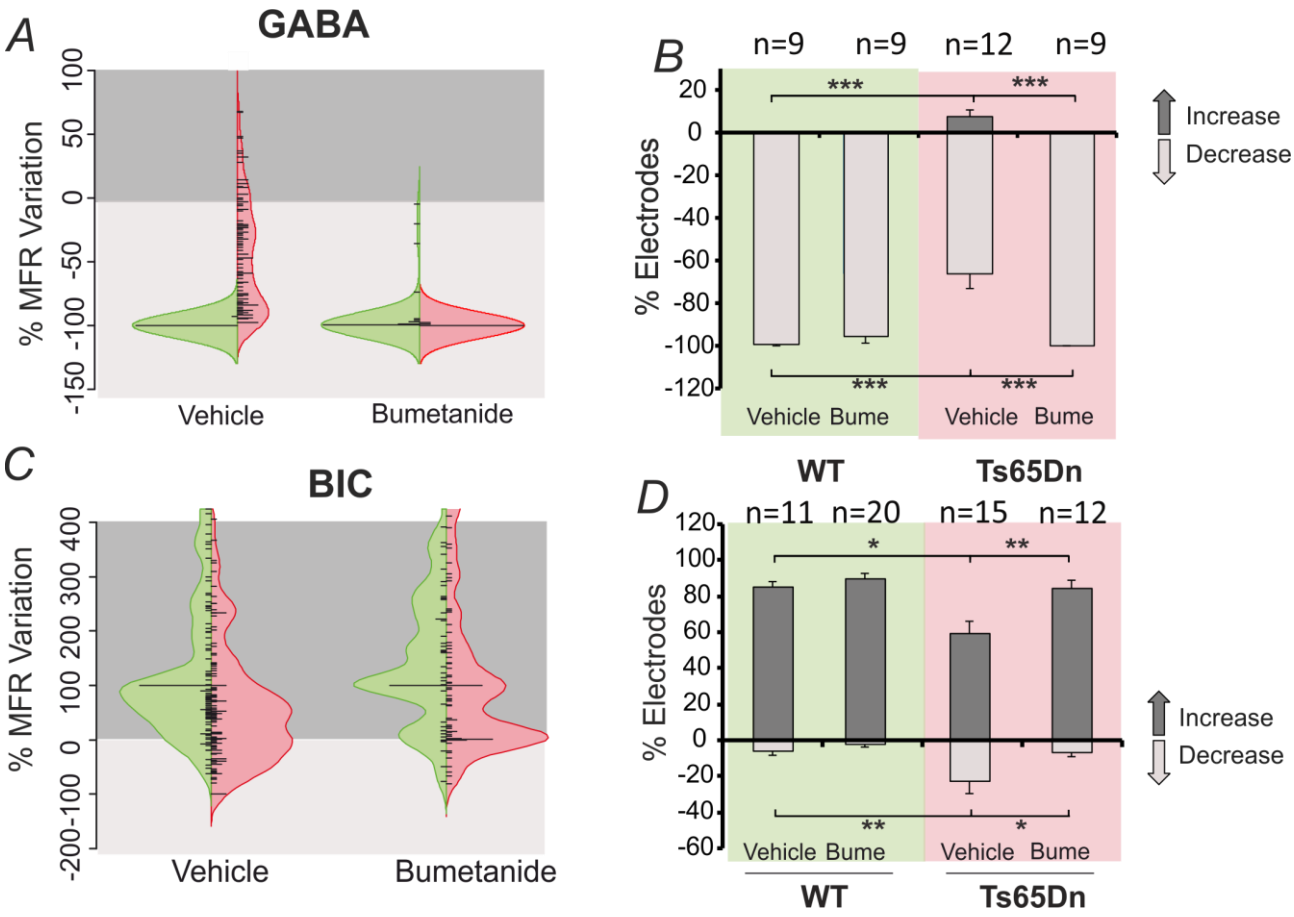

Figure 8.10 Variation in MFR during BIC or GABA application to WT and Ts65Dn cultures. A) Violin plot of the percentage MFR variation during GABA administration for WT (green violin) and Ts65Dn (red violin) pretreated with vehicle (n=9 for WT; n=12 for Ts65Dn) or bumetanide (n=9 for WT; n=9 for Ts65Dn) B) Percentage of channels that changed significantly with respect to their basal conditions during GABA administration. C) Violin plot of the percentage MFR variation during BIC administration for WT (green violin) and Ts65Dn (red violin) pretreated with vehicle (n=11 for WT; n=15 for Ts65Dn) or bumetanide (n=20 for WT; n=12 for Ts65Dn). D) Percentage of channels that changed

*significantly with respect to their basal conditions during BIC administration. All data are presented as the mean +/- SEM. *p<0.05; **p<0.01; *** p<0.001; Tukey's post hoc test following two-way ANOVA.*

8.3 Results obtained with hippocampal slices

In the second part of the present study, we conducted a preliminary examination of the effect of bumetanide on hippocampal slices from WT and Ts65Dn mice coupled to MEA. We performed preliminary experiments with the aim of investigating the efficacy of the treatment on the CA1 hippocampal region. Although recording from brain slices on MEA has several advantages compared to conventional extracellular field potential recording, a compromise between tissue oxygenation and signal-to-noise ratio has to be found; a high perfusion rate (i.e., approximately 2 ml/min) was needed to record signals with high-frequency components(Hajos et al., 2009). In the previous chapter (Chapter 7) we described the customization of the experimental setup and of the MEA chamber that allows us to record activity featuring high- and low-frequency patterns.

Regarding the high-frequency components of the signal (i.e., spike activity), as mentioned earlier for cultures, we filtered the signal above 300 Hz. We computed the percentage of channels that changed significantly upon drug administration using the bootstrap method (see paragraph 8.1.2).

GABA application caused a significant decrease in the MFR recorded at all electrodes in WT slices compared to the basal condition (**Figure 8.11 A**). On the other hand, the majority of electrodes in Ts65Dn slices recorded increased MFR compared to the basal condition (**Figure 8.11 B**). Bumetanide application restored inhibitory GABAergic signaling in Ts65Dn slices, as demonstrated by the decrease in MFR observed at the majority of recorded electrodes (**Figure 8.11 C**). We are still collecting the data obtained for WT slices recorded after preincubation with bumetanide.

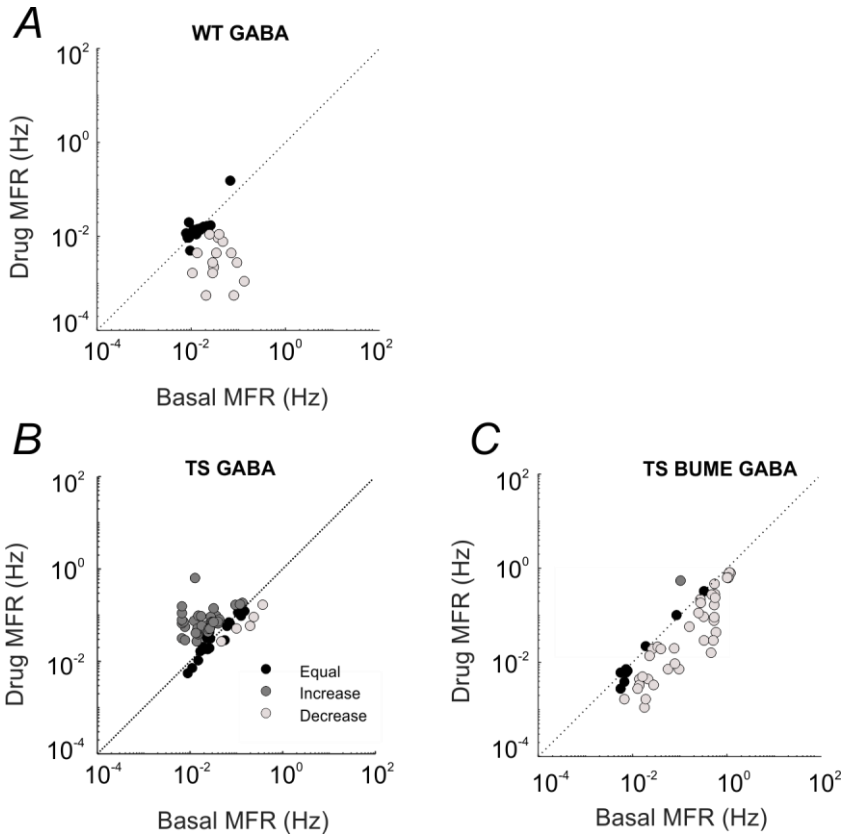

Figure 8.11 MFR comparison between WT and Ts65Dn hippocampal slices. A) MFR of WT slices (n= 6 slices) upon GABA application. B) MFR of Ts65Dn slices (n= 7 slices) upon GABA application. C) MFR of Ts65Dn slices preincubated with BUME (n= 5 slices) upon GABA application. In each plot (A-C), the green dots indicate channels that recorded significantly increased MFR compared to the basal level, the red dots indicate channels that recorded significantly decreased MFR compared to the basal level, and the black dots indicate channels that did not change after BUME application.

On the other hand, upon BIC administration, WT slices showed increased MFR in the majority of channels compared to the basal phase (**Figure 8.12A**). Bumetanide application to WT slices did not cause any changes in MFR (**Figure 8.12B**). Conversely, bicuculline administration to Ts65Dn slices resulted in a higher percentage of channels with significantly decreased MFR than was observed in WT slices (**Figure 8.12C**). Preincubation with bumetanide restored inhibitory GABA signaling in Ts65Dn slices (**Figure 8.12D**).

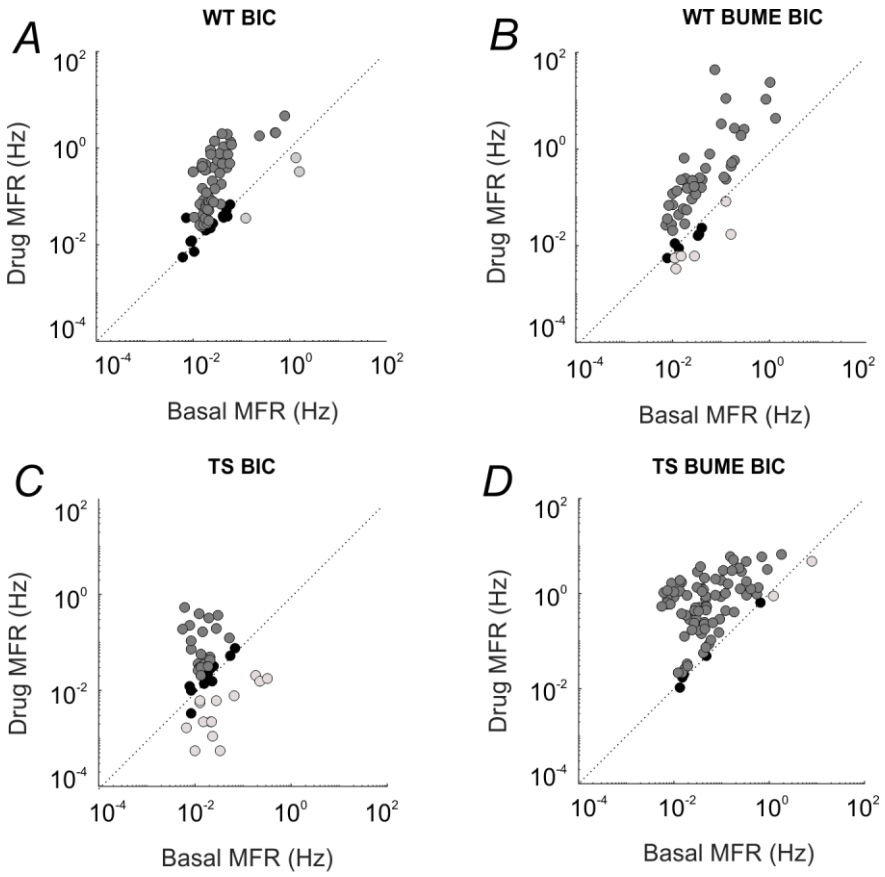

Figure 8.12 Comparison of MFR in WT and Ts65Dn slices. A) MFR in WT slices (n= 6 slices) upon BIC application. B) MFR in WT slices preincubated with BUME (n= 4 slices) upon BIC application. C) MFR in Ts65Dn slices (n= 5 slices) upon BIC application. C) MFR in Ts65Dn slices preincubated with BUME (n= 6 slices) upon BIC application. In each plot (A-C), the green dots indicate channels that recorded significantly increased MFR with respect to the basal level, the red dots indicate channels that recorded significantly decreased MFR with respect to the basal level, and black dots indicate channels that did not change after BUME application.

Local field potential analysis revealed different contributions of frequency band components in the two genotypes following GABA administration. The results of the local field potential analysis of BIC experiments are not shown because we are still analyzing the data.

Figure 8.13 A shows a representative trace for each experimental condition. The signal from Ts65Dn slices showed a robust increase in both frequency and amplitude upon GABA application, whereas WT slices exhibited a marked decrease in activity. Ts65Dn slices treated with bumetanide showed marked decreases in both the amplitude and the frequency of activity after GABA administration.

To quantify the power of the signal for each band, we computed the area under the power spectral density. We normalized each power band to the mean value observed under basal conditions. As shown in **Figure 8.13 B**, all the power bands considered (delta, theta, alpha, and beta) were decreased in WT slices but not in Ts65Dn slices. Once again, bumetanide pretreatment of Ts65Dn slices caused a decrease in the power of the theta, beta and alpha bands, similar to its effect in WT slices.

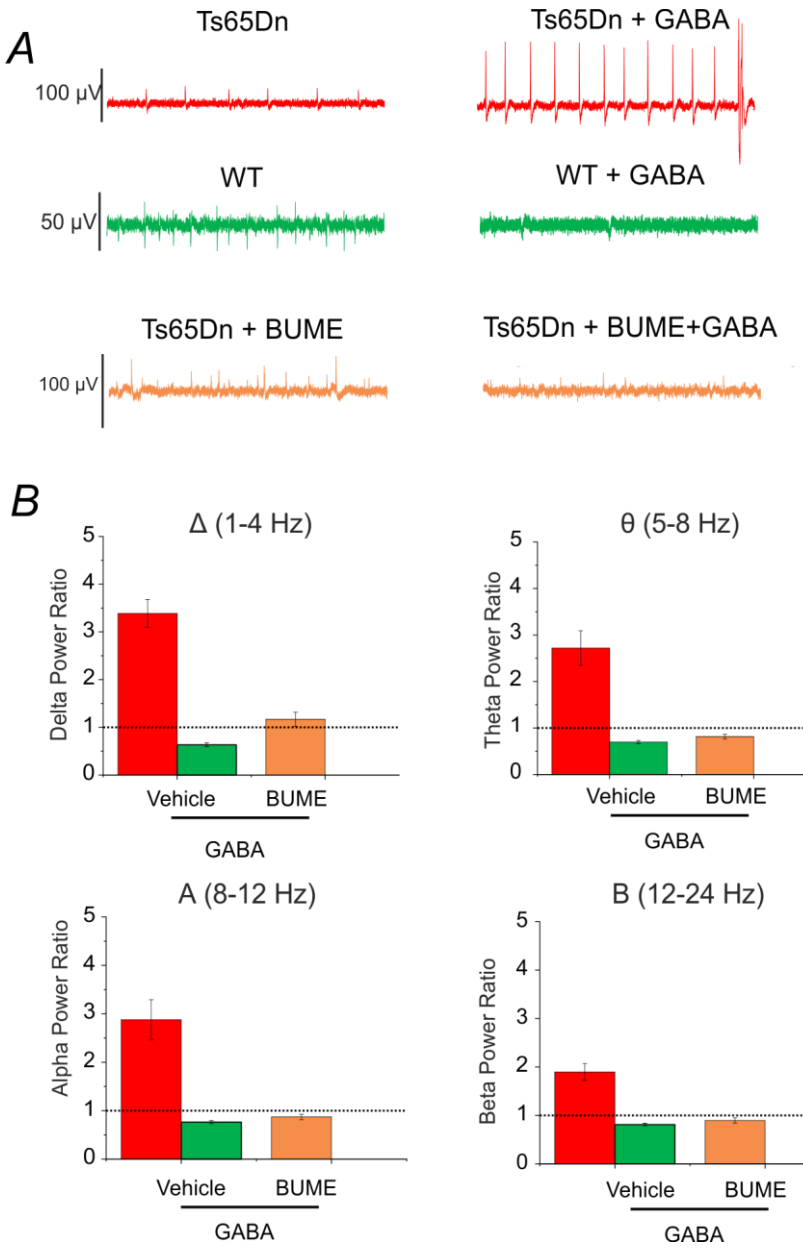

Figure 8.13 Power spectral density analysis for WT and Ts65Dn slices during GABA administration. All power bands were normalized with respect to the basal conditions. A) Representative traces of one channel for each experimental condition: WT (green lines) and Ts65Dn (red lines) upon GABA administration and Ts65Dn with bumetanide pretreatment and GABA administration (orange lines). B) Power estimation for four different bands: delta (1-4 Hz), theta (4-8 Hz), alpha (8-12 Hz) and beta (12-24 Hz).

8.4 Conclusion

In the first part of this study, we showed that GABAergic signaling is altered in hippocampal cultures prepared from Down syndrome mice during development. This alteration was paralleled by overexpression of NKCC1 in Ts65Dn cultures, whereas KCC2 expression was spared. Remarkably, GABA-induced Ca^{2+} responses displayed the same developmental profile as NKCC1 protein expression in Ts65Dn neurons.

Analysis of the single-channel variation of MFR upon bumetanide application to hippocampal cultures revealed that larger decreases in firing rate occur in Ts65Dn than in WT cultures due to the difference in the starting level of GABA inhibitory signaling in DS mice.

We demonstrated that altered GABAergic signaling in Ts65Dn cultures resulted in a lower level of network synchronization. This difference was not mediated by NKCC1 since the application of bumetanide (NKCC1 blocker) did not recover the difference between WT and Ts65Dn.

We then showed that Ts65Dn neuronal network activity exhibited alterations in GABAergic inhibition. Application of bumetanide restored the normal inhibitory action of GABA in Ts65Dn neuronal cultures without altering the behavior of the WT cultures.

We confirmed these results by conducting experiments on the hippocampal CA1 region in which we recorded brain slices on MEA. Although our preliminary results confirmed our previous observations, it will be necessary to increase the number of experiments to assess the reproducibility of the results.

Although bumetanide is an FDA-approved drug, chronic treatment with this drug is limited due to its side effects, which include mild hypokalemia and electrolyte imbalance. Moreover, brain penetration of bumetanide is not optimal, although several studies have reported its efficacy in reaching the brain (Li et al., 2011;Cleary et al., 2013;Deidda et al., 2015a).

To overcome the limitations of drug treatment, we recently established a gene therapy approach that can be used to knock down NKCC1 expression and thereby restore the correct balance of GABAergic inhibition. In future studies, we will perform experiments using adeno-associated viral vectors (AAV) developed in our laboratory with the aim of re-establishing appropriate GABAergic inhibition through the modulation of neuronal $[Cl^-]_i$. AAV vectors have been used in several clinical trials and have demonstrated excellent efficacy and safety when used in the treatment of various neurological diseases (Weinberg et al., 2013). Animals will receive AAV vectors by intracerebroventricular (ICV) injection during the postnatal period, and we will assess the efficacy of the treatment during their adulthood using brain slices on MEAs.

In contrast to pharmacological treatments with NKCC1 inhibitors, a gene therapy approach offers

numerous advantages, including the absence of side effects at the renal level, specificity of action at the neuronal level and single administration. On the other hand, these therapeutic approaches cannot be immediately regarded as a safe therapeutic approach for clinical trials in subjects with DS.

Moreover, since we observed that the treatment with Bumetanide on adult mice was not able to induce permanent changes in the GABAergic inhibition we will try to act on a specific time interval during the development (i.e. between P3 and P15). We believe that the treatment during the development and specifically during the GABA switching, could induce permanent changes that will be maintain during the adult period.

In any case, for both therapeutic approaches, it is important to evaluate the effect of treatment on neuronal activity patterns not only at the level of single neurons but also at the network level. In this context, MEAs have been established as a technological platform for conducting electrophysiological studies with the possibility of recording from multiple electrodes simultaneously. They represent a simple, low-risk, accessible model for evaluating, in terms of electrophysiological activity, the effectiveness of new therapies in the preclinical phase.

In conclusion, MEA coupled to neuronal networks could be used to predict the effectiveness of new therapies in pathologies that exhibit alterations of GABAergic inhibition, such as autism and neurodevelopmental diseases.

Related publications and/or conference abstracts

Conference abstract

Colombi I., Alberti M., Pasquale V., Michela Chiappalone, Contestabile A., Cancedda L. Modulation of electrophysiological activity in neuronal networks of Down syndrome mice using Microelectrodes array. 7th International Summer School of Neuroengineering “Massimo Grattarola” 2018.

References

Aziz, N.M., Guedj, F., Pennings, J.L., Olmos-Serrano, J.L., Siegel, A., Haydar, T.F., and Bianchi, D.W. (2018). Lifespan analysis of brain development, gene expression and behavioral phenotypes in the Ts1Cje, Ts65Dn and Dp (16) 1/Yey mouse models of Down syndrome. *Disease models & mechanisms*, dmm. 031013.

Barker, J., Behar, T., Li, Y., Liu, Q., Ma, W., Maric, D., Maric, I., Schaffner, A., Serafini, R., and Smith, S. (1998). GABAergic cells and signals in CNS development. *Perspectives on developmental neurobiology* 5, 305-322.

Beaudoin, G.M., 3rd, Lee, S.H., Singh, D., Yuan, Y., Ng, Y.G., Reichardt, L.F., and Arikkath, J. (2012). Culturing pyramidal neurons from the early postnatal mouse hippocampus and cortex. *Nat Protoc* 7, 1741-1754.

Ben-Ari, Y. (2002). Excitatory actions of gaba during development: the nature of the nurture. *Nature Reviews Neuroscience* 3, 728.

Ben-Ari, Y. (2017). NKCC1 chloride importer antagonists attenuate many neurological and psychiatric disorders. *Trends in neurosciences* 40, 536-554.

Ben-Ari, Y., Gaiarsa, J.-L., Tyzio, R., and Khazipov, R. (2007). GABA: a pioneer transmitter that excites immature neurons and generates primitive oscillations. *Physiological reviews* 87, 1215-1284.

Ben-Ari, Y., Woodin, M.A., Sernagor, E., Cancedda, L., Vinay, L., Rivera, C., Legendre, P., Luhmann, H.J., Bordey, A., and Wenner, P. (2012). Refuting the challenges of the developmental shift of polarity of GABA actions: GABA more exciting than ever! *Frontiers in cellular neuroscience* 6, 35.

Berninger, B., Marty, S., Zafra, F., Da Penha Berzaghi, M., Thoenen, H., and Lindholm, D. (1995). GABAergic stimulation switches from enhancing to repressing BDNF expression in rat hippocampal neurons during maturation in vitro. *Development* 121, 2327-2335.

Chen, G., Trombley, P.Q., and Van Den Pol, A.N. (1996). Excitatory actions of GABA in developing rat hypothalamic neurones. *The Journal of physiology* 494, 451-464.

Cleary, R.T., Sun, H., Huynh, T., Manning, S.M., Li, Y., Rotenberg, A., Talos, D.M., Kahle, K.T., Jackson, M., and Rakhade, S.N. (2013). Bumetanide enhances phenobarbital efficacy in a rat model of hypoxic neonatal seizures. *PloS one* 8, e57148.

Coghlan, S., Horder, J., Inkster, B., Mendez, M.A., Murphy, D.G., and Nutt, D.J. (2012). GABA system dysfunction in autism and related disorders: from synapse to symptoms. *Neuroscience & Biobehavioral Reviews* 36, 2044-2055.

Colombi, I., Mahajani, S., Frega, M., Gasparini, L., and Chiappalone, M. (2013). Effects of antiepileptic drugs on hippocampal neurons coupled to micro-electrode arrays. *Front Neuroeng* 6, 10.

Contestabile, A., Benfenati, F., and Gasparini, L. (2010). Communication breaks-Down: from neurodevelopment defects to cognitive disabilities in Down syndrome. *Progress in neurobiology* 91, 1-22.

Contestabile, A., Magara, S., and Cancedda, L. (2017). The GABAergic hypothesis for cognitive disabilities in down syndrome. *Frontiers in cellular neuroscience* 11, 54.

Dammerman, R., Flint, A., Noctor, S., and Kriegstein, A. (2000). An excitatory GABAergic plexus in developing neocortical layer 1. *Journal of Neurophysiology* 84, 428-434.

Deidda, G., Allegra, M., Cerri, C., Naskar, S., Bony, G., Zunino, G., Bozzi, Y., Caleo, M., and Cancedda, L. (2015a). Early depolarizing GABA controls critical-period plasticity in the rat visual cortex. *Nature neuroscience* 18, 87.

Deidda, G., Parrini, M., Naskar, S., Bozarth, I.F., Contestabile, A., and Cancedda, L. (2015b).

Reversing excitatory GABAAR signaling restores synaptic plasticity and memory in a mouse model of Down syndrome. *Nature medicine* 21**,** 318.

Dierssen, M. (2012). Down syndrome: the brain in trisomic mode. *Nature Reviews Neuroscience* 13**,** 844.

Duchon, A., Raveau, M., Chevalier, C., Nalesso, V., Sharp, A.J., and Herault, Y. (2011). Identification of the translocation breakpoints in the Ts65Dn and Ts1Cje mouse lines: relevance for modeling Down syndrome. *Mammalian Genome* 22**,** 674-684.

Eilers, J., Plant, T.D., Marandi, N., and Konnerth, A. (2001). GABA‐mediated Ca2+ signalling in developing rat cerebellar Purkinje neurones. *The Journal of physiology* 536**,** 429-437.

El Merhie, A., Ito, D., Colombi, I., Keshavan, S., Mishra, N., Miseikis, V., Diaspro, A., Coletti, C., Chiappalone, M., and Dante, S. (2018). Single layer graphene functionalized MEA for enhanced detection of neuronal network development. *Sensors and Actuators B: Chemical* 277**,** 224-233.

Frega, M., Pasquale, V., Tedesco, M., Marcoli, M., Contestabile, A., Nanni, M., Bonzano, L., Maura, G., and Chiappalone, M. (2012). Cortical cultures coupled to micro-electrode arrays: a novel approach to perform in vitro excitotoxicity testing. *Neurotoxicol Teratol* 34**,** 116-127.

Ganguly, K., Schinder, A.F., Wong, S.T., and Poo, M.-M. (2001). GABA itself promotes the developmental switch of neuronal GABAergic responses from excitation to inhibition. *Cell* 105**,** 521-532.

Gao, X.-B., and Van Den Pol, A.N. (2001). GABA, not glutamate, a primary transmitter driving action potentials in developing hypothalamic neurons. *Journal of Neurophysiology* 85**,** 425-434.

Hajos, N., Ellender, T.J., Zemankovics, R., Mann, E.O., Exley, R., Cragg, S.J., Freund, T.F., and Paulsen, O. (2009). Maintaining network activity in submerged hippocampal slices: importance of oxygen supply. *European Journal of Neuroscience* 29**,** 319-327.

Kaila, K., Price, T.J., Payne, J.A., Puskarjov, M., and Voipio, J. (2014). Cation-chloride cotransporters in neuronal development, plasticity and disease. *Nature Reviews Neuroscience* 15**,** 637.

Khazipov, R., Leinekugel, X., Khalilov, I., Gaiarsa, J., and Ben-Ari, Y. (1997). Synchronization of GABAergic interneuronal network in CA3 subfield of neonatal rat hippocampal slices. *The Journal of Physiology* 498**,** 763-772.

Kleschevnikov, A.M., Belichenko, P.V., Villar, A.J., Epstein, C.J., Malenka, R.C., and Mobley, W.C. (2004). Hippocampal long-term potentiation suppressed by increased inhibition in the Ts65Dn mouse, a genetic model of Down syndrome. *Journal of Neuroscience* 24**,** 8153-8160.

Leinekugel, X., Tseeb, V., Ben-Ari, Y., and Bregestovski, P. (1995). Synaptic GABAA activation induces Ca2+ rise in pyramidal cells and interneurons from rat neonatal hippocampal slices. *The Journal of Physiology* 487**,** 319-329.

Li, Y., Cleary, R., Kellogg, M., Soul, J.S., Berry, G.T., and Jensen, F.E. (2011). Sensitive isotope dilution liquid chromatography/tandem mass spectrometry method for quantitative analysis of bumetanide in serum and brain tissue. *Journal of Chromatography B* 879**,** 998-1002.

Luhmann, H., and Prince, D. (1991). Postnatal maturation of the GABAergic system in rat neocortex. *Journal of neurophysiology* 65**,** 247-263.

Lysenko, L.V., Kim, J., Madamba, F., Tyrtyshnaia, A.A., Ruparelia, A., and Kleschevnikov, A.M. (2018). Developmental excitatory-to-inhibitory GABA polarity switch is delayed in Ts65Dn mice, a genetic model of Down syndrome. *Neurobiology of disease* 115**,** 1-8.

Maric, D., Liu, Q.-Y., Maric, I., Chaudry, S., Chang, Y.-H., Smith, S.V., Sieghart, W., Fritschy, J.-M., and Barker, J.L. (2001). GABA expression dominates neuronal lineage progression in the embryonic rat neocortex and facilitates neurite outgrowth via GABAA autoreceptor/Cl− channels. *Journal of Neuroscience* 21**,** 2343-2360.

Meredith, R. (2015). Sensitive and critical periods during neurotypical and aberrant neurodevelopment: a framework for neurodevelopmental disorders. *Neuroscience & Biobehavioral Reviews* 50**,** 180-188.

Obrietan, K., and Van Den Pol, A. (1999). GABAB receptor-mediated regulation of glutamate-

activated calcium transients in hypothalamic and cortical neuron development. *Journal of neurophysiology* 82**,** 94-102.

Owens, D.F., Boyce, L.H., Davis, M.B., and Kriegstein, A.R. (1996). Excitatory GABA responses in embryonic and neonatal cortical slices demonstrated by gramicidin perforated-patch recordings and calcium imaging. *Journal of Neuroscience* 16**,** 6414-6423.

Reichling, D.B., Kyrozis, A., Wang, J., and Macdermott, A.B. (1994). Mechanisms of GABA and glycine depolarization‐induced calcium transients in rat dorsal horn neurons. *The Journal of Physiology* 476**,** 411-421.

Rueda, N., Flórez, J., and Martínez-Cué, C. (2012). Mouse models of Down syndrome as a tool to unravel the causes of mental disabilities. *Neural plasticity* 2012.

Serafini, R., Valeyev, A., Barker, J., and Poulter, M. (1995). Depolarizing GABA‐activated Cl‐channels in embryonic rat spinal and olfactory bulb cells. *The Journal of Physiology* 488**,** 371-386.

Sernagor, E., Chabrol, F., Bony, G., and Cancedda, L. (2010). GABAergic control of neurite outgrowth and remodeling during development and adult neurogenesis: general rules and differences in diverse systems. *Frontiers in cellular neuroscience* 4**,** 11.

Tyzio, R., Nardou, R., Ferrari, D.C., Tsintsadze, T., Shahrokhi, A., Eftekhari, S., Khalilov, I., Tsintsadze, V., Brouchoud, C., and Chazal, G. (2014). Oxytocin-mediated GABA inhibition during delivery attenuates autism pathogenesis in rodent offspring. *Science* 343**,** 675-679.

Valente, P., Lignani, G., Medrihan, L., Bosco, F., Contestabile, A., Lippiello, P., Ferrea, E., Schachner, M., Benfenati, F., Giovedì, S., and Baldelli, P. (2016). Cell adhesion molecule L1 contributes to neuronal excitability regulating the function of voltage-gated Na+ channels. *J Cell Sci* 129**,** 1878-1891.

Vinay, L., and Clarac, F. (1999). Antidromic discharges of dorsal root afferents and inhibition of the lumbar monosynaptic reflex in the neonatal rat. *Neuroscience* 90**,** 165-176.

Wang, J., Reichling, D.B., Kyrozis, A., and Macdermott, A.B. (1994). Developmental loss of GABA‐and glycine‐induced depolarization and Ca2+ transients in embryonic rat dorsal horn neurons in culture. *European Journal of Neuroscience* 6**,** 1275-1280.

Weinberg, M.S., Samulski, R.J., and Mccown, T.J. (2013). Adeno-associated virus (AAV) gene therapy for neurological disease. *Neuropharmacology* 69**,** 82-88.

Yuste, R., and Katz, L.C. (1991). Control of postsynaptic Ca2+ influx in developing neocortex by excitatory and inhibitory neurotransmitters. *Neuron* 6**,** 333-344.

Conclusion

The study reported in the present PhD thesis aimed to investigate sleep-related network features displayed by primary cultures of cortical neurons plated on microelectrode arrays. In fact, despite their simplicity, these networks retain some basic sleep features similar to those present in *in vivo* sleeping animals.

Our approach involved the following three main steps:

1. We focused on the slow-frequency synchronized activity spontaneously generated by *in vitro* cortical networks, exploiting novel methodological approaches and considering both spikes and local field potentials; we then manipulated the electrophysiological activity by simply altering the membrane excitability with the cholinergic agonist carbachol (CCh), as reported in previously published works (Tateno et al., 2005; Corner, 2013).
2. We delivered electrical stimuli to cell cultures following CCh administration to determine whether CCh affects the complexity of the evoked response, a phenomenon that has been observed in humans.
3. Based on our previous findings (1), we were interested in understanding how brain electrophysiological signaling is altered in pathologies in which sleep is compromised, such as Prader Willi syndrome. To enable us to understand possible differences in the homeostatic and circadian processes, we complemented the MEA recordings by performing gene expression analysis of both *in vitro* and *in vivo* samples.

The main results regarding **sleep-related electrophysiology** can be summarized as follows:

- **In Chapter 4**, we presented electrophysiological and genetic evidence that primary cortical cultures, which usually display synchronized low-frequency firing patterns under spontaneous conditions, are able to encompass some essential features of sleep in a controllable way. LFP analysis complemented MUA analysis and allowed us to look for classical sleep electrophysiological signatures (i.e., slow waves) in our simplified *in vitro* experimental model. The application of CCh represented an efficient experimental strategy for suppressing classical sleep-like properties of activity, resulting in an asynchronous firing pattern with many isolated spikes. Moreover, administration of CCh induced suppression of delta and theta waves, a range encompassing the entire spectrum of sleep *in vivo*. As a complement to the above experiments, analysis of gene expression profiles confirmed the effects of CCh on the

circadian and synaptic homeostatic components.

- **In Chapter 5**, we showed that the Perturbation Complexity Index computed during the baseline period (i.e., in the absence of CCh stimulation) exhibited values similar to that recorded from humans during sleep. Upon CCh administration, the responsiveness of cortical cultures to stimulation decreased in a manner similar to the results obtained in humans. The increase in PCI observed after CCh administration in the majority of the experiments indicated a more complex responsiveness. Interestingly, the PCI of hippocampal cultures on HDMEAs did not show any variation after the application of norepinephrine.
- **In Chapter 6**, we showed that Prader Willi mice display altered synchronized activity compared to WT mice, as displayed by lower latencies. These results suggest that there is lower connectivity within PWS cultures than in WT cultures at the same developmental stages. Since one of the phenotypes of Snord116 mice is delayed development, we can hypothesize that a similar trend also occurs in the neuronal cultures. The analysis of LFP revealed abnormalities in the theta waves similar to those observed in animals *in vivo* and in PWS patients (Lassi). Gene expression analysis both *in vivo* and *in vitro* showed that Homer1a and Cfos were significantly overexpressed in WT animals after sleep deprivation. In contrast, PWS did not show a rebound after sleep deprivation, suggesting an alteration in the control of the homeostatic process.

The foregoing evidence suggests that MEA recordings coupled to cortical cultures represent a favorable model for investigating the essential neuronal network features of sleep *in vitro* under both physiological and pathological conditions. The next step in this research will be to combine new gene editing technologies such as the CRISPR/cas9 system with MEA recording to accelerate the investigation of loss or gain of function due to gene mutations in sleep studies.

In neuropharmacological studies using MEAs, we performed experiments with both hippocampal cultures and hippocampal slices. The main goal of this project was to evaluate the efficacy of bumetanide in restoring inhibitory GABAergic signaling in Down syndrome mice.

Ts65Dn neuronal networks pretreated with BUME showed restored $GABA_A$ inhibitory signaling. In contrast, no significant effects of bumetanide on GABA/BIC-induced spiking activity were found in cultures prepared from WT mice. Then, because we were interested in a specific region of the hippocampus, we performed preliminary experiments using mouse brain slices on MEA. Our preliminary results confirm our previous observations and suggest that MEA coupled to neuronal networks can be used to predict the effectiveness of new therapies in pathologies that lead to alterations in GABAergic inhibition, such as autism and neurodevelopmental diseases.

Appendix A

1) Slicing sucrose-ACSF

Compound	Concentration (mM)
Sucrose	208
KCl	2
KH_2PO_4	1.25
$MgCl_2*6H_2O$	5
$MgSO_4*6H_2O$	2
$CaCl_2*2H_2O$	0.5
D-Glucose	10
$NaHCO_3$	26
L-Ascorbic Acid	1
Pyruvic Acid	3

2) Holding ACSF

Compound	Concentration (mM)
NaCl	115
KCl	2
KH_2PO_4	1.25

$MgSO_4*6H_2O$	1.3
$CaCl_2*2H_2O$	2
D-Glucose	25
$NaHCO_3$	26
L-Ascorbic Acid	1

3) Recording ACSF

Compound	Concentration (mM)
NaCl	115
KCl	3.75
KH_2PO_4	1.25
$MgSO_4*6H_2O$	0.5
$CaCl_2*2H_2O$	2.4
D-Glucose	25
$NaHCO_3$	26
L-Ascorbic Acid	1